

# Tuning the gel structure with temperature controlled sequential gelation

*Relating mechanical properties and structure in microgel  
self-assemblies*

**Erik Maris, BSc**

supervised by Jasper Immink, MSc

LUND UNIVERSITY  
Dr. Joakim Stenhammar  
Prof. Peter Schurtenberger

UTRECHT UNIVERSITY  
Prof. Albert Philipse  
Prof. Willem Kegel

A thesis presented for the degree of  
Master of Science

March 12, 2017



Physical Chemistry  
Lund University  
Sweden



Physical and Colloid Chemistry  
Utrecht University  
The Netherlands

---

---

## Abstract

---

Control over the properties of amorphous materials requires thorough understanding of the relation between structure and elasticity. Colloidal gels have been used as model system to study morphology and mechanical properties, but correlation between these features has not been addressed. No previous work has exploited the potential of sequential gels to control the gel structure, and an extensive study into its morphological and mechanical properties has not been performed yet. In this thesis, the synthesis and characterisation of a binary thermoresponsive microgel system was performed, which was used to form novel gel structures via sequential gelation. To increase resolvability, a binary core-shell system was synthesised with a fluorescently stained polystyrene core and multiple undyed poly(*N*-isopropylacrylamide) or poly(*N*-isopropylmethacrylamide) microgel shells. Aggregation and the formation of secondary nucleates limited the synthesis conditions to a low monomer to core surface ratio and low monomer concentration. The particles could be synthesised in multiple sequential batches with centrifugation rounds in between to remove small newly formed secondary nucleates, which extended the working synthesis conditions and resulted in secondary nucleate-free samples. Excellent control over size was achieved via scaling of the reactants with the core concentration determined with fluorescence spectroscopy. The core-shell particles exhibited very similar swelling behaviour and elasticity in the pair potential as pure microgel colloids, i.e. microgel particles without a core, and its results could be directly put in the context of pure microgel systems. Morphological features were extracted from three-dimensional reconstructions of the gel volume obtained from confocal microscopy data and simulations, which were compared with experimentally obtained rheological moduli. A clear increase in the rheological moduli was found at the gel-gel transition, indicating an increased rigidity, which was explained from the change of the gel structure and increased interparticle attraction. The second particle type deposited homogeneously on the inner network formed in the first gelation step, and created new links between nearby strands, which could be quantified with respectively the volume over surface and the indirectness. The homogeneous deposition appeared to be caused by a weaker attraction between the decorating particles, which could be a result of the gradual collapse or different density of the two particle types at the experimental temperatures. The sequential gel exhibited ageing in the form of large collective rearrangements. However, before temperature equilibration, the gel rearranged quickly and compacted severely, probably as a result of thermally and mechanically activated rearrangements driven by the increase in temperature. Hence, the exact execution of the temperature quench appeared to be a determining factor in the resulting gel structure, and control over this could be essential to obtain reproducible results.

---

---

## List of abbreviations

---

<b>2D</b>	two-dimensions
<b>3D</b>	three-dimensions
<b>ASD</b>	arrested spinodal decomposition
<b>BD</b>	Brownian dynamics
<b>BIS</b>	<i>N,N'</i> -methylenebisacrylamide
<b>CLSM</b>	confocal laser scanning microscopy
<b>DLCA</b>	diffusion-limited cluster aggregation
<b>DLS</b>	dynamic light scattering
<b>DWS</b>	diffusing-wave spectroscopy
<b>EDL</b>	electrical double layer
<b>FFF</b>	field-flow fractionation
<b>FOM</b>	fluorescein O-methacrylate
<b>IDL</b>	interactive data language
<b>VPTT</b>	volume phase transition temperature
<b>MD</b>	molecular dynamics
<b>MSD</b>	mean squared displacement
<b>MRB</b>	methacryloxyethyl thiocarbamoyl rhodamine B
<b>NA</b>	numerical aperture
<b>NIPAm</b>	<i>N</i> -isopropylacrylamide
<b>NIPMAm</b>	<i>N</i> -isopropylmethacrylamide
<b>PMMA</b>	poly(methyl methacrylate)
<b>PNIPAm</b>	poly( <i>N</i> -isopropylacrylamide)
<b>PNIPMAm</b>	poly( <i>N</i> -isopropylmethacrylamide)
<b>KPS</b>	potassium persulphate
<b>PM</b>	pyrromethene
<b>PS</b>	polystyrene
<b>PSF</b>	point spread function
<b>PTBEMA</b>	poly(2,2,2-tribromoethyl methacrylate)
<b>PTFEMA</b>	poly(2,2,2-trifluoroethyl methacrylate)
<b>RLCA</b>	reaction-limited cluster aggregation
<b>rpm</b>	revolutions per minute
<b>SDS</b>	sodium dodecyl sulphate
<b>SLS</b>	static light scattering
<b>UV-Vis</b>	ultraviolet-visible
<b>V50</b>	2-2'-azobis-(2-amidinopropane hydrochloride)
<b>VPTT</b>	volume phase transition temperature



---

## Acknowledgements

---

It's not easy to say goodbye to Lund, and I'll leave the city with a lot of good and happy memories. The peaceful working environment and nice colleagues make Lund, and the Fysikalisk Kemi group in particular, a place where for many goodbye is only temporary. I would like to thank the many people who have helped me with my research project, showed their work, or accompanied me on my adventures through Sweden.

First of all, I would like to thank **Jasper** for all the time and effort you have put in helping me bringing the research project to a good end, and getting me started-up in Lund. I'm glad that you've taken the time during the first months to help me getting acquainted with the various techniques I had only seen in textbooks. This helped me to work independently later on, and I think that we've found a good balance between supervision and collaboration. Specifically, I would like to thank you for the room you've given me to reshape and extent the research plan, and to try new ideas. I hope that the group, and specifically your PhD will benefit from this.

I would like to thank **Peter Schurtenberger** for having me in the group and giving me to opportunity to choose between various projects. Moreover, you could give me a project with practical work, computer analysis, and simulations, which was exactly what I was looking for. For the simulations, I would like to thank **Joakim** for helping me a lot. Even though the simulations were not a major part of the project, I've learnt a lot from you in this period. Your thorough (or 'anal') way to tackle problems and bugs was very effective and instructive, and you've certainly fuelled my interest in simulations.

**Janne-Mieke, Linda, and Maxime**, it was a pleasure to share an office with you. The random jokes and stories were a welcome break in the hard work. The (mostly) spontaneous discussions in the office were crucial for my understanding of the synthesis, confocal microscopy and image analysis. A special thanks goes to Janne-Mieke for giving me the idea of a core-shell approach, which later formed a major part of my thesis. And Maxime, you still deserve my apologies for giving the plants a hard time during the summer break. I hope that you'll forgive me some day for a year without flowers.

Another big thanks goes out to the department of Physical Chemistry for giving me such a warm welcome. First of all, I would like to acknowledge our technician **Christopher** for making sure that the labs were in order, and the equipment in good condition. **Astrid**, it was a pleasure to share the lab doing synthesis until late in the evening. Your tips and tricks were very helpful to improve the synthesis procedure and my personal lab skills. Both our successes were in the last week, what a coincidence! **Niels**, thank you for the discussions about synthesis and particle morphology, it helped me great deal interpreting the results. I would like to thank **Luigi** for your advice on performing and interpreting rheology experiments. Finally, I would like to thank **Léa** for our discussions about science, these discussions have stimulated me to be critical about science and to work thoroughly.

My time in Lund wouldn't be such an awesome time if it weren't for the people from Mölle and beyond. **Janine, Jojo, Jonas, Maxime, and Mirko**, so many bad jokes, I have rarely laughed so much! Also, **Cláudia, and Jacopo**, what a good time we've had. I won't forget the good food, nice Portuguese wine, and many hours on the couch watching series. **Antoine, Caroline, Claudia, Felix, Gabrielle, Helena, Jasmin, João, Judit, Marianne, Marie, Seb, and Tim**, the caring and tolerant culture at Mölle is one you won't easily find anywhere else, so let's keep the Mölle spirit alive! And last but not least, **Betty, Dèlia, Jasper, Michi, and Vicky**, thanks for the movie nights, parties and other good moments!





---

# Contents

---

<b>1</b>	<b>Introduction</b>	<b>1</b>
1.1	Research outline	3
1.1.1	Research questions	3
1.1.2	Research approach	4
<b>2</b>	<b>Theoretical background</b>	<b>5</b>
2.1	Diffusion	5
2.2	Colloidal volume fraction	6
2.3	Light scattering	6
2.3.1	Static light scattering	7
2.3.2	Dynamic light scattering	8
2.4	Rheology	11
2.5	Confocal laser scanning microscopy	12
2.5.1	Optical resolution	13
2.5.2	Image analysis	14
2.6	Spectroscopy	17
2.6.1	UV-Vis spectroscopy	17
2.6.2	Fluorescence spectroscopy	18
2.7	Viscometry	18
2.8	Electrophoretic mobility measurements	19
2.9	Molecular dynamics simulations	20
2.9.1	Reduced units	22
2.10	Thermoresponsive microgel colloids	23
2.10.1	PNIPAm and PNIPMAM	23
2.10.2	Precipitation and emulsion polymerisation	23
2.10.3	Core-shell particles	27
2.10.4	Morphology of the colloids	27
2.10.5	Interparticle interactions	28
2.11	Colloidal gelation	30
2.11.1	Morphology and mechanical properties	31
2.11.2	Physical ageing	33
2.11.3	Bigels	34
<b>3</b>	<b>Experimental</b>	<b>35</b>
3.1	Synthesis	35
3.1.1	Materials	35
3.1.2	Experimental set-up	35
3.1.3	Pure microgel synthesis	36
3.1.4	Polystyrene core synthesis	37
3.1.5	Microgel shell synthesis	38

3.2	Methods . . . . .	39
3.2.1	Confocal laser scanning microscopy . . . . .	39
3.2.2	Electrophoretic mobility measurements . . . . .	40
3.2.3	Light scattering . . . . .	41
3.2.4	Rheology . . . . .	41
3.2.5	Spectroscopy . . . . .	41
3.2.6	Viscometry . . . . .	42
3.2.7	Simulation . . . . .	42
<b>4</b>	<b>Results and discussion</b>	<b>45</b>
4.1	Colloidal system requirements . . . . .	45
4.1.1	Resolvability in CLSM . . . . .	45
4.2	Synthesis and characterisation . . . . .	46
4.2.1	Pure microgels . . . . .	46
4.2.2	Core-shell particles . . . . .	49
4.2.3	Polystyrene cores . . . . .	50
4.2.4	Microgel shell . . . . .	52
4.2.5	Volume fraction . . . . .	65
4.3	Comparison pure and core-shell microgel particles . . . . .	67
4.3.1	Resolvability in CLSM . . . . .	67
4.3.2	CS21/CS22 model system . . . . .	70
4.4	Gelation . . . . .	75
4.4.1	Single particle gels . . . . .	76
4.4.2	Sequential gels . . . . .	77
4.4.3	Physical ageing gel . . . . .	81
4.4.4	Temperature quench dependency . . . . .	84
<b>5</b>	<b>Conclusions and recommendations for future work</b>	<b>87</b>
	<b>Bibliography</b>	<b>90</b>
<b>A</b>	<b>Supplementary figures</b>	<b>97</b>
<b>B</b>	<b>Diffusing-wave spectroscopy</b>	<b>103</b>
<b>C</b>	<b>List of performed syntheses</b>	<b>107</b>
<b>D</b>	<b>Protocols</b>	<b>111</b>
D.1	Protocol PS cores . . . . .	111
D.2	Protocol CS19 . . . . .	112
D.3	Protocol CS21/CS22 . . . . .	115
<b>E</b>	<b>Modelling and simulation</b>	<b>117</b>
E.1	Benchmark Likos electrostatic potential . . . . .	117
E.2	Diffusion in simulation . . . . .	119
<b>F</b>	<b>Pre- and post-processing skeletonization</b>	<b>121</b>
F.1	Pre-processing . . . . .	121
F.2	Post-processing . . . . .	122
F.3	Analysis . . . . .	124

---

## Introduction

---

Controlling the properties of amorphous materials is one of the main goals in material science. To be able to exert sufficient control, a solid understanding of the relation between structure and mechanical properties of such material is required. An important role is played by colloidal gelation, as colloidal systems have been used as model system to investigate universal features of gels and other amorphous materials for decades [1, 2]. A mainly unexplored subgroup are multi-component gels, which greatly extends the toolbox to study colloidal gelation [2–4]. Appel *et al.* recently demonstrated a new type of bigels, in which a sequential gelation can be achieved by using two types of thermoresponsive microgel colloids [4]. A second particle type is gelled on the gel structure of the first particles giving rise to a novel, and tunable, binary gel state. This system opens the way to extensively study the relation between structure and mechanical properties in colloidal gels, which will be the topic of this thesis.

In contrast to atomic and molecular systems, colloids have size, time and force properties easily accessible in a laboratory. Colloids are nanoparticles with at least one dimension in the range of 1 nm to approximately 1  $\mu\text{m}$ . The colloids referred to in this thesis are solid spherical particles dispersed in a liquid with a diameter of roughly 50 nm to 1  $\mu\text{m}$ . As a consequence of their size, the characteristic time and length scales are separated from that of the dispersion medium, which leads to the use of a coarse grained model. The short time scale of the dispersion medium averages out over the long time scales of the nanoparticles, which means that colloids can be described as particles dispersed in a continuous dispersion medium. According to Evans and Wennerström, this coarse grained regime is exactly what defines the colloidal domain [5]. Since the colloidal size is in the order of the wavelength of visible light, the particles can be studied with light scattering and microscopy techniques. Another consequence of their size is that the thermal motion is much slower than for atomic and molecular systems, allowing dynamical studies which would otherwise be impossible. Additionally, the number of bonds in a volume of atoms or molecules is much higher than in the same volume of colloids, therefore, the force required to disrupt the system is much smaller, which opens the way to study a variety of mechanical properties [1, 5, 6].

The simplest interacting system in the field of soft matter consists of hard spheres, which are finite-sized particles with no interactions other than their excluded volume. The system exhibits well-defined phase behaviour arising solely from excluded volume effects [7–9], which made it the reference system for theoretical and simulational studies for a couple of decades [10]. The link with an experimental hard sphere system was made by Pusey and van Meegen in 1986 [11], when they demonstrated that suspensions of sterically-stabilised poly(methyl methacrylate) colloids (PMMA) underwent a first-order phase transition from a fluid to a crystalline state at the concentration predicted by computer simulations of hard spheres (Fig. 1.1) [12]. A year later, the hard sphere phase diagram was further explored, when it was shown that the PMMA colloids underwent a glass transition, i.e.

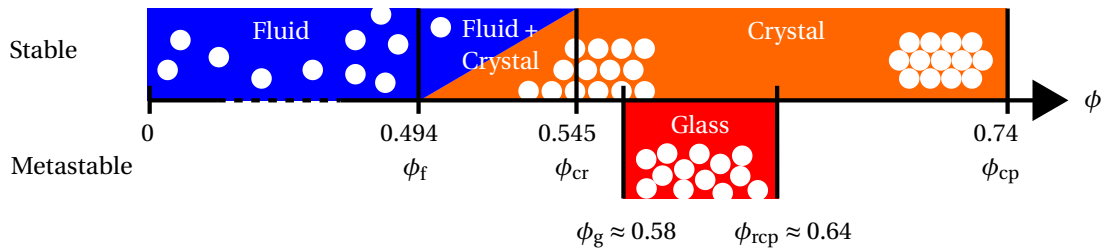


Figure 1.1: A schematic of the stable and metastable phases of a hard spheres dispersion. The phase transitions are solely governed by excluded volume interactions. A glass can be also be formed via a metastable super-cooled liquid state ranging from  $\phi_f$  to  $\phi_g$ , which is not shown here. The volume fraction  $\phi$  is indicated along the axis, where  $\phi_f$  marks the onset of crystallisation,  $\phi_{cr}$  the volume fraction at which the sample is completely crystallised,  $\phi_g$  the glass transition,  $\phi_{rcp}$  the random close packing, and  $\phi_{cp}$  the close packing of a crystal.

to an arrested disordered state, at higher concentrations [13]. In 1991, Pusey argued that Brownian suspensions can be used as experimental equivalent to study condensed matter phenomena such as crystallisation and vitrification, and the ‘colloids as atoms’ paradigm was introduced [14]. However, some differences between atomic and colloidal systems exist. For instance, atomic movement is highly correlated and dominated by collisions with other atoms, while colloids exhibit random Brownian motion due to statistical fluctuations of the surrounding fluid molecules [15]. Furthermore, hydrodynamic interactions influence colloidal motion in complex ways, since colloids interact via the solvent by means of momentum transfer [16–19]. Nevertheless, simulations suggests that long time scale dynamics are similar for both types of systems [19, 20], moreover, a statistical mechanical justification of the ‘colloids as atoms’ analogy can be given [21]. The compatibility with atomic and molecular systems makes colloids an excellent model system, which can be applied beyond the colloidal domain.

Nowadays, the focus is on soft sphere colloids, which in contrast to hard spheres, show a finite repulsion beyond contact, and can have long range interaction giving rise to novel (phase) behaviour [22–26]. The particle interactions are often tunable, which opens the door to model more complex atoms, molecules, and proteins, including anisotropic interactions, to study soft matter theories [27–29]. Moreover, the colloidal field has developed far beyond the modelling application [5, 21], and has found its way to materials science [30], drug delivery systems [31, 32], and catalysis [33, 34]. The particles can be designed as such, that they respond to external stimuli, e.g. temperature and pH, which makes them ideal building blocks for materials which properties can be changed externally, i.e. smart materials [6]. In particular, cross-linked colloidal microgels of poly-*N*-isopropylacrylamide (PNIPAm) or poly-*N*-isopropylmethacrylamide (PNIPMAM) can undergo reversible volume phase transitions upon change of pH, ionic strength or temperature. Specifically, above the volume phase transition temperature (VPTT), the microgel network expels water and undergoes a rapid decrease in size (Fig. 1.2) [30, 35, 36]. This can be exploited to tune the soft interaction potential from repulsive to short-range attractive by only changing the temperature, which results in the formation of a gel structure [37, 38].

A gel is an arrested space-spanning network, which is capable of bearing mechanical stress. Reversible short-range colloidal attraction induces a phase separation in colloid-poor and colloid-rich regimes. At sufficiently high volume fraction, the colloid-rich regions interconnect and solidify. This results in a network of arrested glassy, disordered colloidal strands which are held together by interparticle attraction [39, 40]. Colloidal gels can be found in numerous applications including protein assemblies [41, 42], food science [43], soft matter [1], and biological scaffolds for tissue support and drug release [44, 45]. Despite the numerous studies on the matter, finding the relation between me-

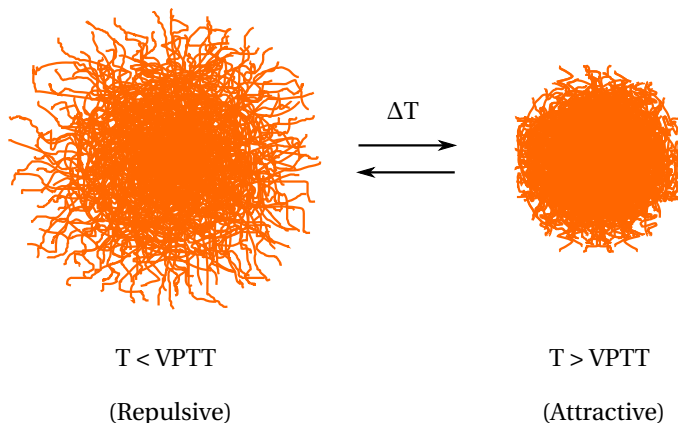


Figure 1.2: Schematic of the reversible volume phase transition of a microgel particle around the volume phase transition temperature (VPTT). Under certain conditions, this can be used to tune interaction potential from repulsive to attractive and vice-versa.

chanical and structural properties is still an open challenge [40, 46].

In order to study the relation between structure and mechanics in sequential gelation, the interaction potential of a two-component system should be independently tunable from attractive to repulsive. To the best of the authors knowledge, a binary mixture of thermoresponsive microgel colloids such as PNIPAm and PNIPMAm, which components exhibit a different VPTT, is the only system in which it is possible to achieve this without disrupting the system. The only research up to date on this topic has been reported by Appel *et al.*, who has found a decorated gel network as result of sequential gelation [4]. The bigel consisted of an inner gel network composed of the microgels with the lowest VPTT, which served as a scaffold for the gelation of the other type of microgel (Fig. 1.3). The overall gel structure appeared to be retained, but the strand thickness had increased. Around equal particle mixing ratios, a clear increase in elasticity was found around each aggregation temperature, which reflects the formation of the inner gel structure and the gelation on top of the existing strands. As the structure of a gel is closely related to the elasticity of the gel network, strand thickness and openness of the gel will result in a different bending and stretching of the gel structure, which alters the mechanical properties. Moreover, the strength of the interparticle attraction can be tuned, which is expected to affect the elasticity of the material. Due to the reversibility of the aggregation, the gel formation can be repeated many times from reproducible initial conditions. Sequential gelation offers a unique approach to study the mechanical properties as function of systematic variation in gel structure and attraction strength [4, 40]. This will lead to a better understanding of colloidal gels, which ultimately can lead to control over the properties of amorphous materials.

## 1.1 Research outline

In this thesis, sequential gelation is studied with a binary mixture of thermoresponsive PNIPAm and PNIPMAm. The simplest possible binary model system is synthesised first, in which the particles are identical in size and charge, and the system is characterised. The colloids are mixed in an 1:1 ratio, and the structure and mechanical properties of the gel phase are studied. Simulations are performed, which results are compared with experimentally obtained structures.

### 1.1.1 Research questions

The research consists of two components, on one hand to relate material properties to morphology by experiments, and on the other hand to explain the observed structure with a model involving an

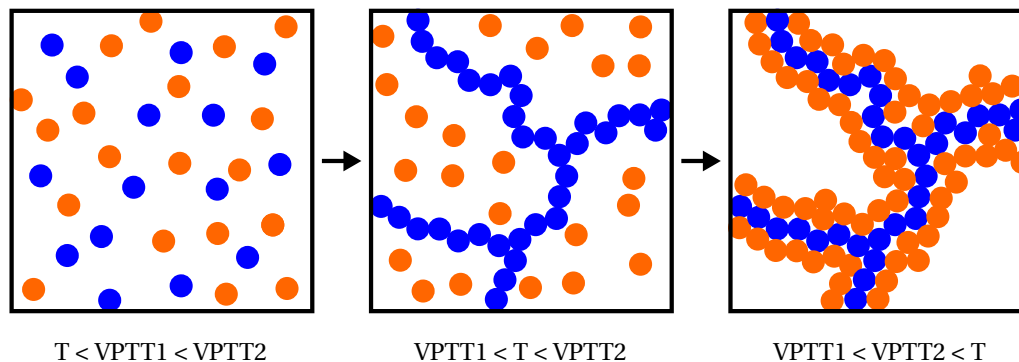


Figure 1.3: A schematic representation of sequential gelation scenario in a binary microgel system with different volume phase transition temperatures ( $VPPT$ ). Here, the blue particles have a  $VPPT1$  and the orange ones a  $VPPT2$ . When the temperature is increased above  $VPPT1$ , but below  $VPPT2$ , only the blue particles are attractive and form an inner network. Decoration of the inner network occurs when the temperature is increased above  $VPPT2$ .

attractive pair potential. The research questions addressed in this thesis are:

1. Can the proposed model system be used to study sequential gels with both fluorescence confocal microscopy and rheological methods?
2. How does the gel structure and its mechanical properties change as a result of the sequential gelation step?
3. Can a model involving only short-ranged attraction reproduce and explain the morphology of a gel formed by sequential gelation?

### 1.1.2 Research approach

In this thesis, the structural and elastic properties of sequential gels are investigated. For comparison, the experiments are performed at fixed temperatures with a constant ionic strength. The structure of the gel is characterised by means of confocal laser scanning microscopy via a three-dimensional (3D) reconstruction of the structure. Brownian Dynamics simulations are performed, of which the 3D volume could be analysed with the same methods as the microscopy data. The structural properties can either be derived from the individual particle coordinates or the collective structure. By fitting the model used in the simulations to the experimental structure, the type and magnitude of the interparticle interactions can be investigated. The elastic properties are investigated by means of mechanical rheology, which results are related to the gel structure.

In order to be able to do these analyses, the traditional ‘pure’ microgel model system is re-evaluated and re-designed. A set of syntheses are performed to acquire a system with the required properties, and control over the particle properties of the model system is attempted. The system is characterised and benchmarked against the traditional microgel system before proceeding with the study of sequential gelation.

---

## Theoretical background

---

A theoretical discussion of the general background, experimental methods, and synthesis and gelation of (microgel) colloids is given in this chapter. In Sections 2.1 and 2.2, diffusion and the volume fraction in colloidal systems are discussed. The experimental methods are covered in Sections 2.3 to 2.9, including light scattering, rheology, spectroscopy, viscometry, electrophoretic mobility measurements, and molecular dynamics simulations. The chapter is concluded in Sections 2.10 and 2.11 with a thorough discussion of the synthesis of microgel colloids, its interparticle interactions, and colloidal gelation.

### 2.1 Diffusion

Diffusion is crucial for understanding particle dynamics in many systems, including arrested ones. At any non-zero temperature, particles have thermal energy and thereby exhibit motion. Atoms or molecules move in a randomized fashion due to collisions with other particles. In this inertia dominated-regime, called ballistic, the particle's motion is highly correlated, and the particles can be considered having a direction and velocity [15, 47]. However, colloids suspended in a medium move around in a random fashion due to the amplification of the statistical fluctuations of the surrounding fluid molecules [48]. Since collisions with the solvent particles have random directions, the average spatial displacement  $\langle \Delta r \rangle$  is zero, but the mean square displacement (MSD) is not. The MSD is defined as

$$\langle \Delta r^2 \rangle = \langle [r(t + \Delta t) - r(t)]^2 \rangle = 2nD\Delta t, \quad (2.1)$$

with  $n$  being the dimensionality and  $D$  the diffusion coefficient, [20, 49, 50]. The distance a dispersed colloid travels is determined by the energy dissipation to the surroundings, and is proportional to the damping of the solvent. So from Eq. 2.2, it can be seen that diffusion is driven by the thermal energy  $k_B T$  and damped by a viscous force. Diffusion without a force- or concentration gradient is called self-diffusion, which will be the focus here. The translational diffusion  $D_0$  coefficient for a single free colloid dispersed in a liquid solvent was given by Einstein [48, 50]

$$D_0 = \frac{k_B T}{f} \quad (2.2)$$

in which  $f$  is the friction factor and  $k_B$  Boltzmann's constant. Eq. 2.2 combined with the Stokes friction factor  $f = 6\pi\eta R_H$  for spherical particles with hydrodynamic radius  $R_H$  suspended in a solvent with viscosity  $\eta$ , yields the Stokes-Einstein (SE) (or Stokes-Einstein-Sutherland) equation [48, 50, 51]

$$D_0 = \frac{k_B T}{6\pi\eta R_H}. \quad (2.3)$$

Self-diffusion of particles in the liquid phase in absence of hydrodynamic interactions is very well understood via the equations shown above.

For gels and other dense systems,  $D_0$  must be split in a short time self-diffusion coefficient  $D_S$  and a long time self-diffusion coefficient, which can be defined in three-dimensions as

$$D_L \equiv \lim_{t \rightarrow \infty} \frac{\langle \Delta r^2 \rangle}{6\Delta t}. \quad (2.4)$$

On short time scales, particles in a gel will exhibit Brownian motion and  $D_S > 0$ . The magnitude of the displacement driven by Brownian motion is related to the bond strength between the neighbouring particles. At longer time scales, the system is arrested and does not move leading to  $D_L = 0$ . The MSD versus time reaches a plateau value for the MSD, which is related to the spring constant of the interparticle bonds.

## 2.2 Colloidal volume fraction

The volume fraction  $\phi$  of a colloidal dispersion with  $N$  spheres of radius  $R$  is defined as

$$\phi = \frac{V_{\text{spheres}}}{V_{\text{total}}} = \frac{4\pi R^3 N}{3V_{\text{total}}}. \quad (2.5)$$

The behaviour of an ideal monodisperse hard sphere suspension is fully controlled by this one parameter, as the phase behaviour is fully driven by excluded volume interactions (Fig. 1.1). Since the early days of colloid science,  $\phi$  has become the standard to characterise colloidal suspensions. In the case of hard spheres, comparison between theory, simulations, and experiments by means of  $\phi$  is straightforward under the condition that it can be obtained accurately from real samples. However, the volume fraction is not as well defined once samples have a significant size distribution, and more complex interactions are involved due to charge and/or soft-sphere character. An effective volume fraction  $\phi_{\text{eff}}$  is adopted in the case of soft microgel particles, which gives a volume fraction of non-hard sphere colloids as if they exhibit pure hard sphere behaviour. Even in the hard sphere case, Poon *et al.* concluded that the volume fraction cannot be determined more accurately than 3-6% error in experiment [10]. Thus the volume fraction is dependent on experimental conditions and the system studied, and requires careful interpretation.

## 2.3 Light scattering

Light scattering techniques are an important tool to study colloidal systems, because the typical length scales, i.e. size and interparticle distance, are on the order of the wavelength of visible light. Scattering is a general phenomenon that occurs when a wave passes through a medium with inhomogeneities, which is a refractive index mismatch in the case of visible light. When light passes through a sample, discrete charges in a material start to oscillate due to the electric field of the electromagnetic wave. Accelerated charges emit waves in all directions, which is the microscopic origin of scattering. If no energy (or little in practice) dissipates during this conversion, the scattering is called to be elastic, which is the case for light scattering discussed in this thesis. The light scattered by a medium is the sum of the scattering of all its subvolumes. In a homogeneous medium, there is always a subvolume half a wavelength away that scatters exactly out of phase, which leads to a total cancellation of all light except in the forward direction. However, for a heterogeneous medium, this argument does not hold because a different material with a different refractive index, i.e. phase length, is present half a wavelength away. No total cancellation of scattered light occurs, and some light is scattered towards another angle than the forward direction [6]. The light scattering techniques discussed in this section are dynamic light scattering (DLS), and static light scattering (SLS). In order to understand the working principle of these techniques, light scattering by simple objects is discussed in the next paragraph.



Two regimes can be discriminated based on the size of the particle with respect to the wavelength of the light. In the case of a particle which is much smaller than the wavelength of the incoming light ( $r \ll \lambda$ ), the particle is in the Rayleigh regime. The particle can be approximated as a single homogeneous induced dipole with a scattering intensity

$$I_S = I_0 \frac{r^6 (1 + \cos^2 \theta)}{2R^2} \left( \frac{2\pi}{\lambda} \right)^4 \left( \frac{m^2 - 1}{m^2 + 2} \right)^2 \quad (2.6)$$

for spherical particles subjected to unpolarised light, with  $I_0$  the intensity of the incoming light,  $\theta$  the angle between the incident beam and the detector,  $R$  the distance to the detector, and  $m$  the ratio between the refractive index of the particle  $n_p$  and medium  $n_0$ . Note the angular and the  $\lambda^{-4}$  dependence of the scattered intensity. In addition, a smaller mismatch in the relative refractive index  $m$  leads to a lower scattering intensity, up to a total elimination for  $m = 1$ . In the situation where the size of the particle is in the order of the wavelength of the incoming light ( $r \approx \lambda$ ), the Rayleigh approximation does not hold any more. Instead of a single homogeneous dipole, the material has to be modelled as an ensemble of oscillating dipoles with the same frequency, but another phase. The resulting  $I_S$  is a superposition of the scattering by all dipoles in the particle. The resulting signal is very complex and can only be solved analytically in a few cases. For spherical particles, this set of equations and its solutions are called Mie theory, which must be evaluated with a computer. The colloids described in this thesis are in the Mie regime, however, for  $m \approx 1$  the Rayleigh approximation holds for these particles as well [6].

A refractive index mismatch between the solvent and the particle results in light scattering. To illustrate this, Rayleigh conditions are assumed for the moment, which does not hold in reality. Even the expanded PNIPAm of 600 nm in diameter, which has a small refractive index mismatch, gives a strongly forward scattering profile according to Mie theory, and the calculated scattering below is simply a ballpark figure. The following proportionality can be taken for a Rayleigh scatterer (Eq. 2.6)

$$I_S \propto \left( \frac{m^2 - 1}{m^2 + 2} \right)^2. \quad (2.7)$$

The refractive index of PS, water, and PNIPAm below and above the VPTT are respectively 1.60, 1.33, 1.34, and 1.42 around 500 nm [52, 53]. The scattering of the microgel increases  $\sim 80$  times upon collapsing in this model, but the PS contributes to a large fraction of the scattering with  $\sim 670$  times more scattered intensity with respect to the expanded PNIPAm. It is clear that scattering is an intrinsic property of the microgel system above the VPTT, however, the PS content should be minimal to reduce scattering as much as possible.

### 2.3.1 Static light scattering

SLS is widely used in the soft matter field to determine size and structure of colloids and colloidal systems. A cylindrical cuvet is illuminated with a laser beam and the intensity of the outgoing light is measured as a function of  $\theta$  (Fig. 2.1a). By fitting the model outlined in the next paragraph to the experimental data, the desired parameters can be obtained.

#### Theory

The scattered light intensity can be calculated rather easily by using the Rayleigh-Gans-Debye (RDG) theory, which derivation is similar to Eq. 2.6 but with the finite size of the particle taken into consideration. Its assumptions hold only when the scattering is not extremely strong, which is true if the following conditions are met

$$|1 - m| \ll 1 \quad (2.8)$$

$$\frac{2\pi n_s}{\lambda} \alpha |1 - m| \ll 1, \quad (2.9)$$

where  $m$  is the relative refractive index,  $n_s$  the refractive index of the medium,  $\lambda$  the wavelength of light and  $\alpha$  the diameter of the colloidal particle. Within this assumption, each small particle portion is hit by the same electromagnetic radiation emitted from the light source and scatters light as independent from the rest of the particle. The following proportionality is found upon derivation [6]

$$I(q) \propto P(q) \equiv \frac{I(q)}{I(0)} \quad (2.10)$$

in which  $P(q)$  is called the form factor and  $q$  the length of the scattering vector, given by

$$q = |\vec{q}| = \frac{4\pi n_0}{\lambda} \sin\left(\frac{\theta}{2}\right), \quad (2.11)$$

with  $n_0$  the refractive index of the solution. Here, the scattering vector is defined as  $\vec{q} = \vec{k}_s - \vec{k}_i$  with  $\vec{k}_s$  the wave vector of the scattered wave, and  $\vec{k}_i$  the wave wavevector of the incident wave (Fig. 2.1a). The scattering particle can be seen as a collection of point scatterers. The form factor describes the interference of the scattered light as function of to the distribution of the point scatterers, i.e. the size and shape of the particle. In the case of a spherical particle, the form factor is found to be [6]

$$P(q) = \left[ 3 \frac{\sin(qR) - qR \cos(qR)}{(qR)^3} \right]^2. \quad (2.12)$$

This function is shown in Fig. 2.1b, however, in a polydisperse sample, the measured signal is a superposition of many sizes which causes the position of the minima to smear. Since the form factor originates from the structure, SLS is a powerful tool to test a structural model with experimental data. For microgel particles, the structure is not a homogeneous sphere, and comparison with the latest models will be made in Section 2.10.4.

Once particles start to interact, the scattered light of the different particles will interfere, and an additional factor should be taken into account,

$$I(q) \propto P(q) \cdot S(q). \quad (2.13)$$

The structure factor  $S(q)$  contains information about the ordering of the particles and can be transformed into the radial distribution function. By performing measurements in the dilute regime, as is done in this thesis, the signal will not interfere and the form factor alone can be obtained [6].

### 2.3.2 Dynamic light scattering

The time-dependent intensity fluctuations of the scattered light are measured in a DLS measurement, which can be used to derive the size of a colloid. Interference of the outgoing light creates speckles, which intensity fluctuates over time due to Brownian motion of the scattering colloids (Fig. 2.2a). By analysing a small scattering volume with a high time resolution, the intensity fluctuation of a single speckle can be measured and correlated over time (Fig. 2.2b). The fluctuations of the scattered light are caused by Brownian motion of the dispersed particles. Bigger particles exhibit slower Brownian motion, which leads to slower overall intensity fluctuations. This can be ultimately used to calculate the diffusion constant, from which the hydrodynamic radius  $R_H$  can be obtained [6, 54].

#### Theory

The intensity fluctuation of a speckle can be parametrized by its autocorrelation function

$$g_2(\tau) = \frac{\langle I(t)I(t+\tau) \rangle}{\langle I(t) \rangle^2} \quad (2.14)$$

at a specific wave vector, where  $\tau$  denotes the lag time,  $I$  the intensity of the speckle, and  $\langle \dots \rangle$  the time average. This can be directly related to the autocorrelation function of the scattered fields via the Siegert relation

$$g_1(\tau) = \frac{1}{\sqrt{\beta}} \sqrt{g_2(\tau) - 1} \quad (2.15)$$

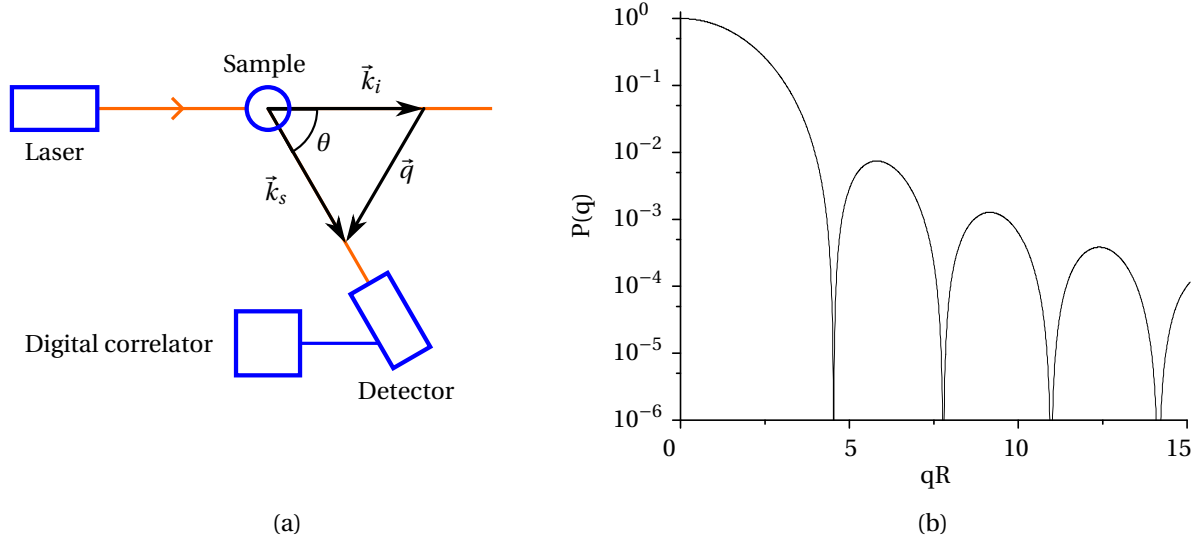


Figure 2.1: a): A schematic representation of an SLS and DLS light scattering set-up from above. The detector measures the intensity of the scattered wave at an angle  $\theta$ . In an SLS experiment, the intensity is probed as function of  $\theta$ , i.e. measured at multiple  $\vec{q}$  values, while in a DLS experiment, the intensity fluctuations in the scattered light are measured at a fixed  $\theta$  and correlated in a digital correlator. b): A plot of the form factor  $P(q)$  of a sphere as function of the length of the scattering vector  $\vec{q}$  multiplied by the radius of the sphere  $R$  (Eq. 2.12).

where  $\beta$  is a parameter dependent on the experimental set-up. It can be shown that for a monodisperse sample of spherical particles,  $g_1(\tau)$  decays exponentially in the form of

$$g_1(\tau) = e^{-\Gamma\tau} \text{ with } \Gamma = q^2 D \quad (2.16)$$

with  $\Gamma$  being the decay rate, which yields

$$\ln \sqrt{g_2(\tau) - 1} = \ln(A) - \Gamma\tau \text{ with } A = \sqrt{\beta}. \quad (2.17)$$

after plugging in Eq. 2.15 and taking the natural logarithm (Fig. 2.2c). The hydrodynamic radius  $R_H$  can be obtained via the Stokes-Einstein relation (Eq. 2.3) [6, 54].

Two procedures to fit DLS data are presented in this subsection, firstly the cumulant method is introduced and secondly the CONTIN method. A plot of the left-hand side of Eq. 2.17 against  $\tau$  yields a straight line for monodisperse samples. However, to take polydispersity into account the model must be expanded, and one of the simplest ways is to do a Taylor series expansion of  $\ln g_1(\tau)$ , which is called the cumulant expansion. The second cumulant is

$$\ln \sqrt{g_2(\tau) - 1} = \ln(A) - \Gamma\tau + \frac{\mu_2}{2} \tau^2 \quad (2.18)$$

with  $\mu_2$  being a measure for the width, i.e. polydispersity, of the sample. The hydrodynamic radius can be obtained from a fit of the first cumulant expansion (Eq. 2.17) or the second cumulant expansion (Eq. 2.18). This model is used throughout this thesis to extract the particle radius from DLS data, and to obtain an indication of the polydispersity. Another widely used technique is the CONTIN method, which has an advantage over the cumulant method, because it is capable of resolving particle size distributions. A multi exponential fit with  $n$  fractions is done following

$$g_1(\tau) = \frac{1}{n} \sum_{i=1}^n w_i(\Gamma_i) e^{-\Gamma_i \tau} \quad (2.19)$$

with  $w_i(\Gamma_i)$  a weighing function of the contribution of particles in size range  $i$ . However, in most cases the cumulant method is the easiest and most reliable option to extract size (distributions) from the autocorrelation function [54].

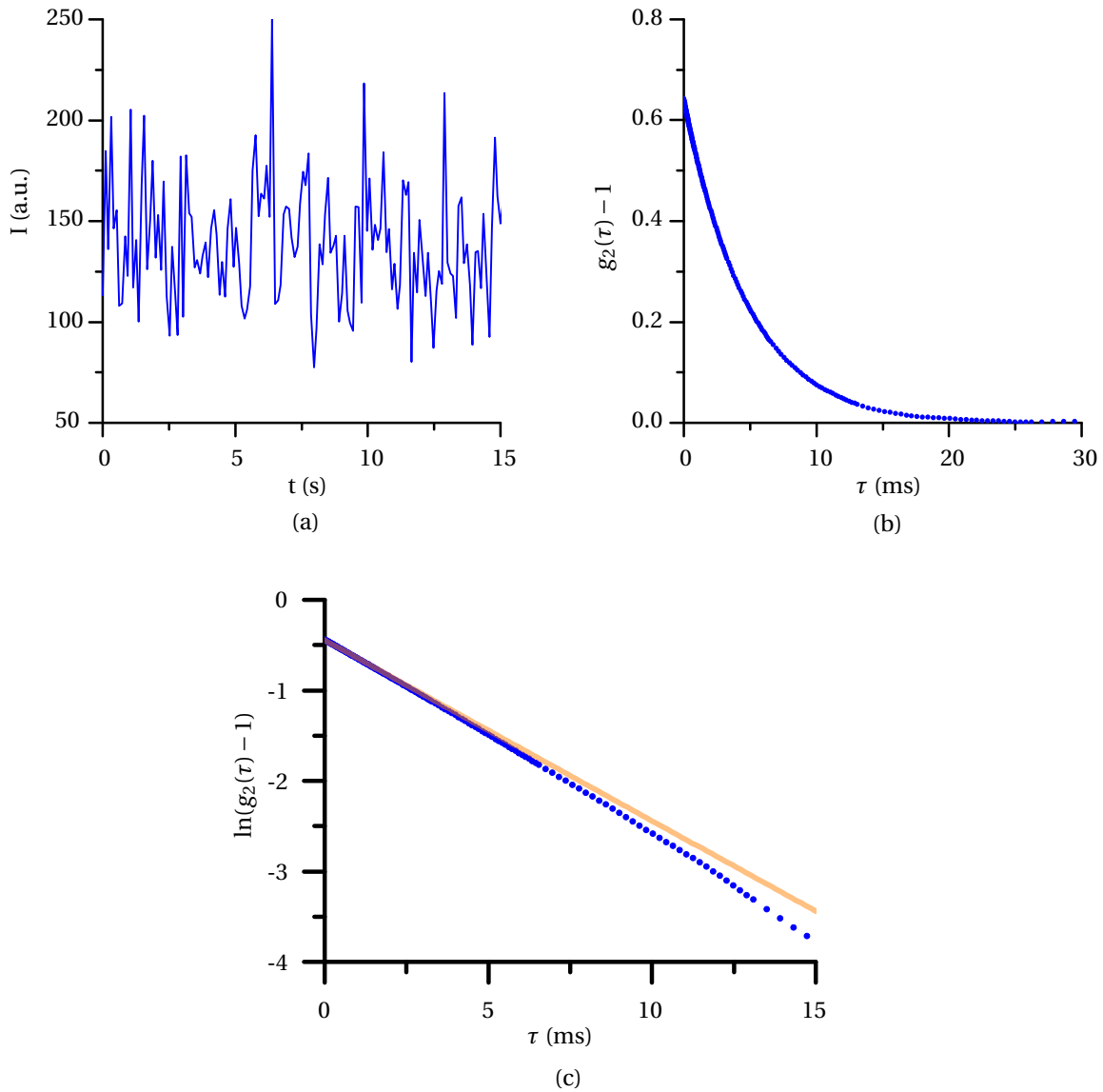


Figure 2.2: a): Example Intensity fluctuations over time as measured directly by the detector. b): Intensity autocorrelation function as outputted by the digital correlator. c): Fit of (b) by the first cumulant Eq. 2.17 up to 5 ms. The fit is usually done in the short lag time  $\tau$  regime, since the data diverges at longer  $\tau$ . The data shown in this example was obtained from a 200 nm microgel sample at 20 °C.

## Method

A DLS measurement is done at a fixed  $\theta$  in same set-up as used for SLS measurements, however a *coherent* laser beam is required here (Fig. 2.1a). The theory described above assumes that the intensity fluctuations originate from single scattering events. In general, this condition can be met by using very dilute samples [6, 54]. Additionally, the few multiple scattering events could be suppressed by including a 3D cross-correlator in the set-up (not shown) [55]. The incident laser beam is split into two beams with a similar wave vector. These beams are focused in the same sample volume and individually measured at a similar  $q$ . As two simultaneous light scattering experiments are performed at the same scattering vector on the same sample volume, the single scattering contribution will be identical in both experiments, but the multiple scattering contribution will be different. However, each detector receives a contribution of scattered intensity originating from both laser beams. As a consequence of the geometry of the set-up, the  $q$  values of both beams with respect to the detector

are slightly different, which results in a very low correlation and thus poor fitting. This issue can be greatly reduced with a modulation unit, which alternates the corresponding beam and detector in high frequency, and thereby separating the light scattering events at different  $q$  in time [55]. Concluding, with modulated 3D cross-correlation light scattering, the multiple scattering contribution can be reduced and more reliable data can be obtained.

## 2.4 Rheology

In rheology, the response of a liquid- or solid-like substance to an applied stress is quantified. This gives information about the flow and deformation behaviour of a material. The obtained quantities play an important role in characterisation of gel structures.

### Theory

A rheometer measures the response of a material when stress in the form of a displaced or moving surface is applied. The material can respond to the stress in different ways, and the two extrema, i.e. an Hookean solid and a Newtonian liquid, are depicted in Fig. 2.3ab. An ideal Hookean solid deformed by a distance  $\Delta x$  would recover its original conformation after removal of the stress (Fig. 2.3a). The shear stress  $\sigma$ , which is defined as the force per area, required for this deformation is given by

$$\sigma = G \frac{\Delta x}{h} = G\gamma, \quad (2.20)$$

with  $h$  being the distance between the surfaces, and  $\gamma(= \Delta x/h)$  the shear strain. In order to relate the stress and the strain, a material dependent proportionality factor  $G$  is required. This factor is called the shear modulus and contains information about the stiffness of the material. An ideal Newtonian fluid would not elastically deform like a solid, but instead starts to flow when subjected to an external stress, and a velocity gradient develops between the fixed lower surface and the moving upper one (Fig. 2.3b). The shear stress required to maintain a fluid velocity  $v_x$  next to the moving surface (with no-slip boundary conditions) of an ideal Newtonian fluid is given by

$$\sigma = \eta \frac{v_x}{h} = \eta\dot{\gamma}, \quad (2.21)$$

with  $\dot{\gamma}$  being the shear rate and  $\eta(= \sigma/\dot{\gamma})$  the shear viscosity. The viscosity quantifies the resistance to gradual deformation [20, 56].

Essentially, the elastic ideal Hookean solid stores the energy that is put into the material, while in an ideal Newtonian fluid, the energy dissipates within the viscous sample. Most materials, including colloidal suspensions, reside between these two extrema and exhibit both elastic and viscous properties. Viscoelastic materials exhibit time dependent strain, which can be studied by application of a low amplitude varying strain in the form of  $\gamma = \gamma_0 \sin(\omega t)$  with an angular velocity  $\omega$ . This contains information about the time the system needs to restore itself. If the elastic stress is dependent on the oscillatory shear strain (Eq. 2.20),  $\sin(\omega t)$ , then the viscous stress is dependent on its derivative (Eq. 2.21),  $\cos(\omega t)$ . So, for viscoelastic materials, a formula for the shear stress can be constructed which combines both the elastic and viscous properties of the system. By defining two new shear moduli, the storage modulus  $G'(\omega)$  and the loss modulus  $G''(\omega)$ , this formula is given by

$$\sigma(t) = \gamma_0 [G' \sin(\omega t) + G'' \cos(\omega t)]. \quad (2.22)$$

Analogous to a damped spring, the elastic part ( $G'$ ) is in-phase with the stress, while the viscous part ( $G''$ ) is  $\pi/2$  out-of-phase (Fig. 2.3c) [20, 56]. The ratio between the  $G'$  and  $G''$  is called  $\tan \delta$ , which quantifies the damping of a material. A larger  $\tan \delta$  corresponds to a greater damping coefficient, which means that the material will be more efficient in energy absorption and dispersion. These quantities are the most important parameters to describe to flow and deformation behaviour of a

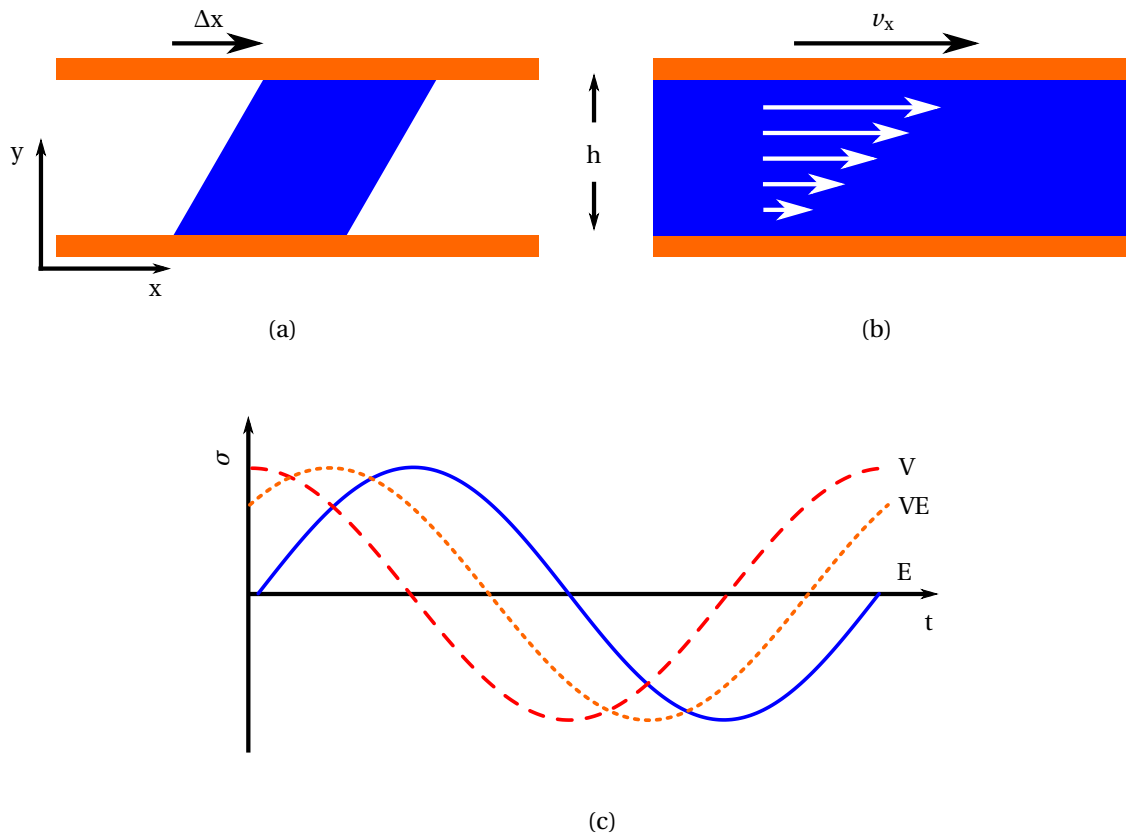


Figure 2.3: a,b): Schematic representation of the interior of a rheometer, consisting of a fixed bottom plate and a displaced or moving upper plate, which is used to measure the feedback of the system. The elastic deformation of an ideal Hookean solid (a) and the viscous flow of an ideal Newtonian fluid (b) are depicted. c): Shear stress under oscillatory flow for viscous (V), elastic (E), and viscoelastic (VE) materials.

material. In order to compare the rheological moduli between samples, the measurements should be done at a deformation within the linear visco-elastic regime, which is indicated by a range of deformations at which the rheological moduli remain constant.

## Method

Mechanical rotational rheology measurements are done in a rheometer. The sample is loaded into the gap of a measuring system, or geometry, which is specifically designed to impose simple shear flow on the sample when rotated. The Couette geometry consists of a cylindrical bucket with a solid cylindrical plunger hung in the middle. The bucket is connected to a micro stepper motor, which applies a stress on the sample by rotating. The response is measured with a transducer, which is connected to the plunger and measures the axial and rotational force.

## 2.5 Confocal laser scanning microscopy

Confocal laser scanning microscopy (CLSM) is an optical technique to image fluorescent samples. The main advantages over widefield optical microscopy are the ability to filter out-of-focus light and the shallow depth of field. These properties make it possible to acquire a 3D image of a sample by scanning along the  $z$ -direction [57]. Confocal microscopy images combined with particle tracking protocols provide a way to extract radial distribution functions and other structural properties of e.g. fluorescently labelled colloidal systems [58, 59].

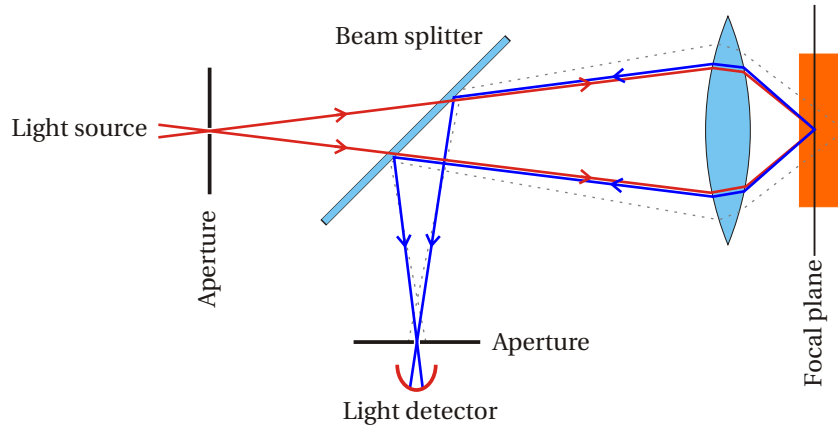


Figure 2.4: A schematic representation of the a confocal microscopy setup. The optical path of the excitation light is shown (red line), and the signal of the emitted light by the fluorophore (blue line), as well as the out-of-focus signal (dashed line). Adapted from Wikipedia.

## Method

A schematic representation of a confocal setup is shown in Fig. 2.4. Modern confocal microscopes use a focused laser beam to illuminate the sample, of which their wavelength should be able to excite the fluorophore. The laser light is focused in the sample via a set of mirrors and lenses. A set of tilting mirrors in the x- and y-direction, which are located in the scan head, direct the focused laser beam in a raster fashion though the sample building up the image pixel-by-pixel. Movement in z-direction by the sample stage completes scanning in all three dimensions. The emitted light travels back and is separated from the incident beam by a beam splitter. The emission is projected on the detector after passing through an aperture, which is called a diaphragm or pinhole. Due to the point illumination in the sample, the out-of-focus emission is filtered by this pinhole, ensuring a high resolution in the focal plane. The pinhole defines thickness of the optical slice, where a thinner slice goes at the expense of the light collection. A sensitive photomultiplier tube detector is required, since only a small fraction of the emitted light of a small volume of fluorophores arrives at the detector [57].

Additionally, a confocal microscope can be operated in brightfield mode, in which the transmission through a sample is recorded. A continuous light source is focused on the sample, and like in fluorescence confocal microscopy, the out-of-focus light is eliminated via a diaphragm [57].

### 2.5.1 Optical resolution

The spatial resolution is defined as the smallest resolvable distance between two points in an image. Theoretically, the spatial resolution is restricted by the numerical aperture (NA) of the objective and by the wavelength of the incident and detected light, i.e. excitation and emission. The NA is a dimensionless number that characterises the angular range over which the optical device can receive light. These factors determine the size of the Airy disk, which is the smallest focused spot of light a perfect lens with a circular aperture can make. The signal from a point source has a diffraction pattern, which intrinsically limits the size of the Airy disk. This means that a point source would be imaged as a 3D object with a finite size, which is called the intensity point spread function (PSF) and limits the resolution of a perfect optical microscope. It is common to define the resolution  $R$  as the spatial distance at which the first diffraction minimum of one Airy disk overlaps with the centre of a second Airy disk. This is called the Rayleigh criterion and is, for widefield microscopes,

$$R = 0.61 \frac{\lambda}{\text{NA}} \quad (2.23)$$

with  $\lambda$  being the wavelength of the light. However, for fluorescence microscopy, the resolution is dependent on the geometric mean of the excitation ( $\lambda_{\text{ex}}$ ) and emission wavelength ( $\lambda_{\text{em}}$ ). The resolution in the  $x, y$ -plane of a fluorescence confocal microscope can be approximated as

$$R_{x,y} \approx \frac{0.32}{\text{NA}} \sqrt{\lambda_{\text{ex}} \lambda_{\text{em}}} \quad (2.24)$$

and along the  $z$ -axis as

$$R_z \approx \frac{1.3n}{\text{NA}^2} \sqrt{\lambda_{\text{ex}} \lambda_{\text{em}}} \quad (2.25)$$

with  $n$  defined as the index of refraction of the sample medium. From these equations, it can be seen that the resolution of a confocal microscope is higher than that of a widefield microscope [57, 60, 61].

## 2.5.2 Image analysis

### Particle tracking

Images of colloidal structures can be converted into quantitative data on particle motion and structure via image analysis routines. Many static and dynamic phenomena can be studied, including diffusion via the MSD, interactions by determining the pair-correlation functions in a dilute suspension, and structure and phase transitions by tracking the particles in three dimensions (3D) [59].

The most established routines for particle tracking and analysis are the ones from Crocker and Grier, which were developed in the 90's [58]. These routines are written in Interactive Data Language (IDL), which is a programming language much used for image analysis, mainly because it can process large amounts of data. Once a particle is imaged with a microscope, the continuous object is captured into discrete pixels, which is shown in Fig. 2.5. The main feature of the image analysis routines is to recover a continuous description of the particle from a discrete image. Once the particle positions are obtained, the movement and structure of the particles can be quantified.

For the image manipulations and fitting of the particles, the image analysis routines assume a Gaussian intensity distribution of the particle. The recorded image is first blurred to eliminate single pixel noise and to smoothen the particle shape (Fig. 2.5). A pixel's intensity is averaged with a specified number of neighbouring pixels. Since a Gaussian intensity distribution of the particle is assumed, the averaging is weighed with a Gaussian distribution, i.e. Gaussian blur. Subsequently, a spatial band pass filter is applied to increase the contrast of the particle with its background. A priori knowledge about the particle's size, which is manually determined (red dashed lines Fig. 2.5), together with the local intensity maxima are used to specify the regions for application of the band pass. The intensity in these regions is increased, while the intensity outside these regions is reduced (respectively green and red areas in Fig. 2.5). The continuous description of a particle is obtained from a Gaussian fit around a local intensity maximum in the processed image, which can be done in 2D and 3D. Particle positions in 3D can be reconstructed from stacked images along the  $z$ -direction, however, this requires non-moving particles on the time scale of acquisition. Sub-pixel resolution can be extracted via the particle fit if the image is not greatly oversampled, otherwise the pixels are too small for interpolation.

Once the particle coordinates are known, the dynamical and structural phenomena can be quantified. The dynamics are usually captured in the MSD, which can be converted into the diffusion coefficient. For this, particles positions in a time series are linked if they are within a certain distance between the frames. The complete trajectory of particles in the focal plane can be reconstructed in this way. Structure can be quantified via the pair-correlation function  $g^{(2)}(\vec{r}_1, \vec{r}_2)$  and radial distribution function  $g^{(2)}(r_{12})$ . The pair distribution function  $\rho^{(2)}(\vec{r}_1, \vec{r}_2)$  is the probability to find any particle in  $d\vec{r}_1$ , and at the same time any other particle in  $d\vec{r}_2$ . Comparison between different datasets is straightforward after normalisation of  $\rho^{(2)}(\vec{r}_1, \vec{r}_2)$  by the density, which yields the pair-correlation function

$$g^{(2)}(\vec{r}_1, \vec{r}_2) = \frac{\rho^{(2)}(\vec{r}_1, \vec{r}_2)}{\rho^{(1)}(\vec{r}_1)\rho^{(1)}(\vec{r}_2)}, \quad (2.26)$$



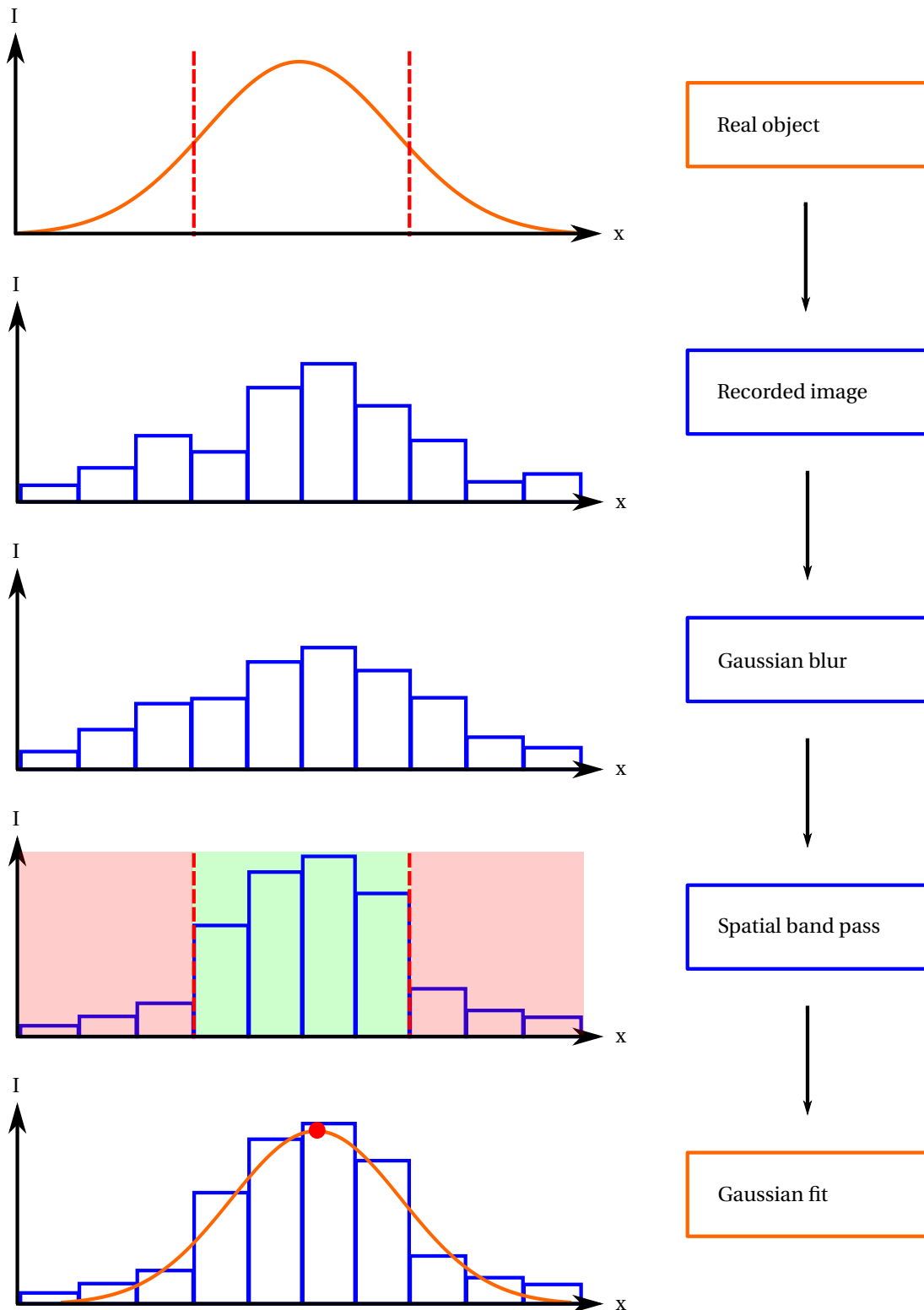


Figure 2.5: A schematic overview of the particle reconstruction from a recorded image via the Crocker and Grier algorithm. The goal is to obtain the centre position of a real object from a recorded image. The continuous signal (orange) is transformed into a discrete signal (blue), i.e. pixels, and reconstructed back to a continuous fit (orange) in the last step. From this fit, the particle centre position (red dot) can be determined with sub-pixel resolution, however, only in a perfect system this coincides perfectly with the real particle's position. The Gaussian blur and spatial band pass filter are manipulations performed on the recorded image to enhance the image for the fitting procedure. The Gaussian blur smoothens the image, and the spatial band pass increases the particle intensity (green area) in a region which corresponds with the particle location (red dashed lines), and reduces the intensity outside this region (red area).

with  $\rho^{(1)}(\vec{r})$  the probability of finding any particle in  $d\vec{r}$ . Only the distance between two particles, i.e.  $r_{12} = |\vec{r}_2 - \vec{r}_1|$  can be taken into account, which yields a normalised probability distribution over the spherical shells around a particle

$$g^{(2)}(r_{12}) = g^{(2)}(\vec{r}_1, \vec{r}_2). \quad (2.27)$$

The subscripts and superscripts are usually dropped in  $g^{(2)}(r_{12})$ , which yields the notation  $g(r)$  for the radial distribution function [6]. For an ergodic system such as a liquid, a  $g(r)$  can be made from a time series of 2D images, which is called pseudo 2D, and yields the same information as a 3D  $g(r)$ . Important is that only particles perfectly in the (focal) plane are taken into the account [26]. Radial distribution functions of static structures can be made via 3D particle coordinates. These analysis tools are available in the Crocker and Grier routines, and in many other software packages including the simulation software package used in this thesis (Section 3.2.7).

### Skeletonization

A topological skeleton of a structure captures the essential framework and connectivity in a skeletal remnant of the original structure. In this way, large amounts of data can be reduced to thin-line patterns, named the skeletons, which facilitates e.g. connectivity and shape analysis. In order to implement a skeletonisation or thinning algorithm, the image has to be binarized first, which means that a pixel can either have a value of 0, which means background, or 1, which means that it is a foreground pixel. The skeleton is defined as the collection of pixels which are equidistant to the background-foreground boundary at more than one point. For example, a thinned structure of a square would consist of an X-shaped skeleton pointed to the corners of the square. In 3D, this definition can be understood as a structure which comprises all centres of inscribed maximal spheres that touch the background-foreground boundary at more than one point [62].

Various skeletonization methods and algorithms are available [63], and the algorithm developed by Lee *et al.* will be used in this thesis [62]. This algorithm is also available in the major image processing programs, such as ImageJ and Fiji. It uses the thinning procedure, which repetitively deletes the border points of an object that satisfy a set of topological and geometrical constraints, until a skeleton results. The topological constraint is the preservation of the Euler characteristic, which describes the shape or structure regardless of the way it is bent, and connectivity. The geometric constraint is set such that the skeleton has the desired width and location. The end product is an accurate approximation of the ‘true’ skeleton. A good algorithm recognises the significant features of the structure, while it is insensitive to boundary noise. If significant, bumps in the structure give rise to spurs, which should be avoided or filtered for connectivity analysis. These features can be reduced by setting a threshold value for the minimum branch length or by 3D smoothing prior to the thinning procedure [62].

### Sampling and particle size

The particle size requirements are closely related to the sampling rate and type of image analysis. The Nyquist sampling theorem gives an indication for the sampling rate, i.e. the interval between samples, to capture all information of a continuous signal by discrete samples. For an optical system with a standard set-up such as used in this thesis, this sampling rate is  $R/2$ . Pawley argues that the Nyquist sampling rate cannot be applied directly to a 2-dimensional (2D) situation, since the same resolution along the diagonal requires more sampling (Fig. 2.6). He showed that the  $z$ -direction can be neglected because the resolution is very low along this axis, and finds a sampling rate of  $\sim 2.8$  in the  $x, y$ -direction [61].

One can oversample, which means that a too high zoom setting, or too small spatial interval is chosen according to the Nyquist sampling theorem. This makes image processing easier, since the images become a bit smoother, but the rate of photobleaching is higher [57].

The voxel (3D pixel) dimensions should be adjusted to the particle size to obtain optimal results with the particle tracking algorithms. Particle tracking with the Crocker and Grier routines works

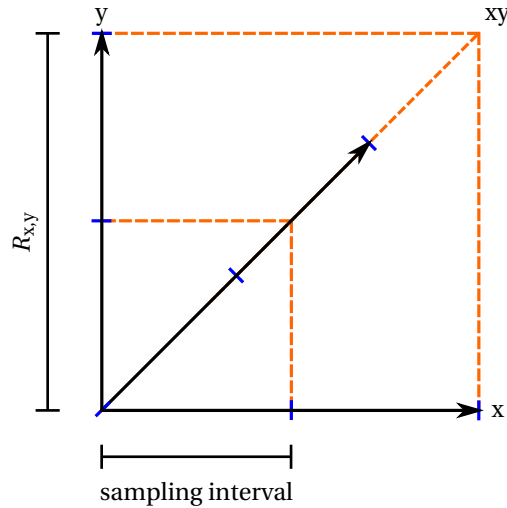


Figure 2.6: A schematic to illustrate the principle of the Nyquist theorem in a plane. The resolution in the plane is denoted as  $R_{x,y}$  and corresponds to the length of the black vectors. The blue marks correspond to a sampling rate of 2 times  $R_{x,y}$ , which is the 1-dimensional sampling rate given by the Nyquist theorem. In a microscope, the plane is sampled along the  $x$  and  $y$  axes. This results in undersampling in the  $x, y$  direction (orange guidelines), since the sampling interval along the diagonal should be smaller (blue ticks). Following the law of Pythagoras, a sampling rate of  $2\sqrt{2} \approx 2.8$  is required.

optimally with particles of  $\sim 10$  pixels in diameter. This amount of data points is required for a reliable Gaussian fit to determine the core position. Oversampling can be advantageous for image processing purposes, however, pinpointing an optimal sampling rate is tricky. Jenkins gives as rule of thumb that the particle diameter should be at least in the order of a micron with a sampling rate of 2 and a resolution of  $0.2 \mu\text{m}$  to obtain the required amount of data points for the fit [59]. A smaller particle size would make sampling following the Nyquist theorem impossible, as the resolution of the microscope is a fixed value.

For skeletonisation purposes, the particles do not need to be resolvable, and only the focal volume should be sampled without loss of information. Hence, the optimal voxel dimensions are independent of the particle size. Some oversampling would be advantageous here as well, which would lead to the same voxel dimensions as the lower limit required for the Crocker and Grier scripts.

## 2.6 Spectroscopy

### 2.6.1 UV-Vis spectroscopy

Ultraviolet-visible (UV-Vis) spectroscopy is a technique which is able to measure the extinction of light, this can be absorption, reflection, or scattering. In colloidal samples, scattering dominates the spectrum, however, surface plasmon resonance can be observed as well for some conducting colloids. For fluorescent samples, a part of the light is absorbed and emitted isotropically at a different wavelength than absorption, which contributes to the extinction.

The UV-Vis light spectrum is scanned using a continuous light source with diffraction grating, and the signal is detected in the extension of the light beam through the sample (Fig. 2.7). The sample is measured in a transparent cuvette with a known length  $l$ . The absorption  $A$  is related to the sample specific extinction coefficient  $\epsilon$  via Beer-Lambert law

$$A = \log_{10} \left( \frac{I_0}{I} \right) = \epsilon c l \quad (2.28)$$

with  $c$  the concentration.

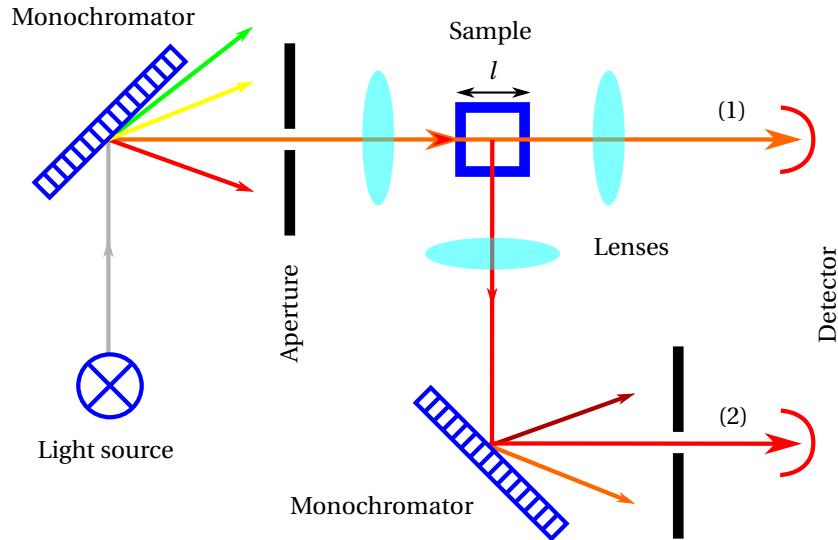


Figure 2.7: A schematic representation of a UV-Vis (1) and fluorescence spectrometer set-up (2). In this set-up, the desired wavelength from a continuous light source is selected with a diffraction grating and aperture. This can be the wavelengths which are scanned for absorption measurements (1), or the excitation wavelength of the fluorophore (2). The transmission is measured with respect to a reference in UV-Vis spectroscopy (1). However, in fluorescence spectroscopy, the emitted wavelengths at a  $90^\circ$  angle are scanned with a diffraction grating and aperture (2).

## 2.6.2 Fluorescence spectroscopy

Fluorescence spectroscopy is a type of spectroscopy that analyses the fluorescence from a sample. The sample is excited with a monochromatic light beam, usually in the UV region, which passes through the sample (Fig. 2.7). The wavelength can be tuned such that it corresponds with the maximum absorption of the sample, and allows the excitation of specific fluorophores in the sample. The fluorescence is detected at a  $90^\circ$  angle to reduce the contribution of scattered light. The technique is much more sensitive than UV-Vis spectroscopy, because the fluorescence can be measured independently from the excitation source, and therefore more sensitive detectors can be used.

## 2.7 Viscometry

The volume fraction  $\phi$  and number density  $n_p$  can be determined by measuring the relative viscosity  $\eta_{\text{rel}}$  with a Micro-Ostwald viscometer. Back in 1905, Einstein predicted that in the limit of  $\phi \rightarrow 0$ , the viscosity of a monodisperse hard-sphere suspension could be given by  $\eta_{\text{rel}} = \eta(\phi)/\eta_0 = 1 + 2.5\phi$  with  $\eta_0$  the viscosity of the solvent [10]. Batchelor extended this equation to the colloidal regime by taking the Brownian motion into account [64],

$$\eta_{\text{rel}} = 1 + 2.5\phi + 5.9\phi^2. \quad (2.29)$$

In the case of laminar flow and Newtonian fluids, which are a good assumptions for highly diluted colloidal suspensions, Poiseuille's law can be applied [64]. Hereof, it can be derived that  $\eta_{\text{rel}}$  can be determined via

$$\eta_{\text{rel}} = \frac{\eta(\phi)}{\eta_0} = \frac{t}{t_0}, \quad (2.30)$$

with the flow time  $t$  and  $t_0$  through a capillary in the viscometer for respectively the sample and solvent (Fig. 2.8). Experimentally, the  $\eta_{\text{rel}}$  can be measured for a dilution series, and the shift factor

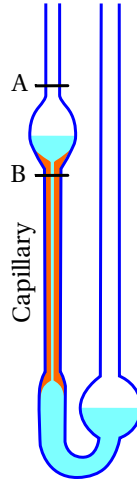


Figure 2.8: A schematic of a Micro-Ostwald viscometer. The relative viscosity can be derived from the flow time  $t$  from A to B. The glass viscometer can be immersed in a water bath for temperature-dependent measurements.

$k$  can be obtained after substitution of  $\phi = k(\text{wt}\%)$  in Eq. 2.29. The  $n_p$  of a suspension consisting of spherical particles with hydrodynamic radius  $R_H$  can be estimated via

$$n_p = \frac{3k(\text{wt}\%)}{4\pi R_H^3}. \quad (2.31)$$

## 2.8 Electrophoretic mobility measurements

An indication of a particle's charge can be obtained with electrokinetic measurements. Electrostatic interactions are often a dominant factor in the interaction between colloids, and usually contribute greatly to colloidal stabilisation of non-oppositely charged particles. Because the surface potential is experimentally not easily accessible, the electrostatics are measured and interpreted in terms of the zeta potential  $\zeta$ .

### Theory

A charged particle with counter ions dispersed in a solution forms an electrical double layer (EDL), which is an inhomogeneous ion distribution which partially screens the charge of the particle (Fig. 2.9). Due to the surface potential, oppositely charged ions get attracted and adsorb on the particle's surface, forming a so-called Stern layer. The second ionic layer is called the diffuse EDL, here, the ions reach equilibrium between diffusion and electrostatic attraction. This layer is characterised by ions that are attracted by the particle in such extent that they get dragged along with the moving colloid. Hence, the outer layer of the diffuse EDL is called the slipping plane, and  $\zeta$  is defined as the potential at this position [5, 65].

The zeta potential can be obtained from electrophoretic mobility measurements, in which the steady state velocity is measured as function of the electric field imposed across a colloidal suspension. The steady state velocity  $\vec{v}$  is a balance between the electrical force on the charged particle and the opposing viscous force, and can be described as

$$\vec{v} = \frac{\vec{F}}{6\pi\eta R} \quad (2.32)$$

with  $\vec{F}$  the external force acting on the particle caused by the electric field  $\vec{E}$ ,  $\eta$  the viscosity of the solvent, and  $R$  the radius of the particle. In general,  $\vec{F}$  is unknown, but in the case of small fields the linear relation  $\vec{F} \approx q\vec{E}$  holds. The electrophoretic mobility  $u$  is defined as

$$u = \frac{\vec{v}}{\vec{E}}, \quad (2.33)$$

and is the primary quantity, since it is directly accessible in an electrophoretic measurement. The zeta potential  $\zeta$  however, is not directly accessible and approximations have to be made. The relation between the electrophoretic mobility and the zeta potential can be written as

$$\zeta = a \frac{\eta u}{\varepsilon_r \varepsilon_0}, \quad (2.34)$$

with  $\varepsilon_r \varepsilon_0$  the dielectric constant, and a prefactor  $a$  which varies between 1-1.5 depending on the approximation made. In the limit of small particles, i.e.  $(R'/\kappa^{-1}) \ll 1$  in which  $\kappa^{-1}$  is the Debye length and  $R'$  is the distance from the particles centre at the slipping plane,  $a = 1$  as given by the Hückel equation. In the limit of large particles, that is  $(R'/\kappa^{-1}) \gg 1$ ,  $a = 1.5$  holds, which is given by the Smoluchowski equation. These limits seldom apply strictly in colloidal systems, and  $a$  lies somewhere in this range. Colloidal systems in aqueous media can usually be described with the Smoluchowski approximation. Here, the double layer is approximated to be small with respect to the particle size, which corresponds to the length scale in colloidal systems and the high dielectric constant of the aqueous medium. Even though absolute numbers are uncertain, the measured  $\zeta$  follows the trends in  $R$  and charge of the particle, and is suitable for comparative studies [5].

It is not straightforward to calculate the charge on a particle from the zeta potential, since in reality, the liquid flow perturbs the EDL and the particles' charge perturbs the electric field. A complete description should also take the mobilities of the counter ions into account, as well as the local viscosities close to the particle. As rough estimate of a particle's charge for e.g. simulations, Eqs. 2.32, 2.33, and  $\vec{F} = q\vec{E}$  can be combined to obtain

$$q = 6\pi u \eta R. \quad (2.35)$$

The actual charge, that is without screening from the EDL, is probably much higher than the one obtained from Eq. 2.35 [5].

## Method

In practice, electrophoretic mobility measurements are performed in an isolated cell with immersed electrodes separated over a known distance. The velocity of the particles is determined with laser doppler velocimetry, which is based on the principle that the wavelength of light scattered by a moving particle is shifted with respect to the incoming beam due to the motion of the particle, i.e. the Doppler effect. The scattered light fluctuates in intensity, which frequency is equivalent to the Doppler shift between the incident and scattered light, and is thus proportional to the particle velocity. The sign of the zeta potential, or the direction of the particle's movement, can be determined by modulating the laser beam with an oscillating mirror [65].

## 2.9 Molecular dynamics simulations

Molecular dynamics (MD) is a type of simulation to compute the physical movement of a classical many-body system, i.e. particles that obey the laws of classical mechanics. This is an excellent approximation for colloidal systems, since their size is orders of magnitude bigger than that of light atoms or molecules which do experience quantum effects. From this physical movement, the transport and equilibrium properties such as the radial distribution function and the diffusion coefficient can be calculated. This calculation can be seen as an experimental measurement which is subject

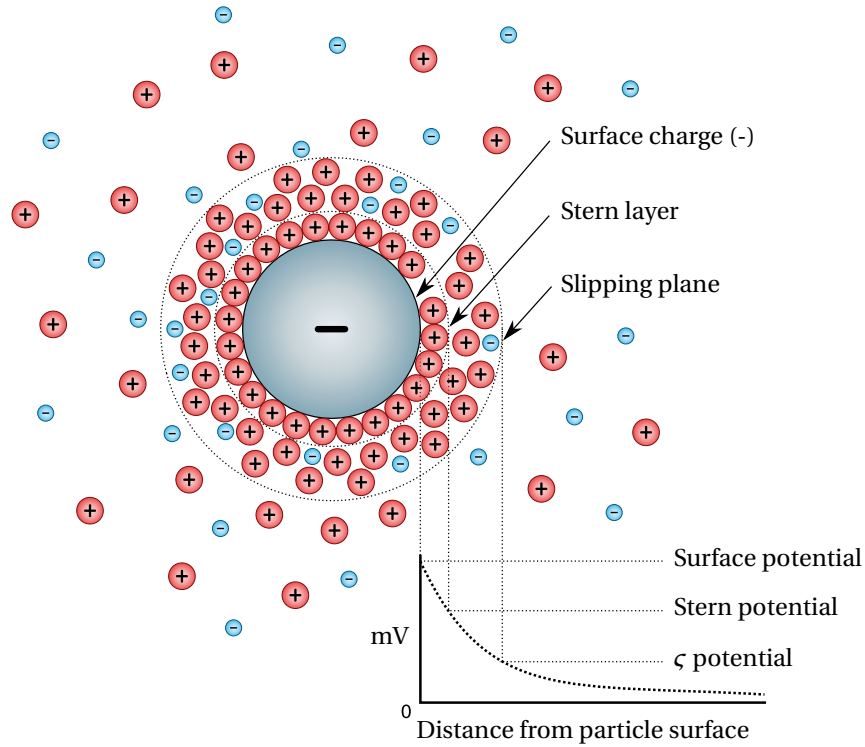


Figure 2.9: Schematic representation of the electric double layer around a negatively charged particle. The first layer consists of tightly bound counter ions, while the second is diffuse and extends unto the slipping plane. These layers are called respectively, the Stern layer and the diffuse electric double layer. The zeta potential  $\zeta$  is defined as the potential at the slipping plane. Adapted from Wikipedia.

to statistical noise, and the simulation parameters should be chosen carefully to provide sufficiently accurate measurements [66].

A MD program is built up out of five essential steps. First, the input parameters are read in, these contain the conditions of the simulation, such as the density, temperature, and pair potentials of the particles. Subsequently, the system is initialised, which means that the initial positions and velocities of the particles are either generated or read-in from an existing configuration file. Crucial is that the particle cores do not overlap in such way that the interparticle forces become unphysical, so an even particle distribution is usually preferred. All information to run the simulation is provided by these first two steps. The simulation itself comprises a loop over the calculation of the force on every particle and the integration of Newton's equation of motion. From this, new particle coordinates can be obtained and the loop can be repeated until the desired simulation time is reached. The final step is the calculation of the to-be-measured properties of the system from the particle coordinates [66].

The two steps of the simulation's core loop will be discussed in more detail in this paragraph. The most time-consuming part of a MD simulation is the calculation of forces. The interaction potential  $U(r)$  is related to the force via

$$\vec{F}_c(r) = -\frac{d\vec{U}(r)}{dr}, \quad (2.36)$$

with  $r$  the interparticle distance. The force between two particles can be obtained by plugging the distance between a particles into Eq. 2.36. Since pairwise additive interactions are assumed in our model, the forces of a particle with all its neighbours are vectorially summed to obtain a resulting force  $\vec{F}_r$ . Usually, a cut-off for the pair potential is set, which reduces the number of neighbours in most cases and thereby the computer time. Once the force on the particles is known, the equations of Newton have to be integrated to obtain the particle coordinates at the next time step  $\Delta t$ . The Verlet algorithm is used in this thesis, and is one of the simplest and best algorithms to do this according to Frenkel *et al.* [66], because it is computationally cheap and reasonably accurate. By taking the Taylor

Table 2.1: A selection of the set of reduced units used in this thesis. The physical quantities are displayed in the reduced units and real units. Here is  $e$  the elementary charge,  $k_B T$  the thermal energy,  $\Gamma$  a constant set to unity,  $f$  the friction constant,  $\tau_B$  the Brownian time,  $\sigma_i$  the diameter, and  $m_i$  the mass of particle  $i$ . A brief discussion of the reduced diffusion coefficient will be given in Section E.2

Quantity	Reduced units	Real units
Charge	1	$e$
Diffusion	$D = k_B T / m \Gamma = 1 / m$	$D = k_B T / f$
Energy	1	$k_B T$
Length	1	$\sigma_1$
	$\sigma_2 / \sigma_1$	$\sigma_1$
Mass	$\sigma_1$	$m_1$
	$\sigma_2$	$m_2$
Time	1	$\tau_{B,1} = \sigma_1^2 / D$

expansion of a particle coordinate  $r$  around time  $t$ ,  $r(t + \Delta t)$  and  $r(t - \Delta t)$ , and rewriting, the Verlet algorithm can be obtained

$$r(t + \Delta t) \approx 2r(t) - r(t - \Delta t) + \frac{F_r(t)}{m} \Delta t^2. \quad (2.37)$$

with  $m$  the mass of the particle. The error in the position at  $t + \Delta t$  is in the order of  $\Delta t^4$ .

In order to model colloids following Brownian Dynamics (BD), a drag force and thermal motion should be incorporated into the resulting force. In the absence of any other interaction than the solvent, the particle moving with a velocity  $\vec{v}$  experiences a frictional drag force  $\vec{F}_f(t) = -\gamma \vec{v}(t)$ , since it undergoes more collisions at the front than at the back [67]. However, this only models the viscous drag of the solvent via Stokes law's friction coefficient  $\gamma$ , but it does not take hydrodynamic interactions into account. The thermal motion of the particle is modelled by a random force  $\vec{F}_s(t)$ , whose magnitude can be derived from the fluctuation-dissipation theorem. By taking the interparticle interactions  $\vec{F}_c(t)$  into the equation,  $\vec{F}_r$  becomes an 'overdamped' Langevin equation

$$\vec{F}_r(t) = \vec{F}_f(t) + \vec{F}_s(t) + \vec{F}_c(t) = -\gamma \vec{v}(t) + \sqrt{\frac{k_B T m \gamma}{\Delta t}} \vec{f}(t) - \sum_{i=1}^N \frac{d\vec{U}(r)}{dr}, \quad (2.38)$$

with  $\vec{f}(t)$  being the random force and the summation going over a particle with all its  $N$  neighbours [67, 68]. For non-dynamical properties as the radial distribution function, the use of overdamped Langevin dynamics is unnecessary as it would give the same results as for a purely classical approach.

The velocity can be obtained by subtracting the Taylor expansion  $r(t + \Delta t)$  and  $r(t - \Delta t)$ , and rewriting, similar to the derivation of the Verlet algorithm. This can be used to calculate the kinetic energy, and via that, controlling temperature of the system [66].

### 2.9.1 Reduced units

It is conventional to write physical quantities that describe the simulated system in reduced units. A convenient unit of energy, mass and length is chosen in which all other quantities can be expressed [66]. For instance, the diameter of a particle ( $\sigma$ ) can be chosen as basic unit of length, setting it automatically to one basic length unit. All other quantities with a length involved should be expressed in this basic length unit  $\sigma$ . For instance, a cubic box of 10 particles in length would be  $10 \sigma$  with a volume of  $10^3 \sigma^3$ . The choice of reduced units is arbitrary, and the scheme adopted in this thesis is shown in Table 2.1.

The use of reduced units has three advantages. Firstly, infinitely many combinations of the physical quantities that set the system are degenerate, that is they are equivalent and have the same reduced units. This can easily be missed when using real SI units. Secondly, the real units are usually a lot smaller or bigger than unity, and therefore may cause underflow or overflow during a standard



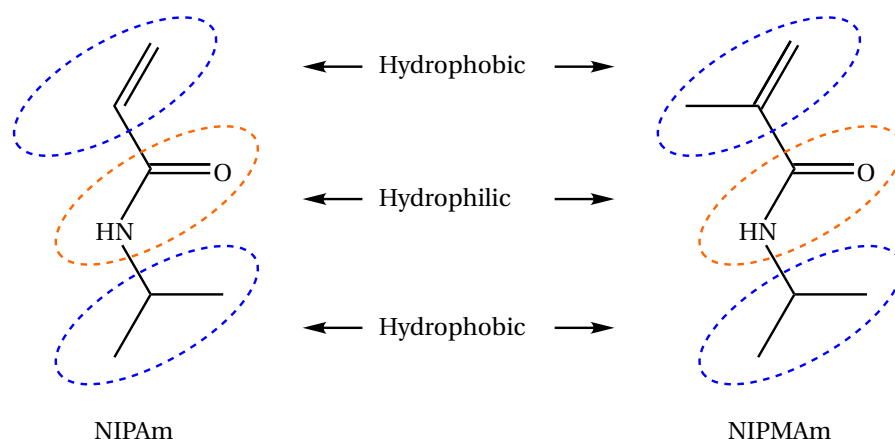


Figure 2.10: A NIPAm and NIPMAm molecule with their hydrophobic and hydrophilic domains indicated. The terminal bonded carbon forms a hydrophobic backbone after polymerisation.

floating point multiplication at a later stage. Most reduced units ought to deviate not more than a couple orders of magnitude from unity, which should not cause these kind of errors. Lastly, errors are easy to spot, since output values far from unity indicate an error in the code or input [66]. Although reduced units are arbitrary, a balanced set of units should be chosen to keep the in- and output manageable.

## 2.10 Thermoresponsive microgel colloids

### 2.10.1 PNIPAm and PNIPMAm

PNIPAm and PNIPMAm are known for their thermoresponsive behaviour. NIPMAm is a methylated form of NIPAm (Fig. 2.10), and both can be used to make polymeric microgel particles. The thermoresponsive behaviour of these polymers originates from the amphiphilic character of its subunits. The subunits consist of hydrophobic and hydrophilic domains. The hydrophilic amide and carbonyl groups form strong hydrogen bonds with the water (Fig. 2.10), however these bonds are increasingly disrupted at higher temperature, which causes the local environment around the hydrophobic domains to change. The subtle balance between polymer-polymer and polymer-water interactions around the hydrophobic isopropyl groups and the methylene backbone determines the thermoresponsive properties. At elevated temperatures, polymer-polymer interactions and intra-polymer hydrogen bonds are favoured at the expense the polymer-water interactions, and a majority of the water is expelled from the microgel. In other words, water becomes a bad solvent at elevated temperatures. The temperature at which this occurs is called the volume phase transition temperature (VPTT) for colloidal microgel particles, which is 32 °C for PNIPAm and 45 °C for PNIPMAm [69–71].

Other factors such as the pH and addition of an inert electrolyte alter the local environment around the hydrophobic domains, causing the microgel to swell or deswell. Depending of the  $pK_a$  and the charges in the proximity, weak acid or base groups will become ionised. Both these factors alter the effective ionic strength, which causes a degree of screening of the electrostatic charges in the particle. Therefore, a higher effective ionic strength will reduce the interaction energy upon approach of the polymer chains, which results in a deswelling of the microgel [30].

### 2.10.2 Precipitation and emulsion polymerisation

Precipitation and emulsion polymerisation are techniques used for the synthesis of monodisperse latex particles. During the reaction, the monomers form polymers via free-radical polymerisation. The synthesis procedure is the nearly the same for both syntheses, but the mechanism differs slightly.

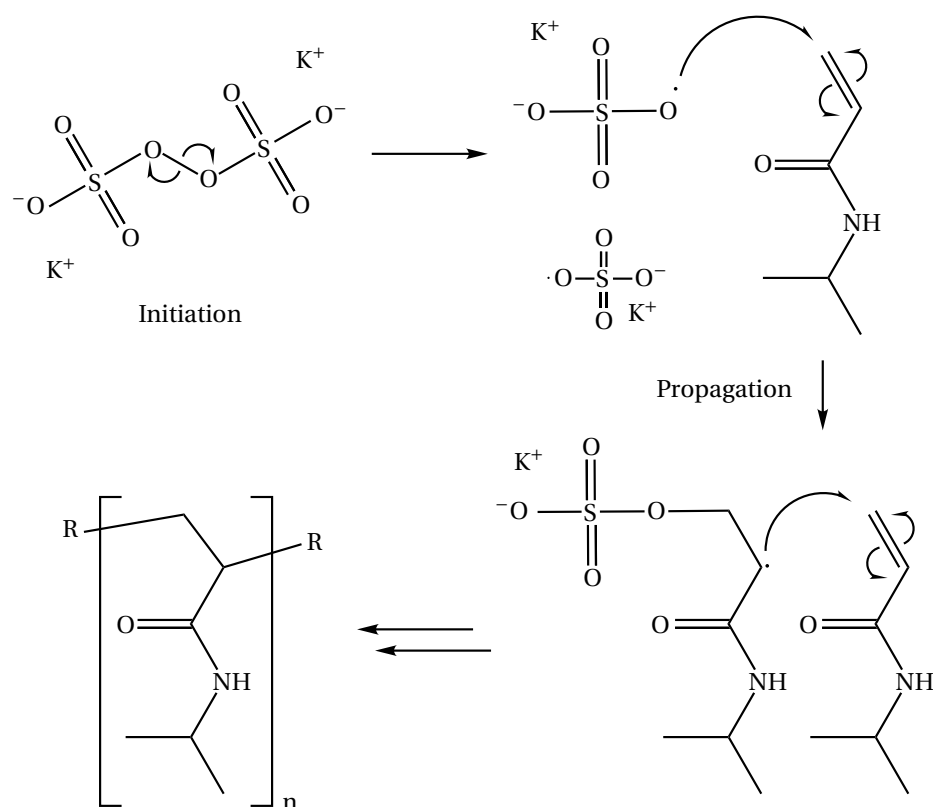


Figure 2.11: The reaction scheme of a KPS initiated polymerisation of NIPAM monomers into a PNIPAM polymer chain. The reaction initiates as the KPS decomposes at elevated temperatures into two persulphate radicals. In the first step of the propagation, the radical attacks the double bond of a NIPAM molecule. The formed radical on the NIPAM molecule can attack the double bond of another NIPAM molecule during the next propagation step, which is repeated until two radicals meet and the reaction is terminated.

PNIPAm, PNIPMAm microgel particles follow the mechanism of precipitation polymerisation, while PS particles follow emulsion polymerisation. The fundamental difference is that in emulsion polymerisation, the monomer is immiscible with the solvent and therefore requires a surfactant to form emulsion droplets, while in precipitation polymerisation, the growing polymer chains become immiscible after a certain length which precipitate onto each other [30, 72].

**Precipitation polymerisation** As with all free-radical polymerisation reactions, the precipitation polymerisation mechanism consist of three important steps, being initiation, propagation and termination (Fig. 2.11). Aggregates consisting of growing chains during the propagation step serve as seed, which maintains a separation between nucleation and growth establishing a monodisperse sample. The reaction is initiated by the radical initiator, which can be for instance V50 or KPS. The latter is used in this thesis and decomposes at reaction temperatures into two negatively charged sulfate moieties with a free radical. The attack of this free radical on the double bond of a NIPAm or NIPMAm molecule initiates the reaction, which propagates when the radical on the NIPAm or NIPMAm attacks another latex molecule. After a certain length, the growing oligomer chains become insoluble in water under reaction conditions and will collapse (Fig. 2.12). These so called precursor particles can either aggregate to form a colloidal stable 'seed' particle, or deposit on existing seed particles. The precursor particles have formed a colloidal stable seed when the surface charge originating from the initiator is high enough to maintain electrostatic stabilisation. More specific, the repulsion of the electrostatic charges on the surface of the seed particles prevents them from aggregating. The seeds grow by the association of precursor particles, and by continuous polymerisation driven by the living radicals in the particles. This continues until the two radical species meet, form an electron pair, and terminate

the chain reaction. At decreasing monomer concentration, the probability of forming a colloidal stable seed particle becomes negligibly small and only growth of existing seeds occurs. By lowering the temperature, the water becomes a good solvent and the particles swell [30, 72].

The size of the particles can be reduced up to approximately 85% by adding SDS as surfactant. SDS adsorbs on the seed particles and increases the colloidal stability of the smallest colloidal stable particles. Furthermore, it prevents access of monomers to seed particle, which yields a higher concentration of seed particles and thus less monomer per particle, which leads to smaller particles [73].

The ionic strength in the reaction mixture is thought to affect the size of the final particles. An increase in the ionic strength reduces the electrical double layer of the precursor particles, which decreases colloidal stability. This has been investigated in the context of a large excess of KPS initiator, which is ionic. According to the model, a larger KPS concentration leads to larger particles, which is reverse to the trend observed by Meunier *et al.*, who has reported that an increase in initiator concentration leads to a decrease in the final hydrodynamic radius [74]. Duracher *et al.* noted that for PNIPAm particles, a similar trend in the hydrodynamic radius occurred, but the hydrodynamic radius at 50 °C and radius observed with SEM showed a trend in the other direction [71]. The amount of material per particle did increase with initiator concentration, but this was counteracted by a decrease in the swelling ratio, which is in line with the model of colloidal stability.

**Emulsion polymerisation** Emulsion polymerisation is a free-radical polymerisation reaction similar to the precipitation polymerisation. According to the micelle nucleation model, the free radicals polymerise with the monomers in the aqueous phase. After a certain chain length, the polymer chain becomes so hydrophobic that it is favourable to enter the surfactant stabilised emulsion droplets. The polymer chain propagates into the droplet until all monomers have been consumed. Since these micelles are stabilised by the surfactant during the reaction, it transforms into a stabilised particle seed. The seed will continue to grow by consuming monomers from the aqueous phase. Because  $10^2 - 10^3$  more micelles than final latex particles are present, the emulsion droplets serve only as monomer reservoir at this point and will dissolve over time to maintain equilibrium with the aqueous phase. In this mechanism, nucleation and growth are separated in time, and monodisperse latex colloids are obtained [75]. A critical note should be made about the nucleation mechanism described above. The coagulative nucleation model describes a two-step nucleation mechanism identical to the precipitation polymerisation mechanism, in which precursor particles coagulate into colloidally stable seed particles. Interestingly, this mathematical model was in qualitative agreement with experimental data of styrene emulsion polymerisation systems [76]. Since the collapsed latex particle is also stable after purification, the surfactant might not be removed during this step, or more likely, the colloidal particle should consist of many chains to ensure electrostatic stabilisation. This observation favours a mechanism in which nucleation occurs due to aggregation of colloidally unstable precursor particles and stabilisation during the reaction is governed by both charge and steric hindrance of the surfactant.

**Core-shell particles** In the case of core-shell particles, the PS core can be functionalised with NIPAm or PNIPAm during the polymerisation reaction. The presence of the microgel monomers, i.e. NIPAm or PNIPAm, changes the emulsion polymerisation reaction mechanism dramatically as the microgel precursor particles serve as seed for the PS core synthesis. The microgel monomer reacts rapidly in the aqueous phase together with the water borne styrene, since the initiator has a high preference for the aqueous phase as well. Duracher *et al.* showed that about 80% of the NIPAm is consumed before the styrene starts to polymerise [77]. The oligomers coagulate at low conversion due to the styrene in the chain, and colloidally stable particles are formed at < 10% styrene conversion in the case of NIPAm. Due to the surface active properties of PNIPAm, the particles will probably adsorb at the surface of a styrene emulsion droplet, and vice versa. As more styrene is consumed in the particle, larger domains of PS form until the PS dominates and the microgel is expelled to the

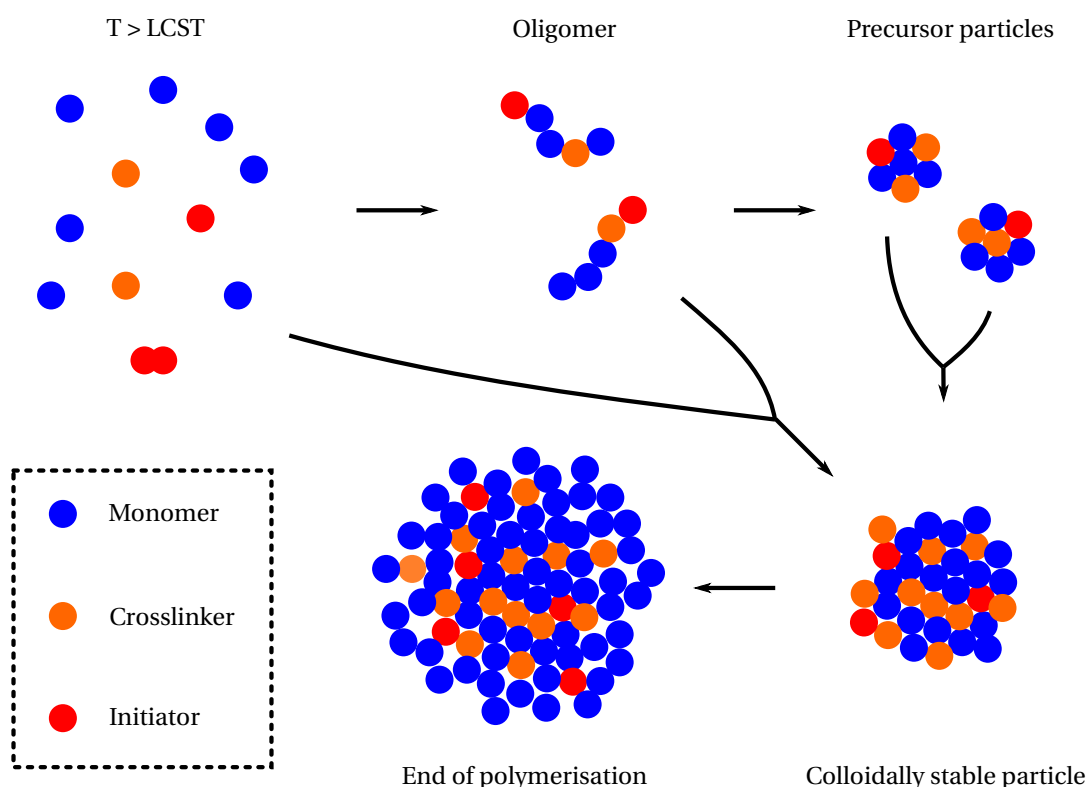


Figure 2.12: Schematic representation of precipitation polymerisation of water-soluble NIPAm and NIPMAm monomers. A particle is called colloidally stable when the surface charge originating from the initiator is high enough to maintain electrostatic stabilisation. This means that the precursor particles do not aggregate with other precursor particles, which maintains separation between nucleation and growth.

surface. The initial amount of monomer controls the particle size and the thickness of microgel shell [74, 77]. During the shell growth, the functionalised PS cores are present as seed for the PNIPAm or PNIPMAm precursor particles to precipitate on, and the cores will be homogeneously encapsulated by cross-linked microgel [78].

**Co-monomers** Various co-monomers such as charged moieties, crosslinkers and fluorescent dyes can be added during synthesis to alter the properties of the microgel. The distribution of the co-monomer in the microgel particle can be controlled by addition either before initiation, as a feed, or later during the reaction. Two co-monomers are used in this thesis. Firstly, BIS is used as a crosslinking agent in PNIPAm and PNIPMAm synthesis, and creates connections between the polymer chains, which is essential to form a microgel. The crosslinker is incorporated in the same way as the other monomers during the propagation step. The effect of BIS on the structure will be discussed in Section 2.10.4. The amount of crosslinking is usually expressed in the crosslinking density, which is the ratio of BIS to monomer molecules in percent. Microgel particles have also been observed without the addition of a crosslinker, this might be due to chain entanglement or propagation from the backbone due to hydrogen abstraction by a radical from another polymer chain [73]. Secondly, the fluorescent dye has a polymerisable double bond and is incorporated in the polymer during the propagation step. It must be noted that the fluorescent pyromethene dye used to stain the PS cores, is not polymerised but remains dissolved in the PS due to its strong hydrophobicity.

### 2.10.3 Core-shell particles

Little work has been done on the synthesis and phase behaviour of PS-PNIPAm particles. A systematic study performed by Appel *et al.* showed that the microgel shell thickness could be varied as function of the ratio between the mass of the monomers and core  $m_m/m_c$  [4]. In their set-up, secondary nucleation, i.e. microgels without a core, was observed for  $m_m/m_c > 5$ . This indicates that an excess of microgel during the shell growth allows the precursor particles to form colloidal stable nuclei before it associates with the PS core. With a fixed initial amount of monomer, Rauh *et al.* showed that a range of core concentrations exists where monodisperse Au-PNIPAm CS particles could be obtained [79]. At lower core concentration, an increasing fraction of the particles did not contain a gold core, and the hydrodynamic radius increased significantly. At higher core concentrations, polydisperse Au-PNIPAm particles were found. Finally, Dulle *et al.* have shown that a homogeneous density profile can be achieved by adding a constant amount of BIS during the first 30 minutes of the reaction [78]. The morphology of a CS PS-microgel particle is very similar to its pure microgel counterpart, which will be discussed in the next section [80]. To illustrate this observation, liquid, glass and gel phases were observed in CS systems, including a gel phase formed via sequential gelation [4, 81]. The tunable volume fraction has been exploited to study the vicinity of the glass transition, and crystallisation was observed in both PS-PNIPAm particles polymerised with and without a charged co-polymer [81–83].

### 2.10.4 Morphology of the colloids

The morphology of pure microgel colloids has been a matter of debate for over a decade. A good understanding of the particles morphology helps understanding the mechanisms of particle formation and growth during the synthesis. More importantly, the morphology determines the interparticle interactions, and with that the phase behaviour of the microgels [74].

In 1999, Senff and Richtering showed that both pure PNIPAm microgels and PS-PNIPAm CS microgels exhibited soft sphere behaviour below the VPTT [23, 80]. Despite the thin shell of the CS particles, which was 42 nm, the rheological behaviour was very similar to the pure microgels in this temperature regime. Pure microgels with volume fractions below 0.5, the mastercurve of the zero-shear viscosity versus the volume fraction overlapped closely with the one obtained for hard spheres. This indicates that the water in the pure microgel must be immobilised, and explains the likeness with the CS particles. For volume fractions above 0.5, the plateau modulus was found to scale with the volume fraction with a power law typical for soft spheres in simulations. In rheology, the pure and CS microgel particles exhibit hard sphere behaviour at low volume fraction and soft sphere behaviour at high volume fraction.

A pure microgel has an CS-like internal structure, which is in line with the similar rheological behaviour of pure and CS microgels. Stieger *et al.* found that a fuzzy sphere model very well described experimental small angle neutron scattering data of PNIPAm colloids. The microgel is approximated in this model with a spherical convoluted Gaussian density profile, which has a hard core character up to  $\sim 0.4R_H$  and a gradual density decay beyond this value [84]. This model has been applied by Meyer *et al.* on SLS data, this leads to an additional term to Eq. 2.12 in which the width of the Gaussian decay is parametrised. A good agreement with experimental data was found [85]. The origin of the morphology can be explained by the different reaction rate of the monomer and BIS. Wu *et al.* found that the swelling ratio  $\alpha$  of PNIPAm increased during the reaction. The swelling ratio is defined here as

$$\alpha(25, 50^\circ\text{C}) = \frac{V_{\text{swollen}}}{V_{\text{collapsed}}} = \left( \frac{R_H^{T=25^\circ\text{C}}}{R_H^{T=50^\circ\text{C}}} \right)^3 \quad (2.39)$$

with  $V_{\text{swollen}}$  and  $V_{\text{collapsed}}$  respectively the volume below and above the VPTT. A higher crosslink density makes the particle denser and to swell less, however above the VPTT at 50 °C, the size is assumed to be independent of the crosslink density. BIS is consumed faster than the monomer, which results in a dense hard-sphere core with a fuzzy shell [86]. This is supported by unpublished data from Boon *et al.*, which shows that a relative reaction rate of 2 between the monomer and crosslinker yields a

radial density profile in perfect agreement with superresolution microscopy data. The form factor calculated from this radial density profile resembled the experimental data along the whole  $q$  range, which is an improvement over the fuzzy sphere model. However, the radius for the fit was significantly smaller than the hydrodynamic radius, which might be caused by a corona of dangling polymer ends and loops, which are of low density and are only picked up with dynamical methods. Moreover, rheological spring constants and shear moduli as function of the volume fraction could be fitted very well with a model consisting of a dense sphere with a brushlike corona, which supports the hypothesis proposed by Boon *et al.* [87].

Control over the internal structure can be achieved by feeding comonomers continuously, such as BIS. Acciaro *et al.* and Dulle *et al.* showed that a homogeneous crosslink density was obtained when the monomer and crosslinker ratio are kept constant within the reaction mixture [78, 88]. By doing so, a constant rate of monomer incorporation for both components is maintained. Dulle *et al.* observed a similar difference in static and dynamic radii as in the work of Boon *et al.*, which indicates that these particles have dangling polymer ends as well [78].

### 2.10.5 Interparticle interactions

Microgel colloidal particles interact through a complex soft interaction potential [26], which is composed of three main components described below.

#### Electrostatic interactions

The ionic initiator residues are dispersed through the particle volume, giving the microgel an overall charge. Upon approach of two colloids, electrostatic interactions will result in either a net attractive or repulsive force depending on the sign of the charged moieties. The salt ions in solution form an EDL, which screens the charges in the particle, thereby reducing the effective electrostatic potential (Fig. 2.9). The length scale of the electrostatic interactions is given by the Debye length

$$\kappa^{-1} = \sqrt{\frac{\epsilon_0 \epsilon_r k_B T}{e^2 I}}, \quad (2.40)$$

where  $\epsilon_0$  denotes the vacuum permittivity,  $\epsilon_r$  the dielectric constant of the solvent,  $k_B$  the Boltzmann constant,  $T$  the temperature,  $e$  the elementary charge, and  $I$  the ionic strength [5, 6]. In water, this corresponds to 0.95 nm for a concentration of  $10^{-1}$  M monovalent salt, such as KCl, and corresponds to 95 nm for  $10^{-5}$  M monovalent salt, conditions which are considered deionised. Screened electrostatic interactions between colloidal particles are commonly written as a Yukawa potential as described in DLVO theory [89],

$$U_{\text{Yukawa}} = Z_1 Z_2 \lambda_B k_B T \frac{\exp(\kappa R_1)}{(1 + \kappa R_1)} \frac{\exp(\kappa R_2)}{(1 + \kappa R_2)} \frac{\exp(-\kappa r)}{r}, \quad (2.41)$$

where  $Z_i$  and  $R_i$  denote respectively the absolute charge in  $e$  and radius of a particle  $i$ ,  $r$  denotes the inter-particle distance,  $\kappa^{-1}$  the inverse Debye screening length, and  $\lambda_B$  the Bjerrum length in the solvent.

The Yukawa potential does not model the overlap of two interpenetrating ions, and more advanced potentials are required to simulate (dense) ionic microgel suspensions. Recently, such a potential was developed by Likos and Colla, which describes explicit penetrable macro-ions in an ionic solution, and models the microscopic ions implicitly via the Debye length [90]. Potentials for a homogeneous and Gaussian charge distribution in the macro-ion are presented in the paper. A homogeneous charge distribution could be taken to model the CS particles. The advantage of the potential is that it does not diverge, as for instance a screened Yukawa (Eq. 2.41), which can lead to an unphysical potential in combination with e.g. a Hertzian potential at small  $r$ . A benchmark of the potential in simulations can be found in Appendix E.1.

### Van der Waals interactions

An atom (or molecule) can be modelled as an instantaneous fluctuating dipole, which originates from the constant motion of electrons around the nuclei. The electric field generated by the dipole polarises the electron cloud of neighbouring atoms, which in turn stabilises the first dipole. The sum of all the electrostatic interactions between the dipoles is usually attractive, and is called van der Waals attraction [91]. This attraction is short range, and corresponds to a  $U_{\text{vdW}} \sim -r^{-6}$  decay of the interaction energy. The van der Waals interaction between two colloids is the sum of all the interacting fluctuating dipoles in the atoms or molecules that build the colloidal particles. This can be written<sup>1</sup> for two spherical particles with radii  $R_1$  and  $R_2$  as [91]

$$U_{\text{vdW}} = -\frac{A_{\text{H}}}{6r} \left( \frac{R_1 R_2}{R_1 + R_2} \right) \quad (2.42)$$

with  $r$  the distance between the particles and  $A_{\text{H}}$  the Hamaker constant. The Hamaker constant comprises the dielectric constant of the particles and the solvent, which reflects the polarizability of the electron cloud. This constant can be altered by changing the solvent, hence the van der Waals interaction can be tuned in this way [91].

Many important attraction mechanisms that drive gelation are short-ranged. In a microgel system, this is thought to be van der Waals forces, however, other mechanisms such as hydrophobic effects and some depletion interactions can also be at play [92]. The exact shape of the potential does not have to be known, since the behaviour of a short-ranged attractive particle system is solely dependent on the reduced second virial coefficient  $B_2^*$  for  $\delta < 0.1$ . The  $\delta$  is defined here as the extent of the attraction in terms of the radius [93]. In the work of Lu *et al.*, the potential used to model the short-ranged attraction indeed did not affect the physics of the gelation [92].

The short-range potential developed in this thesis was designed such that the extent  $\delta$  and potential well  $\epsilon_a$  could be tuned in a continuous way. Used was the interaction potential

$$\frac{U_a(r)}{k_{\text{B}}T} = \frac{\epsilon_a}{2} \tanh\left(\frac{5}{\delta}r - \left(R_1 + R_2 + \frac{\delta}{2}\right)\right) - \frac{\epsilon_a}{2}, \quad (2.43)$$

which consists of a tangent hyperbolic switch function in the range from the particle's radius  $R$  to  $R + \delta$  with an interaction strength approaching zero for  $r > R + \delta$ . As the attraction is existent below  $R$ , the effective radius is reduced as a function of the strength of  $\epsilon_a$  and the repulsive Hertzian term.

### Steric repulsion

The morphology of the microgel particles allows the polymer chains to interpenetrate to a certain degree. This results in an increase of osmotic pressure as the microgel particles overlap, which leads to a net repulsive force. The steric repulsion can be described with e.g. Flory-Huggins theory, which leads to an unpractical expression for which the polymer volume fraction and the Flory-Huggins solvency parameter are required [91]. If the electrostatic interactions are neglected in the model, good agreement between MD simulations and experimental data was found for a Hertzian potential, which models the microgel as an elastic sphere,

$$U_{\text{Hertz}} = \begin{cases} \epsilon_{\text{H}} \left(1 - \frac{r}{R_1 + R_2}\right)^{5/2} & r \leq R_1 + R_2, \\ 0 & r > R_1 + R_2, \end{cases} \quad (2.44)$$

where  $\epsilon_{\text{H}}$  denotes the stiffness of the particles, and  $R_i$  the radius of particle  $i$  [90]. However, for this model to be applied, the prefactor must be fitted to experimental data. The model is able to reproduce

<sup>1</sup>Pairwise additivity is assumed, which neglects the interaction of multiple dipoles at the same time, and presumes that the dipole interaction is instantaneous. The latter is only a fair assumption when the distance between the particles is small enough, otherwise so called retardation effects become significant, and more exact approaches such as Lifshitz theory are required [91].

experimental radial distribution functions of swollen microgel particles in the low  $\phi$  domain [26, 94]. The prefactor  $\epsilon_H$  can be taken a few times higher to mimic the particle in the collapsed state, since the polymer network becomes denser as it contains less water and approaches a hard sphere potential [95].

### Microgel interparticle interactions

In the microgel system used in this thesis, both particle types are negatively charged, hence the electrostatic interactions are repulsive. At low temperatures, the steric repulsion and electrostatic interaction dominate over the van der Waals attraction, and the system is repulsive over all. However, above the VPTT, the density of the particle increases discontinuously, which results in a strongly increased van der Waals attraction and decreased steric repulsion. At low ionic strength, the van der Waals attraction is completely screened by the long range electrostatic repulsion. The net interaction can be tuned by screening the electrostatic repulsion in a certain extent via the electrolyte concentration. In order for this system to form a gel, the electrostatic interactions have to be largely screened, which only results in a short-range van der Waals attraction followed by a steep repulsion [89].

## 2.11 Colloidal gelation

Gels and glasses are metastable states, which means that the colloidal particles are trapped in a local energy minimum, preventing them to reorder into an equilibrium state such as fluids and crystals. Of these non-equilibrium states, only glasses exist in the hard sphere phase diagram (Fig. 1.1), and an attractive interaction component is required to form a gel. Both states are characterised by their stress-bearing properties, i.e. they behave as a solid, which originate from the local arrest of the particles. However, at low volume fractions, this on its own is not sufficient to become solid-like. In this regime, cluster phases may form where particles are locally trapped in a non-equilibrium state. Since these clusters do not form a space spanning network, they are free to diffuse and the system as a whole behaves as a fluid. Consequently, in order to have stress-bearing properties, the system must also be space-spanning, which is called percolation [40]. At low and intermediate densities, an open elastic gel structure is formed, while at high densities, the glass structure becomes arrested due to crowding by neighbouring particles, i.e. caging. In their ideal limits, the distinction between a gel and a glass is well defined. Firstly, the elasticity in a glass arises from caging effects, while in a gel it stems from a percolated infinite network. Secondly, in a glass the density is roughly homogeneous over several particle diameters, while it is inhomogeneous for a gel due to the open structure [1, 20]. The crossover from glass to gel and vice versa appears to be arbitrary in most systems, and the evidence of the existence of a general gel-glass transition is highly disputed [1]. However, Appel *et al.* demonstrated the existence of a glass-to-gel transition in PS-PNIPAm core-shell suspensions [38]. In summary, colloidal gels are systems that exhibit stress-bearing properties, and must fulfil both local particle arrest and the formation of space-spanning networks [40].

The nature of the arrest colloidal gels is governed by both the volume fraction  $\phi$  and strength of the attractive potential  $U$  [96]. At low  $\phi$ , a higher  $U$  is required to form a percolating network (Fig. 2.13a). At sufficiently high  $U$ , the bonds become irreversible on the time scale of gelation leading to diffusion-limited cluster aggregation (DLCA). Here, the kinetics are governed by diffusion, since the particles bond irreversibly upon contact. This means that solely the diffusion of particles into a self-repeating fractal cluster, and the jamming of these clusters determines the gel structure. Once a small energy barrier has to be overcome before irreversible bond formation occurs, the kinetics follow reaction-limited cluster aggregation (RLCA). At low  $\phi$ , this leads to denser fractal clusters, which is reflected in a higher fractal dimension than which was found for DLCA [40, 97]. Both DLCA and RLCA are purely kinetic phenomena, respectively understood by particle motion driven by diffusion, or particle association kinetics driven by their short-ranged attractive potential. In their limits, these two kinetic models can account quantitatively for the rates of cluster formation and consequential cluster

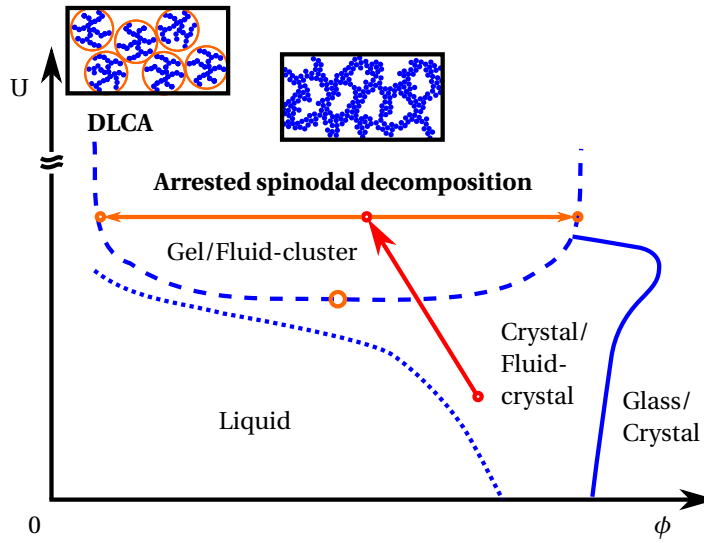


morphology [98]. However, for more complex soft particle interactions outside the high  $U$  and low  $\phi$  limit, this framework is not sufficient [29]. Importantly, these colloidal systems are far more technologically important, and include microgels [92]. Whenever there is attraction between the particles, phase separation into two thermodynamically more stable states can occur via a mechanism called spinodal decomposition [29]. It was not until 2008, when arrested spinodal decomposition (ASD) was accepted as universal mechanism for gelation in colloidal systems in the low  $U$ , intermediate  $\phi$  [92]. Here, gelation occurs as consequence of dynamic arrest that interferes with spinodal decomposition. As the system becomes thermodynamically unstable as result of the interparticle attraction, strong density fluctuations set in favouring the phase separation into a colloid-rich and colloid-poor phase [39, 40, 92, 99]. When the colloid-rich phase reaches the density of that of a colloidal glass, which occurs at sufficiently high  $\phi$ , the density fluctuations become arrested due to the long bonding time of the colloids (Fig. 2.13b) [39, 42, 92]. These vitrified density fluctuations, or clusters, will become arrested themselves as they form a percolating network at a certain  $\phi$ , or below that, will reside in a fluid-cluster coexistence [40, 92]. A characteristic length scale of the density fluctuations was found, which varied as function of the attraction strength during the early stage of ASD, and was reflected in the mesh size  $\xi$  of the gel [100]. In conclusion, the gel phase space is thus a continuous transition between the limits of kinetic arrest (DLCA) and equilibrium thermodynamics (ASD) [29]. Two limiting cases of colloidal gelation can be discriminated, which structure differs as a result of the route of formation. In one case, the constituents of the system vitrify and form a percolating structure as the glassy clusters dynamically arrest (ASD; intermediate  $U$ ,  $\phi$ ). In the second case, the fractal network is formed first, which as a whole vitrifies into a space-spanning structure (DLCA, RLCA; high  $U$ , low  $\phi$ ) [40].

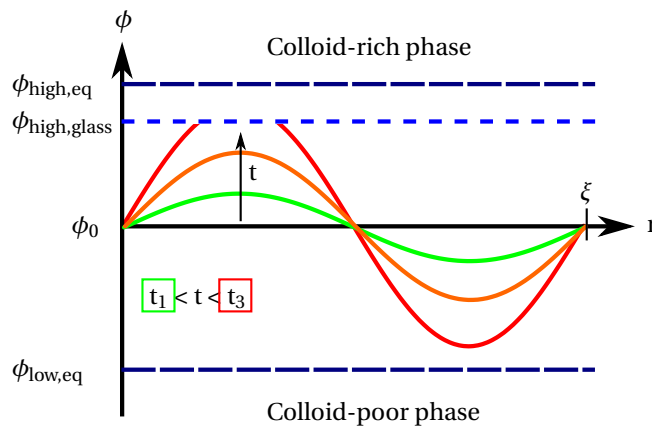
The kinetics of the two gelation routes are similar as they are both diffusion-limited processes. Since the MSD scales with  $1/R_H$  of the object (Eqs. 2.1 and 2.3), the larger growth points are nearly stationary in space and absorb the faster diffusing units around them. Because of this, the distance between these nucleation points is quite well-defined, which is experimentally evidenced via a clear peak in the scattering structure factor (Eq. 2.13). The evolution of this peak over time reflects the self-similarity of the growing units [40]. As time proceeds and nucleation points grow, the peak position of the structure factor  $q_s$  shifts to lower  $q$ , i.e. to larger length scales (Fig. 2.14a). The mass of the object, or scattered intensity  $I(q)$ , scales accordingly as the structure is a repetition of itself. At  $q$ -values larger than  $q_s$ , the scattered intensity is constant over time and decreases with a power law,  $I(q) \sim q^{-d}$ , with  $d = 1.8$  for DLCA and  $d = 3$  for spinodal decomposition. Therefore, a simple normalisation of  $q/q_s$  and  $I(q/q_s) \cdot q_s^d$  leads to a superposition of all curves onto a single master curve (Fig. 2.14b) [101]. As the growing units are just an upscaled version of themselves, they are fractal, and the scaling constant  $d$  is in fact the fractal dimension [29, 101]. Interestingly, at an early stage of spinodal decomposition, the peak height at  $q_s$  grows faster than the scaling via  $d = 3$ , however, this value does give a proper scaling of the tail of the peak [101]. It appears that two length scales are into play in this early stage, which might correlate with the (fractal) clusters and the arrested structure they form [102]. In line with the picture described in the paragraph above, the repeating unit observed in a later stage of ASD is a glassy thick strand or cluster, while it is a fractal aggregate in the case of DLCA [40].

### 2.11.1 Morphology and mechanical properties

Fractal aggregation in the limits of DLCA and RCLA was extensively studied in the 1980s, and the morphology and dynamics of the resulting gel are well understood [97, 103–105]. These gels have a very open structure with low connectivity between the fractal aggregates. As the dangling ends cannot transmit stress, its elasticity arises from a small fraction of connections between the fractal aggregates, which form the stress-bearing backbone. Models relating the size and connectivity of the fractal aggregates to the macroscopic elasticity are in good agreement with experiment [106–109]. As discussed above, different interparticle interactions and higher  $\phi$ , gives rise to gels with very different microscopic structures. Here, the mesoscopic ordering goes from thin and open fractal structures to dense interconnected glassy clusters. These structures lead automatically to a change in the elasticity



(a)



(b)

Figure 2.13: a): Schematic state diagram for colloidal particles with a short-ranged attraction with a representation of the gel structure in the diffusion-limited cluster aggregation and arrested spinodal decomposition limits. The blue lines depict the phase boundaries, where the dashed line represents the spinodal, which marks the region of thermodynamic instability. The fluid-crystal coexistence and the crystal phase are taken together in this schematic for clarity. The quench of a (microgel) particle from the crystal/fluid-crystal regime into the spinodal (red dots and arrow), phase separation occurs into a low  $\phi$  and high  $\phi$  phase. If the colloidal-rich high  $\phi$  reaches the density of that of a glass, the phase separation will be arrested and arrested spinodal decomposition occurs [40]. b): Schematic of the density fluctuations as a function of time ( $t_1 < t < t_3$ ) during an early stage of arrested spinodal decomposition. The initial and equilibrium volume fractions of the concentrated and dilute phases are denoted  $\phi_0$ ,  $\phi_{\text{high}}$  and  $\phi_{\text{low}}$ , with  $\phi_{\text{high,eq}}$  and  $\phi_{\text{low,eq}}$  with the volume fraction of the right and left branch of the coexistence curve as depicted in (a). At a certain moment  $t_3$  (red curve), the volume fraction of the colloid-rich density fluctuations reach the volume fraction of a glass ( $\phi_{\text{high,glass}}$ ), upon which phase separation gets pinned into a percolating gel network with a characteristic length  $\xi$ . Adapted from [100].

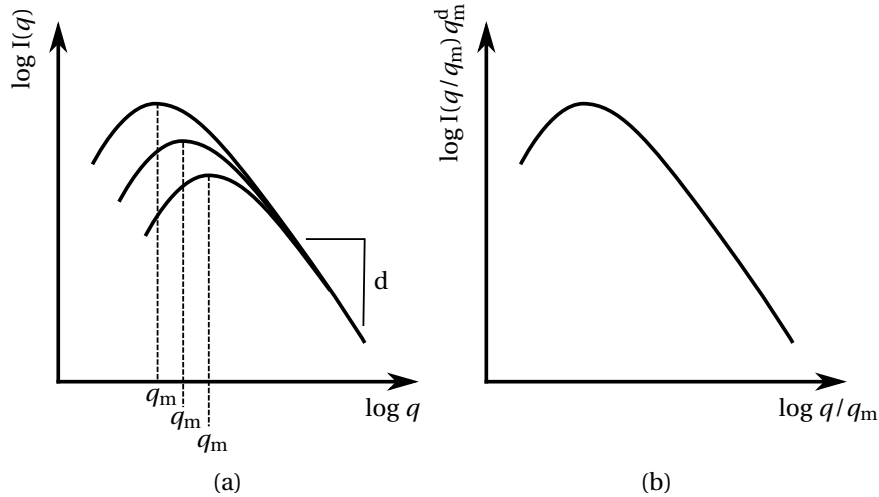


Figure 2.14: a,b): Schematic of the evolution of the scattering structure factor over time during diffusion limited cluster aggregation and/or arrested spinodal decomposition (a). With time, the maximum of the structure factor shifts to lower values of the scattering vector  $q$ , which is indicated with  $q_m$ . In the higher  $q$ -range, the scattering intensity decreases as  $I(q) \sim q^{-d}$ . Normalisation of the  $q$ -axis with  $q_m$  and the  $I$ -axis with  $q_m^d$  scales all scattering profiles onto a single master curve (b). Adapted from [40].

of the material [40].

Despite the lack of a general theoretical description, some observations relating the morphology and mechanical properties have been done in the ASD-regime. Dinsmore and Weitz found a similar fractal dimension in these gels, independently on the  $U$  or  $\phi$ . However, gels with a higher  $U$  or higher  $\phi$  have more flexible joints, which shows that a stronger interparticle interaction reduces the compactisation of the structure. Moreover, they found some resistance to bond bending and rotation due to compression of the polymer layer around their PMMA particles. They reasoned that macroscopic elasticity thus must arise from bond stretching. For increasing attraction, they found that the average number of bonds per particle shifted from  $\sim 4$  to  $\sim 2$  and that the size distribution became narrower. In the limit of DLCA, a strongly peaked distribution around 2 would be expected because of its string-dominated morphology, and these results can be interpreted as a continuous transition to a more DLCA-like gel [110].

### 2.11.2 Physical ageing

Colloidal gels are thermodynamically out-of-equilibrium, and show a physical ageing over time towards a lower energy state. This generally means that the structure becomes more compact, since the particles will maximize the number of attractive interactions. Due to thermal fluctuations, small (co-operative) displacements can occur, and in some cases, bonds between particles break and reform, which allows reorganisation of the gel structure. This process continues until the rigidity of the gel is lost, and according to Sprakel, a true steady state does not exist for colloidal gels [38]. Cipelletti *et al.* showed for PS DLCA-like gels that the ageing is in the time scale of days and leads to a locally more compact structure [111]. Compared to a PS colloidal system, Appel *et al.* observed significant physical ageing on a much shorter time scale for a  $\phi \approx 0.1$  PS-PNIPAm system with 0.1 M KCl [38]. The  $G'$  was found to increase due to ageing, which was faster at higher temperatures, i.e. up to a factor 4 over 2000 s at 55 °C. In line with the model described in this paragraph, the different time scale of the physical ageing can be ascribed to the weaker van der Waals attraction between the collapsed microgel particles, and the higher temperature of the experiment.

### 2.11.3 Bigels

Little work has been done on colloidal and molecular bigels. To put the work into context, three types of bigels will be discriminated by the author, being:

1. sequential gelation
2. instantaneous gelation
3. selective gelation.

To start, sequential gelation was first and only reported by Appel *et al.* in 2015 [4]. A gel is formed by a first species, which serves as scaffold for a second species, yielding a core-shell gel structure. This is only possible if the gelation of a binary mixture is separated in time. So far, only binary microgel systems are able to exhibit this phase behaviour. If the gelation of a binary phase is not separated in time, it is called in instantaneous gelation. In a symmetrical binary system, this would yield the same gel as if it would be a single-type system. However, size and attraction asymmetry would probably give rise to completely new phase behaviour, but this type of gelation has not been reported in literature yet. The last type of bigel is selective gelation and can be seen as a form of instantaneous gelation, since the gelation of a binary phase is not separated in time. Here, the two particle types are selectively attractive to their own kind, and exhibit hard sphere repulsion with the other type. Varatto *et al.* and Di Michele *et al.* showed with simulations and DNA-coated colloids that these bigels follow an ASD mechanism [2, 3]. It was shown that this type of bigels show different mechanical properties than single-type gels, for instance they are more resistant to strain at the same  $\phi$  and have a couple of times higher yield point. Di Michele *et al.* suggested that this is caused by the steric repulsion between the two species, which prevents further demixing and compactification, and thereby preventing complete failure. Many applications in nanotechnology are proposed exploiting its unique morphology and mechanical properties [3]. Moreover, research on these colloidal bigels have stimulated the investigation of molecular bigels, since it is thought that they would have increased drug release rates over ordinary gels [112].

---

## Experimental

---

### 3.1 Synthesis

#### 3.1.1 Materials

The supplier and purity of the used chemicals are listed in this section (Fig. 3.1). Aluminium oxide basic (VWR, not listed), BIS (Sigma Aldrich, 99%), FOM (Sigma Aldrich, 97%), KPS (Sigma Aldrich,  $\geq 99\%$ ), MRB (Sigma Aldrich, not listed), NIPAm (Sigma Aldrich, 97%), NIPMAm (Sigma Aldrich, 97%), PM 546, i.e. 1,3,5,7,8-pentamethylpyrromethene difluoroborate (Exciton, not listed), PM 605, i.e. 8-acetoxymethyl-2,6-diethyl-1,3,5,7-tetramethylpyrromethene fluoroborate (Exciton, not listed), styrene (Sigma Aldrich, ReagentPlus® with 4-tert-butylcatechol radical inhibitor), and SDS (Kebo Lab, 99%) were used as received without any further purification.

Filtered and deionised water was obtained from a Millipore Milli-Q Academic device, which delivers water with a resistivity of 18.2 M $\Omega$ m. Milli-Q water from this device was used for all syntheses and dilutions.

#### 3.1.2 Experimental set-up

Two experimental set-ups for the syntheses were used in this thesis, named set-up A and set-up B (Fig. 3.2). Both set-ups provide an inert nitrogen atmosphere, stirring, heating, and reflux cooling. Set-up A consisted of a stirring-heating plate with an oil bath on top. A three-neck roundbottom flask was placed in the oil bath and a reflux condenser and two latex septa were put on the necks of the flask. A magnetic stirring bar was placed in the three neck roundbottom flask to provide mixing prior and during the reaction. On top of the reflux condenser, a gas bubbler with silicone oil was connected to prevent atmospheric gasses to enter the system. Set-up B consisted of a double-walled glass reactor coupled to a water circulation thermostat. A reflux condenser with gas bubbler and three latex septa were connected to the glass unit closing the reaction vessel. Mechanical stirring was provided for by a motor connected to a branched glass stirrer which was positioned  $\sim 2$  cm above the bottom of the reactor. The set-up used for the synthesis of samples M2-3 was equipped with a magnetic stirring bar. Both set-ups were left unadapted during the reaction.

A CMA 100 micro-injection pump was positioned next to the set-up, and was loaded with syringes briefly before initiation of the reaction. The syringes were equipped with needles, which were led through the septa and hung above the reaction mixture. This set-up enabled the controlled addition of (co)monomers during the reaction.

A discrepancy in temperature set on the thermocontrol unit in set-up A and the real temperature was found at a late stage of the project. The temperatures set at the thermocontrol are given throughout the thesis unless otherwise stated. It was found that increased stirring enhanced the thermal

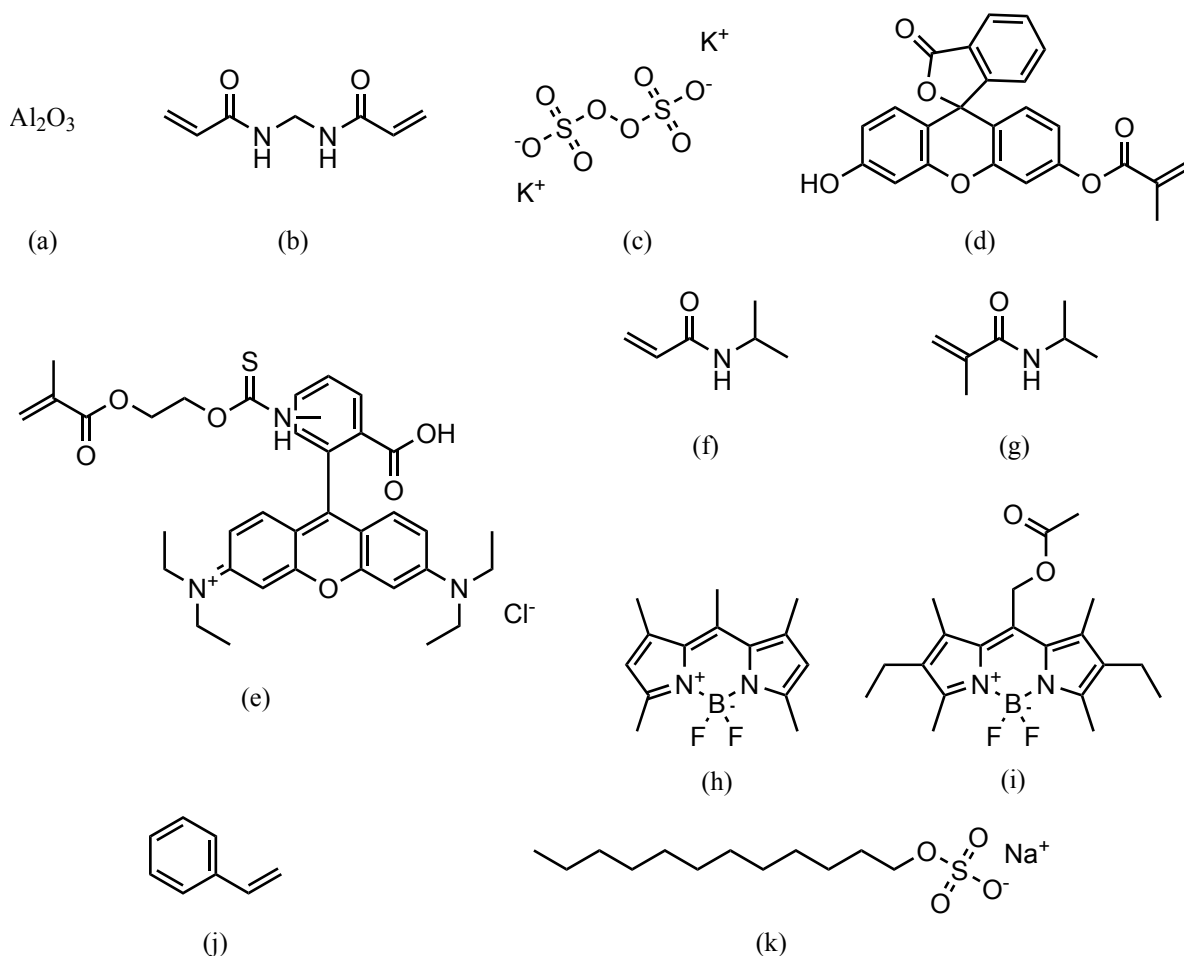


Figure 3.1: Structure of chemicals listed in Section 3.1.1 in alphabetical order. Shown is aluminium oxide (a), BIS (b), KPS (c), FOM (d), MRB (e), NIPAm (f), NIPMAm (g), PM 546 (h), PM 605 (i), styrene (j), and SDS (k).

conduction significantly. A test was run under synthesis conditions, that is 75 °C set on the thermocontrol, 400 rpm stirring, nitrogen flow, and cooling, to quantify this difference. The real temperature was measured with a mercury thermometer, which was hung in solution. The flasks with a maximum volume of 100, 250, 500, and 1000 mL were tested with 3/5 of their volume filled with Milli-Q water. The discrepancy was found to be a constant 6 °C lower than the temperature set on the thermocontrol.

The sample was purified after the reaction by means of centrifugation or dialysis, and optionally condensed via a single centrifugation step. The excess of monomer reactants were removed by repeated centrifugation at 10,000 rpm (16,211 RCF) and redispersion for at least three times. The centrifuge was a Sigma Laboratory 6K15 with temperature control, which was equipped with a Sigma 12256 rotor. In some cases, the excess of reactants were removed via dialysis with a 14-16 kDa Spectrum Labs membrane in Milli-Q water under gentle stirring. The dialysis water was refreshed on a daily basis, and was done for at least two weeks. Before use, the membrane was soaked for thirty minutes and rinsed afterwards with Milli-Q water. Condensation was achieved by centrifuging at 15,000 rpm (21,130 RCF) in a Sigma 3-30KS centrifuge.

### 3.1.3 Pure microgel synthesis

The pure microgels were prepared via a precipitation polymerisation reaction. A typical synthesis would be the following. The dye was dissolved in an amount of Milli-Q water and sonicated for at least 20 minutes. The Milli-Q water, monomer, BIS, SDS, and dissolved dye were added to the vessel under

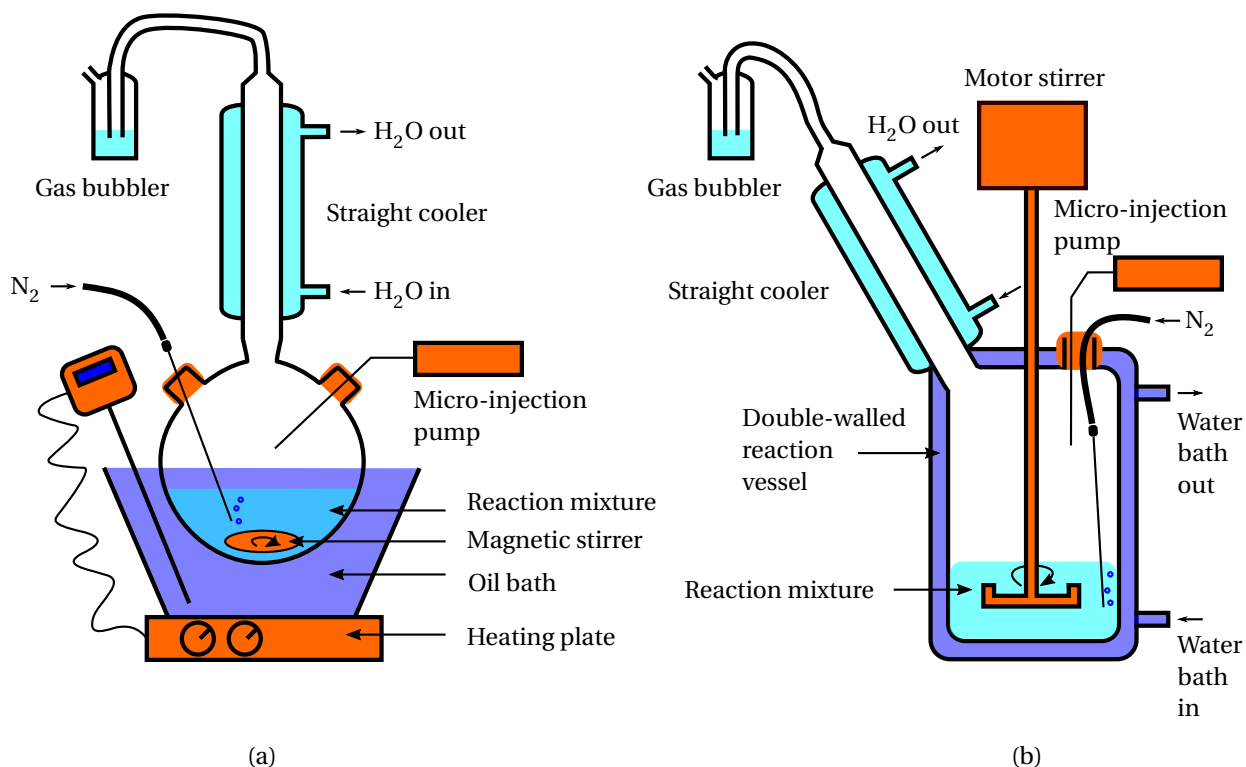


Figure 3.2: Schematic of the experimental set-ups, i.e. set-up A (a) and set-up B (b), used for microgel and PS synthesis. The temperature of the reaction mixture was set via the temperature of the water bath in set-up B.

~400 rpm stirring. The reaction mixture was heated to 60°C under a constant nitrogen flow, vigorous stirring and reflux cooling for at least one hour to remove oxygen from the solution. Subsequently, the reaction mixture was heated to 80°C under a gentle nitrogen flow to prevent the inflow of oxygen. During the purging process, KPS was dissolved in Milli-Q water and degassed by pulling a closed syringe to lower the vapour pressure and thereby removing dissolved oxygen from the solution. After 15 minutes of temperature stabilisation, the reaction was initiated by addition of degassed KPS above the reaction mixture in a dropwise fashion over ten minutes. The clear solution turned turbid 1-5 minutes after initiation. The reaction was continued for four hours and cooled down under stirring to ~50°C. The reaction mixture was filtered over ~45°C glass wool to remove aggregate. The sample was purified by repeated centrifugation and redispersion for at least three times and was condensed in a single step. An overview of the performed microgel syntheses relevant for this thesis is shown in Table C.1.

### 3.1.4 Polystyrene core synthesis

The functionalised PS cores are prepared via an emulsion polymerisation reaction in a set-up type A. About 90% of the Milli-Q water was purged under nitrogen flow and 400 rpm stirring for half an hour to remove oxygen from the solution. The styrene was run over 10cm aluminium oxide in a column to remove the radical inhibitor. The styrene, monomer, BIS, SDS, dye, and remaining Milli-Q water were transferred to the reaction vessel and purged at room temperature under a constant nitrogen flow, vigorous stirring and reflux cooling for at least one hour. Before stirring, a two-layer system was observed in which the upper phase had the same colour as the dye. The reaction mixture turned in a turbid emulsion with a homogeneous colour during stirring. The set-up was covered in aluminium foil to prevent premature bleaching of the dye. Meanwhile, the KPS was dissolved in Milli-Q water and was degassed in a syringe. The stirring was set to 400 rpm, a gentle nitrogen flow was applied to prevent the inflow of oxygen, and the temperature of the oil bath was set to 75°C and was left

15 minutes to stabilise. The needle for the nitrogen inlet was positioned above the reaction mixture to prevent heavy foaming. The KPS solution was injected at once above the reaction mixture and the solution turned more turbid after about 15 minutes. After 24 hours, the reaction mixture was cooled down to room temperature and filtered over glass wool. Purification was achieved via either centrifugation or dialysis. The samples were diluted to 7-15 wt% and stored on a shaker. All samples crystallised immediately on the wall of the centrifugation tubes. An overview of the performed PS core syntheses relevant for this thesis is shown in Table C.2, and the protocol for the core synthesis is given in Section D.1.

### 3.1.5 Microgel shell synthesis

The PS-microgel core-shell particles are prepared via a batch-wise precipitation polymerisation reaction. Some protocols of the core-shell syntheses can be found in Appendix D. Two types of batch synthesis were performed, named batch and semi-batch synthesis. In the first, the reaction was cooled down and filtered between every batch, while for the latter, multiple shells were grown batch-wise by injection of the reactants in the unmodified reaction mixture.

The first part is the same for both the semi-batch and batch synthesis, and is typically the following. About 90% of the Milli-Q water was purged under nitrogen flow and 400 rpm stirring for half an hour to remove oxygen from the solution. The monomer, BIS, and functionalised PS cores were transferred to the reaction vessel. The oil bath was heated to 75 °C under a constant nitrogen flow, vigorous stirring and reflux cooling for at least 45 minutes to remove oxygen from the solution. The KPS and BIS for the feed were dissolved in Milli-Q and degassed in a syringe. The reaction was initiated by the injection of KPS above the reaction mixture. Five minutes after the start of the KPS addition, the BIS was injected over a 30 minutes period with the aid of a micro-injection pump.

#### Batch synthesis

The procedure described above was followed, and after continuing for three hours, the reaction mixture was cooled down and filtered over glass wool. A sample was taken, and the procedure was repeated until the desired size or number of shells was obtained. The outer shell was synthesised without BIS-feed unless stated otherwise.

#### Semi-batch synthesis

The procedure described above was followed first. A stock was prepared with monomer and BIS, which were dissolved in Milli-Q water in a second setup of type A under 500 rpm stirring and constant nitrogen flow. After 30 minutes, the stock solution was heated in an oil bath of 60 °C. The KPS and BIS for the feed were dissolved in Milli-Q and degassed in a syringe. After proceeding the reaction for three hours, the respectively the stock and KPS were added drop wise above the reaction mixture over two minutes each. Five minutes after the start of the KPS addition, the BIS was injected over a thirty minutes period with the aid of a micro-injection pump. The reaction was proceeded two to four hours depending on the reaction conditions, and this procedure was repeated. The outer shell was synthesised without BIS-feed unless stated otherwise. After the growth of four shells, the reaction volume had increased by about 1.8 times and the reaction was cooled down. After filtering over glass wool, the dispersion was concentrated by a single centrifugation step of about two hours at 10,000 rpm. The weight percentage or number of cores was determined and the amount of reactants used for the next batches was scaled with the yield. As example of a semi-batch synthesis, the protocol of CS19 is given in Section D.2.

#### Overview core-shell syntheses

The core-shell syntheses are given in Table C.3. All core-shell syntheses were done in a type A set-up except for CS18.



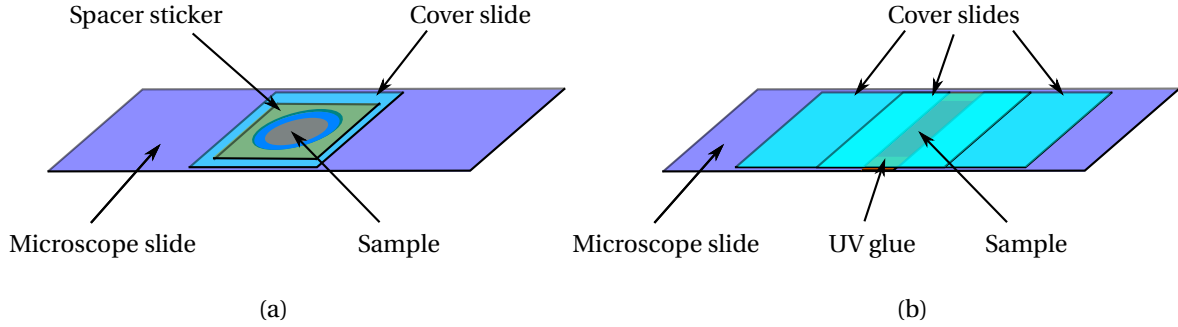


Figure 3.3: Two glass cells used in CLSM experiments. The spacer cell (a) consists of a microscope slide with a spacer sticker, which is closed with a glass cover slip. The glass cell (b) consists of two cover slides on a microscope slide, which are closed with a third cover slide and UV-Glue. The latter cell provides a closed atmosphere for a period in the order of weeks.

## 3.2 Methods

Before sample preparation, the stock solution was put on the shaker for > 3 hours. The volume fraction  $\phi$  was calculated with

$$\phi = n_p \frac{4\pi}{3} R_H^3, \quad (3.1)$$

in which  $n_p$  denotes the number density, and  $R_H$  the hydrodynamic radius. The density of the stock was assumed to be 1 g/mL, since the density of NIPAm is not reported in literature. Homogenisation of the sample after mixing was assumed by vortexing for > 30 minutes.

The core density was approximated as  $\rho_{\text{core}} = c_1 \rho_{\text{PS}} + c_2 \rho_{\text{microgel}}$ , with  $c_1$  and  $c_2$  respectively the fraction of styrene and microgel monomer used in the core synthesis. The volume of the particle could be estimated via its hydrodynamic radius at 50 °C, so the number density  $n_p$  was approximated<sup>1</sup> via

$$n_p = \frac{3(\text{wt}\%) V_{\text{sample}}}{4\pi R_{H,50^\circ\text{C}}^3 \cdot \rho_{\text{core}}}. \quad (3.2)$$

### 3.2.1 Confocal laser scanning microscopy

Confocal microscopy images were recorded with an Leica TCS SP5 confocal laser scanning microscope, which was operated in the inverted stand, and equipped with a 100x zoom/1.4 NA oil immersion objective. A 543 nm helium-neon (HeNe) laser was used to excite MRB and PM 605 fluorescent dyes, and a 488 nm argon laser for the FOM and PM 546 fluorescent dyes. Temperature control with an accuracy of 0.2 °C was achieved with an isolated thermostated enclosure of the microscope.

The sample cells are shown in Fig. 3.3. A Grace-Bio Labs SecureSeal™ 120 μm spacer sticker was used for the spacer cell. For the preparation of the glass cell, the protocol developed by J.M. Meijer was followed. The glass cell was cleaned with a 5% Decon 90 solution, thoroughly rinsed with Milli-Q H<sub>2</sub>O, and dried with N<sub>2</sub> prior to sample loading. For all experiments, the spacer cell was used, except for the ones described in Section 4.4 where the glass cell was used.

### Image analysis

The analysed  $z$ -stacks were recorded with a voxel dimension of 55x55x125 nm, unless otherwise stated. The time series in Section 4.3.2 were recorded with 30x30 nm pixel dimensions. The samples were

<sup>1</sup>Pure microgels contain about 30% water in the collapsed state, however it is unknown what this value is for the CS particles since some styrene is co-polymerised as well [69, 77]. The error is small, since around 30% water content in the microgel layer would result in an error of ~ 3% in the core density for C1-4.

recorded with a line-average of 2-3 and no frame-averaging, except for CS19 in Section 4.3.1, which was recorded with a frame-average of 8, and a line-average of 32.

**Crocker and Grier particle tracking algorithms** The original data were Gaussian filtered, before a spatial band pass filter was applied, and the data was fitted to convert the data into a set of particle coordinates. The parameters were sample and recording settings dependent, and typical set of parameters would be a Gaussian blur kernel with a standard deviation of 2 px, and a spatial band pass filter with a diameter of 10 px. The diameter for the particle fit would be in the order of 8 px. The image analysis and quantification routines were implemented in IDL version 8.4 (Harris Geospatial, USA). The particle tracking and analysis routines can be downloaded free of charge at <http://www.physics.emory.edu/faculty/weeks/idl/>.

**Skeletonization** The original data were Gaussian filtered ([5,5,5]px kernel, standard deviation 4 px) before thresholding was applied to convert the intensity stack into a binary volume with foreground (gel structure) and background (solvent) voxels. The threshold was defined per  $z$ -slice as a fraction (0.7) between the 10% dimmest and brightest pixels. Residual discretization noise was removed by morphological closing (dilation followed by erosion using a [6,6,6]px spherical kernel). The binary volume was further cleaned by discarding objects with a total number of voxels 0.8 times smaller than the biggest object and by converting isolated background components, i.e. holes, into foreground voxels.

The surface and volume of the cleaned binary volume was approximated with Minkowski measures, implemented into MATLAB by Legland *et al.* [113].

The preprocessed binary volume was converted to a single voxel thick medial axis skeleton that is homotopic to the original image using the algorithm developed by Lee *et al.* [62] implemented into MATLAB by Kollmannsberger [114]. The skeleton was converted into a network topology described in nodes and edges, which was corrected for the anisotropic voxel dimensions. The image analysis and quantification routines were implemented in MATLAB 2016b (The MathWorks, Natick, MA, USA) using the image processing toolbox. The MATLAB code is available from the authors request, and a detailed overview and discussion of the used parameters can be found in Appendix F.

## Number density

**2D** A crystalline sample with a known weight percentage was measured in a spacer cell. Images were recorded in the crystal plane, and from this, the average radius  $R_{\text{particle}}$  could be determined. After that, the number of particles was determined via the function ‘number of local peaks’ in ImageJ. An average was taken between the number with and without the edge particles included. The volume of a plane could be calculated via the distance between the face centred cubic (FCC) layers being

$$d_{\text{FCC}} = \frac{2\sqrt{2}}{\sqrt{3}} R_{\text{particle}}, \quad (3.3)$$

from which the number density could be calculated.

**3D** A  $z$ -stack of a crystalline sample was taken and the particle positions were determined with the Crocker and Grier scripts. A sub volume which was about two particle diameters smaller on each side was taken, and from this, the number density could be calculated from the number of particles divided by the focal volume.

### 3.2.2 Electrophoretic mobility measurements

Electrophoretic mobility measurements were done with a Malvern ZetaSizer Nano-ZS equipped with a HeNe laser with automatic optical attenuator. Laser doppler velocimetry was performed at a fixed

17° angle. The mobility was determined over the average of three measurements consisting of 10-100 runs. A Malvern DTS1070 disposable folded capillary cell was used, which was first rinsed three times with Milli-Q water and subsequently three times with sample before loading. The sample was highly diluted and corresponded to roughly  $10^{-2}$  wt% of pure microgel. After each temperature change during a sequence of measurements, the cell was equilibrated for 15 minutes, and subsequently briefly removed from the set-up to remove the air bubbles by application of mechanical stress. After that, the sample was equilibrated for 5 minutes before start of the measurement. The zeta potential was calculated manually using Eq. 2.34 with  $R_H$  obtained from 3D DLS measurements, because the size determination in the Malvern Zetasizer was found to not always give accurate results for fluorescent samples.

### 3.2.3 Light scattering

SLS and DLS measurements were performed using an LS instruments 3D DLS spectrometer with an LS instruments 3D modulation unit and correlator. The set-up was equipped with a Cobolt Flamenco™ 5th generation 100 mW 660 nm diode-pumped solid-state laser. The intensity of the scattered light was measured relative to the transmitted beam using two Perkin Elmer SPCM-AQRH-13-FC photon counting modules. The temperature of the decalin bath could be controlled via a coupled water thermostat with a precision of 0.1 °C. The 5 mm Wilmad® NMR tubes were used as sample cells, and were rinsed three times with Milli-Q water and subsequently three times with sample before loading. The sample had a number density highly diluted and corresponded to roughly  $10^{-2}$  wt% of pure microgel. An equilibration period of at least 20 min was taken prior to the measurement.

**SLS** Angles in the range from 30 to 135° were measured in 3D cross-correlation mode with an increment of 2°. The intensity was averaged over three 300 s measurements.

**DLS** DLS measurements were done at a 60° angle unless otherwise stated. The autocorrelation function was recorded in three consecutive 300 s measurements. The hydrodynamic radius  $R_H$  was determined from the first order cumulant fit in the first 20% of the decay, and averaged over the measurements.

The DLS measurements in Section 4.4.1 were done on a Malvern ZetaSizer Nano-ZS equipped with a HeNe laser at a 173° scattering angle. The size was determined over the average of three measurements consisting of an automatically determined number of runs. A 12.5 mm Brand PMMA disposable cuvette was first rinsed three times with Milli-Q water and subsequently three times with sample before loading. The sample was highly diluted and contained approximately  $10^{-2}$  wt% pure microgel. The sample was temperature equilibrated for at least 20 minutes prior to the measurement, and 300 s between every temperature step.

### 3.2.4 Rheology

Mechanic rheology experiments were done on a TA instruments ARES strain-controlled rheometer. The rheometer was operated with a couette geometry with a sample volume of 9 mL and was covered with two metal half-rings to prevent evaporation of the solvent. For small sample volumes, a couette geometry with a sample volume 2.2 mL was used with a solvent trap as described and used in Subsections 4.4.2 and 4.4.3.

### 3.2.5 Spectroscopy

**Fluorescence spectroscopy** Fluorescence spectroscopy was done on the cores and CS particles with a Varian Cary Eclipse fluorescence spectrophotometer equipped with a full spectrum xenon pulse lamp source with a horizontal beam geometry. The sample cell was a 4x12.5 mm Brand PS disposable cuvette, which was positioned with the longest side parallel to the beam. The cell was rinsed three

Table 3.1: Overview of the used settings for the fluorescence spectroscopy on the PM 546 and PM 605 stained cores and CS particles. The excitation and emission wavelengths are denoted with  $\lambda_{\text{ex}}$  and  $\lambda_{\text{em}}$ , respectively. The slit widths of the excitation and emission and monochromators are indicated respectively with  $d_{\text{slit,ex}}$  and  $d_{\text{slit,em}}$ , and the baseline wavelength is denoted with  $\lambda_0$ .

	PM 546	PM 605
$\lambda_{\text{ex}}$	493 nm	543 nm
$\lambda_{\text{em}}$	500-700 nm	550-750 nm
$d_{\text{slit,ex}}$	2.5 nm	2.5 nm
$d_{\text{slit,em}}$	5 nm	5 nm
$\lambda_0$	700 nm	750 nm

times with Milli-Q water and three times with sample before loading. The settings are shown in Table 3.1. Prior to each measurement, the intensity at the baseline wavelength  $\lambda_0$  is set to zero. A sample with Milli-Q water was taken as blanco and subtracted from each spectrum.

**UV-Vis spectroscopy** UV-Vis spectroscopy was done with a Varian Cary 300 Bio UV-Visible spectrophotometer equipped with a full spectrum xenon pulse lamp source with a horizontal beam geometry. A 12.5 mm Brand PMMA disposable cuvette was first rinsed three times with Milli-Q water and subsequently three times with sample before loading. The intensity was zeroed prior to each measurement, and the spectrum was recorded in a 250-800 nm spectral range.

### 3.2.6 Viscometry

Viscometry was performed with a glass Micro-Ostwald viscometer with a sample loading of 2.5 mL. The sample was temperature equilibrated for at least 30 min in a Parafilm-sealed viscometer. The flow time was measured with a stop watch, and was done six times in total for every weight percentage and temperature.

### 3.2.7 Simulation

BD simulations were performed with LAMMPS simulation software (version 10 Augustus 2015), which was run as MD with Langevin thermostat. The simulations were run on 8 processors in parallel. The micro canonical ensemble was used, which means that the number of particles, volume and total energy is constant, i.e. fixed NVE. The diffusion of the particles was controlled implicitly via their mass (Appendix E.2). An equilibration step prior to the production run was done with a shifted Lennard-Jones potential cut-off at the potential minimum. The time step in the simulations was chosen such that the maximal displacement in one step could not be more than  $10^{-2}$  of the diameter of the particle. The LAMMPS simulation software was operated via a Python wrapper, which enabled more complex sequential simulations, and was written by the author for this purpose. The schematic of the software architecture is shown in Fig. 3.4.

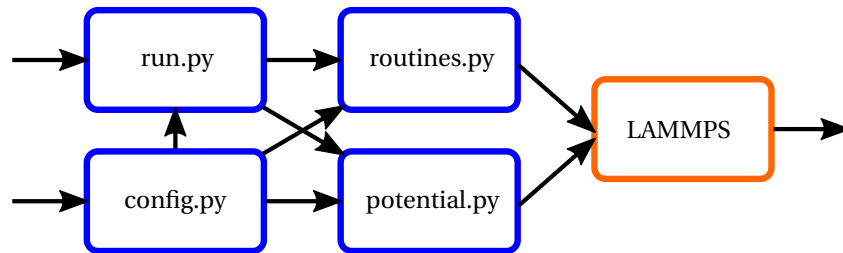


Figure 3.4: Schematic of the Python wrapper to operate the LAMMPS simulation software. The input parameters are set in `config.py`, which are imported in the other python routines. The sequence of simulations are called from `run.py`, which is called by the user to start the software. The LAMMPS simulation software is run with the LAMMPS input files generated in `routines.py`. The particle interactions are fed to LAMMPS via tables in which the force as function of interparticle distance per particle type is defined, which are generated by `potential.py`.



---

## Results and discussion

---

First, the requirements for a colloidal model system compatible with the research approach outlined in Section 1.1.2 are discussed below. The synthesis and characterisation of such model systems is described in Section 4.2, and an in-depth comparison between the synthesised model systems is given in Section 4.3. The chapter is concluded in Section 4.4 with a discussion of the relation between mechanical properties and morphology in single particle and sequential gels during gel formation and beyond.

### 4.1 Colloidal system requirements

To study colloidal bigelation by means of confocal imaging and mechanical rheology, a model system with the following properties was required:

- Good resolvability in CLSM imaging
- Stable fluorescence
- Thermoresponsivity
- Tunable size and properties
- Large batch volume

In the following section, the resolvability in CLSM imaging will be discussed from a theoretical point of view for a pure microgel and core-shell approach. A stable fluorescence was required in order to make large  $z$ -stacks the sample. A high laser intensity was required to be able work with a small pin-hole, and to study deep into the sample since both in- and outgoing light is scattered. In order to systematically study binary gels, the size should be tunable and the thermoresponsivity retained. Finally, large batch volumes were required in order to do mechanical rheology, as multiple experiments were done on samples from the same batch.

#### 4.1.1 Resolvability in CLSM

For good resolvability under measurement conditions, the pure microgel should have a diameter of  $\gtrsim 1 \mu\text{m}$ , and the CS particle of  $\gtrsim 0.6 \mu\text{m}$  and a very small core to minimize scattering. A good resolvability of the particles was required to determine the particle core position with particle tracking algorithms (Section 2.5.2). The resolution could be calculated by using Eq. 2.24 and 2.25, and is shown in Table 4.1. Due to imperfections in the optical system, the real resolution was somewhat lower. By measuring the size distribution of well defined PS particles glued to a grid, Mohanty *et al.* had determined a resolution of 220 nm in the  $x, y$ -plane and 600 nm in the  $z$ -direction for the microscope set-up used in this thesis [26]. Based on the Nyquist theorem and the will to oversample a bit, a sampling rate in the  $x, y$ -plane of 4 and the  $z$ -direction of 3 was used in this thesis. This corresponds to

Table 4.1: A list of the laser wavelength used to excite the dye ( $\lambda_{\text{ex}}$ ) and maximum emission ( $\lambda_{\text{em}}$ ) wavelength of the used fluorescent dyes in this thesis (ref.: supplier's supplementary information). The diffraction limited resolution is calculated in the  $x, y$ -plane with Eq. 2.24 and in the  $z$ -direction with 2.25. A refractive index of 1.33 is taken for the sample medium, i.e. water at 20 °C.

Fluorescent dye	$\lambda_{\text{ex}}$	$\lambda_{\text{em}}$	$R_{x,y}$ ( $\mu\text{m}$ )	$R_z$ ( $\mu\text{m}$ )
MRB	543	534	0.13	0.49
PM 605	543	565 (ethanol)	0.13	0.50
FOM	488	517	0.11	0.44
PM 546	488	519 (methanol)	0.12	0.44

voxel dimensions of 55 x 55 x 200 nm, but could be lowered in the  $z$ -direction if a smaller pinhole was used. With a pinhole of one Airy unit, the best value was found to be 130  $\mu\text{m}$ , which led to the voxel dimensions of 55 x 55 x 130 nm, which were mainly used in this thesis.

The minimum particle size could be estimated from the resolution of the microscope and the sampling rate. For the particle tracking algorithm, around 10 data points are required for the fit, which means the minimum particle size is limited by the resolution of the microscope [59]. The resolvability could be stretched a bit in the case of core-shell particles, since the fluorescently labelled core surrounded by a non-fluorescing shell caused separation of the fluorescent signal of the individual particles, which facilitated particle tracking. Due to the finite size of the laser beam and the point spread function, a core smaller than the resolution was found to have an apparent diameter of approximately 0.44  $\mu\text{m}$ . This would allow tracking of fluorescent cores smaller than the resolution of the CLSM, and it was expected that at least a diameter of 0.55  $\mu\text{m}$  would be required to accurately sample the particles in the  $x, y$ -plane, but in experiment it was found that a larger particle diameter was required due to scattering. It was found empirically that the particle tracking was slightly better for the CS particles at even higher oversampling, as the fitting parameters could be set more precisely. One should bear in mind that the subpixel accuracy was lost with such oversampling, and careful analysis of the output resolution was required.

Scattering of the incoming and outgoing light reduced the signal to noise ratio in a large extent. A blur of the signal, which caused a reduced or diminished resolvability in the case of feature overlap, and some out-of-plane fluorescence was observed as result of scattering. This resulted in a lower resolution, hence a larger minimum particle size required for the particle tracking scripts. In the optical system, two components can introduce additional scattering. Firstly, the particles itself do scatter light, which is more pronounced at high temperatures because of higher density of the microgel particles. Index matching of the solvent with the particles is not an option in this system since the thermoresponsivity is lost upon change of solvent. Secondly, at high temperatures, a mismatch in refractive index between the immersion oil of the objective and the cover glass occurs, which is an intrinsic property of the optical system. No oil compatible with the objective and with the required refractive index at elevated temperatures was on the market at the time of writing.

## 4.2 Synthesis and characterisation

The synthesis of pure microgels, PS cores, and microgel shells will be discussed in this section. The characterisation of the particles will be used to study the synthesis with the ultimate goal to obtain a model system with the properties described above. An extensive comparison of the pure and CS microgels can be found in Section 4.3. This section is concluded with a discussion about the volume fraction and number density the obtained samples (Subsection 4.2.5).

### 4.2.1 Pure microgels

Five pure microgel PNIPAm syntheses were performed, being M2 and M4.1-4.4, and two pure microgel PNIPMAm syntheses, that is M1 and M2. The hydrodynamic radius and swelling ratio of the



particles was determined with DLS measurements, and the zeta potential with electrophoretic mobility measurements, which results are shown in Table 4.2. Pure PNIPAm and PNIPMAm microgels were synthesised in a single batch with 5% crosslink density. KPS was used as initiator, which incorporates a negative residual charge into the microgel network. The reaction proceeded as expected and the turbidity increased suddenly after ~1-5 minutes of initiation until the reaction mixture was completely opaque. This observation agrees with the precipitation polymerisation mechanism (Section 2.10.2).

The samples crystallised easily, which is an indication for low polydispersity, as hard spheres crystallisation does not occur above a ~6% polydispersity threshold [115]. However, this value is expected to be larger for soft spheres as they can overlap. Only M1 crystallised in a very narrow  $\phi$ -range, which indicates a larger polydispersity than the other samples. Homogeneous nucleation is the main requirement for a monodisperse sample and follows from the precipitation polymerisation model. Wu *et al.* observed experimentally that in the first minutes after initiation the particles were formed, which size subsequently slowly increased over time [86]. A linear increase in radius as function of (conversion)<sup>1/3</sup> was observed for PNIPAm and PNIPMAm, which indicates that no new nucleation sites were formed during the reaction [71, 86]. The observed sudden increase in turbidity indicates the onset of polymerisation and is in line with homogeneous nucleation followed by a slower growth of the colloids. Additionally, the size distribution decreased over time in both cases of reaction and diffusion limited growth, which applies to most colloidal systems [6]. For the application in this thesis, the polydispersity should be low enough that a monodisperse model accounts for all phenomena. It was assumed that this criterion was met, since the pure microgel particles crystallised, and it was noted that M1 was more polydisperse than the other samples.

### Factors governing colloidal stability and particle size

All M1-3 syntheses did not satisfy the minimum size as stated in Section 4.1.1, i.e.  $\gtrsim 1 \mu\text{m}$  above the VPTT. With the goal to find reaction conditions that maximize PNIPAm size, a small systematic study (M4.1-4.4) was performed in which some important parameters were varied to test them against a reference synthesis. The conditions for the reference synthesis M4.1 were the same as for M1-3 (Section 3.1.3). The following was changed from M4.1: the KPS was injected at once in synthesis M4.2, the temperature was lowered 10 °C in M4.3, and no fluorescent dye was added in M4.4. Additionally, M1, M2, and M3 were used to study effect of the monomer on the size.

In the following, factors affecting particle size will be discussed in view of the colloidal stability (Section 2.10.2). Following the precipitation polymerisation model, a difference in size is caused by higher amount of cores during the nucleation step. A reasoning that fits the model is that a higher colloidal stability leads to bigger, and therefore less nuclei during the homogeneous nucleation. As a binary mixture with equally sized particles with a diameter of  $>1 \mu\text{m}$  under reaction conditions is required, control over size, i.e. colloidal stability, is key. This was not achieved in such extent that particles with the required dimensions could be synthesised.

**PNIPAm vs. PNIPMAm** Syntheses M1 and M3 produced PNIPMAm particles with a hydrodynamic radius around 550 nm at 20 °C. Synthesis M2 resulted in much smaller PNIPAm particles, which had a hydrodynamic radius of 0.4  $\mu\text{m}$  (Table 4.2). Due to the addition of SDS in the PNIPMAm syntheses, the particles should have become smaller, and the size difference would be even larger in surfactant-free polymerisation conditions [73]. Thus, under nearly the same reaction conditions, PNIPAm and PNIPMAm particles were obtained with about a factor two size difference in favour of the bigger PNIPMAm particles.

The particle size difference between the syntheses with different monomer types indicated that PNIPMAm has a poorer colloidal stability during the nucleation stage than PNIPAm. The lower colloidal stability could be caused by a larger critical chain length for precipitation ( $j_{\text{crit}}$ ) for PNIPMAm than for PNIPAm [71]. With a larger  $j_{\text{crit}}$ , the particles need to grow bigger in order to accumulate enough charged initiator moieties to be charge stabilised. The value of  $j_{\text{crit}}$  is not known, but it can

Table 4.2: An overview of the size and the zeta potential  $\zeta$  at 20 °C for all pure microgels. The swelling ratio is denoted as  $\alpha(20, 50^\circ\text{C})$ , which was calculated following Eq. 2.39. The Hückel approximation (Eq. 2.34) was used to calculate  $\zeta$ .

#	Monomer	$R_H$ (nm)	$\alpha(20, 50^\circ\text{C})$	$\zeta$ (mV)	Comment
M1	NIPMAm	539	6.1	-23.2	
M2	NIPAm	200	8.9	-22.9	
M3	NIPMAm	562	8.8	-34.4	0.13 g/L SDS
M4.1	NIPAm	246			reference
M4.2	NIPAm	249			fast KPS injection
M4.3	NIPAm	216			70 °C
M4.4	NIPAm	270			no dye

be assumed to be in the order of several subunits according to Wu *et al.*, and Duracher *et al.* [71, 86]. It can be argued that a higher VPTT of PNIPMAm indicates that the polymer-water interactions are stronger than for PNIPAm, because the system is disrupted at higher energies. A longer  $j_{\text{crit}}$  is therefore expected for PNIPMAm, as the oligomers have a stronger preference to be solvated, which is in agreement with the experimental results. It could be explained that the different aggregation behaviour of the growing oligomer chains can account of the observed size difference, but it lacks experimental evidence, and more study on the earliest moments of the reaction and  $j_{\text{crit}}$  is required to fully explain the observations.

It had been observed that alkylamides propagate  $\sim 20$  times faster than alkylmethacrylamides, which is reflected in the  $\sim 4$  times shorter reaction time for PNIPAm microgel synthesis compared to PNIPMAm ones [74]. The NIPMAm molecule is more sterically hindered and therefore less prone to an attack from a radical, which might explain the higher precursor formation rate. Duracher has suggested that this would lead to a higher nuclei formation rate, and thus more nuclei, based on kinetic arguments [71]. Indeed, more nuclei would lead to smaller particles, which is in line with the high propagation rate of PNIPAm.

**Injection speed KPS** The hydrodynamic radius of M4.2 was the same as the radius of the reference synthesis M4.1, where respectively the KPS was injected as fast as possible and over a time span of ten minutes (Table 4.2). A slow injection would lead to a lower initiator concentration during the homogeneous nucleation, and thereby affecting the number of nuclei formed. Duracher observed that the hydrodynamic radius above the VPTT and radius observed with SEM was affected in the order of 50 nm in few mol% initiator range, which is large in the context of M4.1 and M4.2 (Table 4.2) [71]. As it was found that the injection method did not affect the hydrodynamic radius significantly in M4.2, the difference in initiator concentration was probably too small to affect size.

**Reaction temperature** Synthesis M4.3 was done to study the effect of a 10 °C lower temperature during the synthesis, which resulted in a  $\sim 30$  nm smaller hydrodynamic radius than of the reference synthesis M4.1 (Table 4.2). An increase in hydrodynamic radius at 20 °C upon decreasing reaction temperature has been reported in literature for both PNIPAm and PNIPMAm [71, 74, 116]. Duracher *et al.* found that the hydrodynamic radius above the VPTT and radius observed with SEM increased monotonically with decreasing reaction temperature, and a drastic increase in  $\alpha$  was observed upon decrease in temperature in a PNIPMAm synthesis, which resulted in a three times increase in hydrodynamic radius at 20 °C over a 10 °C reaction temperature drop [71]. The difference between the results here and in literature cannot be explained, and shows the complexity that arises from the large number of variables. Some explanations for the decreasing size with increasing temperature have been given in literature, but there is no consensus yet.

The propagation rate as function of the initiator concentration and temperature follows qualitatively the same trend, which dependence is an order of magnitude stronger for the temperature. Du-

rather ascribed the size trend to the increase in propagation rate as function of temperature, which would result in a higher precursor formation rate and more nuclei [71].

In the framework of colloidal stability and the precipitation polymerisation model, the increase in temperature would lead to an increase in decomposition rate of the initiator, which reduces the ionic strength as the ion becomes monovalent. A higher temperature would thus lead to a higher colloidal stability. This is in agreement with experimentally observed trend of increasing size as function of decreasing reaction temperature in literature.

Virtanen *et al.* suggested that the kinetic chain length  $\nu$ , which is the average number of monomers that react from a single radical until termination, affects the charge density of the polymer chain and therefore the colloidal stability. A higher  $\nu$  means that less initiator fragments are present per monomer, which would lead to a lower charge density and colloidal stability. The kinetic chain length decreases as function of increasing temperature, due to the exponential dependence of the activation energy for the degree of polymerisation  $E_{\bar{x}_n}$  in the form of  $\nu \sim \exp(-E_{\bar{x}_n}/RT)$ . Note that the  $E_{\bar{x}_n}$  is negative for thermally decomposing initiators [116]. Based on this model, an increase in colloidal stability and decrease in particle size would be expected, which is in line with the experimental results reported in literature. The dependence of the colloidal stability on the kinetic chain length during nucleation is disputable, since it assumes that the colloiddally stable seeds are formed after the chains are terminated. The explanation would hold if  $j_{\text{crit}}$  would be much higher than a couple of monomers, which is in contrast to small molecule studies referred to in [86].

**Dye** The effect of the fluorescent FOM dye on the hydrodynamic radius was studied in synthesis M4.4 (Table 4.2). A larger hydrodynamic radius was observed for M4.4 compared to the reference synthesis M4.1. It was speculated by J.M. Meijer and J.N. Immink that the charge of the dye affected the stabilisation of the precursor particles. However, it would be remarkable if such a low concentration of the dye would be able to account for the larger hydrodynamic radius of M4.4 compared to M4.1. A study with MRB would be interesting as this dye has a positive charge which could destabilise the precursor particles once polymerised, which might explain the large size of the PNIPMAM particles. The complete picture would probably be more complex and contain effects concerning electrostatics, surfactant-like absorption, and  $j_{\text{crit}}$ . More experiments are required to find which properties of the fluorescent dye affect the size, and how it alters colloidal stabilisation during the synthesis.

#### 4.2.2 Core-shell particles

Because the size of the pure PNIPAm microgel particles was not sufficient for particle tracking algorithms, CS particles were designed tailored to the requirements set in Section 4.1. The rationale behind this approach is explained in this section. In short, chosen was for a CS PS-microgel consisting of a small core, which is highly fluorescently labelled, and multiple undyed thermoresponsive microgel shells (Fig. 4.1).

The advantages of CS particles are the control over particle size and composition via the batch-wise shell growth, and in the possibility to use a dye in a hydrophobic environment. As a result of this, the following aspects could be improved over the pure microgel system:

- Good resolvability in CLSM imaging
- Stable fluorescence
- Tunable size and properties

A better resolvability could be achieved by growing multiple shells to obtain a larger particle size. Moreover, separation of the fluorescent signal could be achieved by only using a fluorescently dyed core. To minimize the strong light scattering of PS in water, aimed was for a small core with a radius of  $\sim 75$  nm. The more stable fluorescence would originate from the use of a different fluorophore. Dyes in a hydrophobic environment are usually more stable and a highly fluorescent PS core will be less prone to bleaching. A higher loading of the core will allow the measurements to be done with a lower laser intensity, which altogether leads to a lower bleaching rate, and more stable fluorescence. Control over the shell growth could be exploited to synthesise particles with a composition tailored to

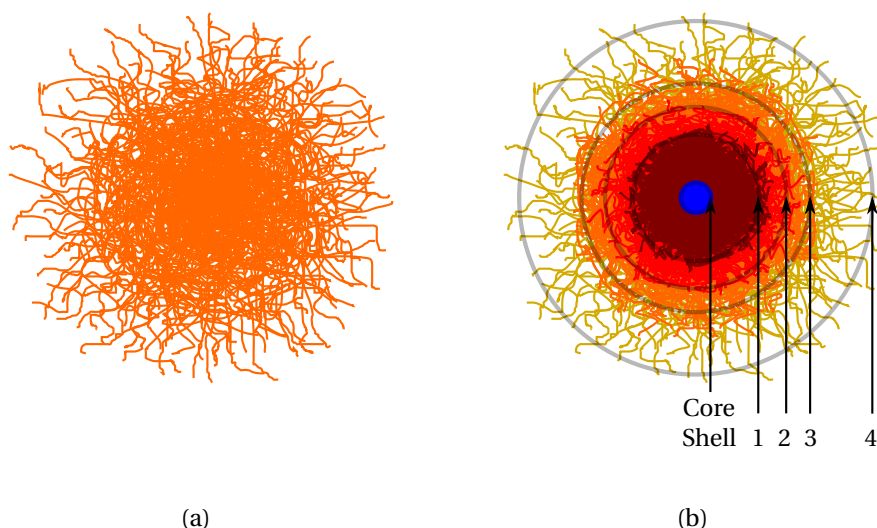


Figure 4.1: In contrast to pure microgel particles (a), CS particles (b) consist of multiple shells, which yields extensive control over size and properties. In order to put the work on CS microgels into the context of pure microgel particles, CS particles were designed to have a similar structure as pure microgel particles. To mimic the density profile of a pure microgel, the inner shells (1, 2 & 3) had a 7.5% crosslink density, in contrast to the outer shell (4), which had a 5% crosslink density, that is the same as for pure microgels. The small core was fluorescently labelled, and due to its small size, has the minimal effect on structural and scattering properties.

the experiment, i.e. designer particles. In this thesis, the CS particles were ‘designed’ such that they would mimic a pure microgel particle.

**Similar properties as pure microgel** In order to put the results into context of work done in the group, the CS particle were designed to have similar properties as pure microgel particles. The core-shell-like structure of pure microgels was mimicked by a homogeneous 7.5% crosslink density in the inner shells, and a 5% crosslink density in the outer one. A homogeneous crosslink density was attempted via a BIS feed, which was performed as described by Dulle *et al.* [78]. The final shell was synthesised without BIS feed to obtain a density profile similar to pure microgel particles (Fig. 4.1b). In principle, a microgel shell larger than the Debye length should be grown to make sure that the interparticle interactions driven by charged residues would originate only from the microgel shell. To illustrate this, Senff *et al.* found that CS particles with a small PS core and a  $\sim 45$  nm PNIPAM shell were colloiddally stable above the VPTT due to the high charge of the core [80]. However, the experiments were performed at  $10^{-1}$  M, which corresponding Debye length is  $\sim 1$  nm, and the shell thickness was of less importance here.

### 4.2.3 Polystyrene cores

Four PS syntheses were done from which syntheses C1 and C4 were NIPAm functionalised, and C2 and C3 were NIPMAm functionalised. The hydrodynamic radius and swelling ratio of the particles was determined with DLS measurements, and the zeta potential with electrophoretic mobility measurements, which results are shown in Table 4.3. KPS-initiated microgel-functionalised PS cores were synthesised in a single batch fashion, following the procedure of Appel *et al.* [4]. The reactions proceeded as expected, and based on its quick crystallisation, monodisperse samples were obtained [115]. Due to the hydrophobicity of the PM dyes, fluorescence was only observed in the styrene phase prior to synthesis, and was not visible in the waste water of the purification. This indicates a high preference of the dye to reside in the core material, which makes desorption of the dye unlikely over long periods.

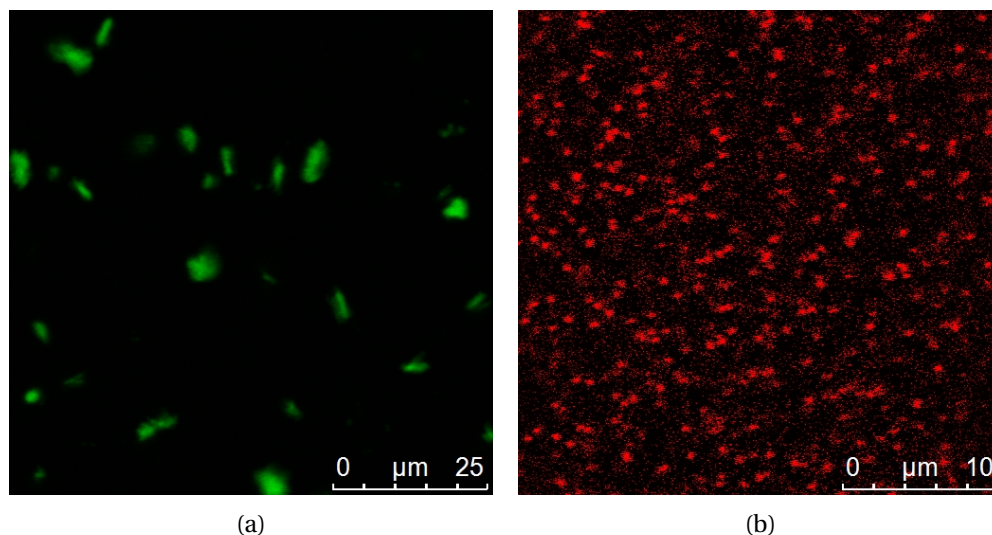


Figure 4.2: a): Confocal image of the micrometer-sized aggregates of microgel functionalised PS cores at the glass plate of the spacer cell after centrifugation (C1). b): Confocal image of monodisperse sample of microgel functionalised PS cores in the liquid phase after dialysis (C3).

### Purification

Purification by centrifugation was found to cause irreversible aggregation of PS cores, which was observed for C1-2, therefore the other samples were purified with dialysis. After centrifugation, a thick whitish plaque was observed at the bottom of the centrifugation vial. The aggregation was reflected in an increase from 97.3 to 190 nm in hydrodynamic radius after centrifugation. The clusters were completely irreversible and could not be separated with sonication, which was reflected in the slightly decreased hydrodynamic radius of 176 nm after sonication. A similar trend was observed with CLSM, and the cluster size was found to be in the order of micrometers (Fig. 4.2a). Once the polymers have overcome the charge stabilisation, they get stuck in a deep attractive potential well caused by the strong van der Waals attraction. Centrifugation is a common way to purify PS particles, but usually at a lower centrifugational force, which can take a lot of time with small particles [4, 78, 79, 82]. Therefore, C3-4 were purified by means of dialysis, which resulted in a clean sample without aggregates (Fig. 4.2b).

### Mechanism and functionalisation

Similar to the synthesis of the pure microgels, small variations in size were observed for syntheses performed under the same reaction conditions (Table 4.3). The cores were slightly bigger than obtained by Appel *et al.*, which might be caused by the  $-6^{\circ}\text{C}$  temperature deviation found in thermocontrol (Subsection 3.1.2) [4]. The PS cores were functionalised with one of the microgel monomers, which is a common procedure in literature [4, 81]. Since the obtained cores showed thermoresponsive behaviour, it was concluded that the functionalisation was successful (Table 4.3). A possible coincidence is that in the syntheses that have been performed in parallel (C1-2, C3-4), the NIPMAm functionalised cores have slightly larger hydrodynamic radius, which is in agreement with postulated higher colloidal stability of PNIPMAm over PNIPAm stated in Subsection 4.2.1.

### Thermoresponsivity

**Size** The temperature dependent collapse of the core particles was similar both NIPAm and NIPMAm functionalisation (Fig. 4.3a). For a V50 initiated analogue of C4, Duracher *et al.* found a swelling ratio of 1.51, which is practically identical to values found for C3-4 (Table 4.3) [117]. The swelling curve of C4 was in good agreement with Duracher *et al.* The collapse occurred over a broader tem-

Table 4.3: An overview of the size obtained with DLS at 20 °C and zeta potential for all PS cores. The samples which were rendered useless due to centrifugation are marked with an x in the column aggregation. The radius given for the samples with aggregation was obtained before centrifugation. The swelling ratio is denoted as  $\alpha(20,50^\circ\text{C})$ , which was calculated following Eq. 2.39. The zeta potential  $\zeta$  was approximated with Eq. 2.34 and a prefactor of 1.25, which is between the Hückel and Smoluchowski limits.

#	Functionalisation	Aggregation	$R_H$ (nm)	$\alpha(20,50^\circ\text{C})$	$\zeta$ (mV)
C1	NIPAm	x	91.8		
C2	NIPMAm	x	97.3		
C3	NIPMAm		78.3	1.52	-68.9
C4	NIPAm		61.8	1.52	-58.7

perature range than for pure microgels, which was probably a result of the co-polymerisation of a couple of mol% styrene. The different polymerisation rates of NIPAm and NIPMAm should not affect the composition of the shell in large extent. As a consequence of the reaction mechanism, the water soluble monomers will be consumed first irrespectively of the polymerisation rate. The collapse temperature does not appear to be shifted to higher temperatures for C3, which might be because of the co-polymerisation with styrene. It could not be validated whether the particle was completely collapsed, since the error in the DLS measurements at 60 °C was larger than the relevant length scale. Based on the swelling ratio, it is assumed that both C3 and C4 were completely collapsed at 50 °C.

The swelling ratio of the microgel shell was calculated to be in the range of 5.2 to 3.2 for respectively 0 to 50 volume% water in the shell. This is much less than the swelling ratio of  $\sim 40$  which was found for pure microgels without crosslinker [118]. The reduced swelling can be ascribed to the hydrophobic character of the co-polymerised styrene, which favours polymer-polymer interactions.

**Electrophoretic mobility** The cores were negatively charged and had a significantly higher zeta potential than the pure microgels, which corresponded to the high (charge) density of the particles (Tables 4.2 and 4.3). The electrophoretic mobility was in the same order of magnitude as the values found by Duracher *et al.* [117]. The zeta potential could be estimated with Eq. 2.34, however as  $(R'/\kappa^{-1}) = \mathcal{O}(1)$  neither the Hückel nor the Smoluchowski approximation applies. The zeta potential was estimated with a prefactor of  $a = 1.25$ , which lies directly between the Hückel and the Smoluchowski limits, respectively  $a = 1$  and 1.5. Qualitatively, the same temperature dependence as for the pure microgels was found for C3, that is the mobility increased as the microgel shell collapses (Fig. 4.3b). The decrease in mobility of C4 could not be explained with the information available.

#### 4.2.4 Microgel shell

Twenty-two (multi-)shell syntheses were done with cores from syntheses C2-4. Syntheses CS1-2, and CS6-7 had granular aggregation and were not analysed. The hydrodynamic radius of the particles was determined with DLS measurements, except CS4 which was not analysed. A wide range of reactant parameters was tried with fixed temperature and initiator concentration. With a fixed mol% of BIS and KPS, the core concentration and the ratio between the concentration of cores and monomers  $C_{\text{core}}/C_{\text{monomer}}$  fixes all reactant parameters. The initial guess was derived from protocols taken from J.M. Meijer and L.K. Månsson, and refs. [4, 78, 79]. Since the procedure given by Appel *et al.* was very detailed regarding core and shell sizes, and started with PS cores identical to the ones used in this work, the temperature and  $C_{\text{core}}$  was taken from this work [4]. Moreover, these conditions were nearly identical to the ones used by Rauh *et al.*, and was used in syntheses CS1-5 (Table C.3) [79]. Dulle *et al.* was followed for the syntheses using a BIS feed, that is CS1, CS12-15, and CS17-22, and the BIS feed was introduced in a later stage of the synthesis work to reduce the number of free variables [78]. It must be noted that the  $C_{\text{core}}$  was  $\sim 100x$  higher than in the work of Appel and Rauh, however this should not affect the result since the polymerisation rate was found to be independent of the particle number concentration [86]. The KS17 protocol developed in this group by J.M. Meijer

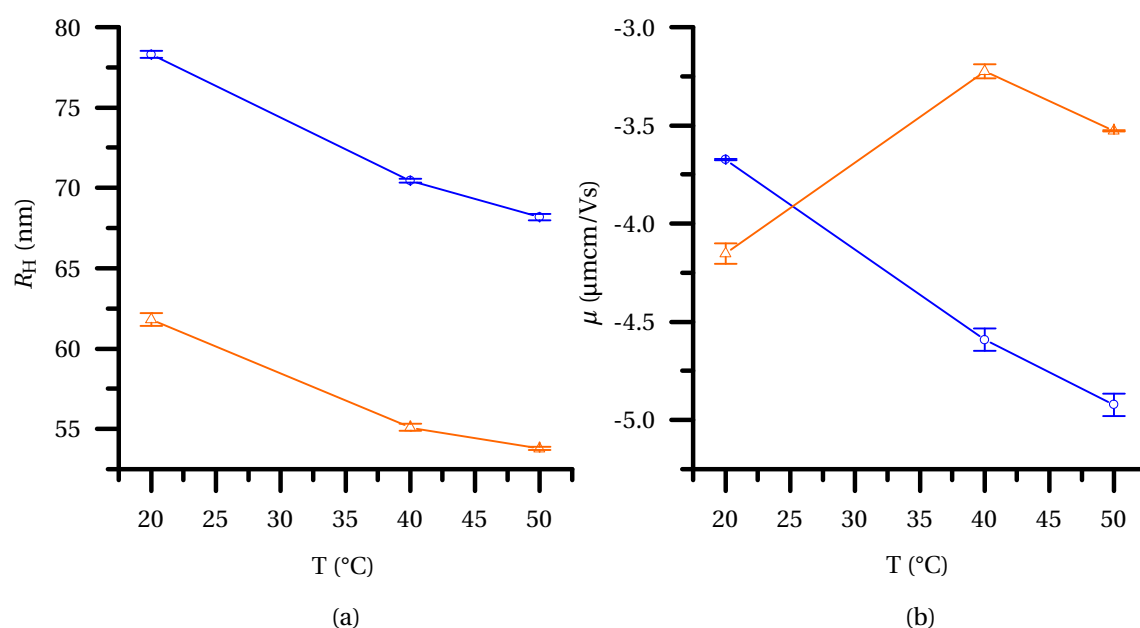


Figure 4.3: Plot of the hydrodynamic radius  $R_H$  (a) and mobility  $\mu$  (b) with error bars depicting the standard error of the mean for C3 (orange  $\Delta$ ) and C4 (blue  $\circ$ ). Interestingly, the trend in size is not reflected in  $\mu$  of C4.

and L.K. Månsson was used to derive the reactant parameters for syntheses CS6-11. The growth of multiple shells was tried in CS12-17, in some cases with increasing reactant concentration per shell. Three large scale production runs were done (CS18-20), however only CS19 met the size requirements for CS CLSM resolvability. CS21-22 were synthesised to be used as benchmarking and further analysis.

The growth of the microgel shell was not straightforward, since there was a trade-off between the thickest possible shell, and the formation of colloidal stable microgels without core, i.e. secondary nucleation. Moreover, the trade-off between the highest total concentration possible, i.e. more product, and aggregation complicated synthesis even further. The goal was to find reaction conditions where the thickest shell at the highest concentration could be synthesised, without having the disadvantageous counterpart.

First, the shell radii will be discussed followed by the two trade-offs mentioned above, i.e. aggregation and secondary nucleation, which define the optimal reactant parameters. In here, centrifugation will be discussed in the context of secondary nucleation and structure. Finally, the batch types and the scaling of reactants after each batch will be discussed.

### Shell radii

The hydrodynamic shell thicknesses or radii of the CS samples prior to centrifugation are shown in Table 4.4. These values were obtained without purification, and deviate from deionised conditions. A few percent increase in  $R_H$  was observed after a dialysis for sample CS11, which was within the experimental error of the DLS. Since samples had to be diluted  $\sim 100$  times for DLS analysis, the salt concentration was already far below reaction conditions in the measured samples. From the pure microgel synthesis, it was found that NIPAm and NIPMAm react differently, and have their own range of parameters. Interestingly, samples in which the first shell was  $>170$  nm, the used monomer is equally divided along NIPAm and NIPMAm. This showed that sufficient shell growth is achievable with both monomers. A decrease in shell radius as function of shell number is a result of the conservation of volume, which means that with the same volume material a thinner shell is grown on a larger particle. However, in some cases the decrease in shell radius could be ascribed to the forma-

Table 4.4: An overview of the thickness of the microgel shell ( $R_H - R_H^{\text{core}}$ ) obtained with DLS at 20 °C. The standard error of the mean of the particles was in the order of 2 nm. The samples were measured without any purification step. The hydrodynamic radius of the core  $R_H^{\text{core}}$  is given for convenience. Please note that the hydrodynamic radii after centrifugation can differ significantly, which will be discussed below. In some cases, the apparent shell thickness decreases because of a contribution from smaller secondary nucleates. The samples in which more than 10% of the particles did not contain a core are marked with ‡, this was determined with CLSM. CS14 was synthesised with NIPMAm in the first shell and NIPAm in the others.

#	Monomer	$R_H^{\text{core}}$ (nm)	$R_H - R_H^{\text{core}}$ (nm)						
			Shell 1	Shell 2	Shell 3	Shell 4	Shell 5	Shell 6	
CS3	NIPMAm	97.3	31.6	128	145				
CS5	NIPAm	97.3	61.7						
CS8	NIPAm	97.3	148 ‡						
CS9	NIPAm	97.3	179						
CS10	NIPMAm	97.3	29.7						
CS11	NIPMAm	78.3	185						
CS12	NIPAm	78.3	172	230	264				
CS13	NIPAm	78.3		231 ‡	239 ‡				
CS14	both	78.3	118	226	255				
CS15	NIPAm	78.3	151	248	242 ‡				
CS16	NIPAm	78.3			214 ‡				
CS17	NIPAm	78.3	150	216 ‡	251 ‡				
CS18	NIPAm	61.8	112 ‡	151 ‡		197 ‡			
CS19	NIPMAm	78.3	183	269	334	364	278	308	
CS20	NIPAm	61.8	160 ‡						
CS21	NIPAm	78.3	171 ‡	227					
CS22	NIPMAm	61.8	178 ‡	247					

tion of smaller secondary nucleates, which will be discussed below. It must be noted that with the same volume, the shell thickness is dependent on the size of seed, and therefore shell volume will be used for comparison later on.

Small variations in the measured hydrodynamic radius were observed after centrifugation, due to a lower electrolyte concentration, removal of secondary nucleates and possibly intra-particle chain entanglement. Only for CS19, a large change in size was observed before and after centrifugation.

**Centrifugation CS19** Centrifugation was found to affect the hydrodynamic radius greatly for CS19, and the radii of shell 5 and 6 deviated strongly from the previous ones (Table 4.4). The hydrodynamic radius of shell 6 increased from 308 to 432 nm after three centrifugation rounds, and to 440 nm after five rounds, which is a decrease in shell volume with respect to shell 4 (Fig. 4.8). No secondary nucleates were observed with CLSM, and since the difference in hydrodynamic radius is very large, secondary nucleates should be observable with CLSM. Thus, a decrease in radius suggests a structural change, but the form factor was identical before and after centrifugation (Fig. 4.4). The minimum could be fitted with a hard sphere model (Eq. 2.12), and corresponds to a radius of  $\sim 330$  nm, which is about 110 nm smaller than the hydrodynamic radius. Firstly, the high scattering contribution of the small PS core makes the particle appear smaller. Secondly, because of the low density of the outer shell, the outer region barely contributes to the form factor. In accordance, Dulle *et al.* found that outer 10-20 nm of their Au-PNIPAm CS particle with a hydrodynamic radius of 77 nm was invisible in light scattering experiments [78]. In CS19, the biggest contribution in SLS comes from the PS core and the inner shells, while the outer shell, which has a large effect on the hydrodynamic radius, is almost invisible in the form factor. Therefore, both a large structural change, and secondary nucleation seems unlikely, and a structural rearrangement in the outer layer and/or dangling ends seems to be the most likely explanation.



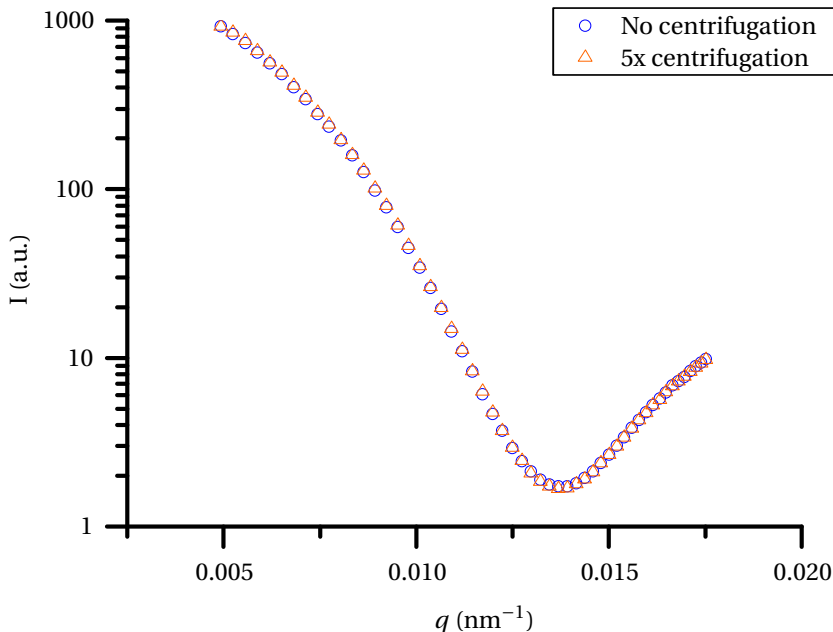


Figure 4.4: SLS form factor of CS19 before and after centrifugation. The minimum corresponds to a hard sphere radius of  $\sim 330$  nm (Eq. 2.12), which is about 110 nm smaller than the hydrodynamic radius. The form factor could not be fitted, since to best of the authors knowledge, the scattering length densities of PNIPAm with respect to PS have not been reported in literature yet.

### Aggregation

Microscopic and macroscopic aggregation has not been a major issue during the shell growth. Some macroscopic flocculation was observed for most syntheses, which is common for pure microgel syntheses as well. In general, less aggregates were observed for the shell syntheses over the pure microgel syntheses. These macroscopic aggregates could be removed via filtration over glass wool. During syntheses CS1-2 and CS6-7, aggregation was prevalent to such extent that all cores were located in macroscopic aggregates. Microscopic aggregates, such as dumbbells and/or small clusters were observed in some samples, however this was usually in  $< 1\%$  of the observed particles, a value which is similar to pure microgel syntheses. Only in sample CS22, microscopic aggregates with a size in the order of micrometers were observed.

A hypothesis is that the total monomer concentration  $C_{\text{monomer}}$  is a determining factor in both microscopic and macroscopic aggregation. Syntheses CS1-2 and CS6-7 were done at a high monomer concentration, that is 0.18-0.19 M and 0.12 M, respectively. It must be noted that the high crosslink density (25%) hampers comparison with samples CS6-7. Syntheses with a similar  $C_{\text{monomer}}/C_{\text{core}}$  as CS6-7 but lower total monomer concentration, i.e. CS8-10 with  $C_{\text{monomer}} = 0.012 - 0.060$  M, did not show any macroscopic aggregation at all. Therefore all other syntheses, including the continuous batch ones, were performed within the range of  $C_{\text{monomer}} \approx 0.010 - 0.060$  M, which is in the same range as in Rauh *et al.* (0.02 M) [79], however much lower than in Appel *et al.* (0.20 M) [4].

Millimeter sized yellow NIPMAm aggregates in Milli-Q water were observed at elevated temperatures. To dissolve the NIPMAm, it was heated to 60 °C under stirring, however flocculation was observed before the monomer was completely dissolved. After vigorous stirring at room temperature for 30-45 minutes, a clear solution was observed, which remained clear after heating to 60 °C. After cooling and reheating, small flocculates were observed, which did not redissolve. Quick phase separation of dissolved NIPMAm at reaction temperature during pure microgel syntheses was reported by L.K. Månsson in the group. Since the reaction mixture of a CS synthesis was turbid due to the presence of cores, this could not be observed at the first step of the continuous-batch and during the batch-batch method. It is therefore not unlikely that the microscopic aggregates in CS22 were caused by

undissolved NIPMAm, which served as (non-charge stabilised) nucleation point for both oligomers and cores.

### Secondary nucleation

Secondary nucleation is a major challenge to overcome, and could not be quantified unambiguously yet, however a rough estimate could be made by means of CLSM. Based on this data set,  $N_{\text{monomer}}/N_{\text{core}}$  is not sufficient on its own to predict the formation of secondary nucleation. The concentration monomer and BIS did not seem to affect the formation secondary nucleates, in contrast to  $N_{\text{monomer}}/N_{\text{core}}$  and  $N_{\text{monomer}}/S_{\text{core,total}}$ , which appeared to be positively correlated to their formation. Low monomer concentration and ratio combined consistently yielded samples without secondary nucleation detectable with CLSM. Poor reproducibility was found for multiple shell growth, which hampered the interpretation in some cases. Moreover, small secondary nucleates could not be observed with CLSM, which makes it impossible to draw definite conclusions, and a proper quantification of secondary nucleates should be achieved first before a systematic study could be performed.

**Detection of secondary nucleation** Observation and quantification of secondary nucleation is hard with the techniques available. Indeed, a decrease in apparent shell radius was observed with DLS (Table 4.4), however a quantification of the amount of secondary nucleates is tricky. A multi-exponential was fitted with the CONTIN method (Eq. 2.19) to split the autocorrelation function in a contribution of the CS particles and the secondary nucleates, which have a smaller size. However, dependent on the settings of the fit, either a very large, or no contribution at all was observed, which means that the parameters are very sensitive and the results are unreliable. Moreover, the fraction of secondary nucleates must be large in order to be detected over the strongly scattering PS cores. It was estimated in Section 2.3 that the core scatters  $\sim 670$  times more than the pure microgel particles below the VPTT. Additionally, as the intensity scattered by a particle scales with its volume squared, that is  $R^6$ , small secondary nucleates are hardly detected [54]. Hence, the secondary nucleates must be either very abundant or very large to be observed, which results in an insufficient resolution for the quantification of these particles with DLS.

It was found that the most reliable method to detect secondary nucleates was CLSM. Like any other microgel, secondary nucleates adsorb to the glass plate, and could be observed in bright field mode, but not in fluorescence mode. They were characterised by their different size, that is usually smaller than the CS particles, and the absence of a fluorescent signal (Fig. 4.5). The resolution of the confocal microscope limited the smallest secondary nucleates that could be observed. In order to reduce the resolvability because of particle overlap, the sample had to be diluted, which in turn reduced the amount of particles that could be observed in the focal plane. At least more than 15 minutes was spent on each sample to acquire enough data for a substantiated conclusion. Despite its disadvantages, this technique was used in this thesis to obtain a ballpark figure for the amount of secondary nucleation. In short, the difficulty of gaining sufficient statistics and the low resolution makes a structural analysis of secondary nucleation impossible at this point and other techniques should be investigated.

Two techniques have a high potential to quantify the secondary nucleates in a sample. Firstly, the CS structure could be visualised with bright field transmission electron microscopy (TEM) in the work of Dulle *et al.* and Rauh *et al.*, due to the nanometer resolution and material sensitivity [78, 79]. However, these cores consisted of gold, which has a high contrast in TEM, and a lower contrast is obtained for organic compounds. It is expected that the PS cores used in this thesis can be resolved because of their higher density than the shell. Secondly, field-flow fractionation (FFF) is technique which separates nanoparticles based on the flow gradient in a column. The particles experience a field (e.g. gravity or solvent outflow) which causes them to move to one side of the column. Dependent on the size, the particles diffuse back to the middle of column where the flow is higher, and the particles get ejected more quickly. Yohannes *et al.* showed that the values obtained with FFF for small

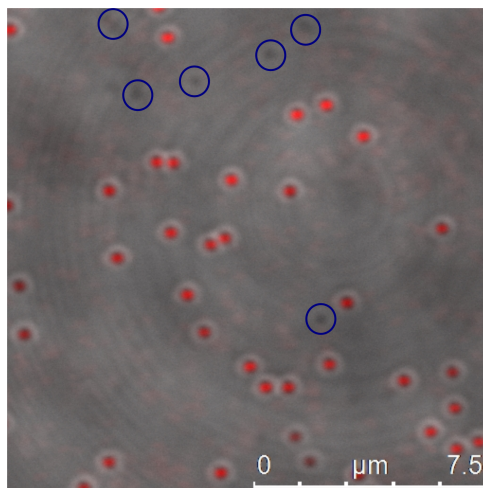


Figure 4.5: Overlay of a fluorescence and bright field confocal image of CS21. Secondary nucleates are marked with blue circles.

PNIPAm particles ( $\sim 40$  nm) were in agreement with DLS measurements [119]. Moreover, FFF performed better than size exclusion chromatography, and should be able to resolve larger particles. The loss of material is  $> 99\%$  and this technique is therefore not applicable as purification method.

**NIPAm vs. NIPMAM** Two semi-batch production runs were done with very similar parameters, that is CS18 and CS19, except for the type of monomer used. No secondary nucleation was found in the NIPMAM synthesis, while about 20% secondary nucleation was observed after the fourth shell of the NIPAm synthesis. Even though the largest shell volumes were equally divided among PNIPAm and PNIPMAM shells, NIPAm seemed to be more prone to form secondary nucleates than NIPMAM in experiment. The latter can be rationalised following a simple model based on colloidal stability (see also Subsection 4.2.1). Secondary nucleation is related to aggregation kinetics and colloidal stability of pure microgels, which can be modelled in a simple way. It can be argued that the reaction kinetics are reaction limited<sup>1</sup>, however, the coagulation of formed oligomers into a colloidal stable seed is expected to be instantaneous and thus diffusion limited. The formation of a stable seed particle can be seen as the precipitation of an oligomer on a small surface, i.e. precursor particle, which is in competition with the precipitation on a core particle. Here, aggregation of slowly diffusing precursor particles is neglected. As the stability of a precursor particle is assumed to be independent of the reactant concentration, the surface per core particle determines the probability of an oligomer to aggregate with either a core or precursor particle at a fixed ratio of the number of monomers over the cores  $N_{\text{monomer}}/N_{\text{core}}$ . A higher colloidal stability means that coagulation more quickly leads to a stable seed, which promotes secondary nucleation. Following this model, a higher colloidal stability and lower core surface per monomer promote secondary nucleation. Indeed, it was argued that NIPAm has a higher colloidal stability than NIPMAM, which suggests that the observed difference in secondary nucleation between PNIPAm and PNIPMAM CS particles is related to colloidal stability.

In line with the model, the normalisation of the number of monomers and BIS  $N_{\text{monomer+BIS}}$  by the total surface area of the cores  $S_{\text{core,total}}$  instead of the number of cores  $N_{\text{core}}$  appeared to give a slightly better separation of samples with and without secondary nucleation (Figs. 4.6 and 4.7).

**Concentration and ratio monomer** The concentration monomer  $C_{\text{monomer+BIS}}$  as a function of the parameters  $N_{\text{monomer+BIS}}/N_{\text{core}}$  or  $N_{\text{monomer+BIS}}/S_{\text{core,total}}$  of samples with the same amount of cross-

<sup>1</sup>Firstly, NIPAm and NIPMAM do have a different polymerisation rate, which is reflected in their reaction time. In the case of diffusion limited kinetics, this would not affect the reaction time. Secondly, the reaction time is in the order of 30-120 minutes, while the time for a monomer to diffuse over an interparticle distance is in the order of seconds, which excludes diffusion limited kinetics [74].

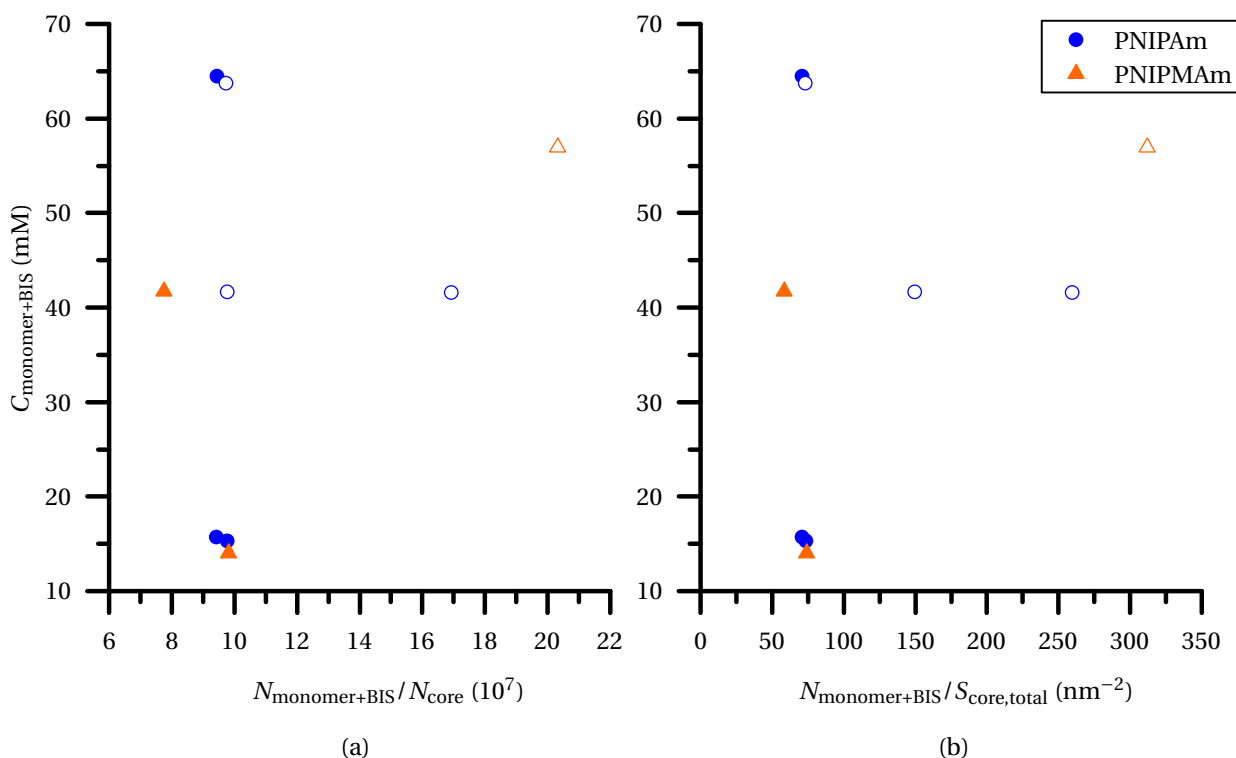


Figure 4.6: Plot of the number of monomers and BIS normalised by the number of cores  $N_{\text{monomer+BIS}}/N_{\text{core}}$  (a), and total surface area of the cores  $N_{\text{monomer+BIS}}/S_{\text{core,total}}$  (b) versus the concentration monomers and BIS  $C_{\text{monomer+BIS}}$ . The open symbols represent samples with more than 10% secondary nucleation, which was determined with CLSM. Only the first shell was taken of samples with 7.5 mol% crosslinker, and a 0.017 KPS to monomer ratio. The hydrodynamic radius of the core was taken at 50 °C for the calculations of  $N_{\text{core}}$  and  $S_{\text{core,total}}$ .

linker and initiator is plotted in Fig. 4.6. Only the first shell was taken since it could not be determined whether secondary nucleation was already present in earlier shells. The concentration monomer and BIS did not seem to affect the formation of secondary nucleates, however, the monomer per core particle  $N_{\text{monomer+BIS}}/N_{\text{core}}$  or surface  $N_{\text{monomer+BIS}}/S_{\text{core,total}}$  appeared to do so. A high ratio of monomer versus core correlates with secondary nucleation in this data set. However, at a fixed ratio of  $N_{\text{monomer+BIS}}/N_{\text{core}} = 10^8$  and  $N_{\text{monomer+BIS}}/S_{\text{core,total}} = 70 \text{ nm}^{-2}$ , both sample with and without secondary nucleation were obtained irrespective of the concentration. The concentration of monomer and BIS appeared to be less correlated with secondary nucleation, as for most concentrations shown, both samples with and without secondary nucleation were obtained. Possibly this corresponds to a threshold value for secondary nucleation, but more likely, other parameters do affect secondary nucleation as well. Only low concentration and monomer ratio combined seemed to suppress secondary nucleation, but more data points should be obtained to check the significance of this observation. It implies that reaction conditions for shell growth without secondary nucleation is limits the shell thickness and number of particles per batch.

Remarkably, with similar  $N_{\text{monomer+BIS}}/N_{\text{core}}$ , no secondary nucleation was reported in Appel *et al.* [4]. Samples from syntheses following the same protocol as described in Appel *et al.* were obtained from the Sprakel group at Wageningen University, and analysed with the CLSM method by the author. Secondary nucleation was observed in these samples as well, and they were very abundant, but had a similar size as the secondary nucleates in CS21. This suggests that they could be removed via repeated centrifugation, which was done for the published experiments. For a multi-shell approach, these conditions could only be used in a batch synthesis with purification between the shell syntheses.

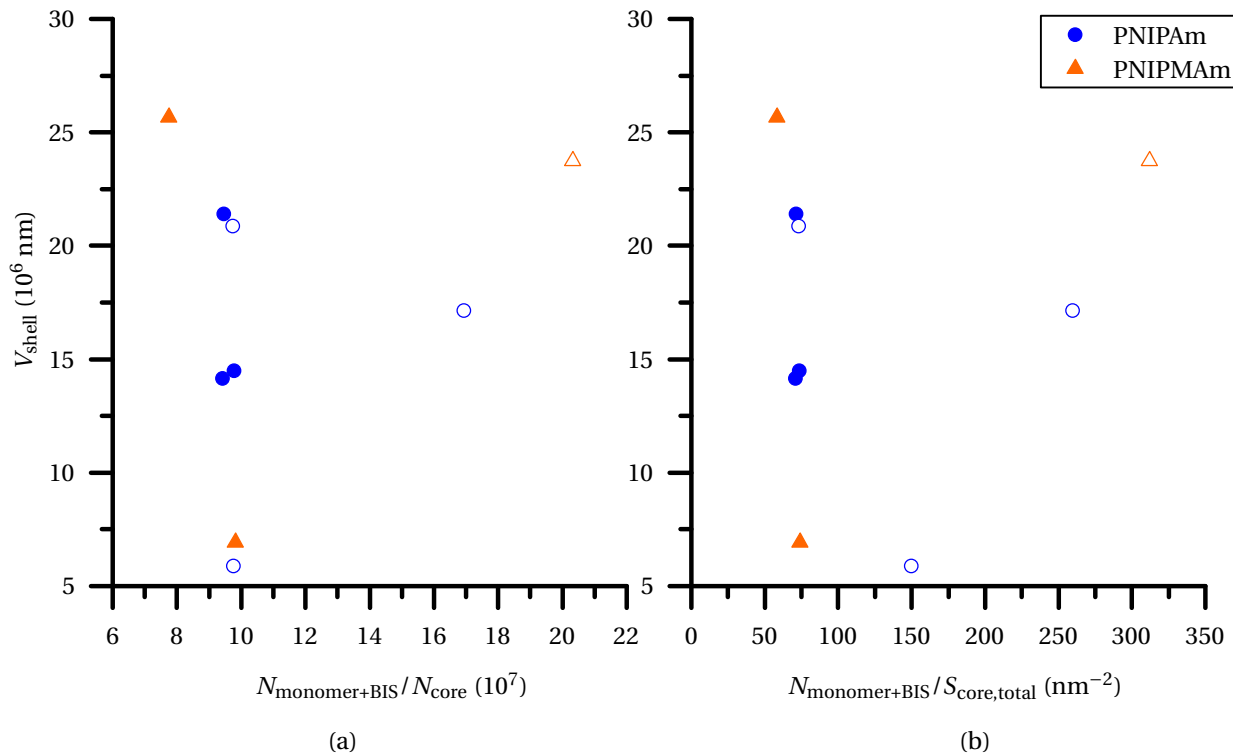


Figure 4.7: Plot of the number of monomers (including BIS) normalised by the number of cores  $N_{monomer+BIS}/N_{core}$  (a), and total surface area of the cores  $N_{monomer+BIS}/S_{core,total}$  (b) versus the shell volume  $V_{shell}$  of a particle calculated from  $R_H$ . The open symbols represent samples with more than 10% secondary nucleation, which was determined with CLSM. Only the first shell was taken of samples with 7.5 mol% crosslinker, and a 0.017 KPS to monomer ratio. The hydrodynamic radius of the core was taken at 50 °C for the calculations of  $N_{core}$  and  $S_{core,total}$ .

**Shell volume and ratio monomer** The shell volume  $V_{shell}$  as function of  $N_{monomer+BIS}/N_{core}$  of the same data set as in Fig. 4.6 was plotted in Fig. 4.7. Since for a same amount material added a similar shell volume is expected for a homogeneous crosslink density [78], lost material could be ascribed to secondary nucleation. From Fig. 4.7b it is clear that varying shell volumes were obtained irrespective of  $N_{monomer+BIS}/S_{core,total}$  for both PNIPAm and PNIPMAm shells. At a fixed  $N_{monomer+BIS}/S_{core,total}$ , shell volumes over a range of a factor five were obtained for both monomer types. A larger  $N_{monomer+BIS}/S_{core,total}$  and  $N_{monomer+BIS}/N_{core}$  was found to have more secondary nucleation, which consequently should lead to a smaller shell volume, however no correlation was found between these quantities. The observations suggest that material has been consumed by secondary nucleates, which could not be detected by CLSM at the time (Table 4.4). Moreover, the large spread in shell volume strongly suggests that the monomer to core ratio on its own is not sufficient to predict the formation of secondary nucleation.

**Upscaling reactants** In order to investigate whether the secondary nucleation scales with the total surface of the seeds, which could either be PS cores or CS particles from a previous (semi-)batch round, syntheses with increasing monomer concentration were performed and the results are shown in Table 4.5. The scaling of reactants in a semi-batch synthesis with number density seemed to work in some cases, that is CS14 and CS19 (CS19 not shown). However, upscaling of monomer concentration in every step was found to lead to a vast increase in secondary nucleates. Even when the scaling of the reactants was well below the surface increase in each previous step, secondary nucleation was observed. Even though the scaling of the reactants with the core surface in the synthesis of the first shell appeared to give a better separation of samples with and without secondary nucleation, such scaling did not hold in later shells. Two explanations seem plausible. Due to aggregation, the effec-

Table 4.5: The shell volumes and secondary nucleation as function of different monomer and BIS concentrations. The surface of the seed particle  $S_{particle}$  under reaction conditions (collapsed state) was estimated with a swelling ratio of 6.67 for the microgel shell [118]. The CS14 is given as reference, however, the first shell was synthesised with NIPMAm. Increasing  $C_{monomer+BIS}$  led to secondary nucleation in almost all cases. The given values for secondary nucleation were obtained via manual inspection of the sample with CLSM.

#	$V_{shell}$ ( $10^6$ nm <sup>3</sup> )			$S_{particle}$	$C_{monomer+BIS}$	Secondary nucleation
	Shell 1	Shell 2	Shell 3			
CS14	6.9	48.4	69.6	1:2.7:5.9	1:1:1	< 1% : < 1% : < 1%
CS15	14.5	64.6	59.9	1:3.5:6.7	1:2:4	< 1% : < 1% : > 50%
CS16	CS15	CS15	41.1	1:3.5:6.7	1:2:2	CS15 : CS15 : > 50%
CS17	14.1	42.3	65.9	1:3.5:5.5	1:1.75:2	< 1% : 20% : 30%

tive amount of cores present in solution decreases over time, which increases the effective scaling. Moreover, a difficulty in interpretation is that it could not be determined at which step the secondary nucleates were formed, since the secondary nucleates might be too small to be observed with CLSM in the first steps. With more material added per step, these undetectable secondary nucleates would grow harder and thus exceed the resolution limit faster, as might have happened in syntheses CS16 and CS17. As in some cases secondary nucleation was observed only in the third or fourth shell, this scenario is not very likely.

The reproducibility of the synthesis is a major problem, which was very obvious for samples CS15 and CS17 (Table 4.5). Even though a lower  $C_{monomer}$  during the growth of the second shell was used for CS17 than for CS15, more secondary nucleation was observed here. Since aggregation is probably not constant per shell and in every synthesis, the reproducibility is very poor. Therefore, detailed conclusions regarding the scaling of reactants following the number density or particle surface cannot be done with this data set, and more systematic and controlled studies are required.

**Removal secondary nucleates with centrifugation** Depending on the size of the secondary nucleates observed with CLSM, the particles could be selectively removed by means of centrifugation. The small secondary nucleates in CS21 bordered the resolution limit (Fig. 4.5) and were removed in a double centrifugation step. However, larger secondary nucleates, i.e. same order of magnitude of the CS particles, in CS18 could not be removed by means of centrifugation, and even when more than half of the volume was sacrificed, >10% secondary nucleates were observed with CLSM. The largest secondary nucleates were the hardest to remove due to the smaller buoyant mass difference with the CS particles. Hence, the removal of the complete size distribution of secondary nucleates could be monitored by following just the biggest ones in CLSM. From these observations it is clear that only the presence of a PS core was not sufficient to separate the particles. The PS core does not yield a large buoyant mass difference with the secondary nucleates, as its density is very close to water, and its volume rather small. The separation with centrifugation is mainly driven by the difference in volume, which means that the secondary nucleates should be removed as quickly as possible, e.g. after each step in a batch synthesis.

### Batch types

Semi-batch and batch syntheses were tried and different results for the syntheses were obtained. The yield, control over secondary nucleation and required time for the synthesis differed greatly between the different methods. For the semi-batch method, a constant shell growth was observed for CS19 after the first shell, which suggests that effectively all reactants were incorporated into the shells (Fig. 4.8). A disadvantage of this method is that secondary nucleation cannot be removed in an early stage with centrifugation. The volume difference between the secondary nucleates and the CS particles reduces after every shell growth, i.e. size sharpening, which is a characteristic of both reaction and diffusion limited growth, and hampers purification by centrifugation [6]. For the batch method with-

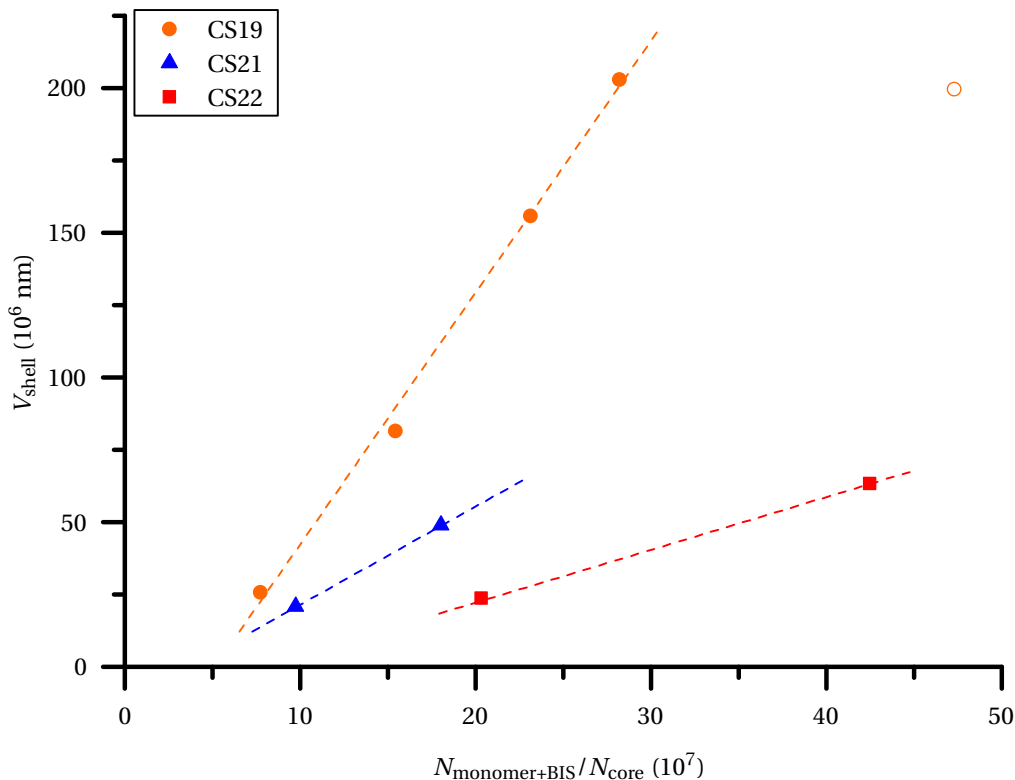


Figure 4.8: Plot of the number of monomers and BIS normalised by the total number of cores  $N_{\text{monomer+BIS}}/N_{\text{core}}$  versus the shell volume  $V_{\text{shell}}$  of a particle calculated from  $R_H$  before centrifugation. The dashed lines are a guide to the eye, which indicate the increase in shell volume per added monomer. The open symbol in CS19 represents shell 6, with the shell volume calculated from  $R_H$  after centrifugation. This value deviates from the trend of the first four shells of CS19.

out purification between the shells, premature initiation was observed, i.e. in synthesis CS12. Since the half-life of the KPS initiator at reaction conditions is in the order of hours, not all KPS was decomposed when the reactants for the next shell were dissolved in the reaction mixture, which resulted in premature initiation by the undecomposed KPS [120]. Hence, the batch method with purification by centrifugation was found to be the best method to control the reaction conditions in each step, and removing secondary nucleation in an early stage. Due to the formation of secondary nucleation, less shell volume was added per amount of monomer, which is reflected in the lower slope of CS21-22 compared to CS19 (Fig. 4.8).

The best method depends on the demands for the synthesis. In the trade-off between time and yield versus control over secondary nucleation, the semi-batch method favours the first, while the batch method favours the second. Since the reactants have to be injected in a dissolved form in the semi-batch method, a maximum of four shells could be grown in one run within the range  $C_{\text{monomer}} \approx 0.010 - 0.060 \text{ M}$ . The batch method is very time consuming, because of the additional centrifugation steps, and takes approximately four times more time than the semi-batch method. During the centrifugation steps, material is lost and the yield can be very low. In short, the semi-batch method yielded good results for CS19, but even little formation of secondary nucleation can render the synthesis useless. The batch method is more time consuming, but allows synthesis in reaction conditions where a little amount of secondary nucleates are formed.

### Yield determined with spectroscopy and weight percentage

The batch method with purification by centrifugation was found to be the best method to control the reaction conditions in each step, and removing secondary nucleation in an early stage. In order to control the size of the microgel shell, which is crucial for synthesis of a binary system with a specific size ratio, the reactants were scaled with the core concentration. For this, the yield had to be determined after each step, which could be done via the fluorescent signal of the cores, or the weight yield. UV-Vis spectroscopy was found not to be a suitable technique to quantify the fluorescence, because of the dominant scattering contribution. Fluorescence and weight yield were successful in estimating the yield, however, fluorescence spectroscopy was preferred since it required less sample and time. Good control over size was achieved, as is displayed for CS21/CS22 binary system (Fig. 4.11).

**Scaling reactants sequential batch by means of weight yield** The reactants can be scaled by the weight yield  $wY$ , which is defined here as

$$wY = \frac{(\text{wt}\%)V_{\text{tot}}}{m_{\text{monomer}} + m_{\text{BIS}} + m_{\text{cores}}} \cdot 100\%, \quad (4.1)$$

with  $m$  denoting the mass of the reactants, and  $V_{\text{tot}}$  being the total volume of a sample with weight percentage  $\text{wt}\%$ . It is assumed that the loss of weight is proportional to the number of cores. If aggregation occurs in early stage of reaction, cores are removed from the reaction mixture and the assumption does not hold any more. This method was used between shell 4 and 5 in sample CS19, which did not result in secondary nucleation. Anyhow, the scaling would not have been significant in the respect of the surface, and this does not validate the scaling unambiguously. As the method is slow, cost a significant amount of material, i.e.  $\sim 0.5$  mL concentrated solution, and requires hard to validate assumptions which differ per synthesis, spectroscopy methods based on fluorescence of the particles were investigated.

**Scaling reactants sequential batch by means of UV-Vis spectroscopy** The fluorescence contributes to the extinction around the wavelength where fluorophore absorbs and emits, which can be measured in a UV-Vis spectrum. Since fluorescence scales linearly with concentration for a monodisperse and homogeneously dye sample, a concentration series could be interpolated linearly. It was observed that the scattering dominates over the extinction, and only a clear peak corresponding to  $\lambda_{\text{em}}$  was present for concentration  $7.6 \cdot 10^{-10}$  M, which is insufficient for a concentration series (Fig. 4.9). In the Rayleigh limit, scattering could be fitted and subtracted from the absorption  $A$  by rewriting Eq. 2.28 to

$$A = \log_{10} \frac{I_0}{I_0 - I_{\text{scatter}}} + A_0 \quad (4.2)$$

and combining with Eq. 2.6, and collecting all variables into a fitting parameter  $c$ , yielding

$$A = \log_{10} \frac{1}{1 - c\lambda^{-4}} + A_0. \quad (4.3)$$

However, this function could not be fitted, which suggest that the Rayleigh approximation does not hold in this situation, and Mie scattering should be incorporated in the model as well. Thus all together, UV-Vis spectroscopy is not a suitable technique to quantify the fluorescence, because of the dominant scattering contribution.

**Scaling reactants sequential batch by means of fluorescence spectroscopy** Fluorescence spectroscopy is a suitable technique to quantify the fluorescent signal from the nanoparticles. Fluorescence spectroscopy is more sensitive than UV-Vis because only the fluorescent emission is measured, and lower concentrations can be analysed at which scattering is less dominant. Moreover, the particles are in Mie scattering regime, and scatter mainly in the forward direction, which does not affect the measurement greatly since the detector is placed at a  $90^\circ$  angle.



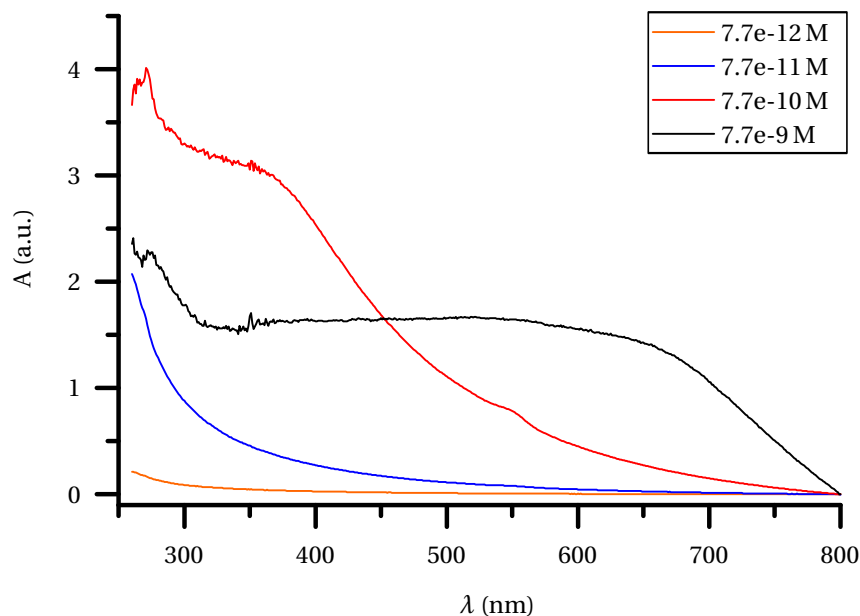


Figure 4.9: UV-Vis absorption spectra of the concentration series of pure C3 cores from  $7.6 \times 10^{-12}$  to  $7.6 \times 10^{-9}$  M. A blanco was subtracted from the spectra, and the intensities were automatically zeroed at 800 nm. Because of this, the incident beam was almost completely scattered away from the detector at  $7.6 \times 10^{-10}$  and  $7.6 \times 10^{-9}$  M, hence the plateau in intensity.

A concentration series of C3-4 was made, which could be fitted linearly (Fig. 4.10ac). Two methods were tested to quantify the fluorescent signal, being the peak maximum and the peak surface  $S$  of the spectrum. The surface area was approximated via trapezoidal numerical integration, which breaks down the surface area between two data points into trapezoids with more easily computable areas. As both methods gave a nearly identical fit, the surface area method was chosen since it is in principle less sensitive to noise in the spectra (Fig. 4.10bd). At high concentration, the surface area started to deviate from the linear trend (inset Fig. 4.10a), as scattering became dominant. A fraction of the emitted fluorescent signal is scattered while it passes through the sample to the detector. For CS particles, this effect might shift to lower concentrations depending on the shell size, since some additional scattering of the shell is expected. However, since the shell is index matched, this is probably relatively small, and this effect will be quantitatively analysed further in Section 4.2.5.

The scaling of the reactants by means of fluorescence spectroscopy yielded excellent results in the batch-wise synthesis of the binary system CS21/CS22. The reactants were scaled on the amount of cores in order to control the shell thickness. In this way, a binary system was obtained with about a 1:1 volume ratio at 20 and 50 °C (Fig. 4.11).

**Comparison weight and fluorescent yield** The yield of the reaction could be determined via the weight yield and the fluorescent signal of the cores. The weight yield over the first four shells of CS18-19 after a single centrifugation step was respectively 93% and 88%. The fluorescence yield after a double centrifugation step was 83% and 68% respectively for CS21-22 (Table 4.6). Comparison is hard since the number of shells grown and number centrifugation steps differ, however all values lie in the same ballpark. The discrepancy between the yield in the first shell of CS21-22 is linked to increased aggregation in an early stage of the reaction. During the growth of the first shell of CS22, the needle for the nitrogen flow was accidentally left in solution, which served as nucleation point, and a layer of highly fluorescent aggregates were observed at the surface. In summary, both methods seem suitable for a ballpark approximation, however, fluorescence spectroscopy is preferred since it requires less sample and time.

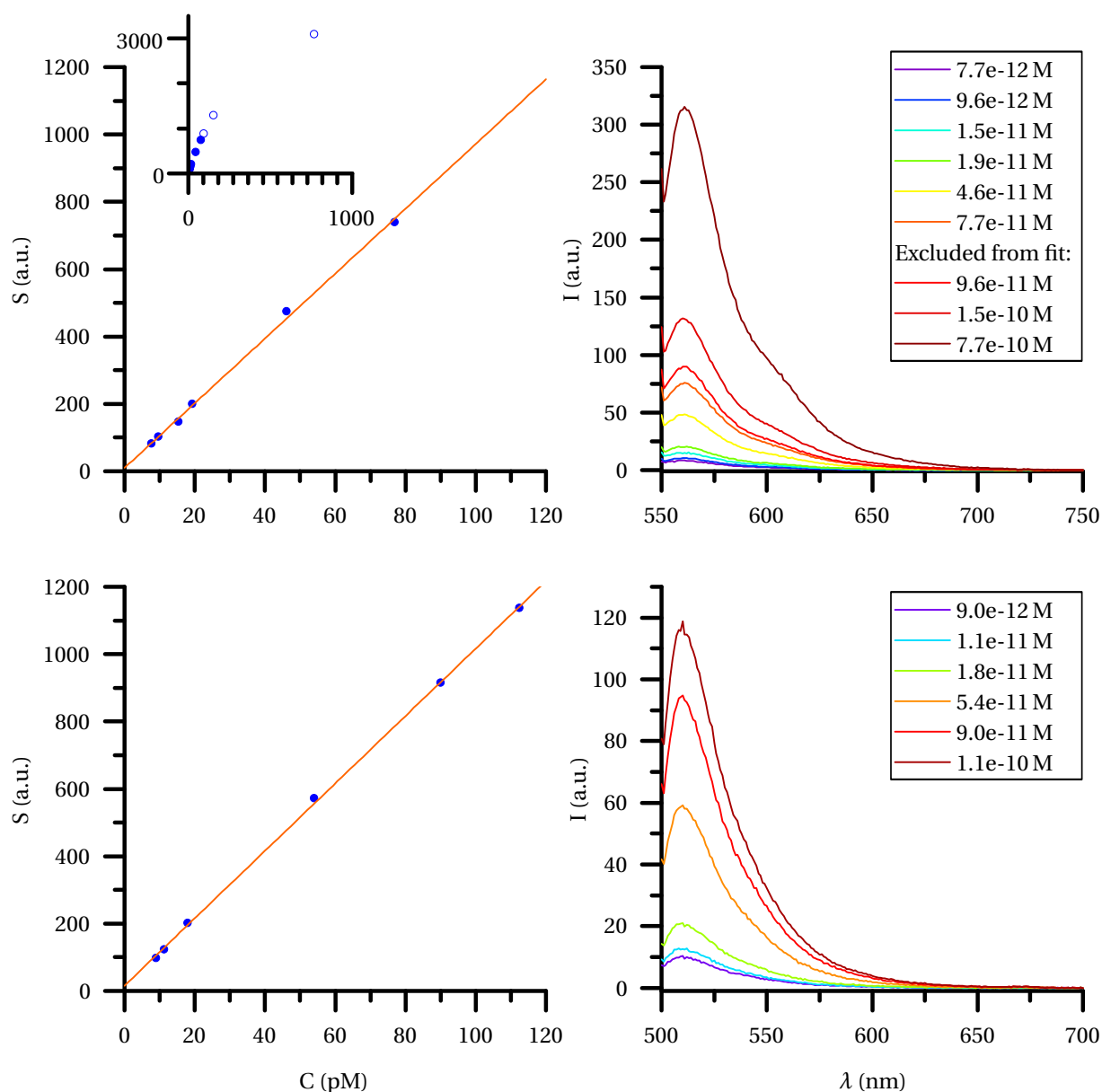


Figure 4.10: Concentration series with the corresponding fluorescence spectra of C3 (a,b) and C4 (c,d). A blanco was subtracted from the spectra, and the intensities were zeroed at the longest shown wavelength. The settings used can be found in Table 3.1. For the fit of C3 (a), the surface of the spectra in the range 556 to 566 nm (b), and for C4 (c), the range of 506 to 516 nm was calculated. The excluded data points in (a) are shown in the inset (open symbols). The coefficient of determination  $R^2$  was evaluated at 0.9981 (a) and 0.9996 (c).

Table 4.6: Absolute and relative yield of CS21-22, before initiation and after a complete shell growth. The sample was centrifuged twice between shell 1 and pre-initiation shell 2.

#	CS21		CS22	
	n (mol)	Yield (%)	n (mol)	Yield (%)
Pre-initiation shell 1	3.03e-10	100	3.68e-10	100
Shell 1	2.81e-10	93	2.67e-10	73
Pre-initiation shell 2	2.52e-10	83	2.49e-10	68
Shell 2	2.13e-10	70	2.25e-10	61

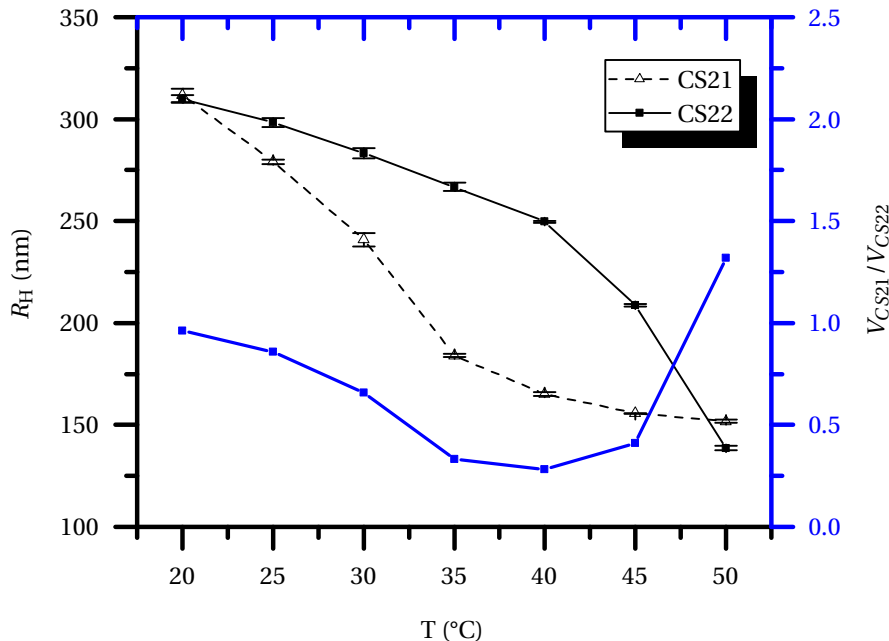


Figure 4.11: Overview of the hydrodynamic radius  $R_H$  as function of temperature for CS21 and CS22. The error bars indicate the standard error of the mean. The volume ratio is indicated in blue.

Table 4.7: An overview of the number densities per weight percent  $n_p/\text{wt}\%$ . The number density determined with fluorescence was based on fits shown in Fig. 4.10ac. The large difference between the  $n_p/\text{wt}\%$  of the CS particles can be ascribed to the different core size and consequent weight contribution to the particle's total mass.

#	$n_p/\text{wt}\%$ ( $\text{m}^{-3}$ )			
	2D CLSM	Viscometry	3D CLSM	Fluorescence
M1	1.62e17	1.26e17		
M2		4.59e18		
M3	1.85e17	4.58e17		
CS21			1.01e18	8.21e17
CS22			2.24e18	1.73e18

#### 4.2.5 Volume fraction

The volume fraction was determined with confocal microscopy in 2D and 3D, viscometry and fluorescence spectroscopy. The number density per weight percentage for M1-3 and CS21-22 is shown in Table 4.7. Comparison of the number density determined with 3D CLSM and fluorescence spectroscopy showed minimal differences, which could be attributed to scattering in the latter.

#### Confocal microscopy

An identifier for the quality of the particle positions in 3D is given by the radial distribution function (Fig. 4.12). The function has deep minima, which indicates few different domains per sample, and good resolvability, since overlap of signal causes particles centres to appear closer. The first peak position is in liquids close to hydrodynamic radius, however a deviation of 6.6% and 14% was found for CS21-22 respectively. This difference is caused by compression of dangling ends into the crystal lattice, and is qualitatively proportional to the number density in the measured sample. Occasional particle position mis-identification or skipping a particle gives rise to an error in the volume fraction [10], therefore the identified particles were cross-checked to the raw data in both 2D and 3D.

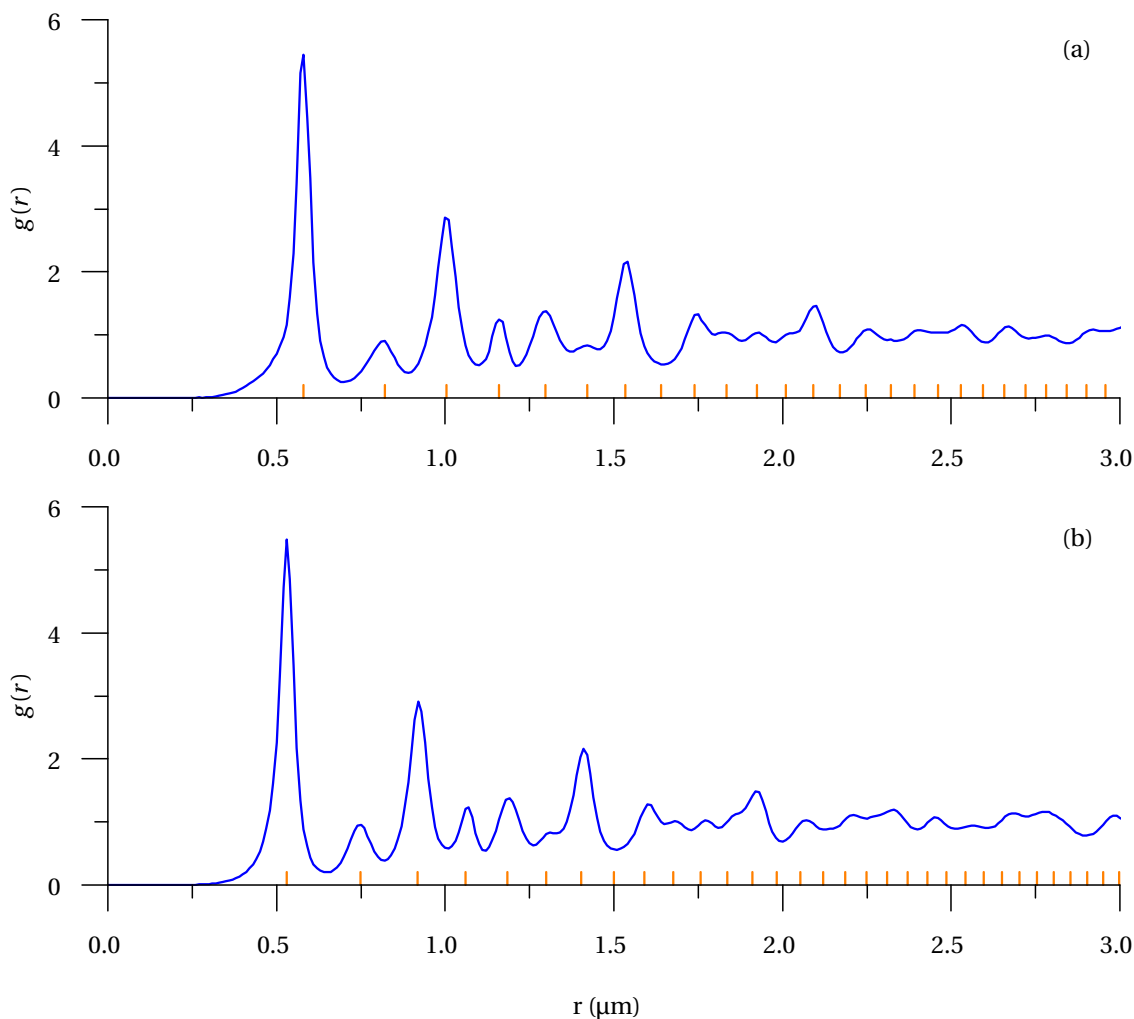


Figure 4.12: Average radial distribution functions of the samples used for 3D confocal number density determination of CS21 (a) and CS22 (b). The FCC peak positions were indicated with the orange marks [121].

Errors in sample preparation, presence of aggregates, and evaporation introduces an error in the number density, however this is probably not more than 5%. The aggregates in the sample were excluded from the particle tracking, which was significant for CS22, and introduces a slightly larger error. Here, one  $z$ -stack was discarded since it contained a big aggregate which occupied a large fraction of the focal volume. In general, confocal microscopy is considered as one of the most accurate and reliable techniques, and will be used to benchmark the other techniques and to calculate the volume fraction in this thesis.

### Viscometry

A fit of the relative viscosity as function of the weight percentage was made to obtain a shift factor, which relates the weight percentage to the volume fraction (Figs. A.1-A.3). A large discrepancy in number density was found for M3, however the values obtained with 2D CLSM and viscometry were in reasonable agreement for M1 (Table 4.7). Based on the similarity of M3 with M1, a similar number density is expected as well, which suggests that the viscometry is inaccurate. Not all assumptions that are made to fit the relative viscosity do hold perfectly and are likely to be origin for the discrepancies (Section 2.7). First of all, hard sphere behaviour is assumed for the Batchelor equation (Eq. 2.29), which does hold in the case of dilution [64]. The same hard sphere action is assumed to determine the hydrodynamic radius, which advocates the conversion from volume fraction to number density via the hydrodynamic radius. It is assumed that the suspension has no shear-thinning behaviour,

i.e. behaves as a Newtonian fluid, which requires large dilutions as well. Therefore, extreme accurate timing is required, as the viscosity of the suspension almost equals that of the solvent. This was not possible with the available set-up and higher volume fractions were measured. A volume fraction of  $\lesssim 0.02$  is required for the fit to be valid. An uncertainty in of 7% in the volume fraction was reported at  $\phi \approx 0.03$ , which reduces to an uncertainty of  $\sim 2\%$  in the number density if the determined radius is free of error [10]. The range used for the fit was  $\phi \approx 0.02 - 0.08$  for M1, and up to  $\phi \approx 0.42$  for M3, which partially explains the large discrepancy between viscometry and confocal number densities in M3. Since for M2  $\phi \approx 0.02 - 0.12$ , the error in the number density is expected to be in the same order of magnitude as M1.

The measurements were done at multiple temperatures to reduce the error, however a large spread was obtained for M3. A better fit was acquired for measurements at lower temperatures and higher volume fraction, even though the assumptions do not hold here. Concluding, number density determination with viscometry was found to be accurate in the order of 20%, even beyond the volume fraction where the assumptions hold, however large discrepancies were obtained at 5-10 times higher volume fractions.

### Fluorescence

Determination of the number density with the concentration series shown in Fig. 4.10ac has a similar error as was found with viscometry, that is an error of 23% and 30% with respect to 3D CLSM for CS21-22, respectively. The lower number density can be explained by two factors. Firstly, the number density of the cores was calculated via Eq. 3.2, which assumes no water content, and introduces an error of a couple percent. Secondly, increased scattering of emitted fluorescent light (inset Fig. 4.10a) by the microgel shells reduces the apparent number density, which is probably the most dominant factor. In theory, this could be corrected for with a scattering model, however this is beyond the scope of this thesis. Interestingly, despite the large contribution of the aggregates in CS22, which were measured with fluorescence, but omitted in the 3D CLSM analysis, the number density with respect to the 3D CLSM analysis was 7% lower for CS22 than for CS21. Despite these errors, fluorescence spectroscopy is a novel technique which is able to give a good estimate of the number density in a short amount of time for this system, and can be improved further by means of a scattering model.

## 4.3 Comparison pure and core-shell microgel particles

Particle tracking was attempted after which a binary CS model system was chosen to study sequential gelation in Section 4.4. The CS particles were compared with pure microgel particles to study their morphology and interparticle potential, which was required to interpret the sequential gelation results.

### 4.3.1 Resolvability in CLSM

The resolvability of pure and CS microgels was tested with CLSM images of respectively a binary gel of M1/M2 and a gel of CS19 (Fig. 4.14ab). CS19 with four shells was used and was one of the largest samples obtained. The resolvability of the inner network of the gel in CS19 had increased greatly, because of the separation of the fluorescent signal and the strong fluorescent signal of the cores. Particle tracking with the Crocker and Grier scripts were performed on the CS19 gel, but the resolvability was insufficient for quantitative analysis, and only skeletonisation analysis would be possible.

A large increase in scattering was observed upon increase of temperature, mainly between 40 and 50 °C, which resulted in a decreased resolvability. This was probably due to the refractive index mismatch of the oil, and is an intrinsic limitation of the set-up.

**PM fluorescent dyes** A comparison between the dyes used in pure microgels (FOM, MRB) and in CS microgels (PM 546 and PM 605) was made by exposing M1, M2, CS21, and CS22 to a fixed laser

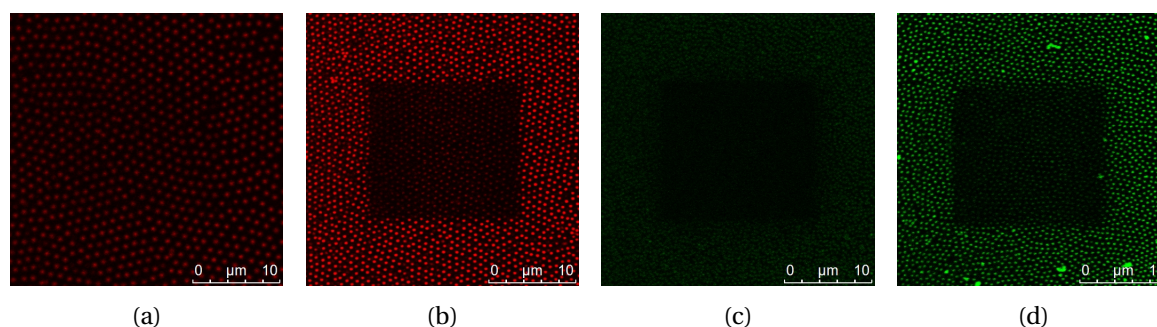


Figure 4.13: CLSM images of M1 (a), CS21 (b), M2 (c), and CS22 (d) exposed at a 546 nm (ab) and 488 nm (cd) laser source for two minutes focussed on the glass plate. The image was taken at the same  $z$ -height as the exposure and 2x zoomed out, and was recorded at the full visible spectrum. The intensity of the PM dyed samples is much higher than of their MRB and FOM counterparts. The bleaching of CS21, M2, and CS22 was severe, and for M2 no fluorescent signal remained after exposure. Please note that the bleaching between samples exposed to different laser sources cannot be compared here.

intensity for a certain time and comparing the fluorescent intensity before and after (Fig. 4.13). If the different sizes of the particles are neglected, it can be seen that the bleaching of PM 546 has a similar rate as FOM. However, MRB performed much better than PM 605 in these conditions. The fluorescent intensity of the PM dyes is much higher than of the FOM and MRB. As the core could be highly loaded with fluorescent dye, the laser intensity could be set lower than for the FOM and MRB dyes during the recording of a  $z$ -stack. As the focus in this thesis is structure analysis, which requires that the  $z$ -stacks can be recorded in a short amount of time, the strong fluorescent signal is a huge advantage of the PM dyes. All together, the PM dyes appear to be the best choice for application in the experiments performed in this thesis.

**Resolvability sequential gel M1/M2** A  $z$ -stack was recorded of a M1/M2 sequentially gelled bigel at  $10^{-2}$  M at 50 °C. The typical core-shell structure of a sequentially gelled bigel is clearly visible in Fig. 4.14a, however, the resolvability of the core is insufficient for particle tracking routines. As noted above, the particles stained with FOM dye had a very low fluorescence, and a high laser intensity and frame-averaging was required to image the gelled particles. Even though the sample was recorded with an extremely high averaging, the green gel core has a very low signal, partially due to bleaching, which became noisy upon increase of contrast. This rendered accurate quantification of the gel core impossible. Moreover, high frame and line-averaging could strongly affect the quality of a recorded  $z$ -stack, as this is a time consuming process, and a small drift would create distortion in the 3D reconstructed image. The gel shell structure of the red particles could be resolved, because of the spatial separation of the particles. The pure microgel system did not meet the requirements set in Section 4.1.1, which is reflected in the poor resolvability of the inner gel network.

**Resolvability gel CS19** A  $z$ -stack of a CS19 gel was recorded and analysed with the Crocker and Grier scripts to test the resolvability. The tracked particle coordinates in the  $z$ -stack of CS19 with 0.1 M salt recorded at 50 °C are shown in Fig. 4.14c. Two clusters can be resolved, which is characteristic for a gel formed via arrested spinodal decomposition. The features tend to pull together as a result of signal overlap, which is reflected in the large abundance of pairs throughout the sample. In some areas, all features which were found manually were also tracked by the routines, and in some regions the feature finding was inconsistent and multiple features were found in a single and vice versa. It must be noted that mainly inside the clusters, the features could neither be distinguished manually nor via the routines. This was probably caused by strong scattering inside the clusters, which in combination with the limited resolution resulted in signal overlap. The signal overlap becomes clear from the  $g(r)$  as well, i.e. peaks were found below the particle diameter (Fig. 4.14d).

In order to do quantitative analysis, sufficient features should be found, i.e. > 20.000 in total, and

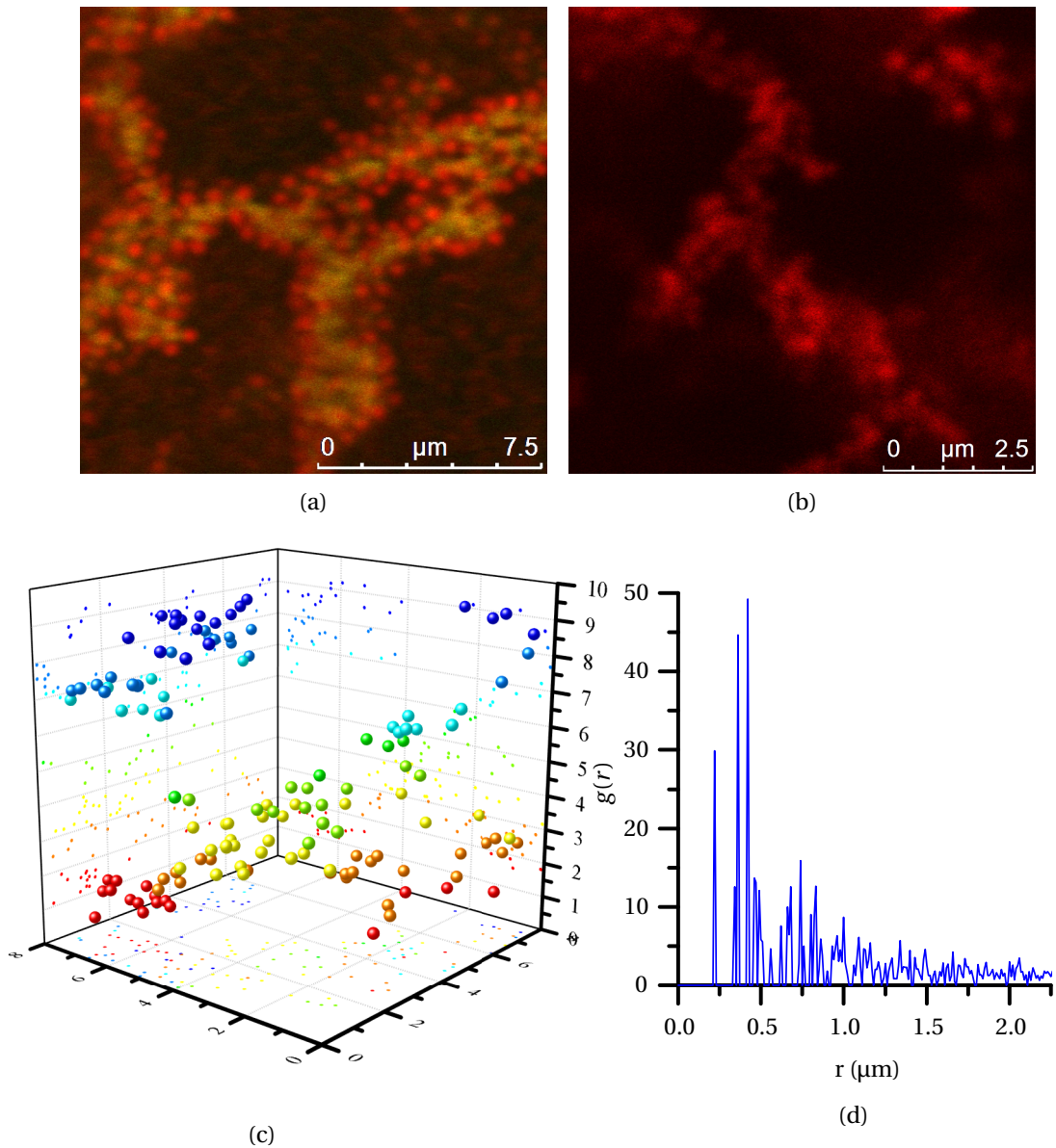


Figure 4.14: a): CLSM image of a sequential gelated bigel composed of M1 (red) and M2 (green) with  $10^{-2}$  M KCl at  $50^\circ\text{C}$ . M1 and M2 have a  $\phi$  of respectively 0.07, and 0.03 at  $50^\circ\text{C}$ . The image was recorded with a frame-average of 8, and a line-average of 32. b): A typical CLSM image in the  $z$ -stack of CS19 with 0.1 M KCl, which was analysed with the Crocker and Grier 3D particle tracking routines. The  $z$ -stack was accidentally highly oversampled which led to an uncertainty in the particle position of  $\sim 7$  pixels. c): 3D plot of the tracked particle coordinates of (b) with colour coding based on the  $z$ -value. Two clusters can be identified in the recorded volume. Note who the features tend to pull together. d): 3D radial distribution function  $g(r)$  for the  $z$ -stack shown in (c). The peak distribution is centred around the particle diameter. M. Bergman is gratefully acknowledged for the image analysis.

Table 4.8: An overview of the size and the zeta potential  $\zeta$  at 20 °C for CS21 and CS22. The swelling ratio of the microgel shell is denoted as  $\alpha(20, 50^\circ\text{C})$ , which was calculated following Eq. 2.39. The Hückel approximation (Eq. 2.34) was used to calculate  $\zeta$ .

#	Monomer	$R_H$ (nm)	$\alpha(20, 50^\circ\text{C})$	$\zeta$ (mV)
CS21	NIPAm	305	8.7	-20.9
CS22	NIPMAm	309	11.9	-39.1

the values found over different  $z$ -stacks could be averaged. In a sample like shown in Fig. 4.14, about 100 features were found, which would mean that even in the case of perfectly homogeneous sample, data acquisition and analysis would take an impossible amount of time.

The criteria for resolvability as defined in Subsection 4.1.1 were almost met by CS19. The particle size of about 500 nm at 50 °C hits the minimum limit. Nevertheless, scattering was found to limit the resolvability inside the clusters in a sample with small particle size. Additionally, not sufficient features could be found per  $z$ -stack in order to do quantitative analysis, which is inherent to the studied system. Structural properties of clusters could be analysed individually, however only local information could be obtained.

### 4.3.2 CS21/CS22 model system

The limited resolvability of CS19 had motivated to analyse the gel structures without individual particle tracking, and to only study the gel volume. Here, the CS approach has an advantage over the pure microgel approach, as the fluorescent intensity is much higher, and control over the morphology and size is much better ('designer particles', Section 4.2.2). The binary model system CS21/CS22 was synthesised for this purpose, and was used as CS model system to study sequential gelation. The samples were synthesised in a small batch volume with a low yield after centrifugation, which limited the number of experiments that could be performed. This was a result of the batch-wise synthesis with a purification round between each shell growth, which is a disadvantage of the CS synthesis over the pure microgel synthesis.

The hydrodynamic radius as function of the temperature was measured with DLS, and the zeta potential with electrophoretic mobility measurements. The hydrodynamic radius and zeta potential of the CS21/CS22 binary system are given in Table 4.8, and the swelling curve is given in Fig. 4.11. The liquid radial distribution function was derived from CLSM time series in combination with particle tracking and is shown in Fig. 4.16. The thermosensitivity, charge and elasticity of the CS and pure microgel particles were roughly the same. However, a larger swelling ratio and more smeared collapse trajectory was observed for the CS microgel. No large discrepancies between the CS and pure microgels, hence the particle types were treated the same in next sections.

### Electrophoretic mobility

The electrophoretic mobility of M1-3 and CS21-22 as function of the temperature is shown in Fig. 4.15bd, and the zeta potential in Tables 4.2 and 4.8. The zeta potential of the pure microgels and CS particles was nearly identical, as the charge of the core is screened by the shell even in deionised conditions ( $\kappa^{-1} = 100$  nm at  $10^{-5}$  M KCl). A decrease in mobility was observed for the PNIPAm samples around the VPTT (Fig. 4.15b), which roughly followed the decrease in volume. On top of the higher effective charge due to the collapse of the microgel, increased mobility of the CS samples was observed, which originated from an additional contribution of the unscreened charge of the core. However, the PNIPMAm samples did not show an increase in mobility (Fig. 4.15d), and probably require a higher temperature for this to be observed.



### Swelling behaviour and internal structure

The swelling curves for M1-3 and CS21-22 are shown in Fig. 4.15ac. The swelling behaviour of the CS particles was similar to that of the pure microgels, and the small differences could be ascribed to the different crosslink density. The decrease in  $R_H$  is similar to that of a pure microgel, but despite the higher crosslink density, the swelling of the microgel shell of CS21 was similar to that of a few percent lower crosslinked pure microgel (Tables 4.2 and 4.8). It is unknown whether this was related to the BIS feed or the seeded growth, however, some literature points in the direction of the first. Accairo *et al.* found a larger swelling for particles prepared with a monomer/BIS feed, as did Dulle *et al.* for highly crosslinked core-shell particles synthesised with BIS feed [78, 88, 118]. Remarkably, a smaller swelling than pure microgels was found by Crassous *et al.* for CS particles with a thin shell of 2.5% crosslink density synthesised without BIS feed [81, 118]. A third, but unintuitive option is that the outer layer contributes the mainly to the swelling, which has a lower crosslink density.

The collapse trajectory of the CS particles was consistently longer than their pure microgel counterparts (Fig. 4.15ac). This is an effect observed for highly crosslinked samples, i.e. 15 mol%, however, a relation with the internal morphology merely speculative. Flory-Rehner theory is able to fit experimental swelling curves of microgel particles, despite its assumption of a homogeneously crosslinked microgel network. By fitting samples with varying crosslink densities, Karg *et al.* found that only the degree of polymerisation between the crosslinks changed consistently [118]. Moreover, this model was able to correctly reproduce the smeared swelling trajectory, which suggests that an increased degree of polymerisation between the crosslinks is a determining factor in the swelling trajectory. A similar trend in correlation length, which is the average mesh size between the entanglements in the internal network of a microgel, was observed with small angle neutron scattering, however such relation was not found by Saunders in an earlier publication [118, 122]. The application of a 7.5 mol% BIS feed during the first shell indeed should have resulted in a more homogeneous crosslinking and higher average degree of polymerisation between the crosslinks, which explains the difference with the pure microgel swelling curve.

### Hertzian elasticity

A liquid radial distribution function  $g(r)$  was made with the Crocker and Grier routines at  $\phi = 0.22$  and 0.42 for CS21, which was compared with the  $g(r)$  of a pure PNIPAm microgel with 5% crosslink density. Both could be fitted with a Hertzian potential from which an elasticity of the particles was derived. The  $g(r)$ s and the Hertzian fits are shown in Figs. 4.16 and 4.12.

**Quality of the  $g(r)$ s** The  $g(r)$  is highly dependent on the integrated intensity threshold (IIT), as this particle specific parameter determines which particles are in focus, and which are not. In a dataset of good quality, the  $g(r)$  must converge to a certain peak shape and height with increasing IIT. The position of the first peak is a good indication, as it increases along both axes for a good data set, and decreases for a mediocre one [59]. Both  $\phi$  is 0.22 and 0.42 datasets yield a  $g(r)$  which is converged well in the tested IIT of 0.8-1.0 of the integrated intensity median. However, a very small decrease in peak height was observed in the tested range, i.e. 2.4% for  $\phi = 0.22$ , and 2.8% for  $\phi = 0.42$  (Fig. A.4), which is probably caused by the small size and fast movement of the fluorescent features. A higher zoom is likely to increase the data quality, however, for the purposes of comparison, this dataset is of sufficiently high quality. Clusters were filtered by setting a maximum mass intensity, which was checked by manual inspection. This did work in most cases, however, not all could be filtered, which enhances the  $g(r)$  at an  $r$  corresponding to the interparticle distance in a cluster. As this is a very small fraction of the dataset  $\ll 1\%$ , it is not expected to affect the  $g(r)$  significantly. The  $g(r)$ s calculated for data recorded at different positions in the  $x, y$ -plane yielded distinct populations (Fig. A.5), which suggest that the sample was not sufficiently homogenised, or the data was recorded too close to the edge of the sample. Since bulk properties will be compared, the average of the  $g(r)$ s was taken for further analysis. Concluding, the peak positions were very robust and only the first peak height had a

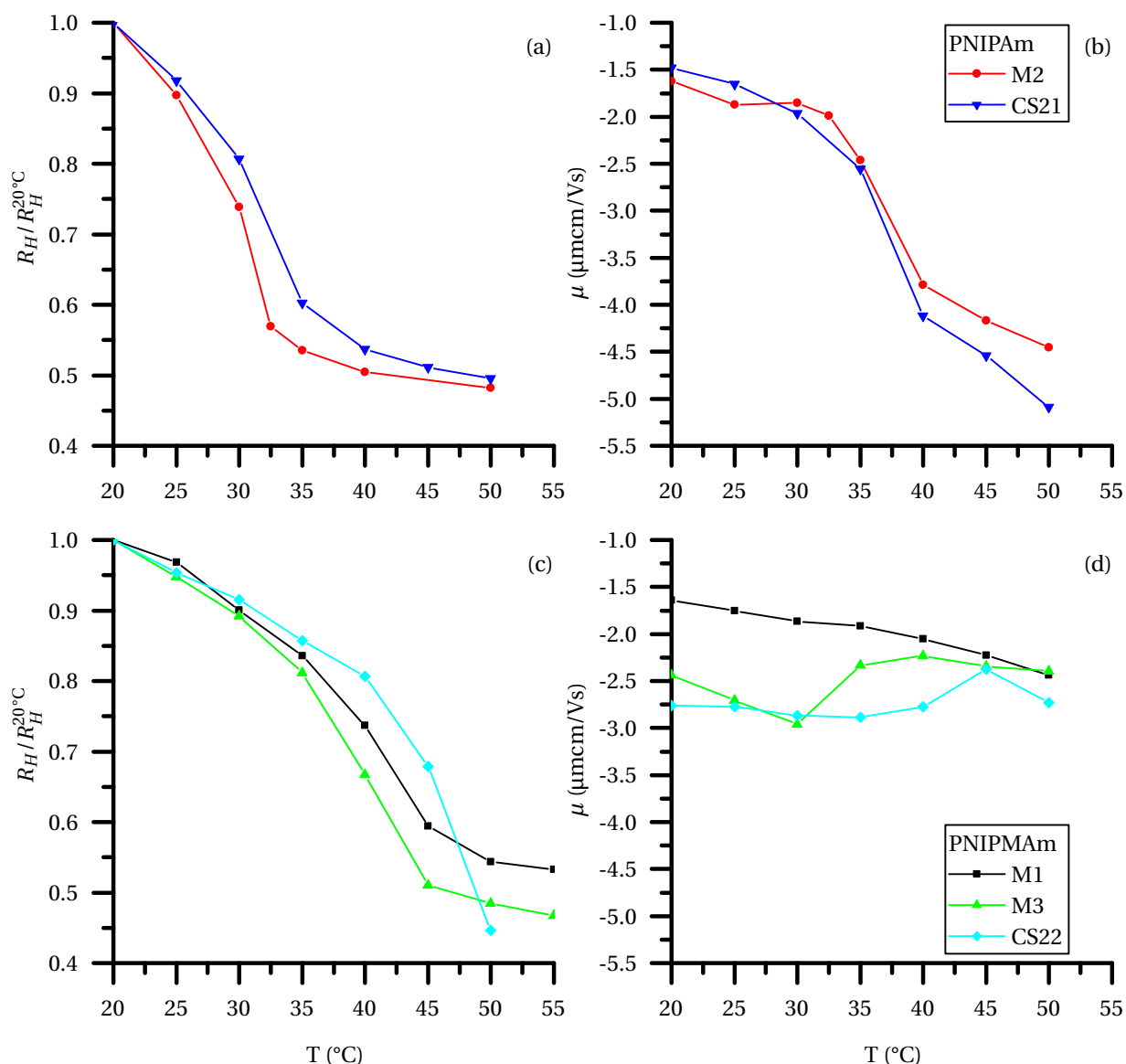


Figure 4.15: Overview of the hydrodynamic radius normalised by the radius at 20 °C,  $R_H/R_H^{20^\circ\text{C}}$ , and the mobility  $\mu$ , sorted by monomer type.

significant error.

**Comparison  $g(r)$ s** The experimental  $g(r)$ s normalised by the hydrodynamic diameter  $\sigma_H$  of the pure microgel and CS21 are shown in Fig. 4.16. The  $g(r)$ s were very similar, which indicates that the CS microgels have a similar structure as the pure ones. Interestingly, the peak positions of the pure microgel were always below  $\sigma_H$ , while this was above  $\sigma_H$  for CS21. This consequent deviation could be attributed the error in  $\sigma_H$ . As real samples are slightly polydisperse, the form factor of the sample is a superposition of the different form factors of all differently sized particles in the sample. Close to a minimum in a form factor such as shown in Fig. 2.1b, the scattering contribution of particle at a certain  $q$  is highly dependent on its size, and depending on the  $q$  of the DLS measurement, a different size distribution is probed. For comparison, both DLS measurements should be done at the same relative position in the form factor. However, both measurements were done at the same

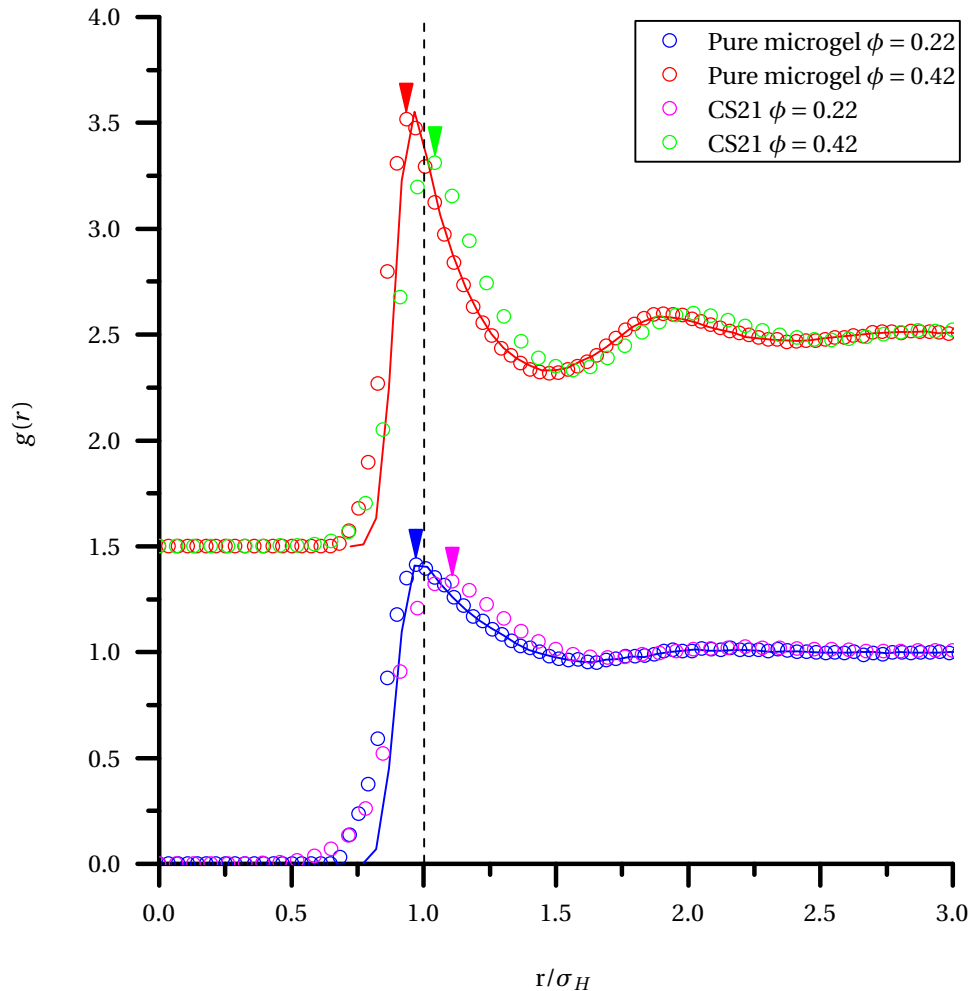


Figure 4.16: The stacked radial distribution function  $g(r)$  of a pure microgel and CS21 at volume fractions  $\phi = 0.22$  and  $0.42$  recorded at  $20^\circ\text{C}$ . The interparticle distance  $r$  was normalised by the hydrodynamic diameter  $\sigma_H$ . The pure PNIPAm microgel particle was prepared with 5% crosslink density, and had a  $R_H$  of  $417\text{ nm}$  and a zeta potential of  $-15\text{ mV}$  at  $20^\circ\text{C}$ . This  $g(r)$  could be fitted from MD simulations of particles with a Hertzian interaction potential (Eq. 2.44) with  $\varepsilon_H = 520k_B T$ , radius of  $0.965R_H$ , polydispersity of  $0.04$ , and a  $z$  noise of  $0.005$ , which are plotted as lines and was consistent for all  $\phi$  and  $T \leq 25^\circ\text{C}$  measured. The  $\phi$  of the pure microgel was taken from the fit, as the values obtained from viscometry, i.e.  $\phi = 0.17$  and  $0.34$ , are not robust. The peak position of the experimental data was indicated with an arrow, and  $r/\sigma_H$  was marked with a dashed line. The pure microgel has  $g(r)$  first peak positions  $r/\sigma_H < 1$ , while these were  $r/\sigma_H > 1$  for CS21. M. Bergman is gratefully acknowledged for the pure microgel data and fits.

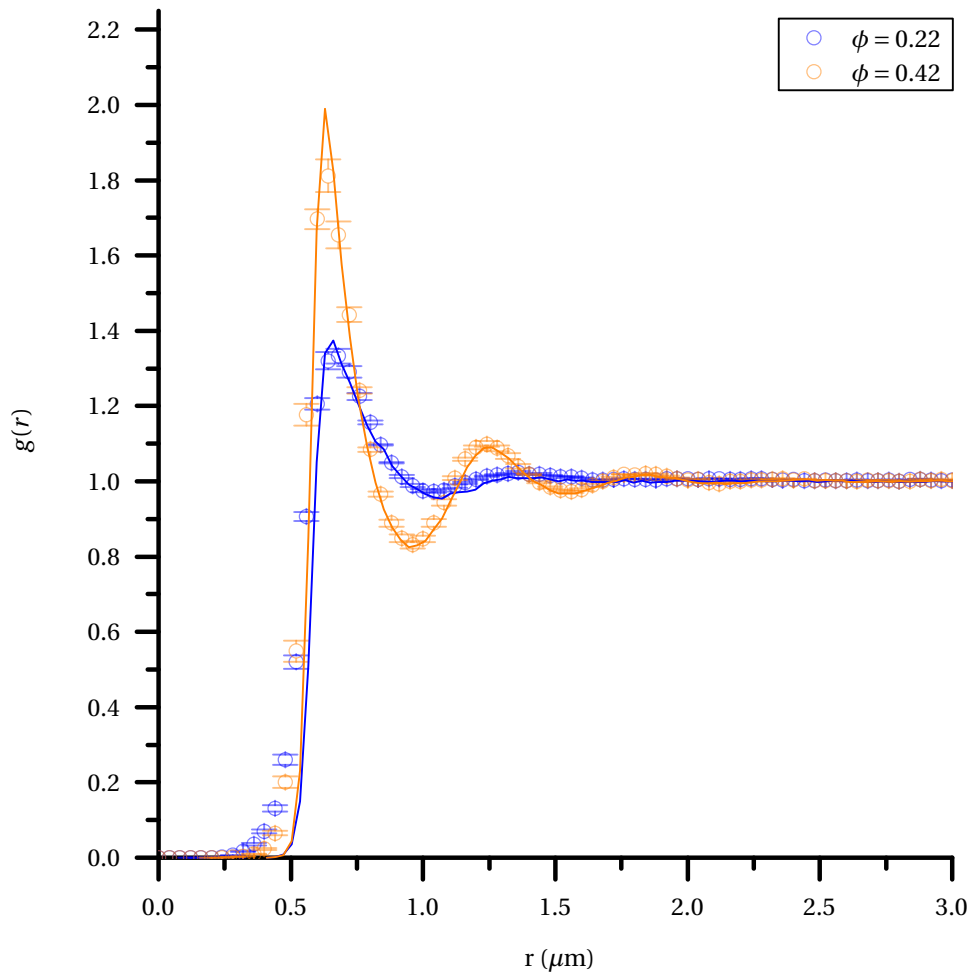


Figure 4.17: The radial distribution function  $g(r)$  of CS21 sample at volume fractions  $\phi = 0.22$  and  $0.42$  recorded at  $20^\circ\text{C}$ . The errorbars represent the standard error of the mean of the  $g(r)$ s obtained at five different positions in the sample. The experimental data could be fitted from MD simulations of particles with a Hertzian interaction potential (Eq. 2.44) with  $\varepsilon_H = 520k_B T$ , radius of  $1.033R_H$ , polydispersity of  $0.04$ , and a  $z$  noise of  $0.010$ , which are plotted as lines. Sample  $\phi = 0.22$  was fitted with the same volume fraction, however, the experimental data at  $\phi = 0.42$  was fitted with  $\phi = 0.43$ . A slight deviation of the fit is observed around  $r = 1.0 - 1.5$  for  $\phi = 0.22$ . M. Bergman is gratefully acknowledged for the simulation data.

$q$  values, but the form factors of the particles differ significantly, due a different particle size and the presence of a PS core. This error is likely the origin of the discrepancy in the peak positions, and it can be concluded that the CS microgels have a similar structure as the pure ones.

**Hertzian fit** The  $g(r)$ s of the pure microgel and CS21 could be fitted with the  $g(r)$  obtained from MD simulations with a Hertzian potential once corrected for the different interaction radius (Eq. 2.44, Figs. 4.16 and 4.17). Standard MD simulations were performed with 50,000 particles with a polydispersity of 0.04 following Mohanty *et al.* [26]. Pseudo 2D  $g(r)$ s were calculated from slices along the  $z$ -direction of the box and the results were averaged over different slices. In order to mimic the poorer resolution in the  $z$ -direction, the particles were randomly displaced along this axis following a Gaussian probability with a standard deviation  $z$ . A more rigorous discussion can be found in [26]. The effect of this treatment is shown in Fig. A.6. The  $z$ -noise reduces the peak height and displaces the peak to larger  $r$ . The simulations with no polydispersity and  $z$ -noise were benchmarked against the Ornstein-Zernike (OZ) equation with Roger-Young (RY closure), which is an analytical approach to calculate a  $g(r)$  from an ensemble of particles with a given pair potential. The results were in good agreement, as it is known that the peak height obtained from the OZ equation has a large uncertainty. A bin size of 0.05 diameter was chosen in order for the simulated  $g(r)$  to become smooth. However, this is the same order of magnitude of the deviation in interaction radius.

The volume fraction which was prepared in experiment was in excellent agreement with the value determined from the fit for CS21. A difficulty in interpretation was introduced by the volume fraction of the pure microgel, which was not very accurate as it was determined with viscometry, and was found to deviate strongly up to  $\sim 20\%$ . The  $\varepsilon_H$  was verified with fits of experimental data at three different temperatures, where the volume fraction was scaled according to the size difference between the temperatures, and three different  $\phi$ . Therefore, the volume fractions obtained with simulations were taken for interpretation above. As the interaction radius probably differed from the hydrodynamic radius, this would automatically result in a change in volume fraction, as these quantities are intrinsically linked. However, the volume fractions of the samples were very closely matched in this data set, thus the fits could be directly evaluated.

Both the pure microgel and CS21 could be fitted best with  $\varepsilon_H = 520k_B T$ , however the fit of CS21 deviated slightly at  $r = 1-1.5$  for  $\phi = 0.22$ . Other strengths and volume fractions were tried as well, as sometimes certain conditions can be degenerate, but within the physical accepted limits, this was not observed. A 0.01  $z$ -noise was used to fit CS21 (Fig. 4.17), in contrast to 0.005 for the pure microgel particles (Fig. 4.16), which could be justified by the sub-optimal dataset as discussed above. Moreover, the IIT was not set very low, which might have resulted in a slightly higher  $z$ -noise. The  $g(r)$  fits were reliable, and strongly indicated a similar elasticity for the CS microgel as the pure microgel in the fluid regime. The more homogeneous crosslink density was not reflected in the elasticity of the particles, which strengthens the relation between the BIS feed and the longer collapse trajectory. Due to the low density in the fluid regime, the particles are little compressed and only the outer corona is probed by the  $g(r)$ , which is not affected by the BIS feed. In fact, the outer corona of the CS and pure microgel particles are probably very alike due to the synthesis method (Subsection 4.2.2), which explains the similar elasticity.

## 4.4 Gelation

The link between the rheological properties and morphological structure of the single particle and sequential gels are discussed in this section. The use of mechanical rheology over DWS is motivated in Appendix B, even though the small sample volume limits the number of rheology experiments that can be done. The morphological structure was determined via processing of  $z$ -stacked confocal images, which is discussed in detail in Appendix F.

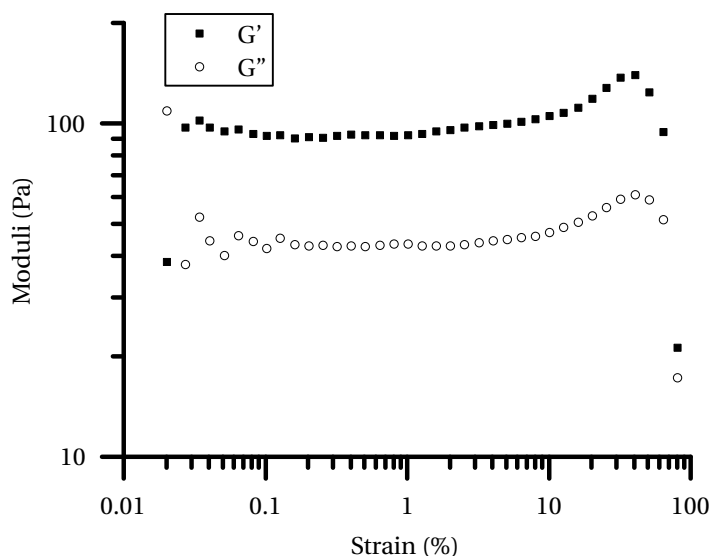


Figure 4.18: Elastic and loss moduli,  $G'$  and  $G''$ , at a frequency of  $1 \text{ s}^{-1}$  as function of applied strain in a  $R_H^{50^\circ\text{C}} = 156 \text{ nm}$  pure PNIPAm microgel sample at  $\phi^{50^\circ\text{C}} = 0.06$  and with  $0.1 \text{ M KCl}$ . The limit of linearity  $\gamma_0$  was found to be  $1.6\%$  with the method defined in the text.

#### 4.4.1 Single particle gels

##### Deformation rheology and structure

The rheological experiments were done within the linear visco-elastic regime, which was determined from a strain sweep on a pure microgel sample of  $R_H^{50^\circ\text{C}} = 156 \text{ nm}$  at  $\phi^{50^\circ\text{C}} = 0.06$  and  $0.1 \text{ M KCl}$  (Fig. 4.18). The highest deformation which can be considered within the linear visco-elastic regime has been reported several times as the strain at which the  $G'$  deviates more than 5% of the plateau value, which yields an upper limit of  $\gamma_0 = 1.6\%$  [108, 123, 124]. In order to reduce noise in the oscillatory measurements, they were performed at the upper side of the linear regime with a strain of  $0.8\%$  at a frequency of  $1 \text{ s}^{-1}$ , unless otherwise stated. Typical values reported in literature are around  $0.1\text{-}1\%$  at a frequency of  $1 \text{ s}^{-1}$  [37, 38]. It is assumed that all the measured gels fall within the linear visco-elastic regime at  $0.8\%$  with  $1 \text{ s}^{-1}$ , as the available sample volume is too small to perform a strain sweep for each condition, however, this assumption is suboptimal and careful interpretation of quantitative data required.

A strong strain overshoot was observed for the PNIPAm microgels, and both moduli show strain hardening behaviour followed by a strain thinning one (Fig. 4.18). This behaviour has been reported for various systems including PNIPAm gels, but is not universal for colloidal gels [108, 123–125]. Gisler *et al.* attributed this deformation behaviour in a low density fractal gel of PS particles to the winding structure of the strands [126]. Under large deformation, the strands would be straightened, which contributes to the increased rigidity of the gel, until the interparticle bonds break and shear thinning is observed [38, 126]. Whereas Gisler observed a constant value for  $G'$  until the onset of the strain hardening, colloidal gels of PNIPAm particles observed in this work and by Liao *et al.*, show a gradual strain hardening [125]. The onset of the strain hardening is very discrete in the DLCA gels from Gisler *et al.*, hence the gel structure probably consist of strands with a well-defined mesh size [126]. Within this model, it can be speculated that the gradual increase in strain hardening indicates a capricious structure with both long and short interconnected strands. Indeed, irregular loops and links were observed in the binarised volume. The origin of the strain hardening in gelating colloidal systems remains obscure, but the results indicate that the linear visco-elastic regime is sensitive to the gel structure.

## Temperature and salt concentration

The point at which a sample gels is strongly dependent on the interparticle attraction, which is dependent on both temperature and ionic strength. Both parameters will be shortly addressed in the context of the gel transition and to motivate the gelation conditions. From DLS measurements, the hydrodynamic radius as function of temperature was followed to determine the aggregation temperature  $T_a$ . At this value, the hydrodynamic radius increased, which indicates the onset of particle aggregation. The critical transition temperature or concentration was determined from frequency sweep rheology measurements at 1% deformation. The crossover from  $G'$  and  $G''$  is a widely accepted as an easy accessible measure for the point at which a system percolates, hence undergoes a critical transition [37].

The  $T_a$  was found to correlate with the critical transition temperature in a pure microgel system (Fig. 4.19). The  $T_a$  was nearly the same for pure and CS microgel particles, and corresponded to the VPTT (Fig. 4.19a). Within the resolution of the temperature, the  $T_a$  correlates directly with the critical transition temperature determined from the crossover of  $G'$  and  $G''$  (Fig. 4.19b).

The elastic modulus levelled off to a plateau value at approximately 10 °C above the critical transition temperature (Fig. 4.19b). As the measurement time was about 30 min per data point, other effects such as ageing and evaporation came into play, which were likely to contribute significantly to the increase in the elastic modulus far above the critical transition temperature.

Failure of M2 was observed at  $\phi^{50^\circ\text{C}} = 0.12$  for temperatures above 40 °C. A decrease in the elastic modulus was observed after which the sample remained phase separated after cooling down to room temperature (Fig.4.19b). This effect became more pronounced at higher salt concentration, and a decrease up to 2 orders of magnitude in  $G'$  was observed. Interestingly, after the almost complete failure of the gel structure, a slight recovery was observed at higher temperatures. The CS PNIPAm analogue CS21 did not exhibit failure at lower volume fraction and it is unknown whether the failure was a result of the sample properties, or the volume fraction.

The elastic modulus was measured as function of salt concentration, and a  $\phi^{50^\circ\text{C}} = 0.12$  of M1 was found to gelate between  $10^{-3}$  and  $5 \cdot 10^{-3}$  M KCl concentration. Below the gelation threshold, a fluid-cluster phase was observed with CLSM. The phase transitions from a fluid to a fluid-cluster, and further to a percolated gel phase were observed with increasing attraction. After percolation, an increase of an order of magnitude in the elastic modulus was observed from the gelation threshold to 0.1 M. The microgel phase behaviour is in line with existing work on colloidal gels (Fig. 2.13a), and exemplifies that the salt concentration is a good way to tune the interparticle attraction in a microgel gel [40].

## Time scale of gelation

The first gel transition was directly observed with CLSM in a period of 1-10 s upon heating to 40 °C. The transition of a fluid to a fluid-cluster phase was observed, which became arrested into a percolating gel structure. Large rearrangements were observed in the first 30 s, and the strands had limited mobility in the first minutes after percolation. The time scale probed with rheology was 10-20 s, which was too long to observe the gel transition. Liao *et al.* reported that the gelation time was highly dependent on weight percentage [37]. As the volume fraction was not given, a rough estimate could be made from the volume fraction per weight percentage collapsed microgel, which was found to deviate maximal 25% for M1-3. Extrapolation of the gelation time as function of the wt% of pure PNIPAm particles reported by Liao *et al.* suggests a value around 10 s for  $\phi^{50^\circ\text{C}} = 0.05$  for a temperature just above the VPTT, which is in qualitative agreement with the observations at 40 °C.

### 4.4.2 Sequential gels

The sequential gelation experiments were done about 5 °C above the  $T_a$ , i.e. 40 and 50 °C, as the strength of the gel was the least sensitive to temperature changes here. The samples were prepared at

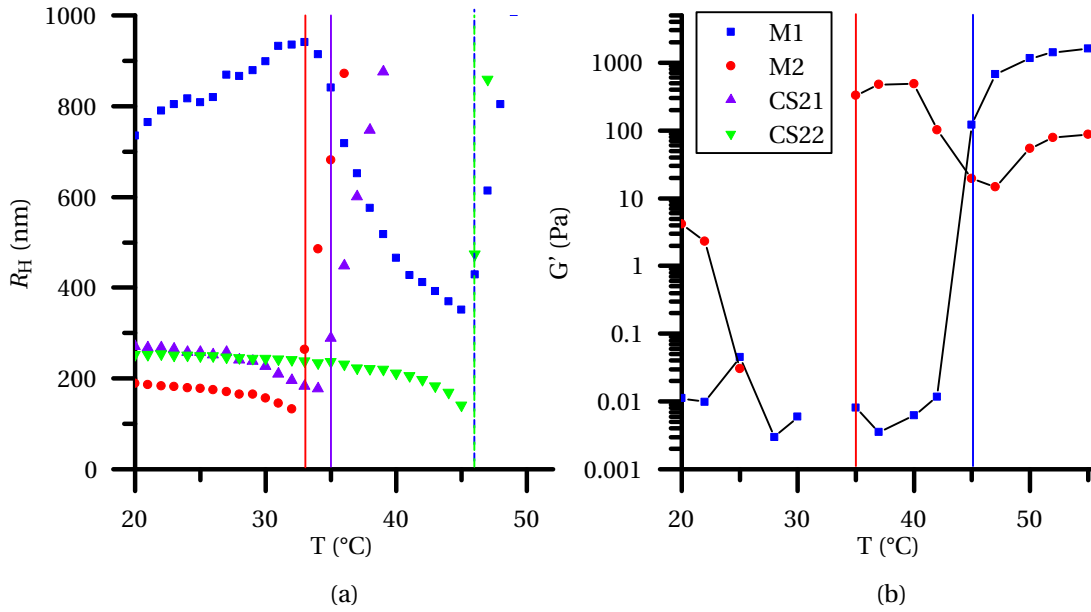


Figure 4.19: a): The hydrodynamic radius  $R_H$  as function of temperature for pure microgel and CS samples at 0.1 M as measured with DLS in dilute conditions. The aggregation temperature is indicated with a vertical mark. b): Elastic modulus  $G'$  was measured at a frequency of  $1 \text{ s}^{-1}$  and a strain of respectively 1% as function of temperature. The samples were measured at  $\phi^{50^\circ\text{C}} = 0.12$  with a salt concentration of 0.1 M KCl. Negative values could not be displayed. The critical transition temperature is indicated with a vertical mark and is in agreement with (a).

$\phi = 0.05$  to prevent irreversible aggregation, which was within the limit of arrested spinodal decomposition [92]. To exclude electrostatic interactions, a salt concentration of 0.1 M was chosen, which corresponded to an Debye length of 1 nm. Thus, a 1:1 ( $\phi/\phi$ ) binary mixture of CS21 and CS22 at a volume fraction of  $\phi_{\text{tot}}^{50^\circ\text{C}} = 0.05$  was used for the following results.

### Model for sequential gelation

The goal of the model is to capture the essential driving force of gelation in a qualitative way, after which the simulation outcome will be quantitatively analysed. The input values were chosen such that they have the same order of magnitude as the experimental system. The particles are modelled below the VPTT with a Hertzian potential with  $\varepsilon_H = 500k_B T$ , which describes the elastic properties of the particles at low salt concentration fairly well (Section 4.3.2). For simplicity, the effect of a higher ionic strength on the size and elasticity are neglected in this model. Above the VPTT, the particles are modelled as the sum of an Hertzian and short-ranged attraction potential with a diameter half of the value below the VPTT. The  $\varepsilon_H$  was  $5000k_B T$ . Zaccone *et al.* found a potential depth of  $12k_B T$  above the VPTT by quantifying the reversible aggregation in PNIPAm particles and relating this with the Kramers' formula for the rate of escape from a square-well potential [127]. This value was taken for  $\varepsilon_a$  with a  $\delta$  of 0.2 and could be varied to mimic different salt concentrations. Once the simulations have to be run quantitatively, the Likos potential can be used to model the electrostatic interactions.

The sequential gelation is modelled in three consecutive steps in which the particles have a different interaction potential. In the first step, both types are modelled below the VPTT. In the second step, one is type is modelled below, and the other above the VPTT. The  $\varepsilon_H$  and  $\varepsilon_a$  for the interaction between the different particle types are estimated with the Berthelot mixing rule [128]

$$\varepsilon_{ij} = \sqrt{\varepsilon_{ii}\varepsilon_{jj}}, \quad (4.4)$$

with  $\varepsilon_{ij}$  the value of an interaction between a particle  $i$  and  $j$ . In the third step, both particle types were modelled above the VPTT (Fig. 4.20). The particles final coordinates were used as input for the



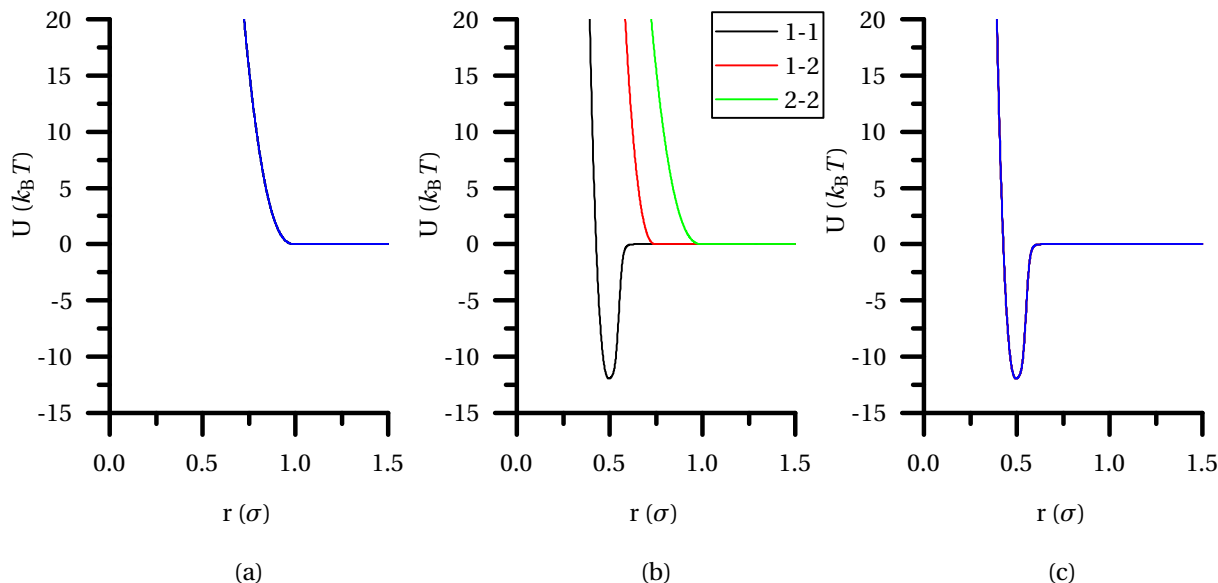


Figure 4.20: a-c): Pair potentials for a symmetrical binary system below the VPTTs (a), above the VPTT of the first particle type (b), and above the VPTT of the second particle type (c), referred to in the text as steps 1, 2, and 3. The interparticle distance  $r$  is given in the reduced unit  $\sigma$ , which is the diameter of the uncollapsed particles. The particles are modelled with  $\varepsilon_a = 12k_B T$ ,  $\delta = 0.2$ , and an  $\varepsilon_H$  of 500 and 5000  $k_B T$  respectively below and above the VPTT. All pair potentials were identical in (a) and (c), and were drawn in blue.

next simulation step. The different temperature in each step was implicitly taken into account via a different scaling of the energy in each step. The physical constants in the interaction potential were not corrected for the temperature.

### Structure and mechanical properties gel-gel transition

The second gelation step, i.e. gel-gel transition, was measured with rheology and via 3D reconstruction of  $z$ -stacked confocal images. The rheological moduli were measured over time as the temperature was increased from 40 to 50 °C. The inner network and full network were measured from 5 sets of  $z$ -stacks recorded 30 min after percolation by measuring the fluorescence from both particle types individually. Sequential gelation was observed over a couple of minutes. Brownian dynamics sequential gelation simulations were done with an interaction potential described above.

The transition was too fast to observe with rheology, and was not characterised by an onset period prior to gelation (Fig. 4.21). It was hard to determine whether there was an onset to the gelation, as there was a time delay between the plotted temperature and temperature in the sample. This taken into consideration, combined with the knowledge that the transition is fast, it could be concluded that no onset was present on the measured time scale.

The gel was found to become more rigid during the gel-gel transition, but the damping of the material remained the same (Fig. 4.21). Both the storage and loss modulus increased during the transition, which means that more energy is required for the same deformation, and could be interpreted as an increased rigidity of the gel structure.  $\tan \delta$  remained virtually the same, and the way the gel stores and dissipates energy was not strongly affected by the second gelation step.

**Homogeneous deposition** During the gel-gel transition, homogeneous deposition of the PNIPMAm particles was observed on the inner network, which served as scaffold for the gelation of the PNIPMAm. Deposition of particles on the existing gel occurred rather homogeneously without the formation of new strands (Fig. 4.22a). The bulges in the gel shell were likely to be initially present clusters, as their occurrence was rare. From the volume over surface ratio ( $V/S$ ), the increase in strand thickness

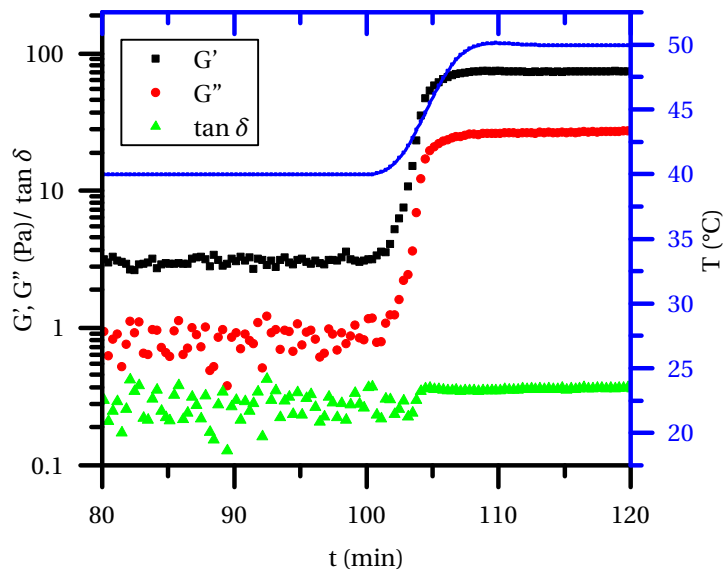


Figure 4.21: Rheological moduli and  $\tan \delta$  around the gel-gel transition. The temperature is indicated by the blue line, which is linked to the right y axis. A solvent trap with slightly moist dish cloth was used (set-up (B)). Neither an onset in the gel-gel transition nor rigorous changes in damping was observed.

Table 4.9: The indirectness and volume over surface ( $V/S$ ) for the binary and single particle samples 30 min after percolation. The  $z$ -stacks of the binary sample at 50 °C were measured in the same focal volume. The indirectness is defined as the path length from an edge node on one side of the focal volume to one at the other side along either the  $x$ - or  $y$ -direction, divided by the Euclidean distance between these nodes. The surface at the edge of the focal volume was not taken into account for the  $V/S$ .

Type	component(s)	T (°C)	Indirectness	$V/S$ ( $\mu\text{m}$ )
Binary	PNIPAm	40	2.69	0.49
Binary	PNIPAm	50	2.79	0.39
Binary	Both	50	2.34	0.47
Single	PNIPAm	50	2.58	0.30

could be approximated (Table 4.9). The gel branches could be modelled as interconnected cylinders with a radius  $R$ , leading to  $V/S = R/2$ . In this model, the average thickness would increase from 1.56 to 1.88  $\mu\text{m}$  in the gel-gel transition, which is about one particle diameter. This would correspond to a volume increase of  $\sim 1.5$ , which is physically acceptable considering the crudeness of the model, and the observation that a large fraction of the PNIPAm was still dispersed. As more particles took part of the gel network after the gel-gel transition, the rigidity increased, but the gel did not rigorously change structure hence the energy storage and dissipation of the gel remained the same.

Homogeneous deposition was not observed in sequential gelation simulations (Fig. 4.23). In the last step of the simulation, the second particle type formed slow moving clusters which collectively adhered to the existing gel network (Fig. 4.23b). An extensive study was done by Linse *et al.*, where they investigated the particle adsorption versus aggregation of particles and surface of the same material [129]. In equilibrium, they found only a narrow range of attraction strength where a fraction of the particles deposited on the surface. This was solely driven by geometric reasons, that is the maximization of bonds. At higher attraction, all particles aggregated, preferably on the surface, which served as nucleation point here. In experiment, some PNIPAm remained dispersed in solution even after 7 hours, which excludes complete particle aggregation. Since the adsorption was driven by geometry, no barrier was found for the formation of multiple layers in simulation, and monolayers were not observed after equilibration [129]. As calculated from the  $V/S$ , the decoration in the sequential gel was in the order of a monolayer thick, which is the maximum for a 1:1 stoichiometry. However,

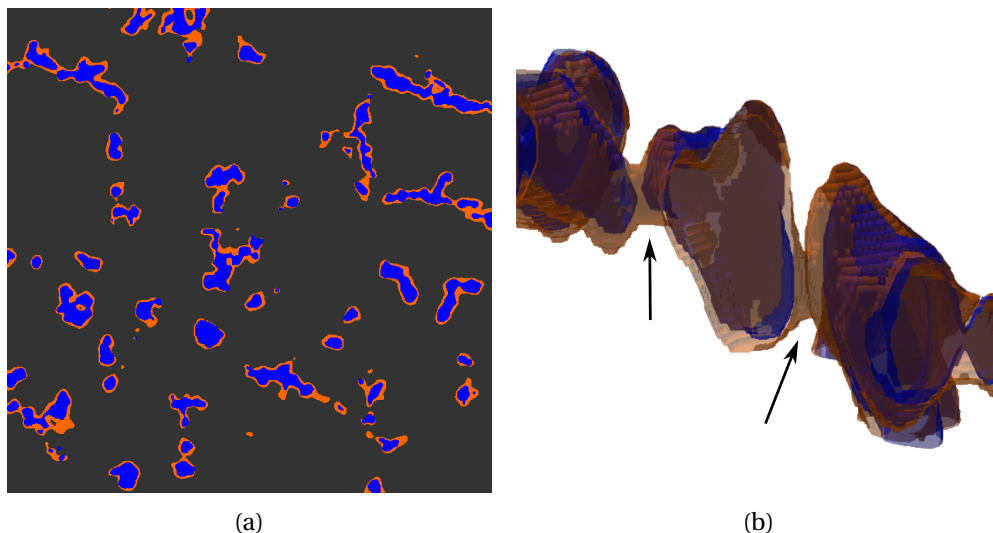


Figure 4.22: a): Overlay of the binarized confocal images of CS21 (blue) and CS22 (orange)  $7.5\ \mu\text{m}$  in the sample. The binary images were taken as slice in a 3D volume prior to cleaning (see Appendix F). b): Detail of the binary volume for CS21 (blue) and CS22 (orange), in which the newly formed links in the second gelation step are indicated with an arrow.

qualitatively, only monolayer decoration had been observed in experiments with a large excess of the second particle type. This suggests that a model with an equal attraction strength for all interparticle attractions, does not represent the experimental system properly. The attraction between the first and second species appears to be favoured over the interparticle attraction between the second species, which causes selective absorption on the existing gel structure. This can be a result of the gradual collapse of the second particle type, or the different density of the two particle types at the experimental temperatures. The increase in rheological moduli at increasing temperature in a single particle gel might also be caused by an increasing attraction strength with higher temperature, but it is unknown how this relates between PNIPAm and PNIPMAM. Intuitively, the attraction strength of PNIPAm would be stronger than PNIPMAM, because the PNIPAm particles are further collapsed at  $50\ ^\circ\text{C}$  (e.g. Fig. 4.11). Here, the particles would be denser, which would lead to stronger van der Waals attraction. The interparticle potential appears not to be trivial and should be further investigated to understand the decoration of the inner network, and to compare the rheological moduli of different (sequential) gels.

**Formation of new links** The formation of new links in the gel network has been observed, these new connections were formed as a result of the decoration of the inner network (Fig. 4.22b). Branches in each others proximity connect due to adhesion of a particle to both surfaces, which is likely to be preferred for geometrical reasons. These connections did not contribute significantly to the damping of the gel, because little were observed and the link only involved a small surface or number of particles. The new links could be quantified with the indirectness of the sample, which was calculated from the path length from an edge node on one side of the focal volume to one at the other side along either the  $x$ - or  $y$ -direction. This divided by the Euclidean distance between these nodes yields the indirectness, which becomes larger as the sample consists of less links. The indirectness of the inner network was found to be larger than the indirectness of the full network, which showed that new links were formed (Table 4.9).

#### 4.4.3 Physical ageing gel

In this section, the physical ageing shortly and long after percolation, respectively minutes and hours, will be discussed. As the rheological properties of the sample are likely to be dependent on the evap-

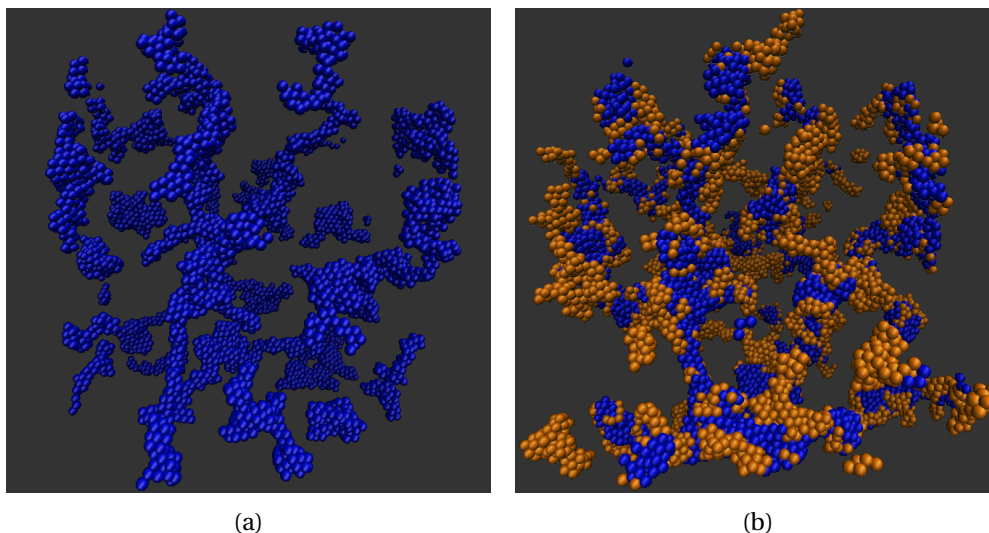


Figure 4.23: *a,b*): 3D plot of the particle coordinates for a simulated sequential gel sequence after the second step (a) and third step (b). The model described in this section was run for  $0.1 \tau_B$  in the first step, and  $100 \tau_B$  in the second and third steps. No homogeneous deposition was observed during the third step.

oration of the water in the sample, this was examined first.

In experiments concerning the sequential gel, a 1:1 ( $\phi/\phi$ ) binary mixture of CS21 and CS22 at a volume fraction of  $\phi_{\text{tot}}^{50^\circ\text{C}} = 0.05$  was used. For experiments concerning the instantaneous gel, a  $R_H^{50^\circ\text{C}} = 0.05$  single particle system of CS21 was used, which is identical to instantaneous gelation of the size-symmetrical binary mixture used to study sequential gelation.

### Evaporation in rheometer

The evaporation in the rheometer was monitored with a 80/20 glycerol/ $\text{H}_2\text{O}$  mixture, which viscosity is very sensitive to the water content. Since a glycerol/ $\text{H}_2\text{O}$  mixture is a Newtonian fluid, the viscosity remains constant over time in the absence of temperature and composition fluctuations. Upon evaporation of the water, the viscosity increases, while a decrease is observed upon dilution [130]. The sensitivity of the rheometer is 10 mPa·s, and the composition of the mixture was chosen such that it remained above this value. The viscosity at 20 °C was in good correspondence with the empirical formula for the viscosity of glycerol/ $\text{H}_2\text{O}$  mixtures derived by Cheng *et al.*, and deviated  $\sim 9\%$  at 50 °C [130]. In Fig A.7, three different set-ups were tried: one without solvent trap (A), one with a solvent trap equipped with single strip of slight moist cloth (B), and one equipped with three strips of wet cloth (C). The solvent trap saturated the air with water, which prevented water evaporation from the sample. At both 40 and 50 °C, an immediate increase in viscosity was observed in set-up (A), which was caused by the rapid evaporation of water. Interestingly, the viscosity decreased after some time at 40 °C as the sample diluted due to the strongly hygroscopic character of the glycerol. An opposite trend was observed in the set-ups with solvent trap, (B) and (C), where first a dilution of the sample was observed due to condensation of the water. A higher condensation rate was observed for set-up (C) as the amount of water released by the cloth unto the sample was much larger. Moreover, at 40 °C, a higher condensation rate was observed as well, because the equilibrium was more shifted to condensation at lower temperatures due to the high hygroscopicity of the glycerol. The minimum in the viscosity ( $t_{\text{evap}}$ ) indicated the moment when all water is evaporated from the cloth, and the air was not saturated with water any more.

The best balance between the lowest condensation rate and the longest  $t_{\text{evap}}$  was found for set-up (B) (Fig. A.7). At 40 °C,  $t_{\text{evap}}$  was found to be 10.5 hours at 50 °C, and 25.5 hours. In order to be on the safe side, the maximum measurement time for a sequential gelation experiment was chosen to be 10 hours. However, discrepancy was found with the microgel samples, as the condensation of water

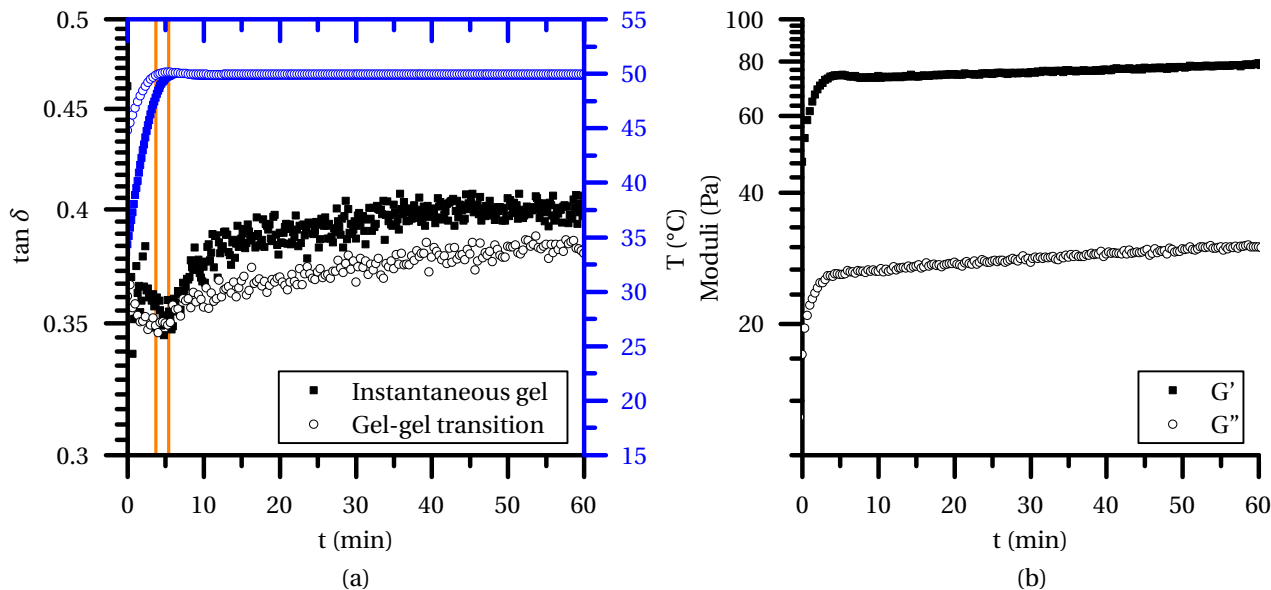


Figure 4.24: a):  $\tan \delta$  as function of time for a single particle gel (instantaneous gelation) and after the gel-gel transition of a sequential bigel at 50 °C. For the single particle gel, the time at which  $G'$  and  $G''$  crossed was chosen as  $t=0$ , and corresponds to the onset of percolation. The time at which  $G'$  started to increase was chosen as  $t=0$  for the sequential bigel. The temperature is indicated in blue, and makes the symbols in the legend. The orange vertical lines indicate the minimum in  $\tan \delta$ . b): Rheological moduli as function of time after the gel-gel transition of a bigel at 50 °C, with  $t=0$  the same as in (a).

due to the hygroscopicity of the glycerol did not occur here and evaporation was accelerated. In a microgel sample, divergence was observed from 4-6 hours depending on the measurement conditions, which was caused by the evaporation of the water.

### Rearrangements after percolation

Ageing was followed with rheology over time, which was compared to confocal images of a single particle gel and sequential bigel. The sequential gel was equilibrated at 40 °C for 90 min, before the gel-gel transition was induced by heating to 50 °C. In CLSM, the sample was equilibrated in the confocal chamber with the desired final temperature. No fundamental different ageing in the single particle and sequential bigel was observed. Around the onset of percolation, a minimum in the  $\tan \delta$  was observed after which the value levelled off for both the single particle gel and sequential gel (Fig. 4.24a). On an even shorter time scale, a compactification in the single particle gel was observed with CLSM over about 100 s (Fig. 4.25ab). No large compactification or rearrangements were observed after that, however discontinuous cluster rearrangements were observed throughout the sample (Fig. 4.25cd). A gradual increase in both moduli was observed over the full measurement range (up to 5 hours), together with a slight increase in damping (Fig. 4.24ab). These long-time ageing effects were strong compared to the evaporation effects discussed above, and was in line with the ageing observed by Appel *et al.* [38].

BD simulations of ageing colloidal gels with weak attraction have shown that percolation is within one Brownian time  $\tau_B$ , which would be in the order of milliseconds for the experimental system studied in this thesis [131]. d'Arjuzon *et al.* observed in their BD simulations three logarithmic regimes in the increase in the number of bonds per particle directly after percolation [132]. The first regime was in the order of  $10 \tau_B$ , which was ascribed to coarsening of thin strands. Since diffusion processes occur on the time scale of  $\tau_B$ , coarsening on a short time scale is expected to be driven by diffusion. On longer time scales, i.e. the third regime  $>200 \tau_B$ , these fast rearrangement processes must be largely inactive, otherwise the gel would fail immediately and equilibrium phases would form. d'Arjuzon *et al.* speculated that the increased rigidity of the strands make quick rearrangements with a low

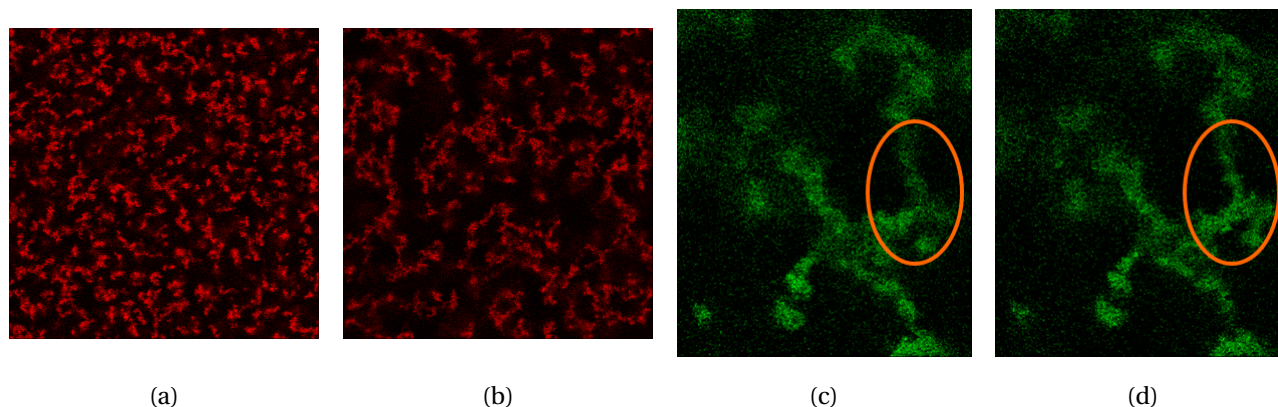


Figure 4.25: *a,b*): Confocal images of the single particle gel at 50 °C around percolation (*a*) and 100 s later (*b*) with a dimension of 54.1x54.1 nm. *c,d*): Zoom of confocal images at  $t=390$  (*c*) and  $t=395$  min after percolation (*d*) of the PNIPAm of the sequential bigel. Within the interval at which the frames were recorded (5 min), a rearrangement was observed in the area marked with an orange circle.

activation energy impossible as many bonds have to break and reform [132]. This slows down rearrangement processes, since it requires collective movement of particle clusters, which has a large activation energy.

**Thermally and mechanically activated rearrangements before temperature equilibration** The time scale of the coarsening observed in experiment was orders of magnitude larger than the most strongly rearranging regimes observed by d’Arjuzon *et al.* in BD simulations [132]. In CLSM, the observed compactification and rearrangements in the first 100 s were likely to be driven by the increase in temperature (Fig. 4.25ab). Increasing attraction, mechanical stress on the network due to further collapse of the microgel particles, and to a lesser extent higher thermal energy, constantly activate rearrangements as the temperature increases. The time scale of the compactification was in the same ballpark as that of the temperature equilibration in the confocal microscope. Similarly, the minimum in the damping correlated with the maximum in temperature both for the single particle and sequential gel (orange marks in Fig. 4.24a). The damping decreased, i.e. the elastic response of the material became stronger, as a result of increased attraction due to increasing temperature. This effect was slower than the rearrangements observed with confocal microscopy, which was in line the much slower temperature ramp in the rheometer (2.5 °C/min) than the equilibration time in the confocal microscope. This suggests that the resulting structure undergoes post-percolation modifications, or activated ageing, which complicates comparison between samples even further.

**Thermally activated rearrangements after temperature equilibration** Collective movement of the gel network and discontinuous cluster rearrangements were observed with confocal microscopy over the full time span of a 7 hours measurement (Fig. 4.25cd). As pointed out above, these rearrangements involve the collective displacement of clusters of particles due to geometrical reasons, which slow down over time as was observed in the rheological moduli (time beyond orange marks Fig. 4.24a and Fig. 4.24b). The rearrangements were likely to result in further compactification, which caused loss of elasticity as the network became denser.

#### 4.4.4 Temperature quench dependency

The indirectness and volume over surface was found to differ significantly for the inner PNIPAm network quenched to 40 and 50 °C, and the single particle system (Table 4.9). Two factors appear to be at stake, the interparticle attraction during the ASD and post-percolation modifications, which are

both controlled by the temperature quench. The speed of the quench, and thereby the attraction during the ASD could not be controlled very well in the confocal chamber, as the sample had to be quenched in the sample holder to prevent shear after gelation. Gibaud *et al.* showed that the attraction strength during the ASD sets the mesh size  $\xi$  independently of the volume fraction (Fig 2.13b) [100]. This would explain the different values for inner PNIPAm network quenched to 40 and 50 °C. Moreover, as the volume fraction of the single particle gel quenched to 50 °C was higher than the inner network of the bigel quenched to the same temperature, it should have a higher volume over surface, i.e. thicker strands. The contrary was observed, which suggests that also the temperature-induced rearrangements after ASD affect the structure, and that more control over the temperature is required in order to quantitatively compare samples.





---

## Conclusions and recommendations for future work

---

This thesis presents steps taken towards a good understanding of the relation between mechanical properties and morphology in (sequential) gels consisting of thermoresponsive PNIPAm and PNIPMAm microgel colloids. A better understanding of pure and core-shell microgel particle properties and synthesis was pursued in order to obtain a system suitable for both morphological and mechanical analysis.

Using a thermoresponsive polymer microgel system, it has been proven difficult to manufacture particles that can effectively be used to probe both morphology and mechanical properties, since poor control over particle characteristics during synthesis yields generally insufficient resolvability in imaging. Hence, a maximisation of the pure microgel particle size was pursued, and a systematic study in which the temperature, initiator injection speed, and presence of fluorescent dye was varied did not lead to size variations more than 20% at 20 °C. Another factor that reduced the resolvability was the insufficient fluorescent signal of the dyes and severe bleaching of the fluorescein O-methacrylate dye. Three-dimensional reconstructions of the gel structure were impossible with this system, and thermoresponsive polystyrene-NIPAm and NIPMAm core-shell particles were designed with a small highly fluorescent polystyrene core and multiple undyed shells to increase resolvability.

Microgel-functionalised PS cores were successfully synthesised, and the functionalisation was confirmed via their thermoresponsivity. Up to six microgel shells were grown over the functionalised cores, and particles with a hydrodynamic radius of maximal 440 nm were obtained. Aggregation and the formation of secondary nucleates limited the synthesis conditions to a low monomer to core surface ratio and low monomer concentration. Up to four microgel shells could be grown with a hydrodynamic radius of 400 nm at 20 °C in a single semi-batch synthesis. However, the reaction was very sensitive to secondary nucleation as the volume difference with the core-shell particles decreased in every step, which rendered purification by centrifugation practically impossible. Alternatively, the particles could be synthesised in multiple sequential batches with centrifugation rounds in between to remove small newly formed secondary nucleates, which extended the working synthesis conditions and resulted in secondary nucleate-free samples. Excellent control over size was achieved via scaling of the reactants with the core concentration determined with fluorescence spectroscopy, which was displayed for a size symmetrical binary system.

Control over colloidal stability appeared to be important to control the reaction outcome in pure and core-shell microgel syntheses. In the precipitation polymerisation model, the colloidal stability affects how easily microgel seed particles are formed, leading to a different amount of nuclei in the pure microgel synthesis, and formation of secondary nucleates during the shell synthesis. The hydrodynamic radii of the pure microgels and the formation of secondary nucleation during the shell synthesis could be qualitatively explained with this model. Better understanding could be achieved via experiments in which the colloidal stability could be tuned. The addition of an inert salt such as

KCl increases the screening of the charged initiator residues, which screens the electrostatic interaction between the precursor particles. In a surfactant free polymerisation, this factor only should affect the colloidal stability, and a lower colloidal stability is expected for increased salt concentrations. This could open the way to tune the size of the pure microgels towards a bigger size, and reduce secondary nucleation in a core-shell synthesis. However, it is unknown whether control over colloidal stability on its own is sufficient to manufacture particles large enough to be resolvable.

Confocal microscopy was the best method available to detect secondary nucleates, however, quantification of secondary nucleates was limited to the ones larger than the resolution limit of the confocal microscope. Alternative techniques such as transmission electron microscopy and field-flow fractionation have a higher resolution and are good candidates to give a reliable indication of presence of secondary nucleation.

In order to mimic the radial density profile of a pure microgel, the core-shell microgels were synthesised with a homogeneous higher crosslink density in the inner shells and a non-homogeneous crosslink density similar to pure microgels in the outer shell. Both the charge and temperature-dependent swelling of the pure and core-shell microgel particles were very similar. The higher crosslink density of the inner shell caused a broader swelling trajectory, but did not affect the pair potential probed in the fluid phase. In this regime, the radial distribution function was very similar to that of a pure microgel, and could be fitted with a Hertzian model with the same fitting parameters. In the fluid phase and under gel-forming conditions, the pure and core-shell microgels were virtually identical in behaviour and pair interactions.

Individual particle tracking was not possible with the largest core-shell particles, due to strong scattering of the polystyrene core and in less extent the collapsed microgel shell. Moreover, a small volume could be probed, which led to insufficient tracked particles to perform quantitative analysis. Both issues are an intrinsic property of the model system and analysis method, which limited the study to gel volumes without individual particle tracking. Large cores with a low refractive index mismatch are suggested as next generation model system to study sequential gelation. The collapsed microgel shell has a large refractive index mismatch with solvent, and the substitution of a core with a small refractive index mismatch such as PTFEMA/PTBEMA (see e.g. [4]) would greatly improve image quality, but is not sufficient on its own to exclude scattering. A large core with a thin shell would reduce this problem, however, the non-index matched microgel layer does need a minimum thickness to have sufficient van der Waals attraction. The particles will have a resolvable size with thermoresponsive properties, which makes this an improved model system over the ones presented in this thesis, but comparison with pure microgel systems is hard due to the different interaction potential.

The single particle gel had a capricious structure, which was directly observed in the binarised volume, and indirectly in the deformation sweep performed with mechanical rheology. The sequential gel had a qualitatively similar morphology before and after the gel-gel transition.

The damping of the gel remained the same during the gel-gel transition, which showed that the way the gel stores and dissipates energy was unaffected. A clear increase in the rheological moduli was found at the gel-gel transition, indicating an increased rigidity. These observations were explained with the change in morphology during the transition. The second particle type deposited homogeneously on the inner network, and created new links between nearby strands, which could be quantified with the volume over surface and the indirectness, respectively. The increased strand thickness resulted in a different bending and stretching of the gel structure, as both the resistance to stretching and bending increase with increased strand thickness. This resulted in the increase in moduli observed during the gel-gel transition, without severely affecting the damping. The strands in each others proximity connected due to adhesion of a particle to both surfaces, which is probably preferred for geometrical reasons. These connections did not contribute significantly to the damping of the gel, because only a few new links were formed and the connections involved a small surface and number of particles.

A model in with sequential gelation was simulated in discrete steps with an equal strength of

the attractive potential did not reproduce experimental observations. During the gel-gel transition, clusters formed which adhered to the existing gel network, and a non-homogeneous deposition was observed. This might be explained by a weaker attraction between the decorating particles, which can be a result of the gradual collapse or different density of the two particle types at the experimental temperatures. Worked was on software routines to convert the particle coordinates obtained by simulations into a binary volume, which could be analysed with the same software as the binarised confocal images. To study the interparticle interactions that drive sequential gelation, the next step would be to compare the experimental and simulated structures quantitatively, and to fit the model to experimental data.

The screening of the electrostatic interactions appears to be an excellent way to tune interparticle attraction and can be exploited to explore the gel mechanical properties as function of morphology and interparticle attraction. These gels can be modelled directly in Brownian Dynamics simulations with the benchmarked Likos potential, and could provide more insight in the role of the attraction strength on the sequential gelation.

Directly after percolation or the gel-gel transition, the damping of the single particle and sequential gel decreased probably due to increased attraction of the collapsing particles. The gel rearranged quickly and compacted severely before temperature equilibration, probably as a result of thermally and mechanically activated rearrangements driven by the increase in temperature. During longer periods of time after percolation, the structure slowly compacted further, often with large collective movements, striving to macroscopic phase separation. Due to this activated ageing, the structure of the single particle and sequential gels did not exhibit the trend in volume over surface expected based the mechanism of arrested spinodal decomposition, and the exact execution of the temperature quench appeared to be a determining factor in the resulting gel structure. A study on the effect of the temperature quench and interparticle attraction on the final gel structure would be a natural starting point for further research.



---

## Bibliography

---

- [1] E. Zaccarelli, *Journal of Physics: Condensed Matter* **2007**, *19*, 323101.
- [2] F. Varrato, L. Di Michele, M. Belushkin, N. Dorsaz, S. H. Nathan, E. Eiser, G. Foffi, *Proceedings of the National Academy of Sciences* **2012**, *109*, 19155–19160.
- [3] L. Di Michele, D. Fiocco, F. Varrato, S. Sastry, E. Eiser, G. Foffi, *Soft Matter* **2014**, *10*, 3633–3648.
- [4] J. Appel, N. de Lange, H. M. van der Kooij, T. van de Laar, J. B. ten Hove, T. E. Kodger, J. Sprakel, *Particle & Particle Systems Characterization* **2015**, *32*, 764–770.
- [5] D. F. Evans, H. Wennerstrom, *Colloidal domain*, 2nd ed., Wiley, **1999**.
- [6] A. van Blaaderen, A. Imhof, W. Kegel, G. J. Vroege, A. Philipse, *Soft Condensed Matter*, Van 't Hoff Laboratory, Utrecht University, **2015**.
- [7] B. Widom, *Science* **1967**, *157*, 375–382.
- [8] R. C. Evans, *An introduction to crystal chemistry*, CUP Archive, **1964**.
- [9] R. Zallen, *The Physics of Amorphous Solids*, Wiley, **2007**.
- [10] W. C. K. Poon, E. R. Weeks, C. P. Royall, *Soft Matter* **2012**, *8*, 21–30.
- [11] P. N. Pusey, W. Van Megen, *Nature* **1986**, *320*, 340–342.
- [12] W. G. Hoover, F. H. Ree, *The Journal of Chemical Physics* **1968**, *49*, 3609–3617.
- [13] P. N. Pusey, W. van Megen, *Physical Review Letters* **1987**, *59*, 2083.
- [14] P. N. Pusey, *Liquids freezing and the glass transition* **1991**, 763–942.
- [15] R. Huang, I. Chavez, K. M. Taute, B. Lukić, S. Jeney, M. G. Raizen, E.-L. Florin, *Nature Physics* **2011**, *7*, 576–580.
- [16] W. Götze, L. Sjögren, *Reports on progress in Physics* **1992**, *55*, 241.
- [17] E. Di Cola, A. Moussaïd, M. Sztucki, T. Narayanan, E. Zaccarelli, *The Journal of Chemical Physics* **2009**, *131*, 144903.
- [18] J. T. Padding, A. A. Louis, *Physical Review E* **2006**, *74*, 031402.
- [19] M. Radu, T. Schilling, *Europhysics Letters* **2014**, *105*, 26001.
- [20] G. L. Hunter, E. R. Weeks, *Reports on Progress in Physics* **2012**, *75*, 066501.
- [21] W. C. K. Poon, *Colloidal Suspensions*, Clarendon Press, **2012**.
- [22] J. Mattsson, H. M. Wyss, A. Fernandez-Nieves, K. Miyazaki, Z. Hu, D. R. Reichman, D. A. Weitz, *Nature* **2009**, *462*, 83–86.
- [23] H. Senff, W. Richtering, *The Journal of Chemical Physics* **1999**, *111*, 1705–1711.
- [24] J. Wu, B. Zhou, Z. Hu, *Physical Review Letters* **2003**, *90*, 048304.
- [25] D. Gottwald, C. N. Likos, G. Kahl, H. Löwen, *Physical Review Letters* **2004**, *92*, 068301.
- [26] P. S. Mohanty, D. Paloli, J. J. Crassous, E. Zaccarelli, P. Schurtenberger, *The Journal of Chemical Physics* **2014**, *140*, 094901.

- [27] E. Bianchi, R. Blaak, C. N. Likos, *Physical Chemistry Chemical Physics* **2011**, *13*, 6397–6410.
- [28] L. K. Månsson, J. N. Immink, A. M. Mihut, P. Schurtenberger, J. J. Crassous, *Faraday discussions* **2015**, *181*, 49–69.
- [29] P. J. Lu, D. A. Weitz, *Annu. Rev. Condens. Matter Phys.* **2013**, *4*, 217–233.
- [30] B. R. Saunders, B. Vincent, *Advances in Colloid and Interface Science* **1999**, *80*, 1–25.
- [31] D. Schmaljohann, *Advanced Drug Delivery Reviews* **2006**, *58*, 1655–1670.
- [32] T. R. Hoare, D. S. Kohane, *Polymer* **2008**, *49*, 1993–2007.
- [33] G. A. Somorjai, F. Tao, J. Y. Park, *Topics in Catalysis* **2008**, *47*, 1–14.
- [34] Y. Lu, S. Proch, M. Schrunner, M. Drechsler, R. Kempe, M. Ballauff, *Journal of Materials Chemistry* **2009**, *19*, 3955–3961.
- [35] R. H. Pelton, P. Chibante, *Colloids and Surfaces* **1986**, *20*, 247–256.
- [36] P. J. Yunker, K. Chen, M. D. Gratale, M. A. Lohr, T. Still, A. G. Yodh, *Reports on Progress in Physics* **2014**, *77*, 056601.
- [37] W. Liao, Y. Zhang, Y. Guan, X. X. Zhu, *Macromolecular Chemistry and Physics* **2011**, *212*, 2052–2060.
- [38] J. Appel, B. Fölker, J. Sprakel, *Soft Matter* **2016**, *12*, 2515–2522.
- [39] S. Manley, H. M. Wyss, K. Miyazaki, J. C. Conrad, V. Trappe, L. J. Kaufman, D. R. Reichman, D. A. Weitz, *Physical Review Letters* **2005**, *95*, 238302.
- [40] E. D. Gado, D. Fiocco, G. Foffi, S. Manley, V. Trappe, A. Zacccone, *Fluids Colloids and Soft Materials: An Introduction to Soft Matter Physics* **2016**, 279–292.
- [41] A. Stradner, H. Sedgwick, F. Cardinaux, W. C. K. Poon, S. U. Egelhaaf, P. Schurtenberger, *Nature* **2004**, *432*, 492–495.
- [42] F. Cardinaux, T. Gibaud, A. Stradner, P. Schurtenberger, *Physical Review Letters* **2007**, *99*, 118301.
- [43] R. Mezzenga, P. Schurtenberger, A. Burbidge, M. Michel, *Nature Materials* **2005**, *4*, 729–740.
- [44] Q. Wang, L. Wang, M. S. Detamore, C. Berkland, *Advanced Materials* **2008**, *20*, 236–239.
- [45] B. Xie, R. L. Parkhill, W. L. Warren, J. E. Smay, *Advanced Functional Materials* **2006**, *16*, 1685–1693.
- [46] H. M. Wyss, E. V. Tervoort, L. J. Gauckler, *Journal of the American Ceramic Society* **2005**, *88*, 2337–2348.
- [47] A. Einstein, *Annalen der physik* **1906**, *324*, 371–381.
- [48] A. Einstein, *Annalen der Physik* **1905**, *322*, 549–560.
- [49] *Diffusion*, MIT OpenCourseWare, **2009**.
- [50] A. P. Philipse, *Notes on Brownian Motion*, Debye Institute, Utrecht University, **2011**.
- [51] W. Sutherland, *The London Edinburgh and Dublin Philosophical Magazine and Journal of Science* **1905**, *9*, 781–785.
- [52] N. Sultanova, S. Kasarova, I. Nikolov, *Acta Physica Polonica-Series A General Physics* **2009**, *116*, 585.
- [53] B. W. Garner, T. Cai, S. Ghosh, Z. Hu, A. Neogi, *Applied Physics Express* **2009**, *2*, 057001.
- [54] J. Sprakel, R. Fokkink, *Research Methods Biomolecules & Interfaces*, Leerstoelgroep Fysische Chemie & Kolloïdkunde, Wageningen University, **2013**.
- [55] I. D. Block, F. Scheffold, *Review of Scientific Instruments* **2010**, *81*, 123107.
- [56] J. N. Immink, MA thesis, Lund University, **2014**.

- [57] D. B. Murphy, M. W. Davidson, *Fundamentals of light microscopy and electronic imaging*, 2nd ed., Wiley, **2013**.
- [58] J. C. Crocker, D. G. Grier, *Journal of Colloid and Interface Science* **1996**, *179*, 298–310.
- [59] M. C. Jenkins, S. U. Egelhaaf, *Advances in Colloid and Interface Science* **2008**, *136*, 65–92.
- [60] K. R. Spring, T. J. Fellers, M. W. Davidson, Resolution and Contrast in Confocal Microscopy, **2012**, <http://www.olympusmicro.com/primer/techniques/confocal/resolutionintro.html>.
- [61] J. B. Pawley, *Handbook of biological confocal microscopy*, Springer, **2006**.
- [62] T.-C. Lee, R. L. Kashyap, C.-N. Chu, *CVGIP: Graphical Models and Image Processing* **1994**, *56*, 462–478.
- [63] K. Saeed, M. Tabędzki, M. Rybnik, M. Adamski, *International Journal of Applied Mathematics and Computer Science* **2010**, *20*, 317–335.
- [64] G. K. Batchelor, *Journal of Fluid Mechanics* **1977**, *83*, 97–117.
- [65] Malvern Instruments Ltd., Ed., Zetasizer Nano User Manual, **2007**.
- [66] D. Frenkel, B. Smit, C. F. Chabalowski, Molecular simulation, **2002**.
- [67] R. van Roij, *Soft Condensed Matter Theory*, Institute for Theoretical Physics, Utrecht University.
- [68] S. Corporation, Ed., LAMMPS Documentation, <http://lammps.sandia.gov/doc/Manual.html>.
- [69] R. Pelton, *Advances in Colloid and Interface Science* **2000**, *85*, 1–33.
- [70] R. Pelton, *Journal of Colloid and Interface Science* **2010**, *348*, 673–674.
- [71] D. Duracher, A. Elaïssari, C. Pichot, *Journal of Polymer Science Part A: Polymer Chemistry* **1999**, *37*, 1823–1837.
- [72] A. Pich, W. Richtering in *Chemical Design of Responsive Microgels*, Springer, **2010**, pp. 1–37.
- [73] W. McPhee, K. C. Tam, R. Pelton, *Journal of Colloid and Interface Science* **1993**, *156*, 24–30.
- [74] A. Elaïssari in *Handbook of Surface and Colloid Chemistry*, Taylor & Francis Group, **2009**.
- [75] C. S. Chern, *Progress in Polymer Science* **2006**, *31*, 443–486.
- [76] P. J. Feeney, D. H. Napper, R. G. Gilbert, *Macromolecules* **1984**, *17*, 2520–2529.
- [77] D. Duracher, F. Sauzedde, A. Elaïssari, A. Perrin, C. Pichot, *Colloid and Polymer Science* **1998**, *276*, 219–231.
- [78] M. Dulle, S. Jaber, S. Rosenfeldt, A. Radulescu, S. Förster, P. Mulvaney, M. Karg, *Physical Chemistry Chemical Physics* **2015**, *17*, 1354–1367.
- [79] A. Rauh, T. Honold, M. Karg, *Colloid and Polymer Science* **2016**, *294*, 37–47.
- [80] H. Senff, W. Richtering, C. H. Norhausen, A. Weiss, M. Ballauff, *Langmuir* **1999**, *15*, 102–106.
- [81] J. J. Crassous, M. Siebenbürger, M. Ballauff, M. Drechsler, O. Henrich, M. Fuchs, *The Journal of Chemical Physics* **2006**, *125*, 204906.
- [82] R. Higler, J. Appel, J. Sprakel, *Soft Matter* **2013**, *9*, 5372–5379.
- [83] J. J. Crassous, M. Siebenbürger, M. Ballauff, M. Drechsler, D. Hajnal, O. Henrich, M. Fuchs, *The Journal of Chemical Physics* **2008**, *128*, 204902.
- [84] M. Stieger, W. Richtering, J. S. Pedersen, P. Lindner, *The Journal of Chemical Physics* **2004**, *120*, 6197–6206.
- [85] S. Meyer, W. Richtering, *Macromolecules* **2005**, *38*, 1517–1519.
- [86] X. Wu, R. H. Pelton, A. E. Hamielec, D. R. Woods, W. McPhee, *Colloid and Polymer Science* **1994**, *272*, 467–477.

- [87] F. Scheffold, P. Díaz-Leyva, M. Reufer, N. B. Braham, I. Lynch, J. L. Harden, *Physical Review Letters* **2010**, *104*, 128304.
- [88] R. Acciaro, T. Gilányi, I. Varga, *Langmuir* **2011**, *27*, 7917–7925.
- [89] E. J. W. Verwey, J. T. G. Overbeek, J. T. G. Overbeek, *Theory of the stability of lyophobic colloids*, Courier Corporation, **1999**.
- [90] T. Colla, C. N. Likos, *Molecular Physics* **2015**, *113*, 2496–2510.
- [91] J. N. Israelachvili, *Intermolecular and surface forces: revised third edition*, Academic press, **2011**.
- [92] P. J. Lu, E. Zaccarelli, F. Ciulla, A. B. Schofield, F. Sciortino, D. A. Weitz, *Nature* **2008**, *453*, 499–503.
- [93] M. G. Noro, D. Frenkel, *The Journal of Chemical Physics* **2000**, *113*, 2941–2944.
- [94] D. Paloli, P. S. Mohanty, J. J. Crassous, E. Zaccarelli, P. Schurtenberger, *Soft Matter* **2013**, *9*, 3000–3004.
- [95] D. Paloli, J. J. Crassous, P. Mohanty, E. Zaccarelli, P. Schurtenberger, *Royal Society of Chemistry* **2010**, **unpublished**.
- [96] M. E. Cates, M. Fuchs, K. Kroy, W. C. K. Poon, A. M. Puertas, *Journal of Physics: Condensed Matter* **2004**, *16*, S4861.
- [97] R. Klein, P. Meakin, *Nature* **1989**, 339.
- [98] D. A. Weitz, J. S. Huang, M. Y. Lin, J. Sung, *Physical Review Letters* **1985**, *54*, 1416.
- [99] G. Foffi, C. De Michele, F. Sciortino, P. Tartaglia, *The Journal of Chemical Physics* **2005**, *122*, 224903.
- [100] T. Gibaud, P. Schurtenberger, *Journal of Physics: Condensed Matter* **2009**, *21*, 322201.
- [101] M. Carpineti, M. Giglio, *Physical Review Letters* **1992**, *68*, 3327.
- [102] Y. Gao, J. Kim, M. E. Helgeson, *Soft Matter* **2015**, *11*, 6360–6370.
- [103] T. A. Witten Jr, L. M. Sander, *Physical Review Letters* **1981**, *47*, 1400.
- [104] P. Meakin, *Physical Review Letters* **1983**, *51*, 1119.
- [105] R. C. Ball, D. A. Weitz, T. A. Witten, F. Leyvraz, *Physical Review Letters* **1987**, *58*, 274.
- [106] P.-G. De Gennes, *Scaling concepts in polymer physics*, Cornell university press, **1979**.
- [107] A. H. Krall, D. A. Weitz, *Physical Review Letters* **1998**, *80*, 778.
- [108] W.-H. Shih, W. Y. Shih, S.-I. Kim, J. Liu, I. A. Aksay, *Physical Review A* **1990**, *42*, 4772.
- [109] H. Wu, M. Morbidelli, *Langmuir* **2001**, *17*, 1030–1036.
- [110] A. D. Dinsmore, D. A. Weitz, *Journal of Physics: Condensed Matter* **2002**, *14*, 7581.
- [111] L. Cipelletti, S. Manley, R. C. Ball, D. A. Weitz, *Physical Review Letters* **2000**, *84*, 2275.
- [112] V. K. Singh, A. Anis, I. Banerjee, K. Pramanik, M. K. Bhattacharya, K. Pal, *Materials Science and Engineering: C* **2014**, *44*, 151–158.
- [113] D. Legland, K. Kiêu, M.-F. Devaux, *Image Analysis & Stereology* **2011**, *26*, 83–92.
- [114] M. Kerschnitzki, P. Kollmannsberger, M. Burghammer, G. N. Duda, R. Weinkamer, W. Wagermaier, P. Fratzl, *Journal of Bone and Mineral Research* **2013**, *28*, 1837–1845.
- [115] M. Fasolo, P. Sollich, *Physical Review Letters* **2003**, *91*, 068301.
- [116] O. L. J. Virtanen, W. Richtering, *Colloid and Polymer Science* **2014**, *292*, 1743–1756.
- [117] D. Duracher, F. Sauzedde, A. Elaïssari, C. Pichot, L. Nabzar, *Colloid and Polymer Science* **1998**, *276*, 920–929.



- [118] M. Karg, S. Prévost, A. Brandt, D. Wallacher, R. von Klitzing, T. Hellweg in *Intelligent Hydrogels*, Springer, **2013**, pp. 63–76.
- [119] G. Yohannes, J. Shan, M. Jussila, M. Nuopponen, H. Tenhu, M. Riekkola, *Journal of Separation Science* **Mar. 2005**, *28*, 435–442.
- [120] E. A. Grulke, E. H. Immergut, J. Brandrup, *Polymer handbook*, Wiley, **1999**.
- [121] M. Parrinello, A. Rahman, *Physical Review Letters* **1980**, *45*, 1196.
- [122] B. R. Saunders, *Langmuir* **2004**, *20*, 3925–3932.
- [123] C. J. Rueb, C. F. Zukoski, *Journal of Rheology (1978-present)* **1997**, *41*, 197–218.
- [124] M. M. O. Eleya, S. Ko, S. Gunasekaran, *Food Hydrocolloids* **2004**, *18*, 315–323.
- [125] W. Liao, Y. Zhang, Y. Guan, X. Zhu, *Langmuir* **2012**, *28*, 10873–10880.
- [126] T. Gisler, R. C. Ball, D. A. Weitz, *Physical Review Letters* **1999**, *82*, 1064.
- [127] A. Zaccone, J. J. Crassous, B. Béri, M. Ballauff, *Physical Review Letters* **2011**, *107*, 168303.
- [128] D. Berthelot, *Comptes Rendus* **1898**, *126*, 1703–1706.
- [129] P. Linse, H. Wennerström, *Soft Matter* **2012**, *8*, 2486–2493.
- [130] N.-S. Cheng, *Industrial & Engineering Chemistry Research* **2008**, *47*, 3285–3288.
- [131] K. G. Soga, J. R. Melrose, R. C. Ball, *The Journal of chemical physics* **1998**, *108*, 6026–6032.
- [132] R. J. M. d'Arjuzon, W. Frith, J. R. Melrose, *Physical Review E* **2003**, *67*, 061404.
- [133] D. A. Weitz, H. Gang, D. Pine, J. X. Zhu, D. J. Durian, *Physica Scripta* **1993**, *1993*, 610–621.
- [134] F. Scheffold, S. E. Skipetrov, S. Romer, P. Schurtenberger, *Physical Review E* **2001**, *63*, 061404.
- [135] T. G. Mason, D. A. Weitz, *Physical Review Letters* **1995**, *74*, 1250.
- [136] D. A. Weitz, D. J. Pine, W. Brown, *New York: Oxford University Press* **1993**, *16*, 652.
- [137] R. Carminati, R. Elaloufi, J.-J. Greffet, *Physical Review Letters* **2004**, *92*, 213903.
- [138] S. Romer, F. Scheffold, P. Schurtenberger, *Physical Review Letters* **2000**, *85*, 4980.
- [139] P. Zakharov, F. Cardinaux, F. Scheffold, *Physical Review E* **2006**, *73*, 011413.
- [140] LSInstruments, Ed., Experimental Guidelines - DWS Sample Preparation, [http://www.lsinstruments.ch/technology/diffusing\\_wave\\_spectroscopy\\_dws/dws\\_experimental\\_guidelines/](http://www.lsinstruments.ch/technology/diffusing_wave_spectroscopy_dws/dws_experimental_guidelines/).
- [141] M. Philipp, R. Aleksandrova, U. Müller, M. Ostermeyer, R. Sanctuary, P. Müller-Buschbaum, J. K. Krüger, *Soft Matter* **2014**, *10*, 7297–7305.
- [142] T. A. Waigh, *Reports on Progress in Physics* **2005**, *68*, 685.
- [143] L. G. Wilson, A. W. Harrison, A. B. Schofield, J. Arlt, W. C. K. Poon, *The Journal of Physical Chemistry B* **2009**, *113*, 3806–3812.
- [144] LSInstruments, Ed., Microrheology, [http://www.lsinstruments.ch/technology/diffusing\\_wave\\_spectroscopy\\_dws/microrheology/](http://www.lsinstruments.ch/technology/diffusing_wave_spectroscopy_dws/microrheology/).
- [145] B. W. Mansel, M. A. K. Williams, P. J. Patty, S. Keen, Y. Hemar, *A Practical Review of Microrheological Techniques*, INTECH Open Access Publisher, **2013**.
- [146] E. Sarmiento-Gomez, B. Morales-Cruzado, R. Castillo, *Applied Optics* **2014**, *53*, 4675–4682.
- [147] N. Otsu, *Automatica* **1975**, *11*, 23–27.



## Supplementary figures

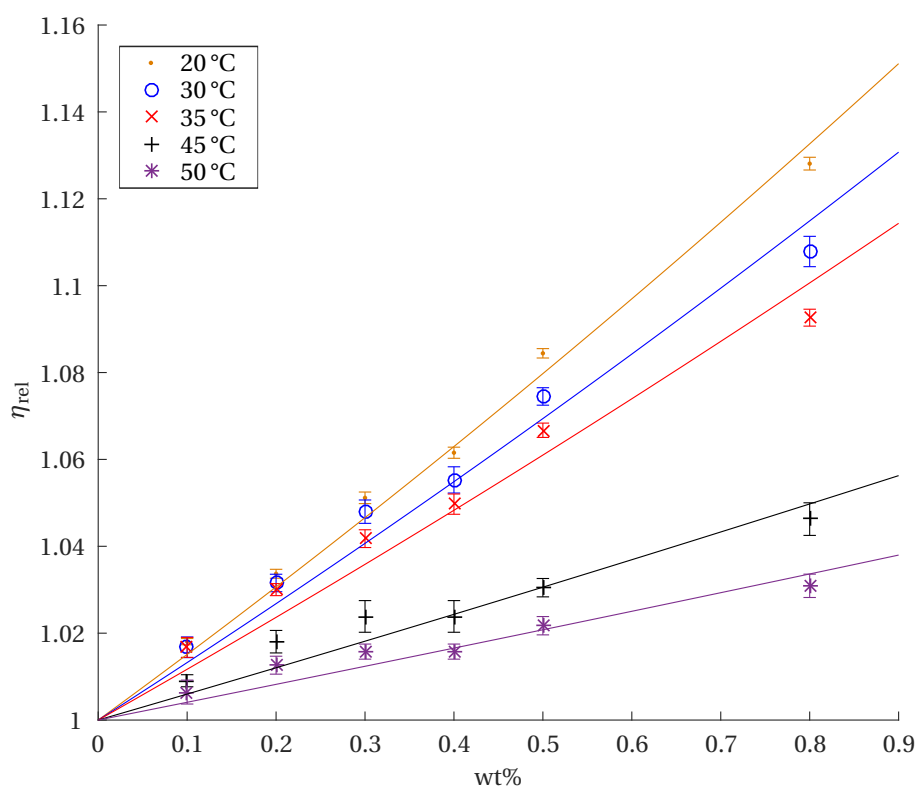


Figure A.1: Fit of the viscometry measurements with Eq. 2.29 of sample M1. The standard error of the mean in the relative viscosity  $\eta_{rel}$  is indicated with the error bars. An average shift factor  $k = 0.0395$  was found.

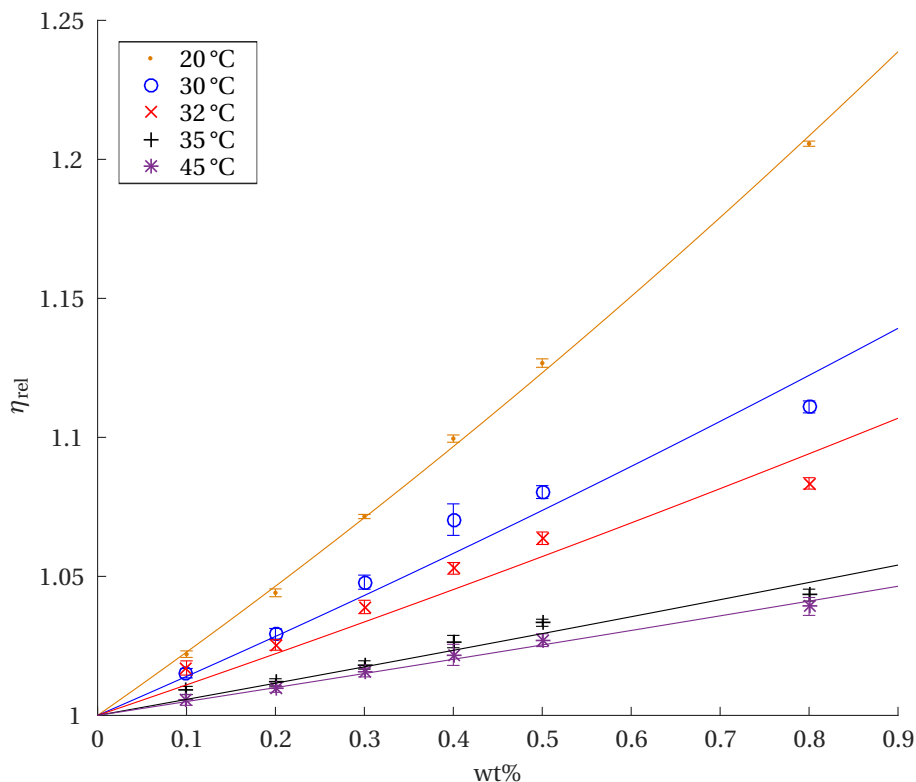


Figure A.2: Fit of the viscometry measurements with Eq. 2.29 of sample M2. The standard error of the mean in the relative viscosity  $\eta_{rel}$  is indicated with the error bars. An average shift factor  $k = 0.0462$  was found.

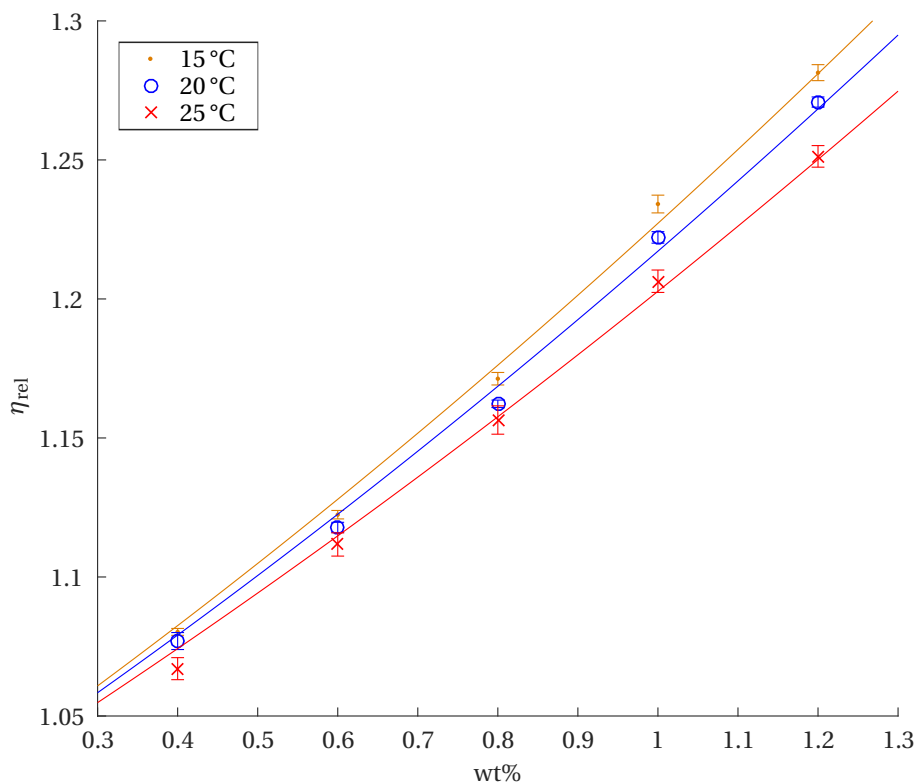
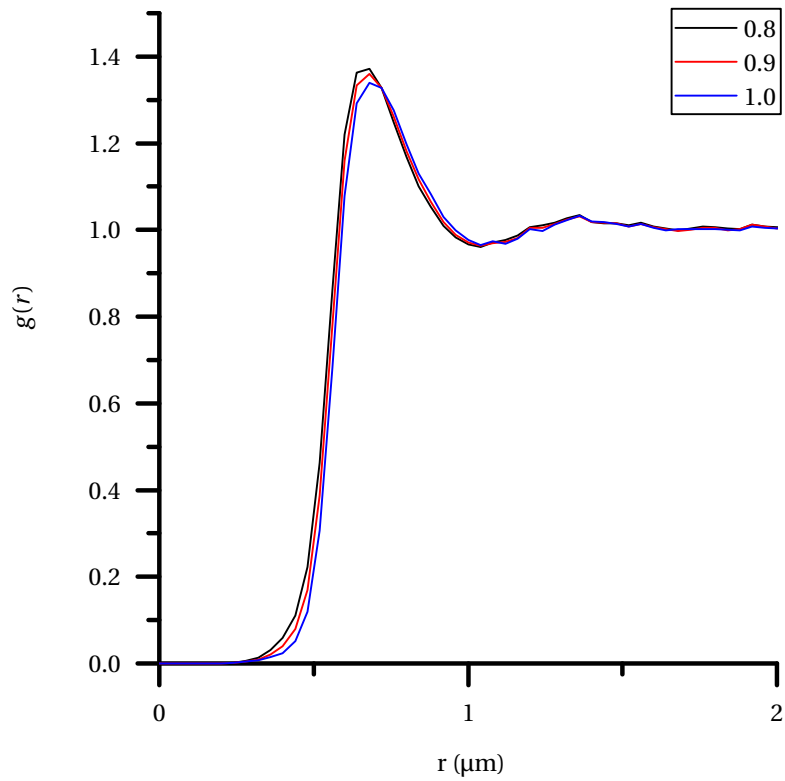
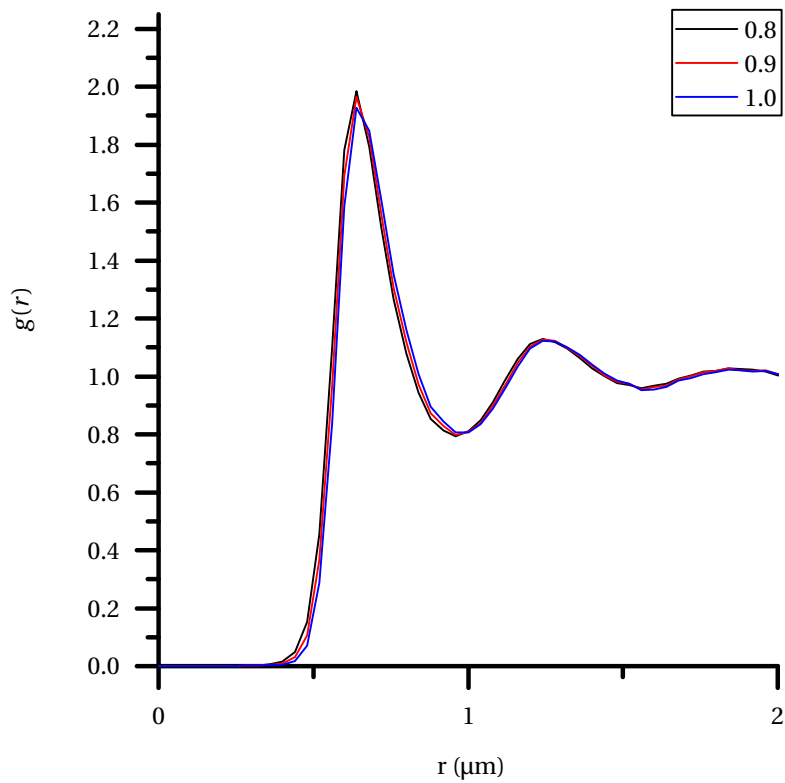


Figure A.3: Fit of the viscometry measurements with Eq. 2.29 of sample M3. The standard error of the mean in the relative viscosity  $\eta_{rel}$  is indicated with the error bars. An average shift factor  $k = 0.0735$  was found.



(a)



(b)

Figure A.4: Radial distribution function  $g(r)$  of CS21 at  $\phi = 0.22$  (a) and  $\phi = 0.42$  (b) recorded at 20 °C. The  $g(r)$  has been rendered with a bin size of 0.04  $\mu\text{m}$ , which roughly corresponds to the resolution. Data symbols were omitted for clarity. The particles were tracked at 0.8, 0.9, and 1.0 of mean integrated intensity, which correlated with a decrease in the first peak height.

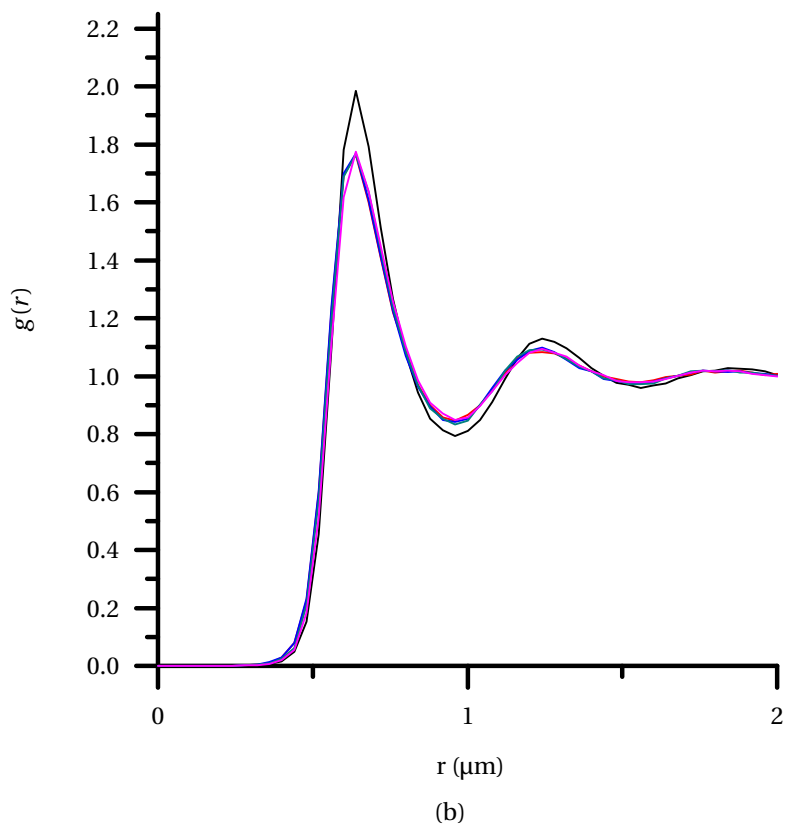
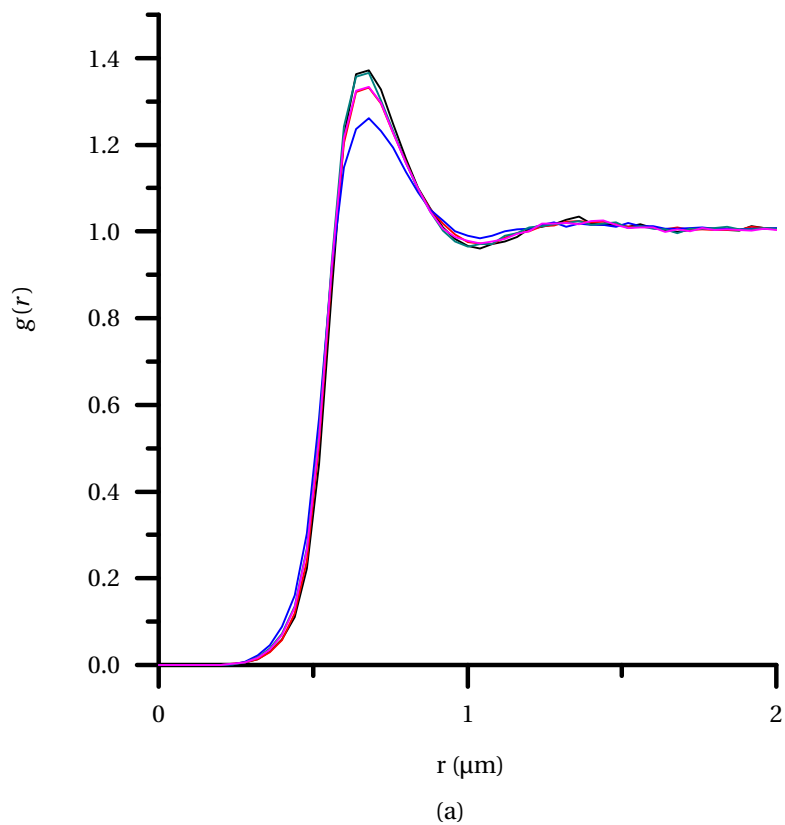
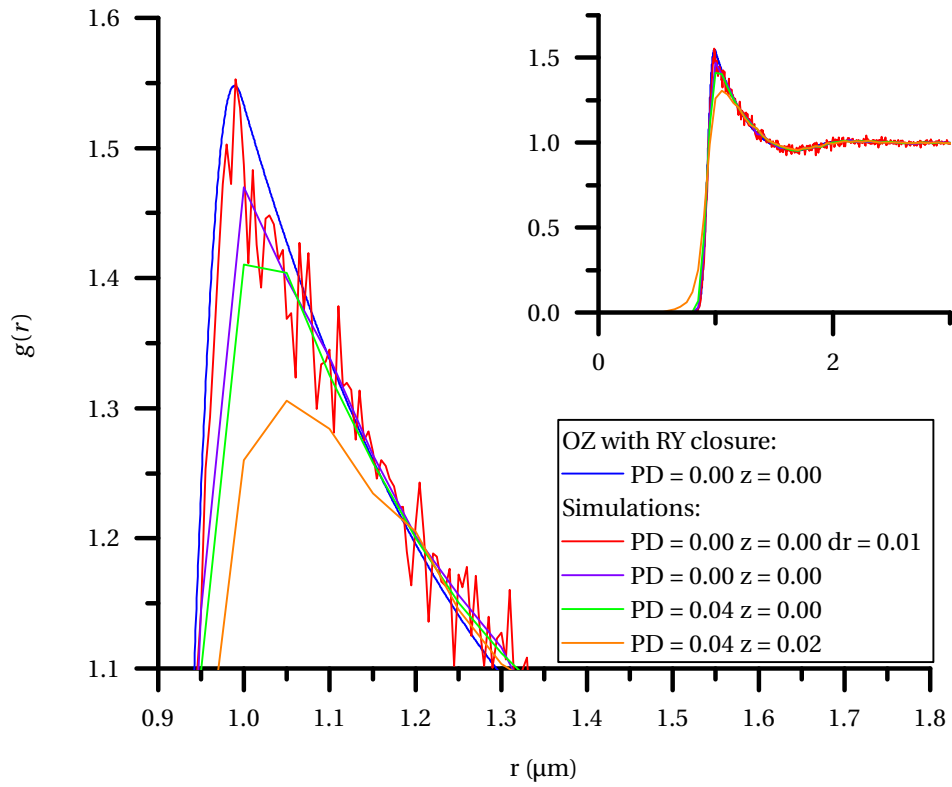
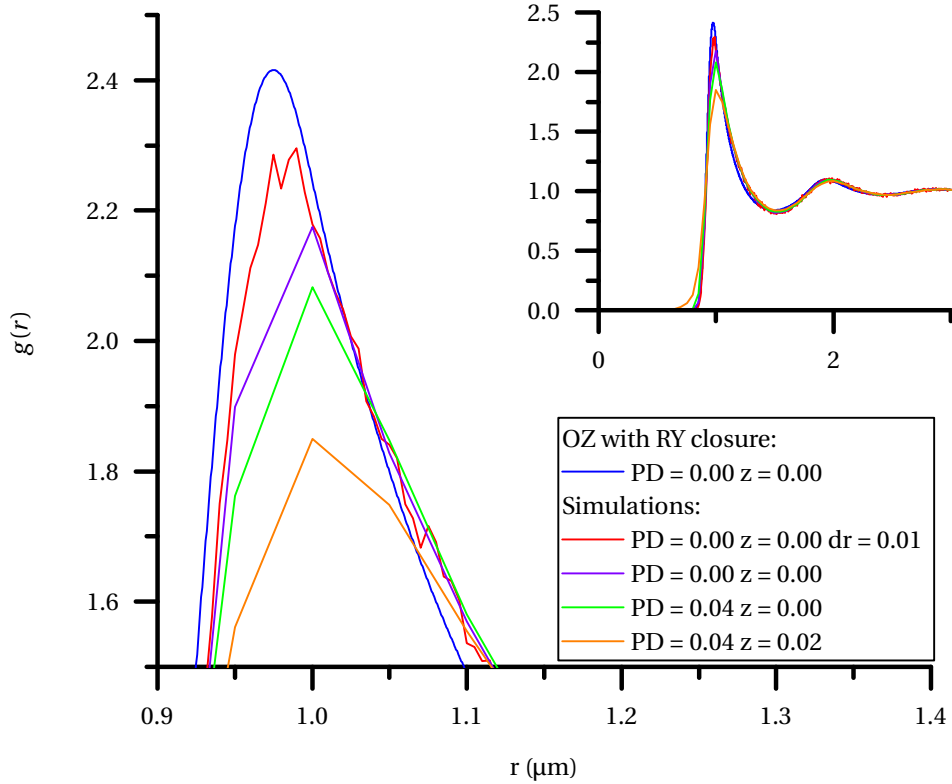


Figure A.5: Radial distribution function  $g(r)$  of CS21 at  $\phi = 0.22$  (a) and  $\phi = 0.42$  (b) recorded at 20 °C. The  $g(r)$  has been rendered with a bin size of  $0.04 \mu\text{m}$ , which roughly corresponds to the resolution. Data symbols were omitted for clarity. The samples were taken at five spots throughout the sample. Three (a) and two (b) distinct populations can be observed.



(a)



(b)

Figure A.6: Zoom of the first peak of the radial distribution function  $g(r)$  of a particle with a Hertzian potential (Eq. 2.44) with  $\varepsilon_H = 520k_B T$  at  $\phi = 0.22$  (a) and  $\phi = 0.43$  (b). Results are shown for the Ornstein-Zernike (OZ) with Roger-Young (RY) closure, and MD simulations with various parameters. PD indicates the polydispersity,  $z$  the  $z$ -noise and  $dr$  the bin size (standard is 0.05). M. Bergman is gratefully acknowledged for the simulations and N. Boon for the OZ with RY closure.

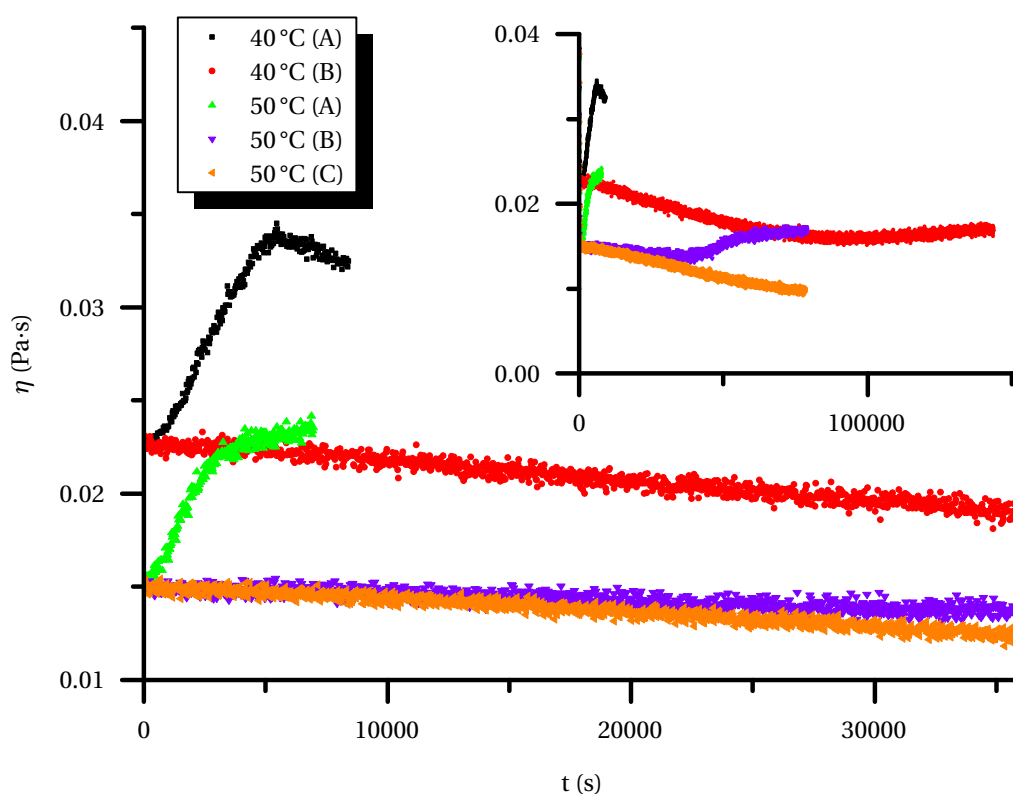


Figure A.7: The viscosity of a 80/20 (w/w) glycerol/MQ- $H_2O$  mixture at 40 and 50°C over time. The viscosity was continuously measured in a dynamical shear measurement with a strain of 100% at  $1\text{ s}^{-2}$ . The evaporation and condensation of water was monitored via the change in viscosity of the sample. Set-up (A) was an open set-up without a solvent trap, set-up (B) was built of a plastic cover with one strip of slightly moist dish cloth, and set-up (C) was made as (B) with 3 strips of wet dish cloth. The data is shown up to 10 hours and the long-time viscosity trends are shown in the inset.



---

## Diffusing-wave spectroscopy

---

Diffusing-wave spectroscopy (DWS) is a coherent scattering technique based on multiple scattering. The path of a multiple scattered photon can be approximated as a diffusion process to extract information about the scatterers in a medium. Both in DLS and DWS, the intensity autocorrelation function is calculated from which the mean-squared displacement (MSD) can be extracted. However, DWS has an order of magnitude better resolution, i.e. sub nanometer displacements, because the photons are scattered multiple times and thus requires a smaller contribution per scatterer to cause detectable interference [133]. This high resolution makes it possible to study slow or non-ergodic samples such as gels, and to indirectly measure the elastic and loss moduli of these systems [134, 135].

### Theory

Like DLS, the intensity fluctuation of a speckle will first be parametrized by their autocorrelation function Eq. 2.14 and the autocorrelation function of the scattered fields Eq. 2.15. The path of a photon through the sample can be treated as a random walk, however this is an approximation and breaks down in some cases. Other (numerical) attempts have been made to get around this so called diffusion approximation [136, 137]. When one assumes that the path is uncorrelated with the other paths, only the contribution of a single path has to be evaluated. These paths can be added at the detector assuming that all interference that contributes to the final signal only comes outside the sample. The following equation can be obtained for a scattering path with  $n$  scatterers

$$g_1^n(\tau) = \exp \left[ -2 \left( \frac{\tau}{\tau_0} \right) \left( \frac{s}{l^*} \right) \right] \quad (\text{B.1})$$

with  $\tau_0 = 1/k_0^2 D_0$  being the characteristic time scale dependent on the diffusion constant  $D_0$  and the wavevector of the incident light  $k_0$ . The first part of the exponent in Eq. B.1 accounts for the decay in correlation due to a single scattering event averaged over all scattering vectors and weighed by the form factor of the particle. The second part of the exponent in Eq. B.1 reflects the effects of multiple scattering, where  $l^*$  is the transport mean free path being the distance over which a photon must travel before its direction is randomised. The longer the path, the smaller the movement of individual particles is required to cause interference in the order of the wavelength of the laser. To obtain the full autocorrelation function, the sum has to be taken over all paths weighed by their probability  $P(s)$  yielding

$$g_1 = \int_0^\infty P(s) \exp \left[ -2 \left( \frac{\tau}{\tau_0} \right) \left( \frac{s}{l^*} \right) \right] ds \quad (\text{B.2})$$

which can be solved for different geometries. The results are fairly complex, but are in excellent agreement with experimental data [133]. From the theoretical fit of the autocorrelation function of the

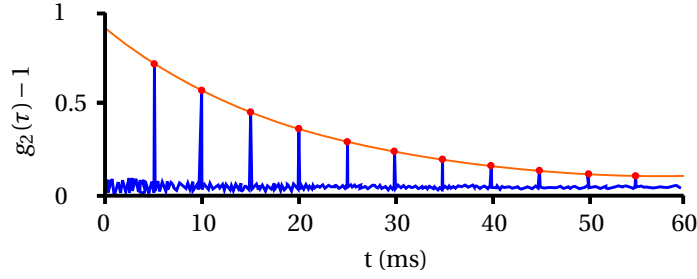


Figure B.1: Schematic of the intensity autocorrelation function (blue) modulated by the spin echoes of a rotating diffuser with a period of 5 ms. The sample autocorrelation function (red) can be derived from the height or surface below the spin echo peaks.

scattered fields  $g_1$ , the characteristic time  $\tau_0$  can be extracted, which provides the diffusion constant from which the mean square displacement  $\langle \Delta r^2(\tau) \rangle$  can be calculated. Moreover, this MSD can be used as input to obtain rheological properties of the system via microrheology (Subsection B).

## Method

In the simplest set-up, a coherent laser beam is sent into the sample and the backscattered or transmitted light is detected by a optoelectronic device as a function of time. The incoming laser beam must be very coherent to ensure that the observed intensity fluctuations can be fully accounted to the diffusion of the particles. Since the average position in non-ergodic samples such as gels is almost fixed, the assumption that the time averaged correlation is as the ensemble averaged correlation does not hold any more [134, 138]. A digital charged coupled device or other camera allows the measurement of many speckles at the same time which enables real-time ensemble averaging. However this method is only restricted to longer correlation times, due to the limited time resolution of the detector. Traditional single mode detection is required for a full range correlation function [139]. Another way to correctly average the experimental data is to rotate the sample to obtain data from different speckles. However, mechanical stress on the sample during a measurement is often undesired. Another method is based on the fact that if an ergodic medium is added in the path of the non-ergodic sample, the combination can still be considered as ergodic [134, 138]. The autocorrelation functions of the non-ergodic  $g_2^{(S)}(\tau) - 1$  sample, the diffusive ergodic medium  $g_2^{(E)}(\tau) - 1$ , and the one that is measured  $g_2^{(M)}(\tau) - 1$  are related via the multiplication rule [134]

$$g_2^{(M)}(\tau) - 1 = \left[ g_2^{(E)}(\tau) - 1 \right] \left[ g_2^{(S)}(\tau) - 1 \right]. \quad (\text{B.3})$$

The autocorrelation function of the sample can be obtained if the one of the ergodic system is known. The diffusive medium could either be a second cell with an ergodic medium or a slowly rotating diffuser [134, 138]. In order to increase the sampling speed, the slowly rotating diffusive ground glass can be replaced by fast rotating one in a two cell (TCDWS) set-up. Every time the diffuser completes a full circle, a peak in the correlation function appears which is called an echo, and the technique is therefore called echo-TCDWS. The peak height, or more robust, the peak area can be taken as a single sample for the autocorrelation function at that lag time. With a high speed rotating diffuser, many samples can be taken in a short amount of time, and the first 1000 echoes can be correlated with the following ones to acquire sufficient statistics. In this way, a measurement is recorded in almost real time [139].

The transport mean free path  $l^*$  can be measured with the instrument or calculated with Mie theory. The length of the cuvette  $L$  should be much larger than  $l^*$  to guarantee multiple scattering, i.e.  $7 < l^*/L < 30$ . Both concentration and cuvette length can be varied to achieve this ratio [140]. Since

the refractive index of the PNIPAM colloids is temperature dependent, this determination should be done at the experiment temperature [141].

### Microrheology

While a rheometer measures bulk quantities, local information about the viscosity and elasticity can be obtained with microscopic and spectroscopic techniques. These techniques are collectively termed microrheology [20, 142]. The movement of a (colloidal) tracer particle, which can either be introduced artificially or be part of the system itself, is followed and the rheological properties of the fluid are measured. This movement can be induced thermally (passive) or externally with magnetic or optical tweezers (active) [142, 143].

The concept of (passive) microrheology can be understood in the following way. The magnitude of the displacement driven by Brownian motion is related to the bond strength between the neighbouring particles. Here, a bond between the particles can be modelled as a spring. A higher spring constant, which represents a stronger interparticle force, yields a more constrained movement of the particles, since the thermal energy is not sufficient to stretch the spring enormously. On the contrary, a lower spring constant will result in larger displacements with the same thermal energy available. At longer time scales, the system is arrested and does not move on average and  $D_L = 0$ . The MSD versus time will reach a plateau value for the MSD, which is related to the spring constant of the system.

The long time MSD is the input parameter from which the storage and loss moduli can be derived. This parameter can be obtained from e.g. video microscopy measurements and diffusing-wave spectroscopy [110, 144]. The Generalised Stokes-Einstein equation containing the viscoelasticity as a frequency dependent viscosity can be used, being [135]

$$G^*(\omega) = \frac{k_B T}{\pi R i \omega \langle \Delta r^2(i\omega) \rangle} = G'(\omega) + iG''(\omega), \quad (\text{B.4})$$

which is analogous to the Einstein equation (Eq. 2.2).  $G^*(\omega)$  is the complex rheological modulus containing a real part  $G'$ , which is the storage modulus, and an imaginary part  $G''$ , which is the loss modulus. These parameters are dependent on the radius  $R$  of the tracer particle and the frequency [144, 145]. In this way, local rheological measurements can be done in a small sample volume.

### Experimental

DWS was performed with a home-made set-up in transmission geometry operated with LS instruments Rheolab 7.1.3 software. The set-up was equipped with a CrystalLaser DL660-050-S 50 mW 660 nm diode-pumped solid-state laser. Temperature control was achieved with two Peltier thermo blocks.

It was observed by M. Bergman and T. Gating that the correlation function was strongly dependent on the concentration of dissolved rhodamine dye. Absorption effects can be corrected for, which is beyond the scope of this project, and motivated the use of mechanical rheology with a small geometry [146].



---

## List of performed syntheses

---

A list of the reactants used in the syntheses discussed in the thesis are given in this appendix. The specifics of the PNIPAm and PNIPMAm microgel syntheses can be found in Table C.1, the PS core syntheses in Table C.2, and the PS-PNIPAm and PS-PNIPMAm core-shell syntheses in Table C.3.

Table C.1: A list of the reactants used in all relevant microgel syntheses. The volume in brackets in the columns KPS and dye is the amount of Milli-Q water in which the material is dissolved and added to the solution. These volumes are not included in the volume Milli-Q (MQ) water displayed in the last column.

#	Set-up	Monomer	(g)	BIS (mg)	KPS (mg)	Dye	(mg)	SDS (mg)	MQ (mL)
M1	B	NIPMAm	10.0	608	99.6 (10mL)	MRB	12.0 (20mL)	52.1	400
M2	B	NIPAm	10.1	679	49.0 (10mL)	FOM	10.1 (19mL)	-	420
M3	A	NIPMAm	10.0	609	50.0 (10mL)	MRB	10.1 (20mL)	49.3	400
M4.1	A	NIPAm	2.52	168	25.7 (2.5mL)	FOM	2.4 (5mL)	-	101
M4.2	A	NIPAm	2.53	168	25.7 (2.5mL)	FOM	2.4 (5mL)	-	101
M4.3	A	NIPAm	2.5	168	25.0 (2.5mL)	FOM	2.4 (5mL)	-	101
M4.4	A	NIPAm	2.5	168	25.0 (2.5mL)	-	-	-	105

Table C.2: A list of the reactants used in all relevant PS core syntheses. The volume in brackets in the column KPS is the amount of Milli-Q water in which the material is dissolved and added to the solution. This volume is not included in the volume Milli-Q (MQ) water displayed in the last column. The column denoted with 'purif.' indicates the method of purification, which can either be centrifugation (C) or dialysis (D).

#	Monomer	(g)	Styrene (g)	KPS (mg)	Dye	(mg)	SDS (mg)	MQ (g)	purif.
C1	NIPAm	3.00	27.1	51.8 (2mL)	PM 546	22.1	199	100	C
C2	NIPMAm	3.02	27.0	54.5 (2mL)	PM 605	21.9	200	99	C
C3	NIPMAm	2.99	27.1	49.7 (2mL)	PM 605	22.5	200	100	D
C4	NIPAm	3.00	27.0	49.3 (2mL)	PM 546	22.2	201	101	D

Table C.3: A list of the reactants used in all relevant core-shell syntheses. The volume in brackets is the amount of Milli-Q water in which the reactant is dissolved and added to the solution. This volume is not included in the volume Milli-Q (MQ) water. The suffix '-S' indicates the shell, if relevant, and its number. The type of synthesis of a multi-shell particle can either be the batch (B) or semi-batch (SB) method. The  $t_{KPS}$  indicates the time over which the KPS was added, where 0 minutes means that the KPS solution was injected at once.

#	Type	Core	(mg)	MQ (mL)	Monomer	(g)	BIS (mg)	BIS feed (mg)	KPS (mg)	$t_{KPS}$ (min)
CS1		EMC3	814	151	NIPMAm	3.50	200	99.1 (5mL)	10.2 (1mL)	0
CS2		EMC3	107	20.3	NIPMAm	0.512	46.2	-	2.7 (1mL)	0
CS3-S1	B	EMC3	441	80.0	NIPMAm	0.199	12.0	-	7.6 (4mL)	7
CS3-S2					NIPMAm	0.176	10.5	-	7.2 (3.5mL)	15
CS3-S3					NIPMAm	0.176	10.6	-	7.3 (3.5mL)	7
CS4		EMC3	435	79.8	NIPMAm	0.502	30.4	-	8.2 (3.5mL)	10
CS5		EMC3	441	79.8	NIPAm	0.181	12.3	-	8.4 (2mL)	12
CS6		EMC3	394	78.0	NIPAm	1.08	283	-	43.5 (1.25mL)	5
CS7		EMC3	382	80.5	NIPAm	1.08	279	-	82.1 (1.25mL)	0
CS8		EMC3	138	300	NIPAm	0.406	26.4	-	33.0 (1mL)	3
CS9		EMC3	338	148	NIPAm	1.02	65.9	-	43.7 (1.4mL)	3
CS10		EMC3	65.7	149	NIPMAm	0.234	13.3	-	17.0 (0.5mL)	2
CS11		EMC4	343	147	NIPMAm	1.15	67.8	-	41.8 (1.25mL)	2
CS12-S1	B	EMC4	261	147	NIPAm	1.03	69.0	34.8 (7mL)	42.2 (1.25mL)	2
CS12-S2					NIPAm	0.986	66.8	34.3 (7mL)	40.1 (1.25mL)	2
CS12-S3					NIPAm	0.955	65.3	38.6 (7mL)	38.6 (1.25mL)	2
CS13-S1	SB	EMC4	63.6	150	NIPAm	0.257	17.3	9.3 (5mL)	10.3 (1.5mL)	2
CS13-S2					NIPAm	0.493 (5mL)	35.0 (2mL)	16.9 (5mL)	19.9 (1.5mL)	2
CS13-S3					NIPAm	0.957 (12mL)	64.9 (3mL)	-	39.6 (1.5mL)	2
CS14-S1	SB	EMC4	63.6	150	NIPMAm	0.255	17.3	9.0 (2.5mL)	10.4 (1.25mL)	2
CS14-S2					NIPAm	0.257 (3mL)	17.1 (1mL)	8.7 (2.5mL)	10.0 (1.25mL)	2
CS14-S3					NIPAm	0.238 (3mL)	16.7 (1mL)	-	9.6 (1.25mL)	2
CS15-S1	SB	EMC4	31.8	75.3	NIPAm	0.1262	8.8	4.3 (1.25mL)	5.4 (1.25mL)	2
CS15-S2					NIPAm	0.235 (6mL)	16.0	8.1 (1.25mL)	9.9 (1.25mL)	2
CS15-S3		50% CS15S-2			NIPAm	0.220 (12mL)	14.5	-	8.6 (1.25mL)	2
CS16	B	50% CS15S-3			NIPAm	0.11	7.5	-	4.8 (1.25mL)	2

Table C.3: A list of the reactants used in all relevant core-shell syntheses. The volume in brackets is the amount of Milli-Q water in which the reactant is dissolved and added to the solution. This volume is not included in the volume Milli-Q (MQ) water. The suffix '-S' indicates the shell, if relevant, and its number. The type of synthesis of a multi-shell particle can either be the batch (B) or semi-batch (SB) method. The  $t_{KPS}$  indicates the time over which the KPS was added, where 0 minutes means that the KPS solution was injected at once.

#	Type	Core	(mg)	MQ (mL)	Monomer	(g)	BIS (mg)	BIS feed (mg)	KPS (mg)	$t_{KPS}$ (min)
CS17-S1	SB	EMC4	85.9	200	NIPAm	0.3407	22.7	11.4 (5mL)	14.5 (1.0 mL)	2
CS17-S2					NIPAm	0.380 (11mL)	40.1	20.1 (5mL)	24.5 (1.0mL)	2
CS17-S3					NIPAm	0.334 (7mL)	23.3	11.3 (5mL)	13.8 (1.0mL)	2
CS18-S1	SB	EMC5	566	400	NIPAm	1.814	122	61.7 (20mL)	13.8 (4mL)	2
CS18-S2					NIPAm	1.8 (80mL)	122	61.2 (20mL)	74.2 (4mL)	2
CS18-S3					NIPAm	1.8 (80mL)	122	62.0 (20mL)	72.7 (4mL)	2
CS18-S4					NIPAm	1.8 (80mL)	122	60.3 (20mL)	75.4 (4mL)	2
CS19-S1	SB	EMC4	566	400	NIPMAm	2.04	123	61.7 (20mL)	74.9 (4mL)	2
CS19-S2					NIPMAm	2.0 (80mL)	122	61.0 (20mL)	73.3 (4mL)	2
CS19-S3					NIPMAm	2.0 (80mL)	122	61.4 (20mL)	73.6 (4mL)	2
CS19-S4					NIPMAm	2.02 (81mL)	121	-	72.6 (4mL)	2
CS19-S5	SB	CS19-S4	463	401	NIPMAm	1.64 (80mL)	99.1	50.5 (20mL)	59.7 (4mL)	2
CS19-S6					NIPMAm	1.65 (80mL)	99.5	-	59.6 (4mL)	2
CS20-S1	SB	EMC5	328	400	NIPAm	1.81	123	61.7 (20mL)	74.2 (4mL)	2
CS20-S2					NIPAm	1.8 (80mL)	122	61.8 (20mL)	73.7 (4mL)	2
CS20-S3					NIPAm	1.8 (80mL)	122	60.7 (20mL)	73.7 (4mL)	2
CS20-S4					NIPAm	1.8 (80mL)	122	60.5 (20mL)	73.3 (4mL)	2
CS21-S1	B	EMC4	254	146.5	NIPAm	1.02	69.4	34.9 (10mL)	42.0 (2mL)	2
CS21-S2					NIPAm	0.86	58.4	35.0 (2mL)	2	
CS22-S1	B	EMC5	145	145.9	NIPMAm	1.02	61.8	36.4 (10mL)	36.4 (2mL)	2
CS22-S2					NIPMAm	0.70	42.6	25.1 (2mL)	2	





---

## Protocols

---

### D.1 Protocol PS cores

#### Chemicals

- 3 g *N*-Isopropylacrylamide (NIPAm) [0.26 M] / 3 g *N*-Isopropylmethacrylamide (NIPMAm) [0.23 M] (monomer)
- 50 mg potassium peroxydisulfate (KPS) [1.8 mM]
- 27 g styrene [2.5 M]
- 200 mg sodium dodecyl sulfate (SDS) [6.9 mM]
- 22 mg pyrromethene 546 [0.82 mM] (green-) / 22 mg pyrromethene 605 [0.57 mM] (red fluorescent dye)
- 100 g Milli-Q H<sub>2</sub>O
- Aluminium oxide

#### Protocol

- Transfer the Milli-Q H<sub>2</sub>O into a 250 mL round bottom flask and purge for 30 minutes with nitrogen at room temperature
- Build set-up with the 250 mL round bottom flask, oil bath, nitrogen flow and straight cooler
- Run styrene over an aluminium oxide column (to remove inhibitor)
- Transfer the microgel monomer, styrene, SDS, and fluorescent dye to the flask and purge under vigorous stirring for 45 minutes Cover flask with aluminium foil.
- Purge with nitrogen at 75 °C for 15 minutes
- Dissolve KPS in 2 mL Milli-Q H<sub>2</sub>O and degas with nitrogen
- Initiate reaction by quickly adding the KPS with a syringe into the reaction mixture @400 rpm stirring
- Proceed for 24 hours
- Filter particles with glass wool
- Purify by means of dialysis over a 2 week period

## D.2 Protocol CS19

### Chemicals

- 3.56 g EMC4 15.9 wt% functionalised cores [0.566 g cores]
- 2.04 g (1) *N*-Isopropylmethacrylamide (NIPMAm) [0.038 M]
- 123.3 mg (1.1), 61.7 g (1.2) *N,N'*-methylenebisacrylamide (BIS) [5%, 2.5% crosslinking] in 20 mL (1.2)
- 74.0 mg (1) potassium peroxodisulfate (KPS) in 4.0 mL Milli-Q H<sub>2</sub>O [0.68 mM]
- 400 g (1) Milli-Q H<sub>2</sub>O

### Protocol shell 1

- Build set-up with a 1 L vessel, nitrogen flow and straight cooler
- Transfer ~360 mL of the Milli-Q H<sub>2</sub>O (1) into the 1 L three-neck round bottom flask and purge for 30 min with nitrogen at room temperature
- Transfer the NIPMAm (1) and BIS (1.1) to the flask and rinse with the remaining Milli-Q H<sub>2</sub>O (1)
- Weigh functionalised cores in flask
- Purge with nitrogen under vigorous stirring at 75 °C for 45 minutes
- Dissolve KPS (1) in Milli-Q H<sub>2</sub>O and degas
- Dissolve BIS (1.2) in Milli-Q H<sub>2</sub>O by heating to 60 °C and degas
- Initiate reaction by adding the KPS (1) with a syringe into the reaction mixture @400 rpm stirring over a period of 2 minutes
- Proceed for 5 minutes after start KPS addition, and add BIS (1.2) solution over a period of 30 minutes with a syringe pump and 2 10 mL syringes
- Proceed for 1.5 hours
- Take 1 mL sample with a syringe
- Proceed for 2 hours hours
- Take 1 mL sample with a syringe

### Chemicals shell 2

- 2.03 g (2) *N*-Isopropylmethacrylamide (NIPMAm)
- 122.8 mg mg (2.1), 61.4 mg (2.2) *N,N'*-methylenebisacrylamide in 20 mL (2.2) Milli-Q H<sub>2</sub>O
- 73.6 mg (2) potassium peroxodisulfate (KPS) in 4.0 mL Milli-Q H<sub>2</sub>O

### Protocol shell 2

- Purge NIPMAm (2), BIS (2.1) and 80 g Milli-Q H<sub>2</sub>O in a 250 mL flask with straight cooler, stirring, and nitrogen flow at room temperature for 45 minutes (solution 2)
- Dissolve KPS (2) in Milli-Q H<sub>2</sub>O and degas
- Dissolve BIS (2.2) in Milli-Q H<sub>2</sub>O by heating to 60 °C and degas
- Heat solution 2 to 60 °C, check for flocculation, and immediately take 80 mL in 2 60 mL syringes and inject above the reaction mixture simultaneously over approx. 2 minutes
- Initiate reaction by adding the KPS (2) with a syringe into the reaction mixture @400 rpm stirring over a period of 2 minutes
- Proceed for 5 minutes after start KPS addition, and add BIS (2.2) solution over a period of 30 minutes with a syringe pump and 2 10 mL syringes
- Proceed for 1.5 hours
- Take 1 mL sample with a syringe
- Proceed for 2 hours hours
- Take 1 mL sample with a syringe

**Chemicals shell 3**

- 2.02 g (3) *N*-Isopropylmethacrylamide (NIPMAm)
- 122.3 mg (3.1), 61.1 mg (3.2) *N,N'*-methylenebisacrylamide (BIS) in 20 mL (3.2) Milli-Q H<sub>2</sub>O
- 73.3 mg (3) potassium peroxydisulfate (KPS) in 4.0 mL Milli-Q H<sub>2</sub>O

**Protocol shell 3**

- Purge NIPMAm (3), BIS (3.1) and 80 g Milli-Q H<sub>2</sub>O in a 250 mL flask with straight cooler, stirring, and nitrogen flow at room temperature for 45 minutes (solution 3)
- Dissolve KPS (3) in Milli-Q H<sub>2</sub>O and degas
- Dissolve BIS (3.2) in Milli-Q H<sub>2</sub>O by heating to 60 °C and degas
- Heat solution 3 to 60 °C, check for flocculation, and immediately take 80 mL in 2 60 mL syringes and inject above the reaction mixture simultaneously over approx. 2 minutes
- Initiate reaction by adding the KPS (3) with a syringe into the reaction mixture @400 rpm stirring over a period of 2 minutes
- Proceed for 5 minutes after start KPS addition, and add BIS (3.2) solution over a period of 30 minutes with a syringe pump and 2 10 mL syringes
- Proceed for 2 hours
- Take 1 mL sample with a syringe

**Chemicals shell 4**

- 2.01 g (4) *N*-Isopropylmethacrylamide (NIPMAm)
- 121.9 mg (4.1), 60.9 mg (4.2) *N,N'*-methylenebisacrylamide (BIS) in 20 mL (4.2) Milli-Q H<sub>2</sub>O
- 73.1 mg (4) potassium peroxydisulfate (KPS) in 4.0 mL Milli-Q H<sub>2</sub>O

**Protocol shell 4**

- Purge NIPMAm (4), BIS (4.1) and 80 g Milli-Q H<sub>2</sub>O in a 250 mL flask with straight cooler, stirring, and nitrogen flow at room temperature for 45 minutes (solution 4)
- Dissolve KPS (4) in Milli-Q H<sub>2</sub>O and degas
- Dissolve BIS (4.2) in Milli-Q H<sub>2</sub>O by heating to 60 °C and degas
- Heat solution 4 to 60 °C, check for flocculation, and immediately take 80 mL in 2 60 mL syringes and inject above the reaction mixture simultaneously over approx. 2 minutes
- Initiate reaction by adding the KPS (4) with a syringe into the reaction mixture @400 rpm stirring over a period of 2 minutes
- Proceed for 5 minutes after start KPS addition, and add BIS (4.2) solution over a period of 30 minutes with a syringe pump and 2 10 mL syringes
- Proceed for 2 hours
- Filter particles over hot glass wool
- Take 1 mL mL sample
- Rinse with Milli-Q H<sub>2</sub>O
- Purify and concentrate by centrifugation and resuspension @10000 rpm in two steps
- Determine the weight yield (wtY, Eq 4.1) to scale the reactants in the following steps (here wtY=0.818)

**Chemicals shell 5**

- Sample ('shell 4') with known wtY and volume  $V_{\text{sample}}$
- wtY·2.04 g (5) *N*-Isopropylmethacrylamide (NIPMAm)
- wtY·123.3 mg (5.1), wtY·61.7 g (5.2) *N,N'*-methylenebisacrylamide (BIS) [5%, 2.5% crosslinking] in 20 mL (5.2)

- wtY·74.0 mg (5) potassium peroxodisulfate (KPS) in 4.0 mL Milli-Q H<sub>2</sub>O [0.68 mM]
- 400- $V_{\text{sample}}$  mL (5) Milli-Q H<sub>2</sub>O

#### Protocol shell 5

- Build set-up with a 1 L vessel, nitrogen flow and straight cooler
- Transfer the Milli-Q H<sub>2</sub>O and 'shell 4' into the 1 L three-neck round bottom flask and purge for 30 min with nitrogen at room temperature
- Transfer the NIPMAm (5), BIS (5.1), and functionalised cores to the flask and rinse with the remaining Milli-Q H<sub>2</sub>O
- Purge with nitrogen under vigorous stirring at 75 °C for 45 minutes
- Dissolve KPS (5) in Milli-Q H<sub>2</sub>O and degas
- Dissolve BIS (5.2) in Milli-Q H<sub>2</sub>O by heating to 60 °C and degas
- Initiate reaction by adding the KPS (5) with a syringe into the reaction mixture @400 rpm stirring over a period of 2 minutes
- Proceed for 5 minutes after start KPS addition, and add BIS (5.2) solution over a period of 30 minutes with a syringe pump and 2 10 mL syringes
- Proceed for 2 hours
- Take 1 mL sample with a syringe

#### Chemicals shell 6

- wtY·2.03 g (6) g *N*-Isopropylmethacrylamide (NIPMAm)
- wtY·122.8 mg (6.1) *N,N'*-methylenebisacrylamide
- wtY·73.6 mg (6) potassium peroxodisulfate (KPS) in 4.0 mL Milli-Q H<sub>2</sub>O

#### Protocol shell 6

- Purge NIPMAm (6), BIS (6.1) and 80 g Milli-Q H<sub>2</sub>O in a 250 mL flask with straight cooler, stirring, and nitrogen flow at room temperature for 45 minutes (solution 4)
- Dissolve KPS (6) in Milli-Q H<sub>2</sub>O and degas
- Heat solution 6 to 60 °C, check for flocculation, and immediately take 80 mL in 2 60 mL syringes and inject above the reaction mixture simultaneously over approx. 2 minutes
- Initiate reaction by adding the KPS (6) with a syringe into the reaction mixture @400 rpm stirring over a period of 2 minutes
- Proceed for 2 hours
- Filter particles over hot glass wool
- Take 1 mL mL sample
- Rinse with Milli-Q H<sub>2</sub>O
- Purify and concentrate by centrifugation and resuspension @10000 rpm (about 3 times)

### D.3 Protocol CS21/CS22

#### Chemicals CS21

- 1.60 g C3/EMC4 15.9 wt% functionalised cores [0.254 g cores]
- 1.02 g (1) *N*-Isopropylacrylamide (NIPAm) [0.06 M]
- 69.4 mg (1.1), 34.7 g (1.2) *N,N'*-methylenebisacrylamide (BIS) [5%, 2.5% crosslinking] in 10 mL (1.2)
- 41.6 mg (1) potassium peroxydisulfate (KPS) in 2.0 mL Milli-Q H<sub>2</sub>O [0.68 mM]
- 146.5 g (1) Milli-Q H<sub>2</sub>O

#### Chemicals CS22

- 2.02 g C4/EMC5 7.2 wt% functionalised cores [0.145 g cores]
- 1.02 g (1) *N*-Isopropylmethacrylamide (NIPMAm) [0.06 M]
- 61.9 mg (1.1), 30.9 g (1.2) *N,N'*-methylenebisacrylamide (BIS) [5%, 2.5% crosslinking] in 10 mL (1.2)
- 41.6 mg (1) potassium peroxydisulfate (KPS) in 2.0 mL Milli-Q H<sub>2</sub>O [0.68 mM]
- 146.5 g (1) Milli-Q H<sub>2</sub>O

#### Protocol shell 1

- Build set-up with a 1 L vessel, nitrogen flow and straight cooler
- Transfer ~360 mL of the Milli-Q H<sub>2</sub>O (1) into the 1 L three-neck round bottom flask and purge for 30 min with nitrogen at room temperature
- Transfer the NIPAm/NIPAm (1) and BIS (1.1) to the flask and rinse with the remaining Milli-Q H<sub>2</sub>O (1)
- Weigh functionalised cores in flask
- Purge with nitrogen under vigorous stirring at room temperature for 30 minutes and at 75 °C for 15 minutes
- Dissolve KPS (1) in Milli-Q H<sub>2</sub>O and degas
- Dissolve BIS (1.2) in Milli-Q H<sub>2</sub>O by heating to 60 °C and degas
- Initiate reaction by adding the KPS (1) with a syringe into the reaction mixture @400 rpm stirring over a period of 2 minutes
- Proceed for 5 minutes after start KPS addition, and add BIS (1.2) solution over a period of 30 minutes with a syringe pump and a 10 mL syringes
- Proceed for 3 hours
- Take 1 mL sample
- Rinse with Milli-Q H<sub>2</sub>O
- Purify by a single round of centrifugation and resuspension

#### Chemicals CS21

- 1.02 g (2) *N*-Isopropylacrylamide (NIPAm) [0.06 M]
- 69.4 mg (2) *N,N'*-methylenebisacrylamide (BIS) [5% crosslinking] in 20 mL
- 41.6 mg (2) potassium peroxydisulfate (KPS) in 2.0 mL Milli-Q H<sub>2</sub>O [0.68 mM]

#### Chemicals CS22

- cY-1.02 g (2) *N*-Isopropylmethacrylamide (NIPMAm) [0.06 M]
- cY-61.9 mg (2) *N,N'*-methylenebisacrylamide (BIS) [5% crosslinking] in 10 mL
- cY-41.6 mg (2) potassium peroxydisulfate (KPS) in 2.0 mL Milli-Q H<sub>2</sub>O

**Protocol shell 2**

- Transfer core suspension into a 250 mL flask and dilute to a known total weight of about 120 g
- Take a sample, and dilute exact 100 times in a volumetric flask. Determine the concentration with fluorescence spectroscopy, calculate the core yield cY, and scale reactants with this value (here  $cY=0.843/0.686$ ).
- Transfer the NIP(M)Am (2), BIS (2) into the flask
- Purge with nitrogen under vigorous stirring at room temperature for 30 minutes and at 75 °C for 15 minutes
- Dissolve KPS (2) in Milli-Q H<sub>2</sub>O and degas
- Take a 200 µL sample through the septum with a syringe and analyse with fluorescence microscopy
- Initiate reaction by adding the KPS with a syringe into the reaction mixture @400 rpm stirring over a period of 2 minutes
- Proceed for 3 hours
- Filter particles over glass wool
- Take 0.5 mL mL sample and analyse with DLS and fluorescence microscopy
- Rinse with Milli-Q H<sub>2</sub>O
- Purify other by repeated centrifugation and resuspension (about 3 times)

---

## Modelling and simulation

---

In this appendix, the electrostatic potential developed by Likos *et al.* is benchmarked, and the diffusion in the simulation was tested [90].

### E.1 Benchmark Likos electrostatic potential

The potential which could be used in the simulations to model the microgel's electrostatic interaction was developed by Likos and Colla back in 2015 [90]. To verify the correct handling of the potential by the simulation software, first the pair potentials were reproduced and compared for the system described in the paper. A Python script was written to generate the tables for the LAMMPS simulation software (in potentials.py Fig. 3.4), the potentials generated by this script are in excellent agreement with Likos *et al.* (Fig. E.1). For a proper read-in, that is without any noise in the small  $r$  regime, the bitmap style was taken for quick lookup in the tables, and a linear interpolation was performed between adjacent table values. Interestingly, other look-up and interpolation methods gave inaccurate approximation of the pair potentials at small  $r$ .

In order to benchmark the potential in simulations, the radial distribution function  $g(r)$  of the systems described in the Likos paper was reproduced and compared (Fig. E.2) [90]. Likos *et al.* used the Ornstein-Zernike (OZ) equation, which they solved numerically with the hypernetted-chain closure in an iterative way. Both simulations and the OZ equation can only approximate the  $g(r)$ , and perfect agreement cannot be expected. The number of time steps and the length of a time step are important to obtain an accurate  $g(r)$  of the equilibrium configuration. The system was equilibrated in the first  $1e5$  time steps for all  $\epsilon_H$  values probed, since the  $g(r)$  averaged over the first  $1e5$  and last  $1e5$  time steps (22.9 s) were exactly the same. Even with ten times smaller time steps or ten times more time steps, the first and last averaged  $g(r)$ s were exactly the same. This quick equilibration is because the start configuration was built with  $\epsilon_H = 100 k_B T$  and had already developed close to equilibrium. The small reordering driven by the different potentials was very quick and explains the short equilibration time. For a time step of  $\leq 1e-5 \tau_B$  ( $\leq 2.29e-5$  s), the  $g(r)$  was independent on the time step. For bigger time steps, the oppositely charged particles with  $\epsilon_H = 750$  and  $2000 k_B T$  (Fig. E.1bc) were less associated. This resulted in a lower primary  $g_{+-}(r)$ , and higher primary and secondary  $g_{++}(r)$ ,  $g_{--}(r)$  peak height, because the attractive well in these positive-negative pair potentials is much smaller compared to the  $\epsilon_H = 100 k_B T$  and the forces are bigger near these potential wells. Additionally, a too big bin size for the  $g(r)$  makes the apparent  $g_{+-}(r)$  primary peak height smaller, and thus less accurate. The  $g(r)$ s are in good agreement with OZ, however, the peak height of the  $g_{++}(r)$ , and  $g_{--}(r)$  peaks is slightly higher and the corresponding shape is different. In conclusion, the Likos potential is correctly generated by the Python routines are properly read-in by the LAMMPS software, which makes it a good alternative to the Yukawa potential.

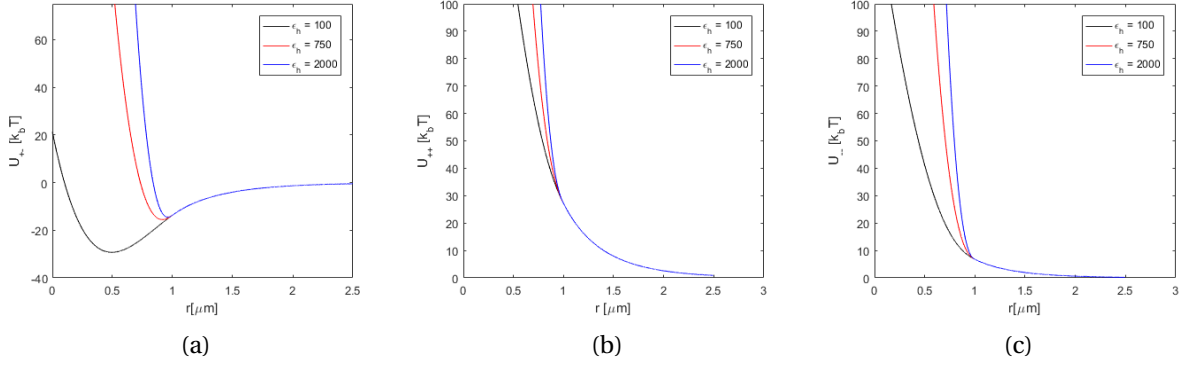


Figure E.1: a-c) The effective pair potentials in a binary system of oppositely charged penetrable macro-ions with a homogeneous charge distribution of charge  $Z_+ = 420e$  and  $Z_- = -210e$ , and a radius  $R_+ = R_- = 0.5\mu\text{m}$ . The pair potentials corresponding to positive-negative (a), positive-positive (b), and Negative-negative interactions (c) are shown. The reduced screening length  $\kappa R = 0.824$  corresponds to a situation where only counter ions of the macro-ions are in solution. The pair potentials with strength parameter of the Hertzian potential  $\epsilon_H$  are shown for  $100k_B T$  (black),  $750k_B T$  (red), and  $2000k_B T$  (blue).

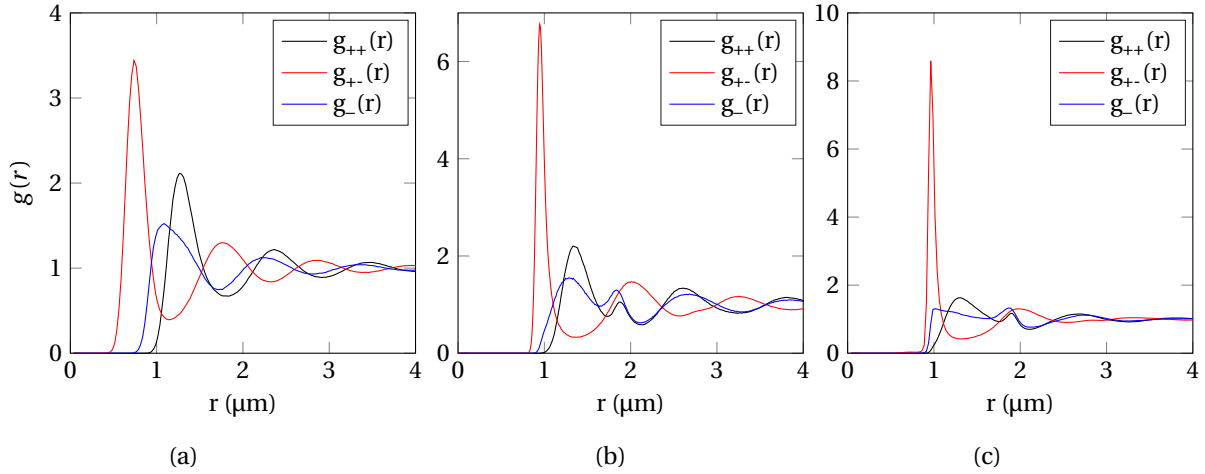


Figure E.2: a-c): The radial distribution functions  $g(r)$  in a binary system of oppositely charged penetrable macro-ions with a homogeneous charge distribution of charge  $Z_+ = 420e$  and  $Z_- = -210e$ , and a radius  $R_+ = R_- = 0.5\mu\text{m}$ . The reduced screening length  $\kappa R = 0.824$  corresponds to a situation where only counter ions of the macro-ions are in solution, and the number density is  $\rho R^3 = 0.06$ . The pair potentials with strength parameter of the Hertzian potential  $\epsilon_H$  are shown for  $100k_B T$  (a),  $750k_B T$  (b), and  $2000k_B T$  (c) between positive-positive (black), positive-negative (red), and negative-negative (blue) macro-ions.



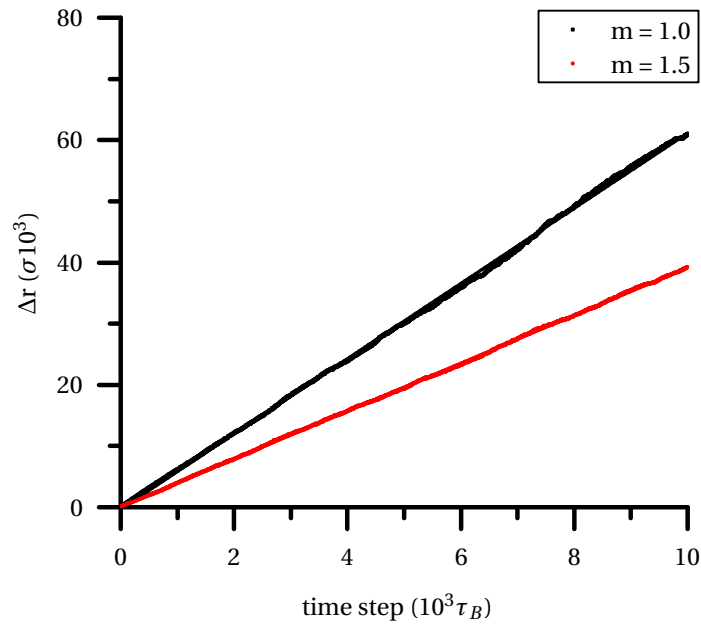


Figure E.3: The mean square displacement of a binary mixture of non-interacting particles with a mass  $m = 1.0$  (black) and  $m = 1.5$  (red) with fit. Each particle type had a number density of  $\rho R^3 = 3e-5$ . The slope corresponds to a diffusion constant  $D = 1.03$  for  $m = 1.0$  and  $D = 0.65$  for  $m = 1.5$ .

## E.2 Diffusion in simulation

As the particle radius was already implicitly incorporated in the interaction potential, the diffusion of the particles in simulation should be controlled without giving them an explicit radius. For this, the Stokes-Einstein equation (Eq. 2.3) in the LAMMPS software was redefined to

$$D = \frac{k_B T}{m\Gamma} = \frac{1}{m}. \quad (\text{E.1})$$

In this equation,  $\Gamma$  is a constant which is set to one, which means that  $D = 1/m$  (Table 2.1), and the mass  $m$  is a way to control the diffusion without giving the particles an explicit radius. In order to check this, a simulation with non-interacting particles was done with a mass 1 and 1.5 (Fig. E.3). The found values retrieved from the slope in the MSD via Eq. 2.1 were in line with Eq. E.1. Therefore, the relation was empirically confirmed, and  $m$  was scaled with the reduced  $\sigma$  in the simulations performed in this thesis.



---

## Pre- and post-processing skeletonization

---

A short and illustrated discussion of pre- and post-processing for skeletonization is given in this appendix. The operations discussed in this Appendix refer to samples imaged with voxel dimension of  $54.1 \times 54.1 \times 125.9$  nm in a  $1024 \times 1024$  px raster. A larger  $z$ -spacing than  $0.13 \mu\text{m}$  was found to give an elongation in the reconstructed binary volume along the  $z$ -direction. A volume up to a depth of  $25 \mu\text{m}$  into the sample could be imaged (Fig. F.1a). The  $z$ -stacks were recorded from deep into the sample to the surface to minimize bleaching deep in the sample, however, bleaching was not observed and scattering was a more dominant factor. Samples recorded at  $40^\circ\text{C}$  were on average of better quality and could be imaged deeper into the sample, because signal was less blurred as a result of scattering. At this temperature, less particles were collapsed, and the refractive index mismatch with the oil was less severe, which led to reduced scattering of the measured signal.

Binarized surface per slice was used as a measure for the data quality, and was found to be roughly constant in a good data set. A  $\sim 10\%$  decrease in surface was found in the slices closest to the surface, as little scattering occurs here, and structure is thus more well-defined. In a good data set, the binarized volume is in excellent agreement with the original image, after manipulation of the image by the steps described below (Fig. F.1g).

### F.1 Pre-processing

**Deconvolution** Deconvolution of the point spread function was expected to increase the contrast at the edge of the features, facilitating binarization. Blind deconvolution of the original image was tried with an initial guess based on Eqs. 2.24 and 2.25. It was found that the initial guess was a determining factor in the outcome of the deconvolution, and the operation could only be optimised by trial and error. This led to an image with increased contrast around the edges, but the image was found to become grained, also within the features, which hampered (automated) binarization (Fig. F.1b). Thus, after deconvolution only, the binarized volume was noisy with jagged edges. Ring-shaped artefacts were observed for some initial guesses, which could be high in intensity. Generally, this could be reduced by omitting the pixels located at the edge of a feature, which caused this artefact, but it defeats the purpose of the operation. The edges of the features became more pronounced after deconvolution, however, this does not outweigh the disadvantageous artefacts and increased contrast within the features.

**Gaussian filtering** Gaussian filtering was required to remove noise and irregularities in the features, mainly in the  $z$ -direction. A large standard deviation ( $\geq 3$ ) had to be chosen in order to obtain a smooth surface in all directions after binarization (Fig. F.1c). A smaller standard deviation in combination morphological closing was found to lead to a rough surface. These irregularities were usually

converted into branches during skeletonization, which complicated analysis of the node structure, and is undesired.

**Binarization** The  $z$ -slices were individually binarized with a set threshold. The minimum and maximum intensity per slice was calculated as the average value of the 10% lowest and highest pixel values. The set threshold in the range of the minimum and maximum intensity was used as real threshold for the binarization (Fig. F.1d). The real threshold was in qualitative agreement with Otsu's method (Fig. F.1h), which is an algorithm to automatically define the optimum threshold value for binarization by minimalisation of the intra-class variance [147]. The threshold determined via Otsu's method could be fitted with a set threshold of 0.5, however, a threshold of 0.7 was found to give the most accurate binarization.

**Morphological closing** Morphological closing is an operation consisting of image dilation followed by erosion, which was performed with an isotropic spherical structuring element. The voxel anisotropy was not accounted for in the structuring element. A small structuring element (e.g. 6 px) did not have much effect, but was performed as back-up to remove irregularities. In general, the data quality was of such good quality that the effects of the morphological closing were negligible (Fig. F.1e). A too large structuring element (e.g. 20 px) was found yield a binary volume which was in discrepancy with the original data as volume was added where the surface curvature was larger than that of the structuring element, and links were created between objects closer apart than the size of the structuring element. A small structuring element was therefore used reduce irregularities to facilitate skeletonization.

**Cleaning** The objects in the binary volume were first identified based on their connectivity, and subsequently removed and the holes were filled (Fig. F.1f). The area of an interconnected object is defined as the actual number of pixels in the region weighed by their position. A connectivity of 26 was used for this determination, which regards adjacent pixels along the diagonal as neighbours within the same object. In general only one big object is found and a multitude of small ones, which are removed. The background pixels that cannot be reached by filling in the background from the edge of the image are filled, which yields a cleaned binary volume which is ready to be skeletonized (Fig. F.2a).

## F.2 Post-processing

**Skeleton to graph** The skeleton was converted into a weighed adjacency matrix (graph) described by nodes and edges as formulated in graph theory. Clusters of voxels with more than two neighbours each were defined as a node, and groups of connected voxels with two neighbours each were defined as edge. The minimum edge length was threshold with 2 px, and all edges below this threshold were merged. The resulting graph was weighed by the Euclidean distance between the centre of mass of the nodes via the voxels in the edge. The distance between two adjacent pixels in the path was calculated with Pythagoras theorem in 3D.

**Cleaning graph** The graph was cleaned by preservation of the edges and nodes that occur in the shortest path length from one box edge node to another in all directions (Fig. F.2b). All box edge nodes were determined, which means that the node has at least one coordinate at the outer border of the focal volume. The shortest distance between the all possible combinations of nodes was determined with Dijkstra's algorithm, and a subgraph was made from all nodes that occur in one or more of the shortest paths. All nodes within 10 px from the outer border of the focal volume in the  $x$ ,  $z$ - and  $y$ ,  $z$ -plane were removed. This subgraph was reduced by first identifying all nodes with a degree of two, and creating an edge between its neighbours with the sum of the weight of the edges connected to the identified node. Subsequently, the identified node and its edges were removed, which

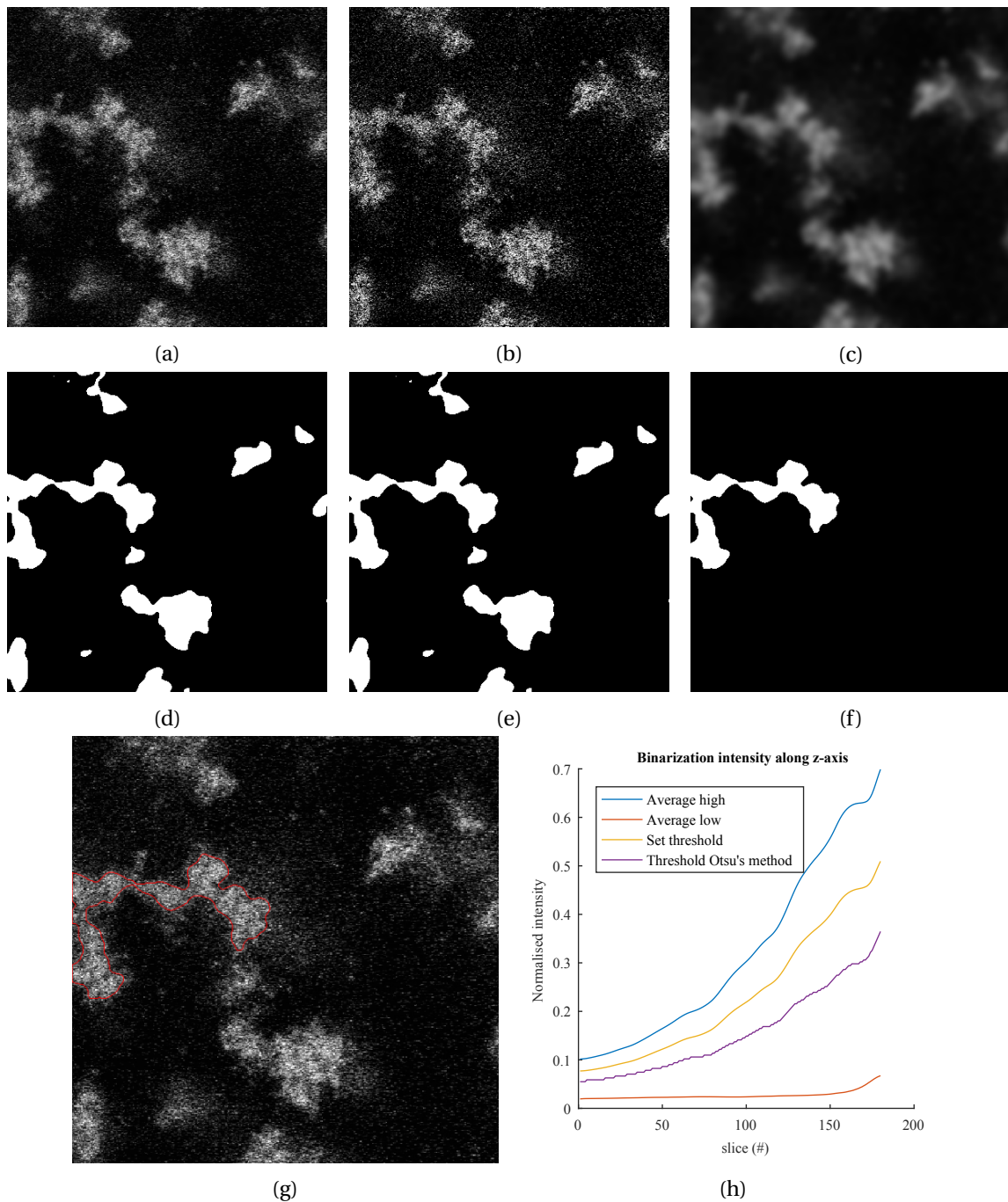


Figure E1: a-g): Deconvolution of the original  $400 \times 400$  px 2D example image taken at  $11 \mu\text{m}$  into the sample (a) was found to increase contrast in the features (b), which complicates binarization. In contrast, accurate binarization was observed after smoothing of the image (a) with a Gaussian filter (c). The binarized image (d) was subsequently morphologically closed (e), which had little effect on a good data set. In a final step, the objects with an amount of pixels smaller than 0.8 times that of the largest object were removed and holes were filled (f). An overlay of the binary contour (red) of (g) on the original image (a) shows that the resulting binary object is in excellent agreement with the input data. Similar performance was found for operations in 3D. h): Plot of the 10% dimmest and brightest pixels and the set threshold as function of the  $z$ -slices. The set threshold is in excellent qualitative agreement with Otsu's method.

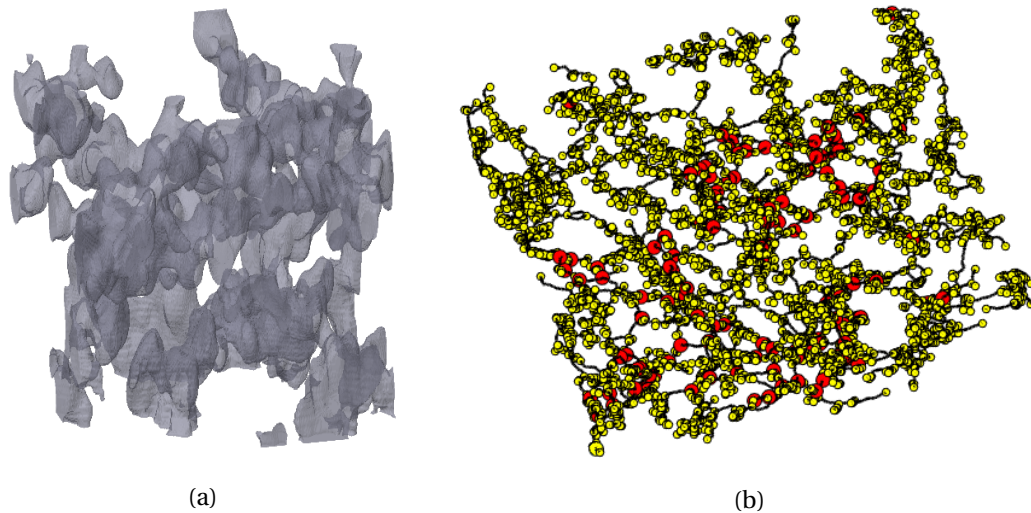


Figure E2: a): Plot of the surface of a cleaned binary volume ( $22 \times 22 \times 23 \mu\text{m}$ ). b): Plot of a skeletonized gel structure in real space ( $55 \times 55 \times 23 \mu\text{m}$ ), with the nodes retained after cleaning indicated in red, and all other nodes indicated in yellow.

effectively resulted in removal of the node with preservation of the weighed connection between its neighbours. Subsequently, all end nodes were iteratively removed, which led to a cleaned structure containing the nodes and edges that contribute to the percolating network. This cleaning procedure was found to be very sensitive to the distribution of the box edge nodes. In the case that the cleaned binary volume does not border the focal volume on one side, the resulting shortest paths do not include a large part of the volume and yields a network with a different distribution of edge weights. Manual inspection showed that the spatial distribution of preserved nodes was very dependent on the distribution of the box edge nodes, and in some cases good results were obtained as shown in Fig. E2b. A smaller zoom would likely yield a more homogeneous spatial distribution of edge nodes as the structure is captured on a larger length scale. The standard deviation in the edge weights is of the same order of magnitude as the edge weight itself, which indeed indicates a capricious structure, and probably poor cleaning. Same results were obtained for other cleaning methods, including the removal of end nodes, and all were very sensitive to set threshold values. The algorithms to clean the graph should be improved further, and could be benchmarked against the mesh size determined with other techniques to check the validity of the edge weights.

### F.3 Analysis

**Volume over surface** The volume and surface of the binary volume was estimated with Minkowski measures, which approximates the surface as being smooth and continuous [113]. The area on the border of the focal volume was not taken into account.

**Indirectness** The indirectness is defined as the path length from an edge node on one side of the focal volume to one at the other side along either the  $x$ - or  $y$ -direction, divided by the Euclidean distance between these nodes. First, the box edge nodes were identified in the  $x, z$ - and  $y, z$ -plane. The shortest path between these nodes was determined with Dijkstra's algorithm, along either the  $x$ - or  $y$ -direction for all possible combinations. This value was divided by the Euclidean, or direct distance to obtain the indirectness. The standard deviation within one sample was in the order of 5-10%, which indicates that the obtained values are significant.